Model-based optimization of magnetic control in the TCV tokamak: design and experiments

Federico PESAMOSCA

EPFL

École
polytechnique
fédérale
de Lausanne

2021

Non chi comincia ma quel che persevera.
- Leonardo da Vinci

Abstract

Thermonuclear controlled fusion is a promising answer to the current energy and climate issues, providing a safe carbon-free source of energy which is virtually inexhaustible. In magnetic confinement thermonuclear fusion based on tokamak reactors, hydrogen fuel in the state of plasma is confined using a system of external and self-generated magnetic fields. This thesis contributes to the development of magnetic confinement fusion research by applying techniques derived from control engineering to designing magnetic controllers for tokamak plasmas. Specifically, a new design for feedback control of plasma shape and position in the TCV tokamak is provided, and its efficacy is studied in dedicated simulations and experiments.

Elongated plasmas lead to improved plasma performance in tokamaks, which is key to sustaining fusion conditions in reactors. The required magnetic field for shaping the plasma column however results in an unstable equilibrium that makes feedback control of the vertical plasma position mandatory. Active stabilization of the axisymmetric plasma vertical instability is a standard feature of elongated tokamaks and will be a fundamental feature in the ITER magnetic control system, since a loss of vertical control and the subsequent plasma disruption can lead to unacceptable heat loads on the plasma facing components.

The TCV tokamak is the ideal benchmark for investigating the effect of plasma shaping on tokamak physics and performance, with its system of 16 independently powered poloidal field coils and a vessel with an elongated cross section. Shape and position control are coupled problems in TCV as they share the same poloidal field coils as actuators, requiring a multivariable approach to designing magnetic controllers.

In this thesis, controller design for TCV is based on a model for the coupled plasma-vessel-coils electromagnetic dynamics: the RZIp model. In this axisymmetric model, the plasma current distribution is fixed but is free to move radially and vertically in the poloidal plane of a toroidal reference frame. An extension to this model is suggested, relaxing the assumption of rigid displacement in the radial direction to include plasma shape deformation and leading to a semi-rigid RZIp model which better fits numerical equilibria.

An improvement to the existing algorithm for shape and position control in TCV is then proposed. In this new approach, tuning of the plasma position controller, in charge of

vertical stabilization, can be performed independently of the shape controller, which itself acts on a stable system. Static decoupling is achieved and the shape controller is designed on the basis of an improved model for the plasma deformation, which includes the plasma contribution to the static magnetic flux perturbation. Simulations in closed loop with the RZIp model are provided to evaluate several optimized schemes.

Finally, the vertical controller is optimized including the plasma dynamics as part of the controller design. Structured H-infinity, extending classical H-infinity to fixed-structure control systems, is applied to obtain a controller using all available coils for position control, and in particular a coil combination optimized for vertical stabilization. Closed-loop performance improvement is demonstrated in dedicated TCV experiments, confirming the simulation results and paving the way for the routine integration of the optimized position and shape controller in TCV discharges.

Federico Pesamosca

Sinossi

La fusione termonucleare controllata è una promettente soluzione per gli attuali problemi energetici e climatici, fornendo una fonte energetica pulita e virtualmente inesauribile. Nella fusione termonucleare a confinamento magnetico basata sui reattori tokamak, l'idrogeno come combustibile nello stato di plasma è confinato usando un sistema di campi magnetici esterni ed autogenerati. Questa tesi contribuisce allo sviluppo della ricerca sulla fusione a confinamento magnetico applicando tecniche derivate dall'ingegneria dell'automazione per progettare controllori magnetici per i plasmi nei tokamak. Nello specifico, propone uno schema innovativo per il controllo in feedback della forma e posizione del plasma nel tokamak TCV, la cui efficacia è studiata in simulazioni ed esperimenti dedicati.

I plasmi elongati permettono di ottenere migliori prestazioni nei tokamak, che saranno fondamentali per mantenere le condizioni di fusione nei reattori. I campi magnetici richiesti per modellare la colonna di plasma determinano tuttavia un equilibrio instabile che rende necessario il controllo in feedback della posizione verticale del plasma. La stabilizzazione attiva dell'instabilità verticale assialsimmetrica è un tratto comune dei tokamak elongati e sarà una caratteristica fondamentale del sistema di controllo magnetico di ITER, in quanto la perdita di controllo verticale e la conseguente disrupzione del plasma può condurre a carichi termici inaccettabili sui componenti della prima parete. Il tokamak TCV è la piattaforma ideale per studiare gli effetti della forma del plasma sulla fisica e sulle performance nei tokamak, con il suo sistema di 16 bobine di campo poloidale alimentate indipendentemente e il suo vessel con una sezione trasversale elongata. Il controllo della forma e quello della posizione sono problemi accoppiati in TCV in quanto condividono come attuatori le stesse bobine di campo poloidale, il che richiede un approccio multivariabile per la progettazione di controllori magnetici.

In questa tesi, il design dei controller si basa su un modello per la dinamica elettromagnetica accoppiata di plasma, vessel e bobine: il modello RZIp. In questo modello assialsimmetrico, la distribuzione di corrente del plasma è fissa ma è libera di muoversi radialmente e verticalmente nel piano poloidale di un sistema di riferimento toroidale. Un'estensione di questo modello è suggerita, rilassando l'ipotesi di spostamento rigido nella direzione radiale per includere le deformazioni del plasma e risultando in un modello semi-rigido che meglio si adatta ai dati sperimentali.

Viene quindi proposto un miglioramento dell'attuale algoritmo per il controllo di forma

e posizione in TCV. In questo nuovo approccio, la taratura del controllo di posizione, responsabile della stabilizzazione verticale, può essere effettuata indipendentemente dal controllore di forma, il quale agisce su un sistema stabile. Si ottiene così un disaccoppiamento statico e il controllore di forma è progettato basandosi su un modello migliorato per la deformazione del plasma, che include il contributo del plasma alla perturbazione statica del flusso magnetico. Delle simulazioni in anello chiuso con il modello RZIp sono effettuate per valutare diversi schemi ottimizzati.

Infine, il controllore verticale è ottimizzato includendo la dinamica del plasma come parte integrante del design del controllore. La sintesi H-infinity strutturata, che estende la H-infinity classica a sistemi di controllo a struttura fissa, è applicata per ottenere un controllore che usa tutte le coil disponibili per il controllo verticale, ed in particolare una combinazione di coil ottimizzata per la stabilizzazione verticale. Il miglioramento delle performance ad anello chiuso è dimostrato in esperimenti dedicati su TCV, confermando i risultati delle simulazioni e aprendo la strada per l'integrazione e l'utilizzo operativo del controllore ottimizzato di posizione e di forma nelle scariche di plasma di TCV.

Parole chiave: fusione nucleare, tokamak, plasma, TCV, controllo in feedback, controllo magnetico, instabilità verticale, H-infinity, sistemi dinamici, ricostruzione dell'equilibrio

Contents

List of Figures

Federico Pesamosca

Federico Pesamosca

List of Tables

1 Introduction

Along its history, humankind developed increasingly complex technology to exploit the sources of energy available in the environment: burning recently harvested plants, consuming fossil fuels formed over geological ages and breaking heavy nuclei synthesized in the core of ancient stars. This journey of progress allowed humanity to release energy which was stored further and further in the past. Taming nuclear fusion would mean digging in the very origin of this Universe and projecting our existence ahead in the distant future.

Nuclear fusion refers to the reaction by which two lighter nuclei merge to form a heavier element. For a set of reactants this determines the release of a large amount of energy due to the increase of binding energy per nucleon. This reaction is a promising answer to the current energy and climate issues, providing a safe carbon-free source of energy whose candidate fuel is as abundant as seawater. Exploiting it in a controlled way requires however extreme conditions to be sustained, where the matter exists only in the plasma state. The most explored technological solution for realizing this is the tokamak concept, which has been developed since the second half of the 20th century. In this machine, the plasma is confined in a toroidal shape due to its interaction with externally and self generated magnetic fields. Physical and technical challenges to overcome in order to build a fusion reactor for energy production have been much harder than expected from the initial, optimistic predictions, with unexpected roadblocks and lucky discoveries. Since the early days of fusion research the accumulated expertise of dozens of experimental machines and a community of thousands of scientists provided a solid foundation to the field of plasma physics, and tokamak technology has made tremendous progress. We are at a point where the exploitation of nuclear fusion as a feasible source of energy is moving from a physics problem, where the fundamental dynamics of fusion plasmas is to be understood, to an engineering challenge, where several reactor prototypes are currently under construction.

The goal of this chapter is to introduce the tokamak concept and the basis of nuclear fusion in a historical perspective up to its present status. A strong emphasis is placed upon the control issues faced in tokamaks, which allows presenting the main topic of this thesis dealing with magnetic control of tokamak plasmas. The application of techniques derived from control engineering to tokamak operations is a success story, which allowed reaching otherwise unattainable performance in fusion plasmas and will provide a paramount contribution in the design and realization of fusion reactors for energy production.

1.1 A brief history of fusion research

1.1.1 The foundation of nuclear fusion and plasma physics

The study of nuclear fusion has its origin in basic questions about the source of energy in stars. By the end of the XIX century, Lord Kelvin estimated the Earth to be less than a hundred million years old, a time which would have been required to cool to its actual temperature following classical thermodynamics [1, p. 1]. This amount of time, however, was contested by geologists and not sufficient even for Charles Darwin to comply with his evolution theory. The Sun, furthermore, posed another question since neither chemical reactions nor gravitational contraction were sufficient to provide an energy output for a time longer than 20 million years in our star.

It was only breaking of the axiom of atom immutability by Antoine Henri Becquerel in 1896 that solved these inconsistencies as radioactivity could explain the Earth's hidden source of heat and suggest a much longer age for stars. The mass defect of various isotopes was indeed measured in the 1920s and explained by a difference in their binding energy in their nuclei by the famous equivalence of mass and energy stated by Einstein in 1905. This was a new form of subatomic energy which could be released during the transmutation of an element into another in a way that chemistry alone could not explain.

The British astronomer Arthur Eddington was among the first to suggest that the conversion of hydrogen into helium could be taking place in the Sun [2]. Some time later, in 1929, Atkinson and Houthermans invoked Gamow's quantum theory of barrier penetration to overcome Coulomb repulsion among nuclei, introducing the concept of nuclear fusion [3]. The effort of numerous physicists was required throughout the golden age of quantum mechanics to finally obtain a complete theory of nuclear fusion by the end of 1930s. It is now commonly accepted that the proton-proton fusion reaction chain provides the fundamental source of energy in stars and at the same time, due to its low reaction rate, it is the ultimate factor determining their long life compared to Earth age. Within a star, as long as nuclear fusion fuel is available, an equilibrium is maintained on astronomical time scales, compensating the gravitational attraction with radiative expansion. In this equilibrium, temperatures and densities are such that the constituting matter of stars is maintained in the so-called plasma state.

A plasma is a system formed of a macroscopic number of charged particles which is highly conductive and is globally, but not necessarily locally, neutral. Such condition can be reached in matter when temperature overcomes a threshold for ionization, therefore collisions among neutral atoms are sufficiently energetic to strip the electrons from the respective nuclei. This state of matter was first defined by Irving Langmuir[I] during experiments on gas discharges in 1928 [4]. In his work he introduced the concepts of plasma frequency and Debye length, important parameters for describing the collective long range behavior characterizing plasmas in opposition to neutral gases.

[I]Langmuir invented metal probes to study the plasma via direct contact, a tool still used nowadays and known as Langmuir probes.

Federico Pesamosca

The description of plasma physics is indeed performed not only through the study of its single components but also with a collective treatment of its dynamics based on statistical mechanics. In this framework a great contribution was provided by Russian physicists in the years before, during and after the Second World War. In particular Anatoly Vlasov considered an extension of Boltzmann equation for the evolution of plasma distribution function including the effect of averaged self-consistent electromagnetic fields in a collisionless plasma [5]. Particle-wave interaction is a fundamental characteristic of plasmas, which was first formalized by Lev Landau in a pioneering work describing the collisionless damping of plasma waves due to particles traveling close to its phase velocity [6]. The study of plasma physics was furthermore of great interest for astrophysics as over 99% of the matter in the observable universe is in the plasma state. In this context, Hannes Alfvén, a Swedish astrophysicist, introduced the concept of guiding center for a particle to study the dynamics of charged particles in Earth's magnetic field. His most important contribution concerned the description of plasma as a single conducting fluid, described in his 1950 book *Cosmical Electrodynamics* [7]. This approach, which granted Alfvèn the Nobel price in 1970, is now defined magnetohydrodynamics (or MHD) and is valid for spatial and temporal time scales larger than the ones defined by Debye length and the inverse of the Debye frequency. From his study, a paramount result emerges in which a carefully designed combination of external and self generated magnetic field counterbalances the tendency of a plasma to expand due to pressure, introducing the concept of magnetic confinement. The possibility of confining a plasma using magnetic fields instead of gravity as it happens in stars is fundamental to exploit nuclear fusion as a source of energy for peaceful purposes as it allows the design of power plant sized reactors.

1.1.2 Towards magnetic confinement fusion

The first large scale human-provoked release of energy from nuclear fusion was the thermonuclear bomb tested by the United States in the Enewetak atoll in 1952 and soon followed by its Soviet counterpart in 1953 developed by a team directed by Igor Kurchatov and Igor Tamm. This is in stark contrast with nuclear fission whose first technical application was a reactor for controlled energy production: the Chicago pile developed in 1942. Although this was notoriously a step of the Manhattan project for developing the first atomic bomb, Enrico Fermi demonstrated that nuclear fission could be used to release a controlled amount of power and set the base for the development of civil nuclear fission reactors in the decades following the Second World War, starting the so-called Atomic age.

An organized effort was initiated under the shroud of secrecy at the beginning of the Cold War in the context of the race for technological primacy. On both sides of the Iron Curtain, one important goal was to be the first in exploiting nuclear fusion as well as a source of energy. Various project were initiated almost independently in US, UK and USSR to obtain a scheme generating plasmas with temperature and density much higher than those obtained during gas discharges to allow sustained and stable nuclear fusion reactions. Most projects relied on the concept of magnetic confinement: linear pinches, toroidal pinches and magnetic mirrors were among the schemes explored in that period. All
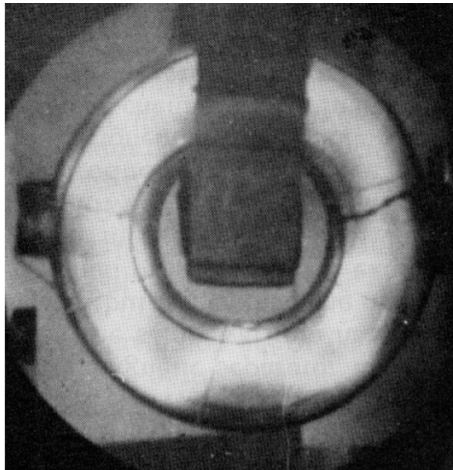
Figure 1.1 − Kink instability in a toroidal pinch of 0.3m major radius (Fig. 1.8 [1]).
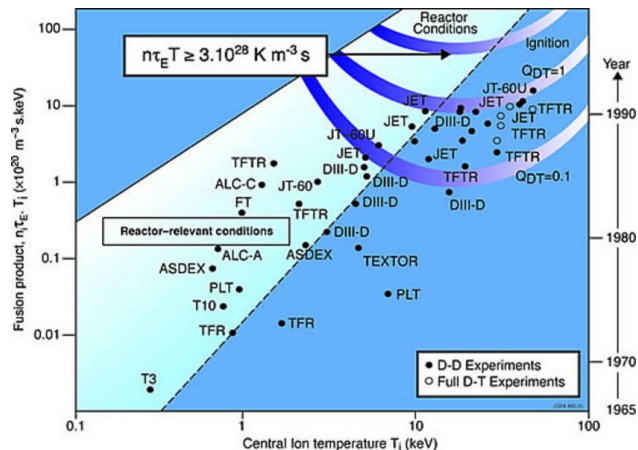
Figure 1.2 − Achieved triple product in various reactors. Source: *EUROfusion.*

nuclear-related projects were however classified and little scientific exchange was possible in the first tense years of the Cold War. No mainstream attention was given to fusion to the point that in the 1955 "Atoms for peace" conference for peaceful exploitation of nuclear energy held in Geneva, nuclear fusion was only briefly mentioned in the opening. The reality was that the hope for a quick success as it happened for fission was facing unexpected roadblocks. Scientists from both East and West were scared that, on the other side of the Iron Curtain, research on thermonuclear controlled fusion was proceeding at a faster pace. Indeed, they were facing the same difficulties. A zoology of plasma instabilities (Fig. (1.1)) led to a reduction in the quality of confinement and consequent plasma losses did not allow closing the gap towards controlled nuclear fusion, let alone the possibility of sustaining those conditions for time scales sufficient for power production. Research topic were overlapping without beneficial competition due to the lack of open communication. As an example, Lev Artsimovich began his contribution at the IAU Symposium on Electromagnetic Phenomena in Cosmical Physics held in Stockholm in 1956 with a derivation of a condition for steady power generation in a thermonuclear reactor, based on a relationship between density n, temperature T and ion lifetime τ_i in a plasma [1, p. 24]. This was essentially the famous criterion derived one year before by John D. Lawson, which was however kept secret and would have been declassified and published only one year later in 1957 [8].

From Lawson's work it is possible to determine the requirements for a plasma composed of 50 % Deuterium and 50 % Tritium to ignite, meaning that it does not require external power injection to sustain fusion conditions. This derivation was performed from a power balance of a generic fusion reactor and results in a condition on density (n), temperature (T) and confinement time (τ_e) of the plasma, where the last is defined as the ratio between

plasma total energy and power losses. This determines a minimum threshold of

$$n \, T \, \tau_e \geq 3 \times 10^{21} \, \text{keV} \quad \text{s} \quad \text{m}^{-3}. \tag{1.1}$$

and it is possible to determine a minimum for D-T reaction of $n \, \tau_e = 1.5 \times 10^{20} \, \text{m}^{-3}\text{s}$ setting $T = 20\text{keV}$. The beauty of this criterion is that it summarizes the complex and multiphysics problem of nuclear fusion to a simple figure of merit and is valid for any rector. Since then and up to present day experimental results in candidate reactors are regularly compared in Lawson diagrams (Fig. 1.2).

Among the numerous reactions which can be considered for controlled thermonuclear fusion, the D-T reaction considered by Lawson has received the most attention from scientists and is still nowadays considered the best candidate for thermonuclear controlled fusion. In this reaction

$$\text{D} + \text{T} \rightarrow {}^4\text{He}(3.5 \, \text{MeV}) + n(14.1 \, \text{MeV}) \tag{1.2}$$
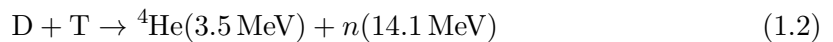
where D is deuteron and T is triton, respectively nuclei of Deuterium ${}^2\text{H}$ and Tritium ${}^3\text{H}$. This reaction is among the most fit for large scale power production, combining a high energy yield and a cross-section [II] peaking at a low average temperature compared to other fusion reactions. Deuterium is furthermore a stable isotope, which is relatively abundant in sea water, while Tritium is a radioactive isotope with a half life of slightly above 12 years. Although the first load will be derived from existing fission reactors, in a power plant it is planned that Tritium will be bred from the reaction of the fusion-produced neutron with the Lithium intentionally placed in the walls surrounding the plasma.

The confinement time in magnetically confined plasmas remained a serious limitation towards a working reactor in the first years of fusion research. The charged particles are in fact subjected to a diffusion process following Coulomb collision that makes the plasma leave its magnetic cage in an unavoidable way. A collisional approach allowed deriving an estimate of the plasma confinement time from classical and neoclassical transport theory, which however resulted way more optimistic than the one observed in experiments. The origin of this discrepancy was the "anomalous" diffusion deriving from plasma turbulence, determining a faster mixing of the hot core plasma with the colder edge. The required dimension of an experimental reactor doomed by the so-called Bohm diffusion was way beyond technical feasibility. Nuclear fusion research focused on finding new configurations to overcome this limit.

1.1.3 The tokamak

In the years after the Second World War, in Soviet Union, thermonuclear controlled fusion research was centralized under the Council on Magnetic Thermonuclear Reactors, headed by Igor Kurchatov with the double goal of developing nuclear weapons and studying the

---

[II]the cross-section in nuclear physics is a measure of the reaction probability which is usually given as an estimate of the effective area which a nucleus offers as a target to the colliding reactant, traditionally measured in barns (b) where $1b = 10^{-24} cm^2$
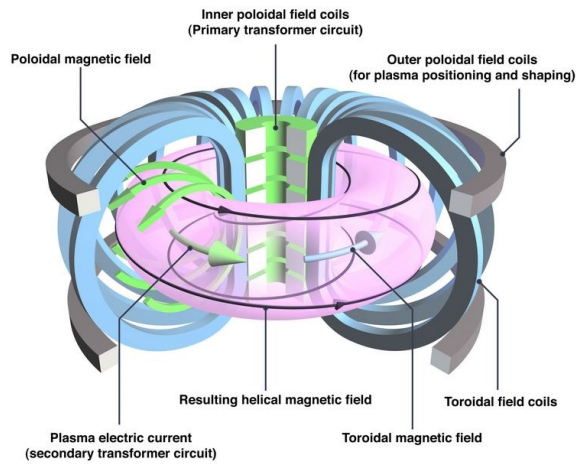
Figure 1.3 – The tokamak main components, including plasma and externally and self-generated magnetic fields.
Source: *EUROfusion.*
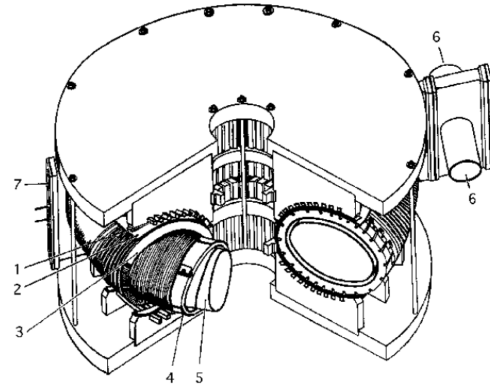
Figure 1.4 – The Moscow Torus 5 or T-1, the first machine to be named tokamak (Fig 5.3 [1])

feasibility of fusion for power generation. Among the various configurations for magnetic confinement that were explored, an evolution of toroidal pinch design was developed by Igor Tamm and Andrej Sakharov where an ohmically induced plasma current and strong stabilizing external magnetic fields confined the plasma [9]. In 1959, the Moscow torus 5 (Fig 1.4), which was later named T-1, was the first to be officially defined *tokamak* which is an acronym for **to**roidalnaya **ka**mera for toroidal chamber and **ma**gnitnymi **ka**tushkami for magnetic coils.

In a tokamak (Fig 1.3), a proper confinement of the plasma is obtained exploiting the Lorenz force to which a charged particle is subjected while moving in a magnetic field. This force is expressed as as $\mathbf{F} = q(\mathbf{E} + \mathbf{v} \times \mathbf{B})$, where q is the electric charge, $\mathbf{v}$ is the velocity and $\mathbf{E}$ and $\mathbf{B}$ are electric and magnetic field respectively. As a consequence of the Lorentz force, charged particles tend to move in helical trajectories along a magnetic field line. Confinement is achieved when the magnetic field lines are closed, such that particles remain in a finite volume. In a tokamak, an axisymmetric magnetic field is obtained with a combination of external and plasma currents. A toroidal field $\mathbf{B_t}$ is generated with currents flowing in a set of coils disposed on the poloidal plane. While it is possible to determine a set of closed magnetic field lines using a toroidal field only, the particle drift determined by field inhomogeneity would lead to charge separation in the plasma and loss of the plasma due to the consequent electric fields. It is therefore necessary to add a poloidal field $\mathbf{B_p}$ generated in a tokamak by a toroidal plasma current. The plasma particles stream along the resulting helical magnetic field with a periodic movement in regions of opposing drifts, allowing a proper confinement and stabilizing the configuration. The plasma current is induced using the plasma as the secondary circuit in a transformer through a current ramp in the central solenoid. Since the primary current cannot rise indefinitely, a tokamak is an inherently pulsed device which can be a drawback for a power plant. Over time, additional

sources of non-inductive currents were discovered, as the self-generated bootstrap current [10], or developed with external sources, such as heating and current drive schemes. A further set of poloidal field coils is used to modify the poloidal magnetic field in a tokamak to counterbalance the tendency of the plasma to expand radially and shape the plasma cross section. An important parameter for plasma equilibrium is the safety factor

$$q = \frac{\partial \phi}{\partial \psi} \tag{1.3}$$

where ϕ is the toroidal magnetic field flux and ψ is the poloidal magnetic field flux. The safety factor can be interpreted as the number of toroidal turns a field line must complete to cover a poloidal turn, indicating the degree of helicity of the field lines, and is paramount in the evaluation of MHD stability.

Early experiments confirmed the validity of Kruskal-Shafranov stability conditions for the safety factor and a successful series of tokamaks was built in Soviet laboratories. However, when Lev Artsimovich reported the staggering results of T-3 at an international conference in 1968 at Novosibirsk, the first reports were met with remarkable suspicion, as they looked too optimistic compared to former results in magnetic confinement machines. These doubts were dissipated when the figure of electron temperature above 1000 eV was confirmed by an independent team from Culham using a new laser-based Thomson scattering technology for plasma diagnostics [11]. Although many devices were reported in Novosibirsk to defy the limits imposed by Bohm's law with improved confinement, the tokamak had the potential to be scaled up to larger performance by increase in size and magnetic field in order to reach fusion conditions.

The tokamak fever spread in the US right before the oil crisis began in 1973, which indirectly contributed to an increased funding for exploring this promising way to an alternative energy source. The Model-C stellerator, whose original design was proposed already in 1951 by Lyman Spitzer, was rapidly converted to a tokamak and soon confirmed the results of T-3. Following a successful series of lectures of Artsimovich at MIT [1, p. 120], the construction of the first tokamak of ALCATOR series began. In San Diego, the General Atomics laboratory started studying extremely shaped plasmas at high elongation, a design that would evolve in the doublet concept where two plasma columns lie separately above each other. The same happened in Europe and Japan where a set of laboratories committed to major investments in this new technology. In France TFR reached a record 400 kA of plasma current. In Italy high toroidal field configurations were explored with FT near Rome. The British paused stellerator research to design their first tokamak DITE in Culham and the same happened in Garching in Germany. In Japan the JAERI site started operating JFT-2, and in the same site it will eventually build JT-60. In Soviet Union the T series was extended with enhanced current in T-4 and introducing coils for time-varying vertical magnetic field, confirming plasma equilibrium theoretical results and standardizing the use of magnetic feedback control in tokamaks [12]. By the end of 1970s there were over 70 tokamaks active world-wide and commercial fusion seemed closer than ever.

As the progress to the higher temperatures and density necessary for fusion proceeded,

new solutions were required to heat the plasma. Ohmic heating was not sufficient anymore since resistivity decreased with temperature in plasmas as $\eta \sim T_e^{3/2}$, a result derived by Lyman Spitzer already at the beginning of the 1950s [13]. Radiofrequency heating, explored already in stellarators, allowed transmitting the energy of an electromagnetic wave generated outside the tokamak and resonating with the plasma. This heating scheme, which includes the possibility of generating extra plasma current drive, is still widely applied having the possibility to control precisely the energy deposition location. Another solution is neutral beam heating where a beam of ions is accelerated, neutralized and subsequently injected into the plasma. The neutral particles, not deflected by the magnetic field, are able to penetrate in depth before ionizing and converting their kinetic energy in plasma energy through a series of collisions. The so-called NBI is still the workhorse of tokamak heating systems and has the further capability of injecting momentum regulating plasma rotation.

Plasma physics research proceeded steadily with new steps towards fusion condition at each new generation of tokamaks. Anomalous diffusion was however always the main obstacle to the realization of a reactor for energy production. Despite the improved heating systems, confinement time was observed to scale with the inverse of heating power, an observation confirmed with experiments on multiple machines which would have required extremely large and uneconomical reactors. A turning point was the discovery in 1982 of a new state of the plasma in the ASDEX tokamak plasmas: the so called H-mode [14], characterized by a confinement time higher by a factor two compared to the standard L-mode. The enhanced confinement is caused by turbulence suppression in the edge of the plasma thanks to poloidal plasma sheared flows, which can be sustained with a sufficient power input. The L-H transition could be reproduced in tokamaks around the world able to shape the plasma into a diverted cross section including a magnetic null on the last closed flux surface. In this period an always increasing comprehension of the plasma stability limits was developed, especially in terms of magnetohydrodynamic hard and soft limits, such for example the Beta limit described by Troyon [15], combining theoretical, numerical and experimental efforts.

This enhanced understanding allowed the design of optimized tokamaks, with growing focus on shaping and plasma-wall interaction (DIII-D, ASDEX Upgrade, JT-60, Alcator C-Mod) that were realized in the second half of the 1980s. The way to overcome the confinement limitation following the validated multi-machine scaling laws was open: machines were upgraded increasing in size, with ever more powerful heating systems and magnets [16]. By the early 1990s, the astronomical temperatures required for fusion were achieved routinely on several experiments and the progresses mapped on Lawson diagrams (Fig 1.2) resembled those predicted by Moore's law for electronics. The triple product $nT\tau_E$ increased by orders of magnitude from the results obtained in the first magnetic confinement devices presented in the meeting on Peaceful Uses of Atomic Energy held Geneva in 1958.

In 1991, JET, still at present the flagship European tokamak, carried out experiments with a mixture of D and a reduced amount of T for two pulses, each producing a peak

fusion power of 1.7 MW and demonstrating safe operation of tritium handling systems [17]. In 1993, TFTR began a three year campaign using 50% T 50% D plasmas, the fusion fuel mixture envisioned for the first fusion power plants, releasing a peak of over 10 MW of fusion power [18]. A new field of research was estabilished, focusing on the study of alpha particle collective effects and the dynamics of fast ions which will be generated in fusion plasmas. The current fusion record is still held by the last D-T JET campaign of 1997, when in a set of ≈ 100 shots a peak of 16 MW was released [19]. However, in all these experiments, the fusion gain Q defined as

$$Q = \frac{\text{fusion power}}{\text{heating input power}} \tag{1.4}$$

was always lower than unity. In the case of ignition, where no power is required to maintain the reaction and the heat leaving the plasma is compensated by the one generated by fusion, $Q \rightarrow \infty$ would be achieved. In a commercial fusion power plant, the necessary condition is reaching $Q > 1$, which means that the reactor behaves as an energy amplifier. This is the goal of future prototype fusion power plants.

1.1.4 Future fusion reactors

In 1985, at the meeting of American and Soviet leaders Reagan and Gorbachov in Geneve, a collaboration between the two superpowers for studying the feasibility of a thermonuclear fusion reactor was initiated [20]. This led to the ITER agreement reached in 1987 at Reykjavik among different nations, which determined the start of the study for an international fusion facility. The choice of the name has a dual significance, being both latin for "the way" and an acronym for **I**nternational **T**hermonuclear **E**xperimental **R**eactor. The path to ITER was not straightforward. The end of the Cold War and the dissolution of Soviet Union determined new equilibria in a multipolar world and the collaboration for the realization of the ITER project was deeply affected. At present, the members to this international effort include China, the European Union, India, Japan, Korea, Russia and the United States. Following the Engineering Design Activity developed from 1992 to 2001, the site where the reactor would be built was set only in 2005. In 2013 the construction began in Cadarache (France) and at present it is still ongoing, with the first plasma to be realized in 2025. The main goal of ITER is determining the viability of nuclear fusion as a source of energy [21]. Apart from plasma Ohmic heating, the external power input used for reaching sustained fusion conditions will be guaranteed by radiofrequency heating of 40 MW and a NBI system able to provide 33 MW [22]. This will allow producing up to 500 MW of fusion power out of 50 MW of absorbed power from a D-T plasma. Two main scenarios are predicted for ITER, one in pulsed operation reaching $Q = 10$ and one in steady state operation for $Q = 5$. In the first scenario, a plasma current of up to 15 MA will be generated mainly by flux swing of the central solenoid with a pulse duration up to 400 s. In the second scenario, steady state is maintained with a combination of different sources of non-inductive current, sustaining a plasma current of 9 MA up to 3000 s. The plasma facing components will have to withstand a large heat load, and ITER features a Be
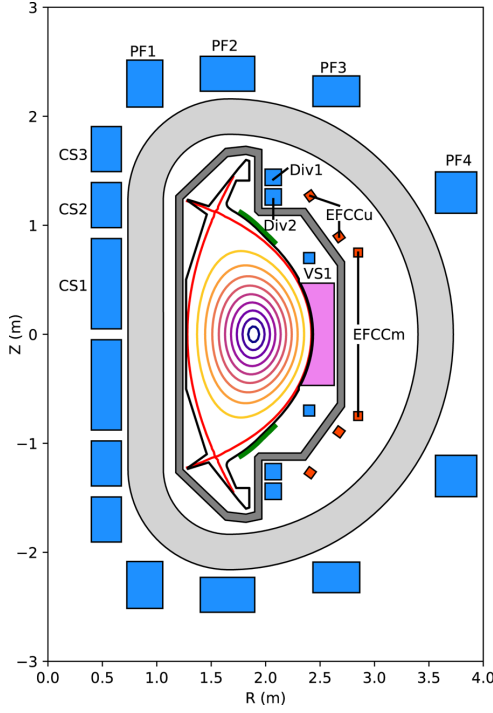
Figure 1.5 – Cross section of the SPARC tokamak, highlighting the central solenoid (CS), the poloidal field coils (PF), the divertor shaping coils (Div) and the error field correction coils (EFCCu). Note in particular the vertical stability coils (VS) internal to the vacuum vessel (Fig. 2 [24]).
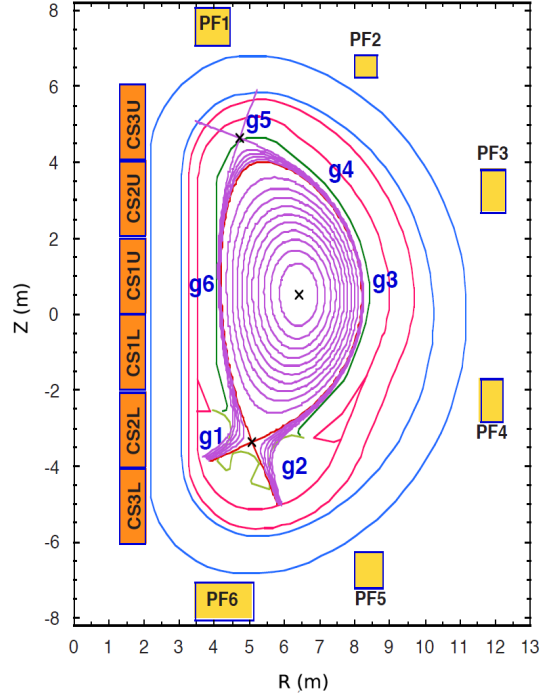
Figure 1.6 – Cross section of the ITER tokamak, highlighting the central solenoid (CS) and the poloidal field coils (PF). The vertical stability coil is not represented. The location of gaps to be controlled are reproduced with g in the original design. (Fig. 1.2.1-5 [25])

first wall along with a modular divertor in W. Despite not being designed to produce net electricity, ITER will have a leading role for studies on superconducting magnets, plasma facing components and tritium breeding and handling. Superconducting Nb_3Sn magnets maintained in cryogenic conditions will generate a toroidal magnetic field that can reach 5.3 T within a vacuum chamber of 837 m^3 and the plasma is envisioned to have a major radius of 6.2 m and a minor radius of 2 m (Fig. 1.6). The experience developed during ITER operation will pave the way for DEMO [23], the first plant which has been designed as a prototype for a commercial reactor to produce electricity from fusion. At present, main parameters of DEMO are still being discussed and its operation is predicted after 2050.

The high field path to fusion is another promising field which had a resurgence in recent years. Tokamak performance in terms of confinement improves with increasing toroidal magnetic field, since this reduces the gyro-radius of ions which corresponds to a minimization of turbulent transport step size [26]. Furthermore hard limits for plasma pressure, density and current all increase with larger magnetic field. The recent development of high temperature superconductors allows building a much smaller device, similar in

scale to current medium size tokamaks but aiming to the same Q factor of ITER. This is exactly the objective of the SPARC device under development [24]. The main goals of the SPARC tokamak are to create and confine a plasma that produces net fusion power with a minimum fusion gain of $Q > 2$ up to $Q \approx 11$ in the best case scenario and to test the rare-earth barium copper oxide (ReBCO) high-temperature superconductor magnets in a reactor environment. The magnets, currently being tested, will allow a toroidal magnetic field reaching 12.2 T and the central solenoid and poloidal field coil set will be capable of producing magnetic flux to initiate and drive the plasma current up to 8.7 MA with a plasma flattop time of 10 s. The large toroidal field allows a more compact plasma cross section compared to ITER which in the present design features a major radius of 1.85 m and a minor radius of 0.57 m (Fig. 1.5). The only auxiliary heating system will be the largest ICRF ever deployed in a fusion experiment and must therefore operate reliably and robustly providing a maximum of 25 MW to the plasma which will generate up to 140 MW of fusion power. The large power density of the core plasma will determine one of the main challenges for the plasma facing components. Both C and W are currently being considered for this purpose. The beginning of tokamak assembly is expected in 2021 and will take four years to complete, moving to D-T operation as soon as 2025. A large focus is put on collaboration with private companies, with MIT spin-off Commonwealth Fusion Systems collaborating with numerous ventures.

The SPARC device, along with intensive studies for the effect of large neutron flux on materials, will be the main step towards ARC, the **A**ffordable **R**obust **C**ompact reactor [27]. Its design originated from a graduate course project at MIT and is under constant development. The ambitious objective of ARC is exploiting the capability of the same HTS technology operated in SPARC to obtain a fusion power comparable to ITER while ensuring a smaller size.

Moving from basic questions on energy generation, nuclear fusion research is now at a turning point where the new objective is realizing a fusion power plant competitive with existing energy sources. There exist several challenging operational problems to be solved or optimized for high performance operations in a tokamak. Many of these fundamental issues can be treated with the tools provided by automatic control which will be discussed in the next section.

1.2 Automatic control in tokamaks

Control theory and engineering deals with influencing the behavior of a dynamical system with the objective of controlling its evolution to a desired specification. The concept of control allows defining a physical system in terms of inputs, outputs and its internal dynamics, using mathematical modeling and in particular the concept of Laplace transform for linear systems. The main goal of controller design is to reach a pre-defined level of performance, using a set of theoretical tools applied on a model of the real dynamics and implementing the real controller on the system with available technology. The solution results either in an open loop configuration, where the output of the system is not observed

by the controller, or in a closed loop configuration, where the measured result of the control action on the system dynamics is reprocessed by the controller itself for adjusting the plant input, ideally in real time. In this section, following a short historical introductions, the main control issues in tokamaks will be discussed along with the state of the art.

1.2.1 The development of control engineering

Control is often referred to as a *hidden technology* for its essential role in many systems while remaining mainly out of sight. This discipline had a steep development in the last two centuries that has evolved in the field of control systems design, whose applications are nowadays pervasive in the modern world, from cell phones to jumbo jets, and, as it will be discussed, in tokamaks.

The origins of automatic control can be traced back to antiquity, with early examples of float valve regulator for the control of water clocks and the liquid level in vessels developed during the Hellenic period. The first technical applications were developed in the 17th century, mainly for rotation regulation in mills or temperature control, such for example the incubator of Cornelis Drebbel [28].

The first mechanism with the characteristic of a feedback controller in a modern interpretation was the steam engine (or fly-ball) governor, which contributed to the Industrial Revolution in a way that it is hard to overstate. The steam engine governor was used to maintain a constant speed of a rotating engine regulating the steam flow in input in order to guarantee continuous water draining from underground coal mines. This invention, developed by James Watt in 1788, was however prone to instability with the engine speed occasionally growing in an uncontrolled way. Watt was a practical man and did not engage in the theoretical analysis of his invention, a study which was undertaken in a 1868 paper entitled "On Governors" by James Clerk Maxwell [29]. In this work, a model of various mechanisms of the fly-ball governor was provided in terms of linearized differential equations. The issue of unstable behavior observed in the controlled steam engines could then be treated theoretically since the stability was determined by the location of the zeroes of a characteristic equation of the model. The problem of determining a general condition for stability of a dynamical system described by linear differential equations was successively developed in 1877 by Edward J. Routh [30], which provided what is now know as the Routh-Hurwitz criterion, a topic still studied by control engineering students nowadays.

Theoretical studies, such as the one developed by the Russian mathematician Alexander M. Lyapunov for stability of nonlinear differential equations [31], were thriving at the end of the XIX century together with technical applications of feedback control. These included temperature, pressure and flow control in various industrial processes, but also steam hydraulics for controlling increasingly larger ships and engines. The development of electricity was opening a new range of applications for controlling voltage, current and frequency of electrical motors and electrical signals used in telecommunication.

The use of amplifiers allowed avoiding using larger wires for long distance communication, but the high number of repeaters meant that even small nonidealities in the single amplifier

led to large distortion in the received signal. Harold Black solved such issue in 1927 introducing for the first time a negative feedback electronic circuit able to remove the disturbance originated in the non ideal amplifiers. Black was assisted in his work by Harry Nyquist, who had to develop a new technique to analyze the stability of the system, since it was observed that high gain in the controller could determine an unstable loop in an unpredicted way. This issue could not be treated with the Routh-Hurwitz criterion due to the high dimensionality of the problem and Nyquist used a graphical representation of the frequency response of dynamical systems based on complex analysis. The work started at Bell Telephone Laboratories was eventually formalized by Hendrik Bode in 1945 and resulted in what is now called *Classical control* that relies on frequency-domain analysis of the system allowing the combination of experimental and calculated data [32].

Following extensive development of feedback system during the Second World War, especially for the aiming mechanisms of heavy anti-aircraft guns developed at the Radiation Laboratory at MIT, civil application of control engineering became an industrial standard. In the last years of the war Ziegler and Nichols developed their famous rule to determine the ideal gains for PID controllers [33], but the study of an optimal solution to control problems was just at the beginning and was a main topic of research in the 1950s. Attention was focused again on ODE (ordinary differential equations) systems as ideal models for controller design and the main theoretical question was the definition of the best controller for a given plant. Launching, maneuvering, guidance and tracking of missiles and space vehicles - the famous "rocket science" - was at that point the driving force behind automatic control research. The so-called state space approach was the base of the study developed by Kalman and Bucy for attacking the filtering problem [34]. In their work they were able to show the duality that existed between multivariable feedback control and state estimation, with applications which are still used nowadays, for example in navigation and aircraft control, and were fundamental for bringing the man to the Moon during the Apollo missions. The resulting LQG regulator combined the linear quadratic estimator for the system states with the optimal linear quadratic regulator. The complexity of this algorithm relies on digital computers for its technical applications, as most optimal control techniques do [35]. The inclusion of computers as standard tools in the field of automatic control is what characterizes the field of *Modern control*.

Following the great success of LQG controllers in the early 1970s, it became progressively clearer that their application was sensitive to variations in plant parameters and unmodeled high frequency dynamics. This is now defined as robustness problems. In classical compensator design robustness is guaranteed by providing sufficient gain and phase margins, but in multivariable problems this may not be sufficient. Advanced techniques, such as H_∞ developed by Doyle from 1975, provide the way to obtain the desired performance and stabilize a family of plants with a set of parameters distributed over an anticipated range [36].

This approach is part of the extension of SISO (single-input-single-output) frequency domain design into MIMO (multi-input-multi-output) systems which is based on the concept of singular values indicating the magnitude of the maximum possible output of a

matrix. Several concepts of modern control and MIMO control will be applied throughout this thesis with particular emphasis on H_∞ control in Chapter 5.

1.2.2 Control issues in tokamaks

From the control point of view, tokamaks are high-order distributed parameters nonlinear systems, characterized by a large number of instabilities, some of them leading to a catastrophic termination of the plasma (disruption) which in large devices can lead to long term damage to the reactor itself. The objective of control in tokamaks is therefore maintaining the plasma at a desired operational point and away from its instability boundaries for its entire duration. For this purpose, various diagnostics measure in real time the response of the plasma and regulate the output of a set of actuators to steer or maintain the plasma in the desired state during the discharge.

Historically, tokamak control was a tool developed from a combination of theoretical comprehension of the physical system and empirical tuning of the controllers. This was in line with the objective of the first experiments aiming to improve the knowledge of basic physics issues in tokamaks. In the first devices, feedforward control was operated, estimating the equilibrium field and pre-programming the evolution of currents mainly based on trial and error [37]. As the discharge duration increased, feedback control was included at first for counteracting the plasma tendency to move from its equilibrium position and initial attempts were made to shape it to a non-circular cross section [12]. The possibility to correct plasma instabilities in closed loop further improved the capability of reaching fusion conditions. In a power plant, the developed technology should be optimized to reach a desired level of performance, guaranteeing robust and reliable operation with an ever increasing required level of precision.

Especially in recent years, most of the modern control techniques introduced in Sec. 1.2.1 have been applied successfully to control tokamak plasmas. Until recently, however, tokamak control problems have been mostly addressed separately in dedicated experiments. The trend in this field, especially in view of a fusion reactor, is to be able to satisfy all physical and operational constraints during a unique controlled plasma discharge. The main challenge consists in the fact that actuators and sensors are often shared among different control schemes, and any redundancy in the actuators in a fusion reactor would be anti-economical for the cost of energy production. The solution emerging in recent years was that of supervisory control, where different control problems receive automatically a different priority depending on the phase of the discharge. This allows the optimal assignment of available actuators to different tasks allowing safe operation and maintaining high performance plasmas.

In the remainder of this section, a selected subset of control issues in tokamaks are introduced, highlighting their effects on plasma dynamics and describing the corresponding control scheme which has been developed.

1.2.3 Control of bulk plasma quantities

The most fundamental scalar quantities which are required to be controlled for a plasma in a tokamak are its position, the total plasma current and the average density. Typical controllers in this case are standard PID controllers.

The plasma positon is among the most simple quantities to estimate and control in order to avoid undesired contact of the plasma with the tokamak walls. The main actuators are linear combinations of poloidal field coils, able to generate a Lorentz force on the plasma column in the vertical and radial direction. The plasma position is estimated from a set of magnetic measurements that typically include Mirnov coils, flux loops and currents in the conducting structures outside the tokamak sensitive to the plasma displacement.

Radial position control is required to avoid the tendency of a toroidal plasma to expand in the radial direction. Although a preprogrammed magnetic field is included during the discharges, feedback control of the radial position allows rejecting unpredicted disturbances during the discharge.

Another requirement of position control involves the stabilization of the plasma vertical instability [38]. In synthesis, most tokamaks operate with an elongated cross section for the plasma column which results in improved transport and stability, but makes the plasma unstable in the vertical direction. This makes feedback not only beneficial but mandatory for stable operations since unstable systems cannot be operated in feedforward.

The plasma density should be controlled to a desired reference regardless of the different transport regimes which can occur. Furthermore, reaching the Greenwald density limit [39] would cause a hard termination of the plasma and should be avoided. For this purpose, an interferometer can be used to estimate the measured average density and regulate the opening of gas valves or the rate of injection of frozen fuel pellets.

The current ramp in the central solenoid creates a loop voltage necessary to induce a current in the plasma. This is however a secondary circuit whose resistance and shape can vary during the discharge. In order to maintain the current to a desired reference, the slope in the ramp of the central solenoid can be modified according to the plasma current error. An estimate of the plasma current can be obtained measuring the magnetic field around the plasma column, either employing a Rogowski coil or combining different poloidal magnetic field probes.

1.2.4 Shape control

In a tokamak plasma the last closed flux surface (LCFS) is the outermost closed magnetic surface that is entirely contained in the vacuum vessel. Charged particles moving out of the LCFS due to unavoidable transport stream along magnetic field lines which end on the walls and are lost on a fast time scale compared to confinement time.

Shaping the plasma column to an elongated cross section leads to improved performance in tokamaks despite the vertical instability and is highly desirable. Furthermore, advanced configurations (such as diverted, double nulls and snowflake plasmas) have several advantages compared to limited ones, among which an easier access to H-mode and a

lower degree of core plasma impurity contamination. Volume (and thus cost) optimization in a reactor for power production requires an extreme proximity of the LCFS with the vacuum vessel and their intersection is usually limited in designed divertor chambers while spurious contact should be carefully avoided. Finally, the coupling of the core plasma with resonance heating is determined by resonance locations, which in turn depend on the plasma shape and position.

The possibility to control the plasma shape is therefore highly desirable in a tokamak, resulting in reproducible discharges and rejecting unavoidable disturbances. The objective of shape control in tokamaks [40] is controlling the location of the LCFS to a desired reference, while internal profiles evolution is usually treated as a disturbance. In principle, the poloidal projection of the LCFS is a continuous curve which can only be fully characterized by an infinite set of parameters. Due to the intrinsic discreteness of finite MIMO controllers, the solution is to discretize the controlled variables as well. The number and type of these parameters characterizes the shape and is usually pre-programmed.

A first approach consists of defining shape momenta characterizing the LCFS. Elongation, triangularity and squareness define the deviation from a circular cross section and can be defined analytically only for limited plasmas. For more advanced configurations, other parameters are included for characterizing the shape such as the X-point(s) and the strike points locations on the walls. When the plasma location has to be controlled with high accuracy, two main schemes are used. The first one (gap control) aims to control the distance between the plasma and the wall in a finite set of locations around the LCFS. The second one (isoflux control) aims to equalize the flux measured on a finite set of points around the LCFS, possibly including the strike points, and the magnetic field and its gradient at the X point.

The plasma shape cannot be directly measured but can be reconstructed with different approaches which should be suited for real time implementation. The most advanced ones in tokamaks are magnetic equilibrium reconstruction codes [41] [42], whose algorithm is discussed in Appendix A.1.2, and optical boundary equilibrium reconstruction [43]. At present, only magnetic reconstruction is regularly used for shape control in tokamaks. The main actuators for shape control are the poloidal field coils surrounding the plasma. Modifying their currents leads to a different Grad-Shafranov equilibrium with the consequent plasma deformation. This problem is tightly coupled with the position control and requires a MIMO approach to be solved, in the context of the general field of magnetic control.

Plasma shape control is one of the main topics of this thesis and will be treated in detail for the TCV case in the following Chapters 2 and 4.

1.2.5   MHD instability control

A toroidally confined plasma is subject to a set of magnetohydrodynamic instabilities [44], whose stability threshold determines a set of soft and hard limits for the plasma discharge. Many high performance scenarios operate close to these limits, and various solutions are developed for limiting or controlling the unstable evolution of non-axisymmetric modes in order to prevent the loss of plasma confinement.

- The resistive wall mode (**RWM**) is an external kink instability which deforms the plasma in a helical fashion when the plasma pressure overcomes a critical value. The corresponding magnetic field moves with the plasma and induces a set of eddy currents in the surrounding conductive elements, slowing down the instability characteristic time to the point where feedback control is possible. Two main solutions were developed for stabilizing the RWM in tokamaks. The first uses magnetic control to oppose the perturbed magnetic field moving with the plasma through a set of non-axisymmetric coils disposed around the tokamak [45]. This is made possible by the presence of two low-n dominating toroidal modes, leading to simple control-oriented models of the instability. The second method involves regulating the plasma rotation, for example through NBI, since when the toroidal rotation of bulk plasma remains above a critical frequency, the RWM instability is completely stabilized [46].

- The H-mode of toroidally confined plasmas provides improved confinement but is not a stationary equilibrium, being subjected to cyclical Edge Localized Modes (**ELM**) [47]. A combination of MHD instabilities takes place in the edge of the plasma, causing the pressure gradient in the pedestal to regularly collapse. The ELM crash happens on a sub-ms time scale, but does not determine in general the termination of the plasma discharge. The ELM repeats itself at a variable frequency (10-10^3 Hz) depending on the time required for a new buildup of the pressure gradient from energy flux injected in the plasma. At the ELM crash, confinement is temporarily degraded and a significant fraction of the plasma energy flows out of the LCFS. The resulting heat and particle flux on the surrounding plasma facing components can be unsustainable in a fusion reactor. Several scenarios have been developed in which the H-mode confinement is maintained in absence of ELMs, opening the way to Super-H mode [48]. Other solutions involve the regulation of ELMs frequency, for example with three-dimensional magnetic perturbations [49] or pellet injection [50].

- The regions most subjected to MHD instability within a plasma lie on rational surfaces where the safety factor reaches rational values. When resistivity is included in MHD equations for this region, it emerges that magnetic field can diffuse, tearing the magnetic geometry apart. The further addition of neoclassical effects, in particular the presence of bootstrap current, results in the neoclassical tearing mode (**NTM**) [10]. The deformation of magnetic geometry causes the otherwise nested magnetic surfaces to overlap and reconnect resulting in the development of magnetic island. The consequent increased radial particle transport has a detrimental effect for confinement which should be avoided and, under some conditions, the island can grow to the point that the plasma terminates with a disruption. It is therefore necessary to either develop an operational regime with no island or attempt to control them. This can be performed in most present tokamak using localized ECCD as an actuator to determine a reduction of the island size up to a complete suppression [51]. The main reason of its efficacy is the ability of ECCD to compensate the missing bootstrap current which is one of the main mechanisms driving the NTM unstable.

- The **Sawtooth** instability [52] is characteristic of tokamaks and appears when $q < 1$ in the central regions of the plasma, as q tends to grow from the plasma axis to the boundary. The name derives from the appearance of the measured signal (typically X-ray emission) used to detect it, showing a sawtooth-like time evolution with a long buildup and a fast crash when the $m = 1$, $n = 1$ kink instability grows on MHD time scales. While not causing a plasma termination, this instability can trigger NTMs which are undesired in fusion reactors. Consequently, several solutions have been developed to control them, either using NBI [53] or ICRH [54] to influence the ion population varying the stability threshold, or varying EC deposition location [55], angle [56] or power [57] to influence the sawtooth period.

1.2.6   Plasma profile control

The study of plasma advanced scenarios with significantly improved confinement requires a precise tailoring of the plasma internal profiles. This allows for example maintaining to a desired value the bootstrap current, where the non inductive current is regulated modifying plasma pressure profile. Another advantage is the development of internal transport barriers, where the shearing of q profile determines a region of steep temperature and density gradients within the plasma. Maintaining this condition requires treating distributed parameters models modeled with PDEs and run them in real time, since controlling the q-profile or the current profile is equivalent from the point of view of plasma physics and requires considering the effects of current diffusion and energy deposition location [57]. Furthermore, the current profile cannot be directly measured and should be reconstructed in real time. The main actuators are in this case the auxiliary heating and current drive systems. Profile control is usually defined in the three main phases of the plasma discharge with a combination of feedforward and feedback. During plasma ramp-up, the profiles evolve towards a stationary state and their trajectory is dynamically defined. Once flat-top is reached, the obtained profiles should be maintained in time avoiding disturbances. Finally, at the termination of the plasma discharge, measures are taken to avoid violating the various hard limits that would lead to a plasma disruption.

1.2.7   Detachment and heat load control

High performance in future tokamaks for energy production requires to take particular care of the heat load on plasma facing components. Safe operations will be guaranteed maintaining the so-called detached regime in the plasma edge, in order to maintain the detached state where a large fraction of the energy flowing from the core plasma is radiated before reaching the target. In this scenario feedback control is mandatory in order to provide reliable and robust divertor and target conditions regardless of external disturbances and reducing the detrimental effects on core plasma. Two main strategies are being developed for control of the heat load on plasma facing components, the first one requiring control of fueling and seeding rate and the second one based on magnetic control.

In the first scheme, the goal is the control of the radiation front in the divertor. In this

case, typical actuators currently available in most tokamaks mainly consist of deuterium and nitrogen gas puffing. At present, the most common scheme is based on SISO (single-input-single-output) controllers, which attempt to control the radiation front basing on a set of proxies for the detachment, such for example electron temperature or saturation current at the target [58], [59], or the reconstructed location of the radiation front [60].

The second scheme for controlling the walls heat load relies on the mature field of magnetic control but is not yet routinely used in existing tokamak operations, mainly since power fluxes in present research machines are tolerable also in static conditions. Fundamentally, this approach requires to modify and control in real time the flux expansion [61], [62] and/or the strike points on the target and the angle of the divertor leg [63]. In this way, the wetted area on plasma facing components can be varied, reducing the power per surface area, or the strike point on the wall can be dynamically modified allowing larger heat fluxes than in static conditions. The main advantage of this method when compared to fueling/seeding control is the higher bandwidth at which it can operate, since the latency due to gas valves is much larger than the characteristic time required to modify the magnetic geometry in the divertor region.

1.3 Motivation for this thesis

Elongated plasmas lead to improved performance in tokamaks, both in terms of magneto-hydrodynamic stability [64] and reduced transport [65], which will contribute in sustaining fusion conditions in reactors. The required magnetic field for shaping the plasma column however results in an unstable equilibrium that makes feedback control of the unstable vertical plasma position mandatory. Active stabilization of the axisymmetric plasma vertical instability is a standard feature of elongated tokamaks and will be a fundamental feature in the ITER magnetic control system [66] due to the fact that a loss of vertical control and the subsequent plasma disruption can lead to both high heat loads and unacceptable forces, stresses, and torques on in-vessel components. A discussion on the state of the art of vertical control in tokamaks is presented in Sec. 5.1. Modern tokamaks operate regularly with elongated plasmas and have so far provided key inputs for the design of ITER axisymmeric and shape control.

Model-based decoupling control of plasma shape and position is the standard in modern tokamaks [67] and for ITER control system design [68]. In ITER shape control [69], diverted plasmas will be realized with the control of the six gaps between the separatrix and the plasma facing component (see Fig. 1.6). Gap (called segment) control along with the X-point position control is performed in EAST [70]. Also in WEST, where the shape controller is synthesized with $\mathcal{H}_\infty$ techniques [71], a set of radial outer gaps are controlled to maximize the coupling with plasma heating and current drive system and and the X-point location is controlled. On the ASDEX Upgrade tokamak, the control algorithms for shape and position are decoupling PID matrix controllers which acts on a number of gap position and other geometric variables among which inner and outer strike points to regulate the coil current references [72], [73]. The largest operating tokamak, JET,

features an eXtreme Shape Controller (XSC) using a singular value analysis to identify the principal directions for shape modification [74]. An XSC-like shape controller, including flux expansion control capabilities, has also been implemented for the EAST tokamak [61] and is also envisioned for the JT-60SA magnetic control system [75]. Shape control in DIII-D is performed basing on an isoflux algorithm, modifying the coil current references of individual coils or coil directions to control magnetic flux at target points and field at the X-point [76]. This algorithm has been recently upgraded to include flux expansion control [62]. In NSTX-U, the gap control method is used during the start-up and shutdown phases of discharges, while, during the main phase of the shot, isoflux control is performed acting on the coil voltages directly (i.e. not modifying the coil current reference) [77]. Both DIII-D and NSTX-U feature dedicated coils for the divertor region, facilitating the control of the X-point(s).

The TCV tokamak [78], described in detail in Chapter 2, is particularly suited for studying the effect of plasma shaping, thanks to its elongated vessel and a set of independently powered poloidal field (PF) coils, which are the main actuators for magnetic control. The G coil located within the vacuum vessel is designed to generate an axisymmetric radial field faster than the unstable growth rate of most elongated plasmas, while its fast switching power supply (FPS) cannot sustain continuous current for plasma positioning on time scales comparable to the shot duration. The 16 external E and F coils, each having an independent power supply, are used for plasma shaping and contribute to vertical plasma stabilization on longer time scales, due to the shielding effect of the conducting vacuum vessel. A synergy of the two systems allows reaching extreme elongations during TCV plasma discharges.

In order to explore candidate fusion reactor regimes, a digital shape and position controller was designed and tested on TCV [79], improving access to advanced configurations such as snowflake plasmas by correcting in real time the coil currents references with an isoflux algorithm. In TCV, position and shape control share the same set of actuators, the poloidal field coils. In standard operations, the first relies on existing physics operator experience and is tuned on a shot by shot basis. The digital shape and position controller of [79] also contributes to vertical stabilization, requiring further tuning of gains to find the correct operational space. Furthermore, the shape controller relies on a magnetic equilibrium reconstruction code [41], which introduces a computational delay in the feedback loop comparable to the vertical instability growth rate of most elongated plasmas, reducing the stability margins for stable operations.

The objective of the present work is to exploit the potential of the TCV tokamak magnetic control, providing a formal approach for decoupling of position and shape control problems. The position controller should be in charge of vertical stabilization and positioning, and the corresponding observers should include the both fast magnetic diagnostics of the TCV tokamak at high frequencies, and the equilibrium reconstruction at low frequencies. This provides an offset-free measurement of the plasma position, while avoiding the degradation of the vertical control stability margins due to the time delay of the equilibrium reconstruction. The shape controller should then be able to correct shape

deformations resulting from various disturbances in real time but on longer time scales. Shape observer and corresponding actuation direction are defined to be orthogonal to those used for position control and the shape controller is always designed in this thesis to act on a stabilized system. In this way, it is possible to separately design the controllers and optimizing the performance in experimental runs.

More in general, this thesis explores the merits and limits of performing model-based design of magnetic controllers. It shows that, if sufficiently accurate control-oriented models are available, controllers with improved robustness and performance can be designed which deliver superior performance with respect to manually tuned controllers.

1.4   Outline of this dissertation

This thesis deals with magnetic control in tokamaks focusing on model-based design of plasma position and shape controllers, and experimental tests of these controllers on the TCV tokamak. A chapter-by-chapter outline of the thesis is given below:

- Chapter 2 describes TCV, the tokamak located at the Swiss Plasma Center in École Polytechnique Fédérale de Lausanne (Switzerland). The main diagnostics systems are introduced, with a particular focus on magnetic diagnostics. The digital real time control system SCD provides the basis for this work, including the real time equilibrium reconstruction code LIUQE. In conclusion, the shape control algorithm that was included in SCD will be described, introducing its extension which is proposed in this thesis.

- Chapter 3 is focused on the models used for magnetic control in this thesis. A discussion on the vertical instability in tokamaks introduces the fundamental requirements for vertical control. The design of the new scheme for position and shape control presented in this work is based on the RZIp model, which describes the coupled electromagnetic dynamics of plasma vessel and coils under the constraint of rigid plasma movement. The RZIp model is extended, relaxing the assumption of a rigid plasma displacement in the radial direction to a semi-rigid model which better fits numerical Grad-Shafranov equilibria. At the end of this chapter, a model for TCV power supplies is presented, determining an important constraint in the design of vertical control.

- Chapter 4 presents the main approach of this thesis for decoupling the design of vertical and shape control. The separation of these controllers is done at the level of observers and actuators, since it involves different time scales for the two control problems. This method provides a way to guarantee plasma position stabilization and control while the remaining degrees of freedom are used to correct only the plasma shape deformation. A new set of estimators for the plasma position is used, combining fast analog observers with the results of equilibrium reconstruction. The actuation directions for position control are derived from the shape controller and guarantee low frequency decoupling.

- Chapter 5 introduces the application of $\mathcal{H}_\infty$ for the design of the vertical controller. Two different optimal combinations of poloidal field coils for vertical control actuation are established from control theory and used on different time scales for controlling the plasma vertical position. On fast time scales, the priority is input minimization, while on long time scales position control is designed to be compatible with shape control. Structured $\mathcal{H}_\infty$ design, extending classical $\mathcal{H}_\infty$ to fixed-structure control systems, is subsequently applied to obtain an optimized controller, using all available coils for position control. Closed-loop performance improvement is demonstrated in dedicated TCV experiments, showing a reduction of input requirement for stabilizing the same plasma, thus reducing the risk of power supply saturation and consequent loss of vertical control. The material in this chapter has been submitted for publication in Fusion Science and Technology.

- Finally, Chapter 6 summarizes the results of this work and provides an outlook for the possible applications of the techniques presented here both for position and shape control, focusing on the integration in the TCV control system.

2 | The TCV tokamak

The TCV tokamak [78] along with its main diagnostic systems, actuators and control system is described in this chapter. The **T**okamak à **C**onfiguration **V**ariable is a medium size tokamak featuring a highly elongated vessel located at the Swiss Plasma Center - EPFL, Lausanne (Switzerland). Its main aim is to investigate the effect of plasma shape on tokamak physics and performance [80].
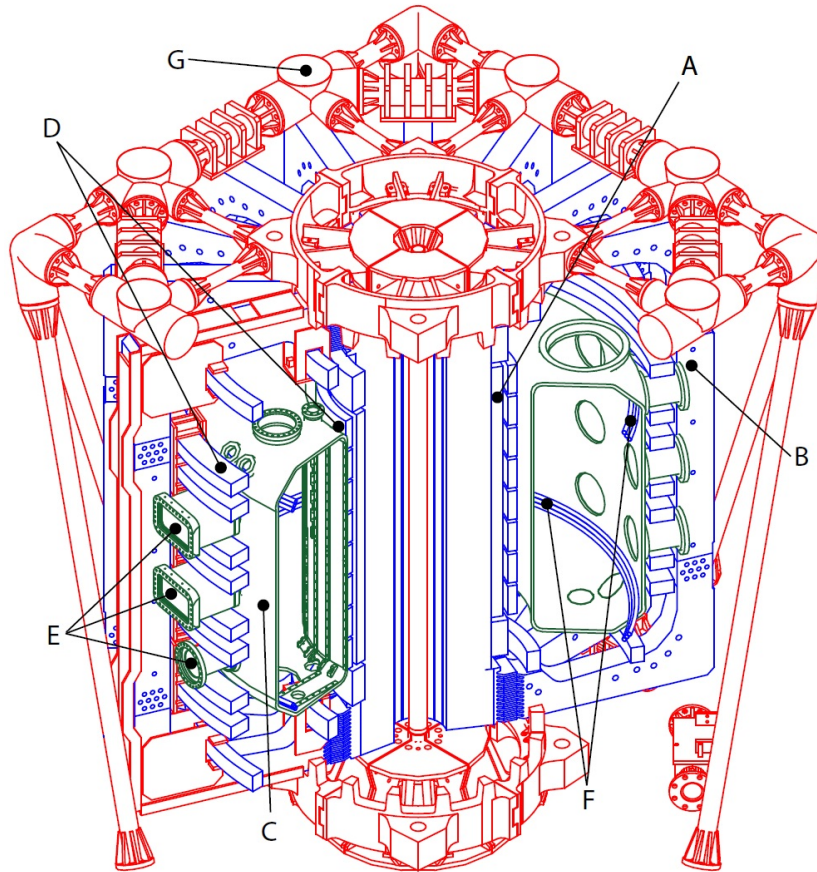
Figure 2.1 – The TCV tokamak: (A) the central solenoid, OH coil, (B) toroidal field coils, (C) the vacuum vessel, (D) poloidal field coils E and F, (E) diagnostic ports, (F) internal vertical stability G coils, (G) mechanical support structure (readapted from Fig. 1 [80])

2.1 Overview

Parameter	Symbol	Value
Major radius	R_0	0.88 m
Minor radius	a_0	0.25 m
Toroidal field on axis	$B_\phi(R_0)$	≤ 1.54 T
Plasma current	I_p	≤ 1 MA
Plasma elongation	κ	$0.9 \div 2.8$
Plasma triangularity	δ	$-0.8 \div 1$
Electron density	n_e	$\leq 20 \times 10^{19}$ m^{-3}
Electron temperature (EC heating)	T_e	≤ 15 keV
Ion temperature (NBI heating)	T_i	≤ 2.5 keV
Vessel resistance	R_{VV}	45 mΩ
Vessel RL time	τ_{VV}	6.7 ms
Vessel elongation	κ_{VV}	3
Vessel vacuum	p_0	$\leq 10^{-7}$ mbar
OH heating power	P_{ECH}	< 1 MW
EC heating power	P_{ECH}	< 4.5 MW
NBI heating power	P_{NBH}	< 1.3 MW
Ohmic flux swing	Φ_T	3.4 Vs
Pulse duration	T_s	$\leq 4s$
Inter shot delay	T_D	>400 s
Helium glow discharge	t_G	300 s

Table 2.1 − Main TCV parameters.

The TCV tokamak produced its first plasma in 1992 with full tokamak operations starting in 1993. The elongated cross section of its vessel allows generating a wide variety of plasma shapes, among which the snowflake configuration [81]. A sketch of TCV with its main mechanical components is reproduced in Fig. 2.1 and its main parameters are summarized in Table 2.1. Typical plasma duration is around 2 s for which TCV was designed, which is longer than the current redistribution time allowing studies of steady state scenarios.

One of the main characteristics of TCV is the magnetic coil system, described in detail in Sec. 2.3 for the poloidal field (PF) coils in particular. TCV features 16 independently powered poloidal field coils external to the vacuum vessel, two coils internal to the vacuum vessel featuring a fast power supply (FPS), a seven-coils Ohmic transformer primary system comprising the central solenoid and six auxiliary coils, and sixteen toroidal field coils.

The heating system of TCV results in a larger than average power density compared to other medium size tokamaks. The tokamak features an Electron Cyclotron Resonance Heating (ECRH) and Electron Cyclotron Current drive (ECCD) system.(Fig. 2.2), consisting of two 82.7 GHz gyrotrons coupled in a cluster for heating at the second harmonic of the electron cyclotron resonance, two dual frequency (84 and 126 GHz) gyrotrons in
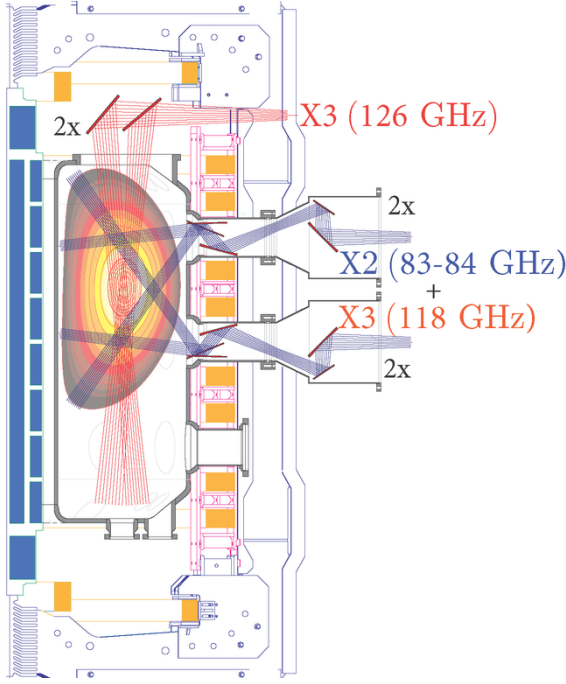
Figure 2.2 – Poloidal cross section of TCV including the toroidal field coils, the PF coils and highlighting the X2 and X3 ECRH/ECCD launching systems, along with their poloidal steering range.
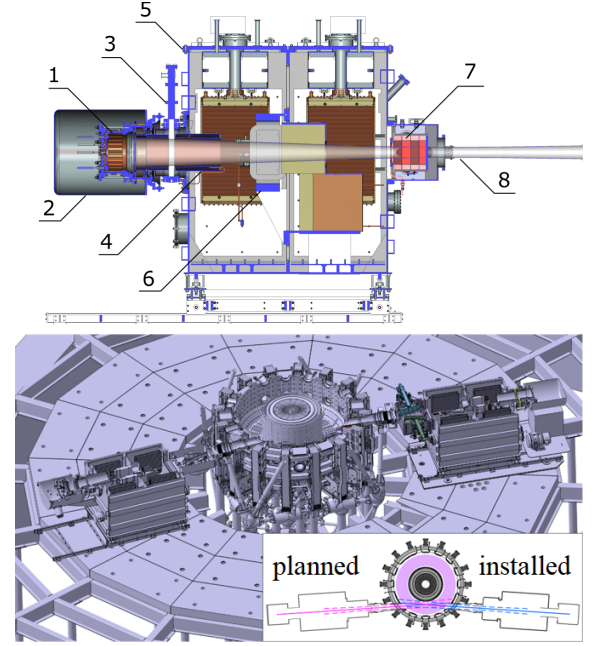
Figure 2.3 – (above) Section of the NBI: 1-RF plasma source, 2-magnetic screen, 3-ions source gate-valve, 4-neutralizer, 5-vacuum tank, 6- bending magnet, 7-calorimeter, 8-neutral beam. (below) The integration of the installed and planned NBI systems with TCV.

another cluster for heating and the second or third harmonic, and two 118 GHz gyrotrons in a third cluster for heating at the third harmonic. The total power injected can peak at slightly less than 3.5 MW for the second harmonic and 3 MW for the third. The power can be injected with a set of 6 launchers, located at the top and the side of the vacuum vessel. The poloidal angle of injection can be regulated during a shot while the toroidal one can be varied between shots to modify the fraction of current drive. The neutral beam injection (NBI) system is the other main power deposition scheme for TCV (Fig. 2.3), providing preferential ion heating using D or H as main species. Since 2015, a first neutral beam was installed which is now capable of providing 1.3 MW at nominal beam energy of 27.8 keV, which can be controlled in real time during discharges for a maximum pulse duration of 1 s and limited by a maximum energy of 1.3 MJ. The total daily usage is constrained by a neutron dose evaluated in the adjacent control room, which is protected by a concrete wall. An extension is envisioned, including a second beam which would inject in counter current adding a further 1 MW of power.

The stainless steel vacuum vessel is continuously welded (15 mm thick on top and bottom, 20 mm on the side) and is characterized by a low toroidal resistance (45 mΩ comparable in magnitude to the resistance of a single poloidal field coil), to provide
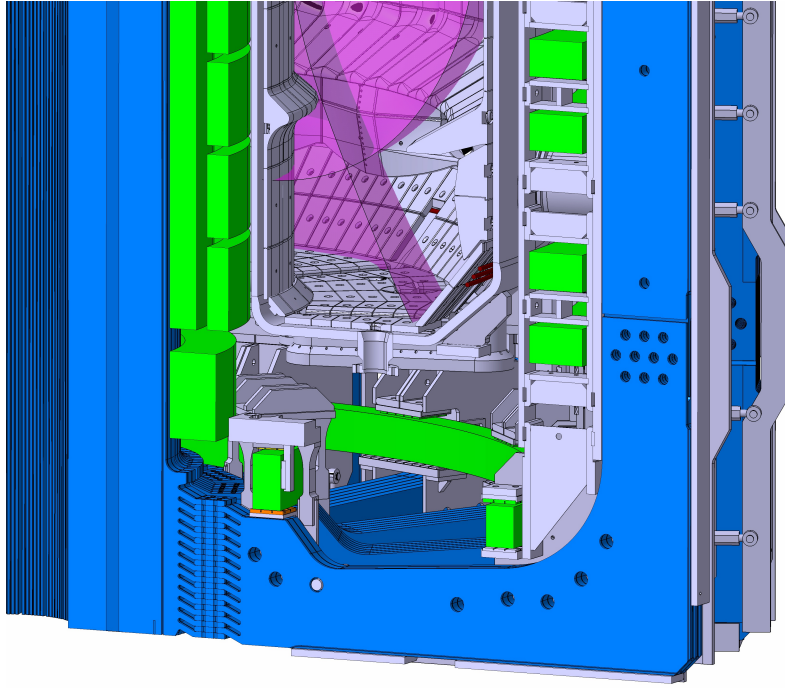
Figure 2.4 − A cutout of TCV, showing the internal structure of the tokamak. In particular, the system of tiles and the baffles can be recognized within the vessel (grey), generating a divertor chamber for the plasma (purple). Part of the toroidal (blue) and PF coil system (green) can be also observed.

passive vertical stabilization of the vertical instability. This implies that large toroidal vessel currents in the order of 100 kA are induced during breakdown, when there is the largest magnetic flux variation, or during vertical displacement events (VDEs). These eddy currents are accounted in the calculations for the coil current references in the breakdown phase, during plasma transients and in the magnetic diagnostics.

The vacuum vessel is protected with a set of graphite tiles, covering the internal surface area and constituting the first wall of TCV. The main impurity in TCV plasmas is therefore C, but other impurities gradually accumulate (e.g. O_2 and N_2) following air exposition or gas injection, therefore the tiles are regularly baked at 250°C and boronized to create a layer of protective B for improved performance. Between plasma shots, a glow discharge is performed with He for the same purpose.

A recent upgrade was the installation of an in-vessel structure (baffle) to form a divertor chamber of variable closure and an increase of the pumping capability in TCV [82]. The baffles provide a varying degree of divertor closure and are interchangeable and removable through 2-3 week interventions. This allows a significantly higher compression of neutral particles in the divertor region, further increasing the capability of the TCV tokamak to realize and study reactor relevant scenarios.

2.2 Diagnostics

TCV features a large set of plasma diagnostics. The main ones are briefly described in this section, with a major focus on magnetic diagnostics.

- **AXUV**: Absolute eXtreme UltraViolet bolometer cameras are two sets of 6 pinhole cameras. The cameras measure the radiated power along 20 line of sight per camera, such that after tomographic inversion, the calculation of the 2D emission profile in the plasma is possible.

- **BOLO**: The foil bolometers system consists of 8 pinhole cameras (one top, one bottom and six lateral) each with 8 channels - golden foils which heat up due to incident photons and neutral atoms from the plasma. Tomographic reconstruction provides 2D information on the radiated power.

- **CXRS**: The Charge eXchange Recombination Spectroscopy measures density, temperature and velocity of a specific impurity species (C for TCV), following its excitation in charge exchange reactions generated by the interaction with a diagnostic neutral beam (DNBI) designed to not perturb the plasma.

- **DSS**: The Divertor Spectroscopy System measures the spectrum of the light in the visible range from multiple chord integrals. The system consists of of a vertical and horizontal system, both with 32 view lines each, with chords crossing the plasma leg in the divertor region.

- **ECE**: The Electron Cyclotron Emission of electrons gyrating along the magnetic field in the plasma is analyzed in order to determine the radial electron temperature profile with a resolution of 1 cm. Two antennas (LFS and HFS) measure the radiation and a waveguide connects them to the radiometers.

- **FIR**: The Far InfraRed interferometer is used to measure the line-integrated density along parallel chords in the vertical direction. The measurement along the central chord is used for real time control of the plasma density. The FIR laser beam passes through the plasma and interferes with a reference beam due to the phase delay following the plasma refractive index, proportional to the plasma density.

- **FIDA**: The Fast Ion D α diagnostic is based on a CXRS method applied to fast Deuterium neutrals. The charge exchange reaction of a fast ionized D with a neutral is typically provided by NBI in TCV.

- **FastCam**: A Fast visible Camera is installed in a lateral port, measuring visible light to recover information on spatio-temporal distribution of fast varying events (breakdown, ELMs, etc.) thanks to its 250 kfps acquistion frequency.

- **GPI**: The Gas Puff Imaging is a diagnostic that images light emission from a localized gas puff using with high temporal resolution (100s of kHz to MHz). Using a two-

dimensional array of chords approximately parallel to the magnetic field, GPI provides 2D measurements of edge turbulence.

- **HXRS** The Hard X-Ray Tomographic Spectrometer is a tomographic hard x-ray (HXR) camera system that measures the bremsstrahlung emission coming from a poloidal slice of plasma along a discrete set of different angular views. The radiation detected is fed to a tomographic routine returning the 2D poloidal bremsstrahlung emission profile. HXR bremmstralhung emission comes from collisional slowing down of suprathermal electrons on ions.

- **IR**: A combination of vertical (VIR), horizontal (HIR) and tangential (TIR) infrared cameras are included in TCV to measure the power deposition onto the bottom, central column and lower outer wall of the vacuum vessel respectively. The cameras work at high acquisition rate (up to 25 kHz for VIR) and allow reconstructing the heat fluxes on plasma facing components.

- **LP**: The Langmuir probe system consists of 114 probes located along the poloidal direction on the wall and measuring ion saturation current or floating potential at 200 kHz. Langmuir probes are also found on the RDPA and RPTCV systems.

- **MANTIS**: A real-time, 10-channel, multispectral imaging system features a tangential view of approximately the bottom half of TCV. The light from the volume of the plasma (usually along the divertor length) is distributed to the cameras by a series of beam splitters to observe a specific line in the visible part of the spectrum.

- **PD**: A set of 18 photodiodes are installed on TCV. Different filters are installed in front of the diodes to acquire different lines of the spectrum, either H_α radiation or specific impurity excitation lines at 50 kHz.

- **SPRED**: The Survey, Poor Resolution, Extended Domain diagnostic measures spectral lines between 10 and 120 nm to provide information about impurities in the plasma estimating Z_{eff}.

- **TC**: A range of TCV graphite protection tiles is equipped with thermocouples to complement heat flux measurements with IR thermography or wall mounted Langmuir probes. Since the thermocouples are located several millimeters below the surface of the tiles, the temperature rise is only detected several seconds after the plasma discharge.

- **TS**: The Thomson Scattering system is the main diagnostic for the measurement of the spatial profiles of the electron temperature and density on TCV. The profiles are measured along the path of 1 to 3 Nd:YAG laser beams passing the plasma in vertical direction near the magnetic axis of the TCV plasma. Wide-angle camera lenses, installed on 3 horizontal ports, collect the scattered light from the observation volumes in the plasma and focus it onto sets of fiber bundles. At present, there are 109 observation positions, covering the region from Z=-69cm to Z=+55cm.
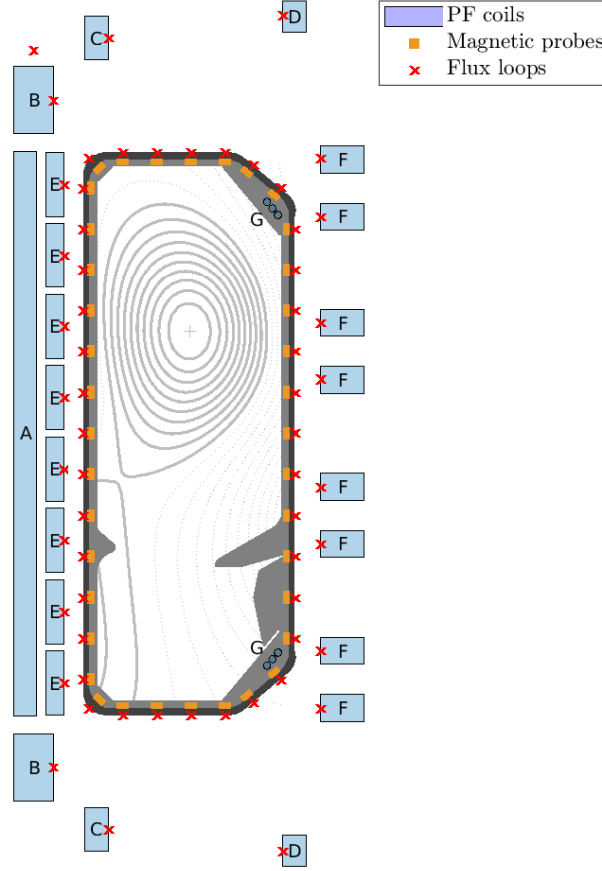
Figure 2.5 – TCV poloidal cross section highlighting the poloidal field coils along with the main magnetic diagnostics used in this thesis: magnetic probes and flux loops.

2.2.1 Magnetic diagnostics

The magnetic diagnostic system of TCV includes magnetic probes, flux, saddle and diamagnetic loops [83]–[85]. Figure 2.5 illustrates the poloidal location of magnetic probes and flux loops, the main magnetic diagnostics considered in this thesis for magnetic control, along with the PF coils, the main actuators used in this thesis for magnetic control. The coil system is discussed in detail in Sec.2.3.

Magnetic probes

The magnetic probes measure the local poloidal magnetic field in several locations along the poloidal cross section of the TCV wall. A magnetic probe is constituted by a set of N_p windings of a conductive wire each featuring an area A_p such that the integral form of Faraday's law reads

$$U_p = N_p A_p \frac{dB_p}{dt} \tag{2.1}$$

where U_p is the voltage measured at the probe open extremes (tips). It is assumed that the poloidal field B_p is orthogonal to the area A, which is reasonable if the characteristic size

of the probe is small compared to the field gradient length. The field variation dB_p/dt can be therefore derived from the voltage measured at the probe tip, and is typically used to study the growth of fast instabilities such as the vertical instability. Integrating the signal allows determining the total magnetic field at a given time which is used for equilibrium reconstruction and plasma position and current estimation (Appendix A). The integration requires a precise calibration in the phase before the shot, removing the spurious poloidal field created by the ramping current in the toroidal bus for the toroidal field coils. Both signals (standard and integrated) are stored in the TCV MDSPlus database.

A set of 38 probes is featured within the TCV vacuum vessel in four sectors, separated by 90 degrees in the toroidal direction. Signals from opposite sectors, used for equilibrium reconstruction, are added to remove toroidal asymmetries. The magnetic probes within the vacuum vessel are protected from direct contact with the plasma by the graphite tiles. Their location avoids the vessel shielding effect making them suited for characterizing MHD modes with a time scale comparable to or lower than the vessel characteristic time. The magnetic probes are the fastest magnetic diagnostics available with a bandwidth of 10 kHz for equilibrium reconstruction and 500 kHz for MHD analysis. The non idealities of the probe (capacitance of the cable and shield circuit) determine a second order transfer function between the field derivative and the voltage with cutoff at 134 and 390 kHz respectively [83]. For the purpose of this thesis, the response is considered ideal since the phenomena of interest (vertical instability) lie in the low kHz range.

The probes consist of a 1mm THERMOCOAX mineral insulated coaxial wire which is wound in one layer around a ceramic body (see Fig. 2.6). The windings are designed to minimize the effective areas perpendicular to the main probe axis. The whole probe is compatible with the temperatures reached during baking of the vacuum vessel. Furthermore, the probe wire has no discontinuities from the magnetic probe to outside the vessel therefore no connection is required inside the vessel. Since no Rogowski coil is present in TCV, the plasma current is estimated with trapezoidal integration of the discrete magnetic probe measurements. As an addition to the standard loop measurements, a set of fast 3D local measurements of the magnetic field (LTCC3D) has recently been installed.

Flux loops

The flux loops measure the vertical magnetic flux ψ_z at a given radial and vertical location defined following the convention of Fig. 2.7. In this case, it is not possible to assume that the magnetic field in the whole measurement area is constant as for the magnetic probes, therefore the following holds

$$U_{fl} = -\frac{d\psi_z}{dt} = -\frac{d}{dt}\int_0^R 2\pi B_z(R', z)dR', \qquad (2.2)$$

where B_z is the vertical magnetic field and U_{fl} is the induced voltage, which is then integrated to obtain the measure of the poloidal flux, used for equilibrium reconstruction and plasma position estimation.

A first set of poloidal flux loops is given by windings on the outside of the vacuum vessel
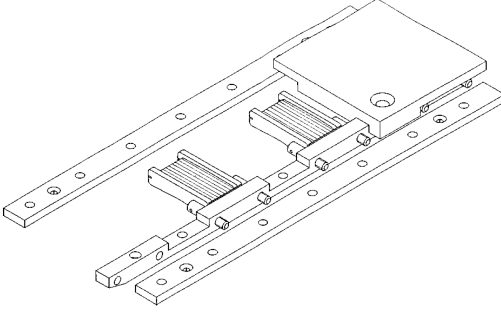
Figure 2.6 − Drawing of the central ceramic core and the magnetic probe assembly on the vacuum vessel (Fig. 3 [83]).
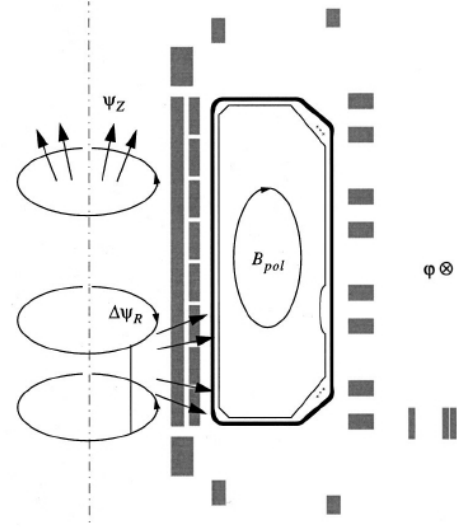
Figure 2.7 − The sign convention for magnetic fields and fluxes used in TCV (Fig. 26 [83]): COCOS 17 from [86].

whose poloidal location is located in correspondence of the magnetic probes [I]. Furthermore all PF coil, (with the exception of the A coil) are equipped with a poloidal flux loop. Obviously, due to the tokamak geometry, the measured flux is dominated by the one induced by the central solenoid and in order to remove its contribution, the flux measured from the first flux loop is subtracted from the remaining ones.

Vessel flux loops are made of one turn of 1 mm diameter THERMOCOAX, mineral insulated coaxial wire, while those mounted on PF coils are made of one turn of adhesive copper band applied on the coil outer insulation. Due to the presence of several diagnostic ports, not all of the vessel flux loops can run on a constant radius around the vacuum vessel thus only a selected subset of 10 loops is used to measure the full poloidal flux. Furthermore, any small misalignment with respect to the toroidal direction leads to a disturbance in the flux measurement due to the dominant toroidal magnetic field in a tokamak.

Saddle loops

A further set of 24 flux loops termed saddle loops are installed around TCV at three different vertical positions with each loop covering two toroidal sectors. The loops measure the flux derivatives $d\psi_R/dt$ and, after the integration, the flux ψ_R in the radial direction of the reference frame of Fig. 2.7.

Diamagnetic loop

The diamagnetic measurement diagnostic on TCV uses the signal from a set of loops wound outside the vessel in combination with auxiliary measurements giving an estimate of the

---

[I]The numbering of both magnetic probes and flux loops around the vacuum vessel 1-38 starts from the HFS midplane probe and proceeds in clockwise sense with the TCV sign convention.

induced vessel current. This diagnostics, estimating the actual toroidal flux ψ_ϕ allows determining the diamagnetism of TCV plasma from the perturbation it induces on the toroidal flux due to the TF coils. Furthermore, it provides an estimate of the total plasma energy.

2.3   Coils system and power supplies

The unique TCV shaping capability is provided by its coil system. The toroidal field is generated by a set of 16 TF coils connected in series through a bus. The poloidal field coils are shown in Fig. 2.5. Two circuits are used to generate the flux swing sustaining the plasma current: OH1 (coil A) and OH2 (coils B, C and D in series). The OH coils are designed to minimize the stray poloidal field within the vessel during the ramp, since TCV is an air core tokamak. The 16 PF coils (E1-8 and F1-8, numbered along increasing z) are in charge of plasma positioning and shaping. Each of the 16 PF coils is connected to an independent power supply, which imposes the voltage/current required by the control system. The poloidal bus for the TF coils is included as T in Fig. 2.5, featuring two connections with the current flowing in the same direction and one for the return loop. Coil currents are measured with LEM modules which are basically iron transformers whose secondary current is adjusted to cancel the magnetic field produced by the bus bar current.

The power supplies for the aforementioned coils are based on thyristor semiconductors. Each power supply consists of 12-pulse thyristor rectifiers: two six pulse bridges (3900A-1800V) are connected in series (OH,E,F) or in parallel (TOR) for pulses limited to 4 s every 5 minutes. In order to be independent of the electrical network, a motor generator (including a flywheel) is used to deliver the peak power as the principal power source during operations. The decreasing frequency (120 to 96 Hz) during a pulse is compensated with the adaption of the maximum firing angle of the thyristor.

The rectifiers can be controlled in three ways:

- Current feedback (A), where the current is controlled by the internal PID controller to a current reference and limited in amplitude at the same time, which is the usual mode of operation for the TF coils.

- Open loop voltage mode (B), where the control system provides the voltage reference and the firing angle is modified consequently, which is the mode used in this thesis (and in general during TCV shots) for controlling the PF coils.

- Hybrid mode (C), which is a combination of the two above, where a pre-programmed current reference can be overwritten with the external voltage requirement from the control system during a shot.

The vertical instability of most elongated TCV plasma cannot be stabilized using only coils external to the vacuum vessel. This is due to the maximum switching frequency of the rectifiers and to the shielding effects of the vessel. Therefore, two low impedance coils are included within the vacuum vessel and driven in antiseries using a fast power supply

[87]. The power supply includes a DC power source, which is again based on a thyristor rectifier to provide a fixed DC voltage of 280 V during shots. The fast output stage of the power supply is an H-bridge IGBT inverter which operates at a switching frequency of 10 kHz and can impose a nominal current of 2 kA in 250 μs to flow on the G coil. The dead zone close to 0 is a further nonlinearity which ignores any reference voltage in the range ± 10 V. In standard operations the current on the G coil is limited to 1.6 kA and a safety system for over-voltage and over-current protection is included. For thermal protection, no DC current can flow in the G coil and if this condition is violated a thermal alarm is triggered terminating the shot following a threshold on the current integral. Further details, used for the FPS modeling in simulations, are discussed in Sec. 3.4. For the FPS three modes of operation are possible

- voltage mode, where the voltage request from the control system is compared to a triangular wave regulating the switching of the H bridge.

- current mode, where a reference current is imposed on the coil through a hysteresis switching limited bang-bang controller internal to the power supply.

- hybrid mode, which is not yet implemented in operations and would allow driving the switches of the H-bridge directly with an input signal.

The main coil and power supply characteristics are summarized in Table 2.2, and further details on the coil hardware can be found in [80].

Coil	Power supply		Parameters	
	$\mathbf{U}_{max}$ [V]	$\mathbf{I}_{max}$ [kA]	$\mathbf{R}_a$ [mΩ]	$\mathbf{L}_a$ [mH]
TOR	626	78		
OH	1400	31	15 (OH1) /13.3 (OH2)	6.9 (OH1) /4.8 (OH2)
E	651	7.7	11.8	1.7
F	1250	7.7	39.1	7.4
G	566(280)	2(1.6)	32	0.1

Table 2.2 – Characteristics of the power supplies and active coil parameters. For the G coil in antiseries, the typical limits imposed during shots are indicated in parenthesis.
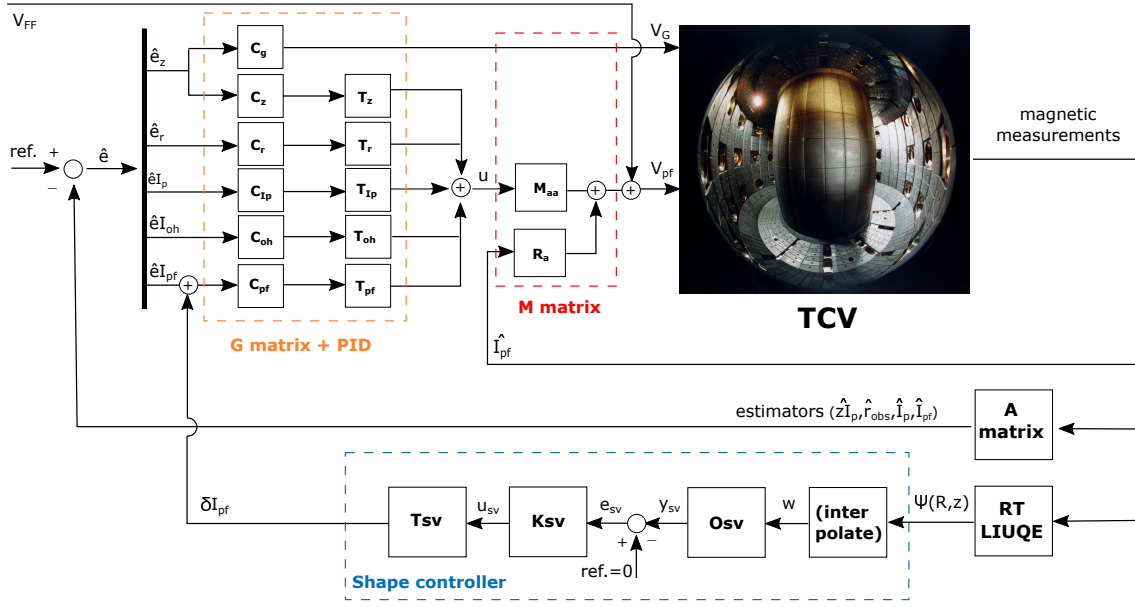
Figure 2.8 – TCV magnetic control loops and shape controller. References ($ref.$) and feedforward voltages (V_{FF}) are designed in advance during the shot preparation. The only remaining loop of the hybrid controller not represented here is density control, which actuates the main fuelling gas valve.

2.4 Real time control in TCV

During TCV operations, two systems can be used to control plasma evolution in feedback. One is the original control system ("hybrid") that was designed with the tokamak while the second is the new digital control system ("SCD") which is gradually replacing it. Both systems were used during the experimental work of this thesis. Individual switches determine the choice of the actuation signals on TCV between the ones coming from the analog control system of the DAC outputs of the digital one. In this section, their main characteristics are illustrated and a more detailed explanation of magnetic control is provided.

2.4.1 The analog plasma control system

The TCV "hybrid" (analog, linear, matrix-based) control system is based on a set of switching matrices [80] that are defined before each shot with the routines of the FBTE [88] and MGAMS suites [89]. This control system was built at the time of initial design and construction of TCV to guarantee the required control bandwidth, the constraint being mainly given by the expected vertical growth rate of the most unstable plasmas.

Starting from a desired plasma shape evolution in time, the free boundary code FBTE computes the necessary poloidal field currents to obtain the required equilibria, along with the voltage feedforward and the sign bits (polarity switching time). These signals and the associated references for plasma current, position, density and optionally elongation are

stored in the MDSPlus database for each shot. Observers and controller gains are computed using MGAMS. The observers are obtained as linear combinations of available TCV measurements and stored in a unique matrix called A matrix (see Appendix A for details). The controller gains are stored in G1 G2 and G3 matrices, which determine amplification of the proportional-integral-derivative (PID) circuits output signal and projection along the desired actuation direction. The PIDs feature a rolloff $R_o(s) = 1/\left[(1 + s\tau_1)(1 + s\tau_2)\right]$ with $\tau_1 = 10^{-4}s$ and $\tau_2 = 1.02 \times 10^{-4}s$ for the derivative term and $1/(1 + s\tau_p)$ with $\tau_p = 6.8 \times 10^{-5}s$ for the proportional term. These values are selected to filter out high frequency noise at higher frequencies than the expected bandwidth, and can be determined from the characteristics of the circuit of the analog control system. In typical shots the only integral contribution in G1 is for density and I_p control. The G matrix output signals for the coils u, with the notable exception of the G coil voltage, are treated with a mutual decoupling and resistive compensation block called M matrix such that the actual actuator commands to the PF coils reads

$$V_{pf} = M_{aa}u_{pf} + R_a\hat{I}_{pf} + V_{FF} \qquad (2.3)$$

where $\hat{I}_{pf}$ is the coil current measurement, V_{FF} is the precalculated voltage feedforward stored in a wavegen before the shot and M_{aa} and R_a are respectively the mutual inductance and resistances of the coils, stored in MDSPlus nodes for the static properties of TCV. Note that u_{pf} is expressed in A/s. In this way, a quasi-integral effect (any uncertainty of the coil resistances makes the resistive compensation non-ideal) is included in the controller and the coil dynamics is decoupled in order to use decentralized control for coil current control.

Despite providing robust and reliable operation since the first experiments, the analog control system has a series of disadvantages due to its technical constraints. One of these is the ability to perform only linear operations, which excludes for example the inclusion of nonlinear observers (e.g. equilibrium reconstruction) or control schemes other than PID. Another one is the fixed number of input (128) and output (20) channels which means that only a limited number of variables and actuators can be controlled, constraining the capability of extending the control to new systems that can be integrated on the TCV tokamak over time as happened with the ECRH and NBI extension.

2.4.2 The digital plasma control system

The Système de Contrôle Distribué (SCD) is a digital, modular, massively multichannel control system that was designed to overcome the limitations of the analog hybrid controller and envisaged to gradually replace it [90]–[92].

This system allows connecting several diagnostic acquisition modules and performing real time signal processing to generate an output signal for any actuator connected to the system DACs (at the moment, PF coils, gas valves, the ECRH/ECCD and the NBI system). The control algorithms are built using Simulink, which allows a flexible and user-friendly controller design based on a block scheme approach. This lets the user focus

on the control design procedure without dealing with input/ouput mapping.

The SCD is constituted by a set of nodes (industrial PCs) with different sampling rates featuring an inter node connection based on reflective memories and optical fibers, such that the data written on the shared memory is available to all nodes with a sub-ms delay. Each node hosts a Simulink-based code for signal processing, which is converted in C and compiled for real time run at its specific cycle time. Only five out of the actual seven nodes are connected to a crate hosting one or more D-TACQ [93] ACQ-196 acquisition cards with 96 ADCs, and output cards housing 16 or 32 DACs. Reference and feedforwards signals are read from MDSPlus. Nodes not featuring DAC/ADCs are only connected via the reflective memory network and act as computational nodes.

There are several advantages of operating with the digital control system compared to the hybrid analog controller. Firstly, there is the possibility to perform nonlinear signal operations and implementing more complex control schemes than PID, since Simulink provides several libraries for signal processing. A digital system is by definition not sensitive to analog electronics issues such as , noise pick up and drifts.Furthermore, the number of channels for input-output connection is much larger compared to the hybrid controller. Finally, it is possible to perform open loop simulations of the whole control chain both for verifying a new controller or reprocessing data from a former shot for quick debugging or troubleshooting even between plasma discharges.

Among the various applications of the digital control system, some are listed here to underline its great flexibility

- replication of the former analog controller (hybrid emulator) [90]

- model-based control of the plasma profile [57]

- shape and position controller [79]

- stabilization and the prevention of NTMs by means of ECCD control [94]

- analysis of fast MHD modes based on SVD of the magnetics measurements [95]

- the first development of integrated supervisory control in TCV [96]

- control of the C-III detachment front using the impurity injection as actuator [60]

At the moment, the stabilization of the plasma vertical instability using internal coils is still handled by the legacy analog controller system as the latency of the digital control system was too large, but a recent upgrade allowing the cycle time for the hybrid emulator to move down from 0.1 to 0.04 ms allows including also FPS in the digital control system although requiring a careful tuning of the high frequency rolloff.

2.4.3 Magnetic control

Figure 2.8 shows the control loops from magnetic measurements to the voltage applied to the poloidal field coils to track a set of preprogrammed references, summarizing magnetic control in TCV, along with shape control discussed in detail in the following section. The main roles of magnetic control are stabilizing the vertical instability, controlling plasma current and position to their reference and tracking the preprogrammed coil currents.

The controlled variables, outputs of the A matrix, include the currents flowing in the coils external to the vessel $\hat{I}_{pf}$, the plasma current times the vertical displacement $z\hat{I}_p$, a radial observer $\hat{r}_{obs}$, the plasma current $\hat{I}_p$ and finally the difference between the two OH circuit currents $\Delta_{OH} = \hat{I}_{OH1} - \hat{I}_{OH2}$ which should be kept close to zero to minimize the stray (unwanted) field in the plasma region. A derivation of the linear combination of magnetic measurements providing plasma position and current estimates can be found in Appendix A. These estimates are subtracted from their corresponding references and the resulting error signals are the inputs to the controllers whose output corresponds to integral (I), proportional (P) and derivative (D) channels respectively. A system of three tuneable switching matrices G_1 G_2 and G_3 multiply respectively the outputs of the I, P and D blocks, providing the controller gain (via signal amplification) and actuation directions (applying the signal to a selected PF coil). The output of G_1, G_2 and G_3 is summed and the resulting signal is fed to the the mutual decoupling and resistive compensation block, which provides the control commands to the E F OH and G coils power supplies.

At this point this results in an underactuated system since it is not possible to control the whole set of estimators (19 coil current errors plus $z\hat{I}_p$, $\hat{r}_{obs}$, $\hat{I}_p$, Δ_{OH}) to their reference with a smaller number of actuators ($V = [V_{pf}^T \, V_G]^T \in \mathbb{R}^{19}$), i.e. already controlling all the coil currents to their reference would use all actuators. The solution developed for standard operation is to select only a subset of variables to be controlled using one or more coils in various combinations $T_j \in \mathbb{R}^{19}$ to accomplish separate tasks with the constraint of orthogonality $T_j^T T_k = 0 \; \forall j \neq k$. In this description, we describe the block G matrix + PIDs using directions T and controllers $C(s)$ as reproduced in Fig. 2.8:

- The OH coils, used in T_{Ip} and T_{OH}, are dedicated to plasma current control, due to their geometrical structure maximizing the flux enclosed by the plasma while minimizing the field generated within the vessel. Proportional-integral control (C_{Ip}) is applied on the plasma current estimator error or the OH current error, and a proportional controller (C_{OH}) is used to minimize the error between the coil currents. The current control loop will not be treated in more detail in this work as the focus is on the E F and G coils.

- The internal (G) coil design is optimized for the control of the vertical instability as it avoids the field shielding by the vessel and cannot sustain DC currents. This is accomplished by applying purely derivative control on the plasma vertical position error with gain $G_{z,std} \in \mathbb{R}$, which is equivalent to velocity control, ideally providing a zero voltage request to the power supplies when the plasma position has reached

a steady state. Note that pure derivative control is not sufficient to stabilize the vertical instability for non-ideal circuits [97]. The resulting controller is

$$C_g = sG_{z,std}R_o(s) \tag{2.4}$$

- Among the 16 poloidal field coils outside the vessel (E and F coils), two coil combinations $T_{z,std}$ and $T_{r,std}$, both $\mathbb{R}^{16}$ (excluding the two OH coils and the G coil) are selected for vertical and radial plasma position control respectively. These directions and gains are stored in the TCV MDSPlus database and are read during shot preparation. Typical control directions include four of the outer (F) coils, chosen mainly based on physical intuition [80] and experimental evidence [98] about the required vacuum field necessary for inducing a vertical or radial displacement of the plasma column. The control is proportional in the case of the radial position estimator $\hat{r}_{obs}$ error, with gain $P_{r,std}$, whereas it was found that proportional-derivative control of the vertical $\hat{zI}_p$ error was required for vertical stabilization and control, with gains $P_{z,std}$ and $D_{z,std} \in \mathbb{R}$ [99]. It is noted that this separate position control supplies the necessary proportional feedback on vertical position to fully stabilize the vertical mode[II] This results in the controllers

$$C_r(s) = P_{r,std}/(s\tau_p + 1) \tag{2.5}$$
$$C_z(s) = P_{z,std}/(s\tau_p + 1) + sD_{z,std}R_o(s). \tag{2.6}$$

- The values of the currents in the linear combination of coils $T_{z,std}$ and $T_{r,std}$ will be determined by the vertical and radial errors, therefore it is no longer possible to control the PF coil currents in these directions. Hence, only the poloidal field coil current combinations orthogonal to $T_{z,std}$ and $T_{r,std}$ can be controlled. Equivalently, only the columns of $N_{pf} = \text{Im}(\ker [T_{z,std} \quad T_{r,std}]) \in \mathbb{R}^{16 \times 14}$ define orthogonal linear combinations of E and F coil currents that can be tracked exactly. In this way the matrix used for current control can be defined as

$$T_{pf} = N_{pf} N_{pf}^T \in \mathbb{R}^{16 \times 16}. \tag{2.7}$$

Diagonal proportional control C_{pf} is applied, considering that the coils at low frequency (i.e. for timescales longer than the characteristic vertical instability growth time) have the dynamics to achieve integral behavior thanks to mutual decoupling and resistive compensation. In this way, the proportional gain determines the bandwidth of the current controller.

[II]the choice of $\hat{zI}_p$ is an artifact of directly using a Shafranov moment estimator, which does not compensate for I_p variation. See Appendix A.2.3 for more details on the analog position observer.

2.5 Shape control in TCV

The digital shape control as operated in TCV is discussed in this section in more detail, highlighting its results and the possible extension studied in this thesis.

With the exception of plasma elongation control based on a linear estimator [100], shape control in TCV is usually controlled in feedforward, computing the coil current reference for attaining a given shape with FBTE. Unavoidable or unmodeled disturbances (external heating, ELMs, blocked coils etc.) can lead to a different and undesired shape of the plasma cross section compared to the predicted one. The development of a digital shape controller for TCV [79] relying on the real time equilibrium reconstruction code LIUQE-rt [41] allowed moving from feedforward to feedback thus correcting shape deformations in real time instead of doing so on a shot-by-shot basis.

Shape controller design in TCV as proposed in [79] is based on isoflux control and includes the control of plasma position. Its design and implementation consists of the following steps, which are performed during a shot preparation once the preprogrammed plasma equilibrium flux ψ_{eq} is available:

1. definition of position and shape observers

2. derivation of a model-based decoupling control scheme including input constraints

3. controller tuning and inclusion in TCV digital controller

2.5.1 Shape and position observer

In order to design the shape and position observer, it is assumed that the plasma equilibrium is reconstructed with LIUQE in real time, such that at any instant the flux $\psi(R, z)$ is available on the LIUQE computational grid. The flux at n_b boundary points $(\mathbf{R_b}, \mathbf{z_b})$ is evaluated by interpolation. In the case of diverted plasmas, the flux at n_d strike points and the magnetic field vector at n_x X-points is also evaluated yielding a measurement vector $w \in \mathbb{R}^{n_w}$ where $n_w = n_b + n_d + 2n_x$. The errors that should be taken to zero when performing isoflux shape control are the flux difference between boundary points [III], the radial and vertical magnetic field at the X-point and the flux difference between the strike points and the X-point. For this purpose, a matrix M_Δ is defined such that the flux errors at the boundary $\Delta\psi_b$ at the strike points $\Delta\psi_d$ and field errors ΔB_x are

$$
\begin{bmatrix} \Delta\psi_b \\ \Delta\psi_d \\ \Delta B_x \end{bmatrix} = \begin{bmatrix} M_b \\ M_d \\ & & I^{2n_x \times 2n_x} \end{bmatrix} w = M_\Delta w \in \mathbb{R}^{n_y}.
\tag{2.8}
$$

where $n_y = n_w - 1$. Scaling is introduced in order to have quantities comparable in magnitude such that

$$
y = M_\Delta S_0 w
\tag{2.9}
$$

[III]The shape controller is designed to control the flux difference between neighboring points for limited shapes, and the differences with respect to the X-point(s) for diverted shapes

where S_0 scales the fluxes by the inverse of the absolute value of the pre-programmed magnetic flux on axis ψ_{ax} and the magnetic field by the pre-programmed absolute value of the total magnetic field at the X-point. Since proportional control of the plasma vertical position is necessary for vertical stabilization and in order to correct radial errors explicitly, an estimate of the plasma vertical and radial displacement from measured flux difference at the boundary are derived as [IV]

$$\Delta z = O_{\Delta z} \Delta \psi_b = - \left(M_b \frac{\partial \psi_{eq}}{\partial z} \Big|_b \right)^T \left\| M_b \frac{\partial \psi_{eq}}{\partial z} \Big|_b \right\|_2^{-2} \Delta \psi_b \in \mathbb{R} \tag{2.10}$$

$$\Delta R = O_{\Delta r} \Delta \psi_b = - \left(M_b \frac{\partial \psi_{eq}}{\partial R} \Big|_b \right)^T \left\| M_b \frac{\partial \psi_{eq}}{\partial R} \Big|_b \right\|_2^{-2} \Delta \psi_b \in \mathbb{R} \tag{2.11}$$

where $(\partial \psi_{eq}/\partial z)|_b$ and $(\partial \psi_{eq}/\partial r)|_b$ are the vertical and radial gradients of the pre-programmed flux distribution ψ_{eq} evaluated at the boundary points. These observers are obtained inverting the relation for flux difference between interpolation points following a rigid plasma displacement

$$\Delta \psi_b (\Delta z, \Delta R) = -M_b \nabla \psi_{eq}|_b \begin{bmatrix} \Delta z \\ \Delta R \end{bmatrix} \quad \text{where} \quad \nabla \psi_{eq}|_b = \begin{bmatrix} \dfrac{\partial \psi_{eq}}{\partial z} \Big|_b & \dfrac{\partial \psi_{eq}}{\partial R} \Big|_b \end{bmatrix} \tag{2.12}$$

as a least squares problem. Note however that in general $(M_b \nabla_R \psi_{eq}|_b)^T (M_b \nabla_z \psi_{eq}|_b) \neq 0$, and Eq. (2.10) and (2.11) are valid only in the assumption of an exact vertical and radial displacement only respectively. The observers are subsequently scaled in order to be dimensionless and comparable in magnitude with the remaining errors. This is obtained defining

$$\begin{aligned} y_z &= \overrightarrow{\psi}_z \frac{1}{|\psi_{ax}|} \Delta \psi_b = O_{\Delta z} \left\| M_b \frac{\partial \psi_{eq}}{\partial z} \Big|_b \right\|_2 \frac{1}{|\psi_{ax}|} \Delta \psi_b \\ y_r &= \overrightarrow{\psi}_r \frac{1}{|\psi_{ax}|} \Delta \psi_b = O_{\Delta r} \left\| M_b \frac{\partial \psi_{eq}}{\partial R} \Big|_b \right\|_2 \frac{1}{|\psi_{ax}|} \Delta \psi_b. \end{aligned} \tag{2.13}$$

The scaled position, flux and field error estimates are therefore obtained from the interpolated fluxes and fields as

$$y_{es} = \begin{bmatrix} y_z \\ y_r \\ y \end{bmatrix} = Ow = \begin{bmatrix} \overrightarrow{\psi}_z M_b & 0 & 0 \\ \overrightarrow{\psi}_r M_b & 0 & 0 \\ & [M_\Delta] & \end{bmatrix} S_0 w \in \mathbb{R}^{n_o}, \tag{2.14}$$

such that $n_o = n_y + 2$. Note that the rows of O are not linearly independent since the position observers are linear combination of flux differences: the rank of O is n_y.

[IV]In [79, p. 32] the observer definition is slightly different but in the following it is kept with the present notation.

2.5.2 Decoupling scheme

Once the observers are in place, a decoupling scheme is developed such that off diagonal coupling is minimized in order to tune a simple diagonal (decentralized) controller.

Steady state decoupling is considered [101, p. 92] basing on a static model since shape control is applied on long time scales compared to the plasma dynamics. The model proposed in [79] for TCV is a real matrix whose elements are electromagnetic Green's function determining flux generated in vacuum (e.g. ignoring the plasma) at the boundary ($\psi_{b,v}$) and strike ($\psi_{d,v}$) points and the field generated at the X points ($B_{x,v}$) from perturbations in the static currents δI_{ef} flowing in the n_c (typically $n_c = 16$) E and F coils:

$$G_0 = \left[\begin{array}{c} G_b \\ G_d \\ G_x \end{array} \right] = \left[\begin{array}{c} \partial\psi_{b,v}/\partial I_{ef} \\ \partial\psi_{d,v}/\partial I_{ef} \\ \partial B_{x,v}/\partial I_{ef} \end{array} \right] \in \mathbb{R}^{n_w \times n_c}, \tag{2.15}$$

such that $w = G_0 \delta I_{ef}$. This approach is analogous to the one discussed in [102] in which the influence of the controlled currents on the shape observers is due to the flux generated by the currents alone, while the changes in the plasma and passive elements currents are neglected. A discussion on the validity of this model is performed in Sec. 4.5.

A constraint is added to the inputs of G_0, namely the E and F coil current perturbations, such that the average addition of poloidal flux at the boundary points is zero, avoiding coupling with the plasma current controller. This is obtained defining $N_c \in \mathbb{R}^{n_c \times (n_c-1)}$ as the basis of the null space of $\mathbf{1}^T G_b$ effectively limiting the number of coil directions for shape and position control to $n_c - 1$.

Steady state decoupling is obtained using a system of pre- and post-compensators from a singular value decomposition of the non-diagonal plant determining the effect of the available coil current directions on the position and shape observers. Diagonal weighting W_t is added to the outputs of the observer matrix O to prioritize position observers as the main contribution to the first two singular values of the system in the subsequent singular value decomposition.

The model of the plant to be decoupled is consequently defined as

$$P_0 = W_t O G_0 N_c \in \mathbb{R}^{n_o \times (n_c-1)} \tag{2.16}$$

and a singular value decomposition [101, p. 520] of the plant reads

$$P_0 = U_0 \Sigma_0 V_0^T. \tag{2.17}$$

In this way, including pre-and post-compensators as $(\Sigma_0 V_0^T)^\dagger$ and U_0^T respectively, the plant to be controlled with diagonal control becomes

$$L_{dec}^{SC} = U_0^T P_0 (\Sigma_0 V_0^T)^\dagger = \left[\begin{array}{cc} I^{n_{sv} \times n_{sv}} & \\ & 0^{(n_o-n_{sv}) \times (n_o-n_{sv})} \end{array} \right], \tag{2.18}$$

where use is made of the properties of orthogonality of U and V derived from the SVD
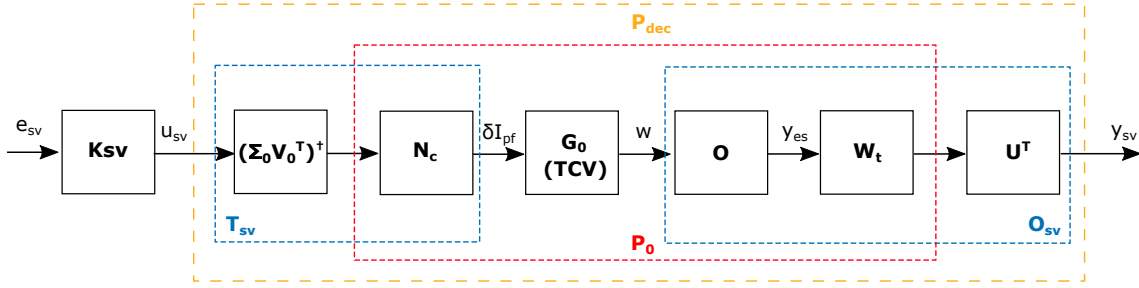
Figure 2.9 – TCV shape controller open loop block scheme.

of the system $U^T U = I^{n_o \times n_o}$ and $V^T V = I^{(n_c-1) \times (n_c-1)}$. Furthermore the Moore-Penrose pseudoinverse † was used for the precompensator, where to prove the equality of Eq. (2.18) one can use $(\Sigma_0 V_0^T)^\dagger = V_0 \Sigma_0^\dagger$. In Eq. (2.18), $n_{sv} = \min(n_y, n_c-1)$ is the number of singular values of P_0 which corresponds to the maximum number of variables that can be controlled and is given by its rank, and n_o is its row dimension. Using pre- and post-compensators for the static plant, off-diagonal coupling is removed, allowing decentralized control. This is obtained since the controller acts on P_0 along the orthogonal input singular vectors (columns of V_0) and controls its outputs (weighted position and shape observers) projected in the space defined by orthogonal output singular vectors (columns of U_0). It is underlined that that the first two outputs of L_{dec}^{SC}, despite being mainly aligned with the position observers following weighting W_t, do not have the exact same physical meaning since they include contributions from other shape observers. The open loop block scheme is reproduced in Fig. 2.9. The diagonal system corresponds to

$$y_{sv} = \begin{bmatrix} z_{sv} \\ r_{sv} \\ b_{sv} \end{bmatrix} = L_{dec}^{SC} u_{sv} \in \mathbb{R}^{n_o} \tag{2.19}$$

where z_{sv} is the output mainly aligned with the scaled vertical observer y_z, r_{sv} is the output mainly aligned with the scaled radial observer y_r and b_{sv} are the output mainly describing the plasma boundary deformation. The degree of alignment of position observers in the sense of the first two rows of O_{sv} being parallel to the first two rows of O depends on the weighting set in W_t.

Only the largest $N_{sh} \le n_{sv}$ variables are selected to be controlled since they correspond to the singular values which are most easily controllable and observable. This is obtained keeping only the first N_{sh} columns of U_0 and V_0 and setting the remaining to 0.

2.5.3 Controller tuning

The shape controller acts on the plasma using the coil combinations given by the columns of

$$T_{sv} = N_c (\Sigma_0 V_0^T)^\dagger \in \mathbb{R}^{n_c \times n_o} \tag{2.20}$$

such that $\delta I_{EF} = T_{sv} U_{sv}$ and combines the interpolated outputs of LIUQE with the rows of

$$O_{sv} = U_0^T W_t O \in \mathbb{R}^{n_o \times n_w} \tag{2.21}$$

such that $y_{sv} = O_{sv} w$. The goal is to control to zero the set of $N_{sh} \leq n_{sv}$ selected variables corresponding to the largest singular values such that $e_{sv} = -y_{sv}$ and the controller used to perform this is a diagonal PI controller K_{sv}.

Inclusion of the shape controller in TCV is performed by correcting the coil current reference of the E and F coils as represented in Fig. 2.8. Note that correcting the errors is equivalent to correcting the reference. In this way, the coil current perturbation δI_{EF} required by the shape controller is tracked by the PF coil current controller: the model G_0 is valid for time scales longer than the reciprocal of the PF current controller bandwidth. The shape and position controller is in charge of plasma position control on these time scales. When performing shape control during plasma discharges in TCV, all PF coils currents track their modified reference (in contrast with standard magnetic control). This is done setting T_I as a diagonal matrix and removing proportional vertical and radial control.

The pre- and post- compensation controller allows exact decoupling of a stable, static plant G_0. The actual controller included on TCV requires precise tuning due to the vertical instability of elongated plasmas and the dynamics of the PF coils. For the purpose of vertical stabilization, the controller proposed by [79] maintains the derivative vertical control of standard magnetic control in the loop. The shape control loop, including O_{sv} and T_{sv}, is closed and K_{sv} is tuned to stabilize the vertical instability and control the shape to a desired reference based on the RZIp model, which includes the coil, vessel and plasma unstable dynamics (see Sec. 3.2). This and the selection of weights in W_t are the only steps performed offline for shape controller tuning.

2.5.4 Proposed extension

The controller was tested on several TCV shapes, providing a precise shape control of several plasma configurations, but required extensive manual tuning despite the preliminary tuning performed with RZIp. The work proposed in this thesis aims to extend the capability of this useful tool with an approach based on control engineering for SISO and MIMO controller synthesis.

In particular the following topics will be developed:

- The RZIp model will be refined and extended to improve its predicting capability for tuning magnetic controllers (Chapter 3).

- Position control will be decoupled from the shape controller in a more systematic way, allowing independent tuning (Chapter 4).

- Finally, optimization of vertical instability control will be studied in order to maximize the flexibility of the shape controller and provide a further useful tool for TCV operation (Chapter 5).

3 The RZIp model for magnetic control

The design of linear controllers for plasma shape and position is based on control-oriented linear models describing the dynamics of interest. In the present study, this is the coupled dynamics of the plasma within the tokamak and the currents in the conducting elements surrounding it: the vessel and coil system. This chapter is devoted to introducing the unstable vertical dynamics of an elongated plasma in a tokamak with a simplified model. The RZIp model, which is the main modeling tool used for controller design and simulations in this thesis, is then introduced and its open loop dynamical properties are discussed along with a discussion on the model used for the power supplies.

Among the existing models that are used to describe tokamak dynamics (a review can be found in [103], [104]), the RZIp model [79], [105] is particularly suited for optimizing the control of the vertical instability in TCV, being linear and adaptable to match the electromagnetic characteristics of this tokamak, although it does not consider plasma shape deformations. In this axisymmetric model, the plasma current distribution is fixed but is free to move radially and vertically in the poloidal plane of a toroidal reference frame, while the evolution of currents in the conductive elements is considered.

The chapter is structured as follows.

In Section 1 a simplified dynamical model comprising one coil, one vessel mode and one plasma filament is presented. This model allows a simple analytical treatment and some of the dynamical properties of the RZIp model emerge already from its study.

In Section 2 the RZIp model is presented. The model is compared with the single filament model for the vertical dynamics and the vessel modeling is briefly discussed.

In Section 3 the assumption of rigid displacement is relaxed allowing deformation following a radial plasma displacement, thus leading to a semi-rigid RZIp model which better fits experimental data. This extension of the RZIp model is a novel contribution of this thesis.

In Section 4 the power supplies dynamics and modeling is discussed. Furthermore, for the G coil a nonlinear model of the fast power supply is also presented for improving the quality of closed loop simulations.

3.1 Single filament model

Modeling for magnetic control should always consider the vertical instability of elongated plasmas. The fundamental dynamics of interest can be analyzed with the single filament model of [106] [38], which is re-derived here with the inclusion of the corresponding analytical transfer functions.

3.1.1 Derivation of the single filament model

The simplest model for the plasma vertical dynamics describes the plasma as a toroidal filament with constant current I_{p0} subjected to an axisymmetric Lorentz force due to the currents flowing in the conductive elements outside of it: coils and vessel. The plasma is constrained to move in the vertical direction only, maintaining a radial equilibrium at position R_0: hoop and tire tube force expanding the plasma radially are compensated by a radial Lorentz force thanks to the vertical magnetic field generated by equilibrium currents. The currents in the conductive elements evolve accordingly to Kirchhoff's law, considering an external voltage generated by the power supply on the coil as input. Two scalar currents, one flowing toroidally in a coil I_a and one in a single vessel current distribution I_e, evolve dynamically and are able to generate a radially directed field at the filament location. For the vessel, only the first vertically asymmetric mode in an eigenvalue representation is considered. The dynamical model of [106] [38] in (R, ϕ, z) reads

$$
\begin{cases}
m_p \ddot{z} = -2\pi R_0 I_{p0} B_R(z, I_a, I_e) \\
L_e \dot{I}_e + R_e I_e + \dot{\psi}_{ep}(z) + M_{ea} \dot{I}_a = 0 \\
L_a \dot{I}_a + R_e I_a + \dot{\psi}_{ap}(z) + M_{ae} \dot{I}_e = 0
\end{cases}
\tag{3.1}
$$

Here m_p is the plasma mass, B_R is the radial field due to all external conductors varying along the z coordinate, $L_{a,e}$, $M_{ae,ea}$ and $R_{a,e}$ are the self and mutual inductances and resistances associated with the lumped parameter circuit equations for the dynamical currents. The term $\dot{\psi}_{ae,p}(z)$ quantifies the time rate of change of the flux enclosed by each circuit due to motion of the plasma. Finally the radial force balance is considered to always satisfy

$$
0 = m_p \ddot{R} = 2\pi R_0 I_{p0} B_{z,0} + \frac{1}{2} \mu_0 I_{p0}^2 \Gamma
\tag{3.2}
$$

where $B_{z,0}$ is the equilibrium vertical field due to conductors other than the plasma evaluated at the filament position and Γ is the Shafranov parameter

$$
\Gamma = \ln \frac{8R_0}{a\sqrt{\kappa}} + \frac{\ell_i}{2} + \beta_p - \frac{3}{2}
\tag{3.3}
$$

Here a is the plasma minor radius, κ the elongation, β_p the poloidal beta and ℓ_i the plasma self inductance which are given parameters. The model is linearized around the equilibrium point (z_0, I_{e0}, I_{a0}) considering (z, I_e, I_a) as perturbations. In the following, all partial derivatives are evaluated around the equilibrium.

Radial magnetic fields

Linearization of the dynamics requires the evaluation of the magnetic field around the equilibrium point. This is done by separating the contribution from the vessel and the coil

$$B_R(z, I_a, I_e) = B_R^a(z, I_a) + B_R^e(z, I_e) \tag{3.4}$$

and making use of

$$B_R^{a,e} = -\frac{1}{2\pi R}\frac{\partial \psi_{p,ae}}{\partial z} \tag{3.5}$$

where the flux enclosed by the plasma filament and generated by the currents outside of it is $\psi_{p,ae} = M_{p,ae}I_{p,ae}$ and $M_{p,ae}$ is a geometric mutual inductance. The term $M_{p,ae} = M_{ae,p}$ is computed from a toroidal plasma current distribution $J_p(R, z)$ using the expression

$$M_{ae,p} = (1/I_{p0})\int M_{ae,x}(R, z)J_p(R, z)dRdz \tag{3.6}$$

where $M_{ae,x}(R, z)$ is the mutual inductance between the points on the poloidal plane, where J_p is provided, and each discrete conductor (a or e). In this way the vessel contribution to the radial magnetic field results in

$$B_R^e(z, I_e) = B_{R,0}^e + \frac{\partial B_R^e}{\partial z}z + \frac{\partial B_R^e}{\partial I_e}I_e \tag{3.7}$$

$$= B_{R,0}^e + \frac{\partial}{\partial z}\left(-\frac{1}{2\pi R}\frac{\partial M_{pe}}{\partial z}I_e\right)z + \frac{\partial}{\partial I_e}\left(-\frac{1}{2\pi R}\frac{\partial M_{pe}}{\partial z}I_e\right)I_e \tag{3.8}$$

$$= -\frac{1}{2\pi R}\frac{\partial M_{pe}}{\partial z}I_e \tag{3.9}$$

where it was assumed that $I_{e,0} = 0$ and $B_{R,0}^e = 0$.

For the coil contribution instead, the equilibrium current is generally not null and the magnetic field satisfies $\nabla \times \mathbf{B}^a = 0$ at the plasma location. Consequently

$$\frac{\partial B_R^a}{\partial Z} = \frac{\partial B_Z^a}{\partial R} = -\frac{B_{Z,0}}{R_0}\left(-\frac{R_0}{B_{Z,0}}\frac{\partial B_Z^a}{\partial R}\right) = \frac{\mu_0 I_{p,0}\Gamma}{4\pi R_0^2}\,n, \tag{3.10}$$

where n is the decay index of the vertical field along R as included in [38]

$$n = -\frac{R_0}{B_{Z,0}}\frac{\partial B_Z^a}{\partial R}. \tag{3.11}$$

Note that $n < 0$ for a vertically elongated plasma [107], regardless of the current direction. The term $B_{Z,0}$ is the magnetic field required for radial equilibrium from Eq.(3.2) reading

$$B_{Z,0} = -\frac{\mu_0 I_{p,0}\Gamma}{4\pi R_0}. \tag{3.12}$$

The coil contribution to the linearized radial field is then

$$B_R^a(Z, I_a) = B_{R,0}^a + \frac{\partial B_R^a}{\partial Z} z + \frac{\partial B_R^a}{\partial I_a} I_a \tag{3.13}$$

$$= \frac{\mu_0 I_{p,0} \Gamma}{4\pi R_0^2} n\, z \; + \frac{\partial}{\partial I_a}\left(-\frac{1}{2\pi R}\frac{\partial M_{pa}}{\partial Z} I_a\right) I_a \tag{3.14}$$

Where it was considered that at the equilibrium position

$$m_p \ddot{Z}_0 = 0 = -2\pi R I_p(B_{R0}^a + B_{R0}^e) \quad \rightarrow \quad B_{R0}^a + B_{R0}^e = 0 \tag{3.15}$$

Vertical dynamics

Substituting the linearized radial magnetic fields of Eq. (3.9) and (3.14) the linearized vertical equilibrium reads

$$m_p \ddot{z} = -2\pi R I_{p0}\left(\frac{\mu_0 I_{p,0}\Gamma}{4\pi R^2} n\, z \; - \frac{1}{2\pi R}\frac{\partial M_{pa}}{\partial Z} I_a - \frac{1}{2\pi R}\frac{\partial M_{pv}}{\partial Z} I_e\right) \tag{3.16}$$

and introducing in analogy with [38] the term

$$\omega_1^2 = \frac{\mu_0 I_{p,0}^2 \Gamma}{2 m_p R_0} \tag{3.17}$$

leads to the linearized dynamics of the plasma in the vertical direction

$$\ddot{z} + \omega_1^2 n\, z - \frac{I_{p0}}{m_p}\frac{\partial M_{pa}}{\partial Z} I_a - \frac{I_{p0}}{m_p}\frac{\partial M_{pe}}{\partial Z} I_e = 0. \tag{3.18}$$

Neglecting the coils and the vessel dynamics, $p_z = \pm \omega_1 \sqrt{-n}$ represents the poles of the plasma vertical position dynamics, one of which is unstable for elongated plasmas ($n < 0$). While n can be estimated for the actual equilibrium, it is treated in the following as a free parameter to study the effects of elongation.

Circuit equations

The lumped parameters circuit equations modeling the current dynamics are

$$L_e \dot{I}_e + R_e I_e + \frac{\partial M_{ep} I_p}{\partial t} + M_{ea}\dot{I}_a = 0 \tag{3.19}$$

$$L_a \dot{I}_a + R_a I_a + \frac{\partial M_{ap} I_p}{\partial t} + M_{ae}\dot{I}_e = V_a \tag{3.20}$$

where the flux due to the plasma seen by the conducting elements is $\psi_{ae,p} = M_{ae,p} I_p$. Recalling that the model is evaluated for a constant plasma current I_{p0} and radius R_0 and

$M_{ae,p} = M_{ae,p}(z)$, the linear circuit equations are written as

$$L_e \dot{I}_e + R_e I_e + I_{p0} \frac{\partial M_{ep}}{\partial z} \dot{z} + M_{ea} \dot{I}_a = 0 \tag{3.21}$$

$$L_a \dot{I}_a + R_a I_a + I_{p0} \frac{\partial M_{ap}}{\partial z} \dot{z} + M_{ae} \dot{I}_e = V_a \tag{3.22}$$

Singular perturbation

Combining Eq. (3.18) (3.21) and (3.22), the linearized single filament model is

$$\begin{cases} m_p \ddot{z} + m_p \omega_1^2 n\, z - I_{p0} M'_{pa} I_a - I_{p0} M'_{pe} I_e = 0 \\ L_e \dot{I}_e + R_e I_e + I_{p0} M'_{ep} \dot{z} + M_{ea} \dot{I}_a = 0 \\ L_a \dot{I}_a + R_a I_a + I_{p0} M'_{ap} \dot{z} + M_{ae} \dot{I}_e = V_a \end{cases} \tag{3.23}$$

where the $'$ symbol here and in the following is the derivative with respect to z and $M'_{pe} = M'_{ep}$, $M'_{pa} = M'_{ap}$. The model has the structure

$$\begin{cases} \epsilon \dot{x} = f(x, I) \\ \dot{I} = g(x, I, V_a) \end{cases} \tag{3.24}$$

where $x = [\dot{z}\ z]^T$ and $I = [I_a\ I_e]^T$ and $\epsilon \ll 1$ is a small parameter. In the case of vertical force balance ϵ is determined by the different time scales of the inertial term and the Lorentz forces, such that the former can be neglected using a singular perturbation method. This allows removing the fast time scale of the system and considering a quasi-steady-state model for the vertical dynamics meaning that the plasma satisfies an instantaneous force balance $0 = f(x, I)$. Since g is linear, one can express x as a function of I and redefine the model with a system of just two circuit equations. Expressing z as a function of the currents

$$z = \delta_a I_a + \delta_e I_e \tag{3.25}$$

where

$$\delta_{a,e} = \frac{1}{n} \frac{I_{p0}}{m_p \omega_1} M'_{a,ep} = \frac{1}{n} \frac{2R_0}{\mu_0 \Gamma} M'_{a,ep}, \tag{3.26}$$

the model $\dot{I} = g(z(I), I, V_a)$ now reads

$$\begin{cases} \left(1 + \frac{n_e}{n}\right) \dot{I}_e + \gamma_e I_e + \frac{1}{L_e} \left(M_{ea} + \frac{N}{n}\right) \dot{I}_a = 0 \\ \left(1 + \frac{n_a}{n}\right) \dot{I}_a + \gamma_a I_a + \frac{1}{L_a} \left(M_{ea} + \frac{N}{n}\right) \dot{I}_e = \frac{V_a}{L_a}. \end{cases} \tag{3.27}$$

In this expression, the coil and vessel decay indexes were introduced as

$$n_{a,e} = \frac{I_{p0}^2}{m_p \omega_1^2 L_{a,e}} \left(M'_{a,ep}\right)^2 = \frac{2R_0}{\mu_0 \Gamma L_{a,e}} \left(M'_{a,ep}\right)^2 > 0, \tag{3.28}$$

Furthermore the coil and vessel inverse characteristic times

$$\gamma_{a,e} = \frac{R_{a,e}}{L_{a,e}} > 0 \tag{3.29}$$

and a further coupling index

$$N = \frac{2R_0}{\mu_0 \Gamma} M'_{ap} M'_{ep} \tag{3.30}$$

Transfer functions

Defining inputs and outputs, the transfer function of model Eq. (3.27) obtained with the Laplace transform, provides the basis for the fundamental observations on the dynamics of the single filament model. The input is V_a and the outputs (y) are the coil current I_a and the plasma position z which can be reconstructed in a real tokamak using magnetic measurements. In state space form the dynamics evolves as

$$\mathbf{E}\dot{I} = \mathbf{A}I + \mathbf{B}V_a \tag{3.31}$$

$$y = \mathbf{C}I \tag{3.32}$$

and writing it explicitly

$$\begin{bmatrix} (1+n_e/n) & 1/L_e(M_{ea}+N/n) \\ 1/L_a(M_{ae}+N/n) & (1+n_a/n) \end{bmatrix} \begin{bmatrix} \dot{I}_e \\ I_a \end{bmatrix} = \begin{bmatrix} \gamma_e & \\ & \gamma_a \end{bmatrix} \begin{bmatrix} I_e \\ I_a \end{bmatrix} + \begin{bmatrix} 0 \\ 1/L_a \end{bmatrix} V_a \tag{3.33}$$

$$\begin{bmatrix} z \\ I_a \end{bmatrix} = \begin{bmatrix} \delta_e & \delta_a \\ 0 & 1 \end{bmatrix} \begin{bmatrix} I_e \\ I_a \end{bmatrix}. \tag{3.34}$$

The transfer functions for a voltage input is derived as

$$y(s) = G(s) V_a(s) = \mathbf{C}(s\mathbf{E} - \mathbf{A})^{-1}\mathbf{B} V_a(s) \tag{3.35}$$

where s is the Laplace variable. The single elements of $G(s) = [G_z(s) \ G_I(s)]^T$ are

$$G_z(s) = \frac{1}{P(s)} \left[s \left(1 - \frac{M'_{ep}M_{ae}}{M'_{ap}L_e} \right) + \gamma_e \right] \frac{\delta_a}{L_a} \tag{3.36}$$

$$G_I(s) = \frac{1}{P(s)} \left[s \left(1 + \frac{n_e}{n} \right) + \gamma_e \right] \frac{1}{L_a}. \tag{3.37}$$

Here $P(s)$ is the characteristic polynomial of the model

$$P(s) = s^2 \left[1 + \frac{n_a}{n} + \frac{n_e}{n} - \frac{M_{ae}}{L_a L_e} \left(M_{ae} + \frac{2N}{n} \right) \right] + s \left[\left(1 + \frac{n_e}{n} \right) \gamma_a + \left(1 + \frac{n_a}{n} \right) \gamma_e \right] + \gamma_e \gamma_a. \tag{3.38}$$

and the roots of $P(s)$ are the poles of the system. The solutions of $P(s) = 0$ reads

$$p_{1,2} = \frac{-\left[\left(1 + \frac{n_e}{n}\right)\gamma_a + \left(1 + \frac{n_a}{n}\right)\gamma_e\right] \pm R}{2\left[1 + \frac{n_a}{n} + \frac{n_e}{n} - \frac{M_{ae}}{L_a L_e}\left(M_{ae} + \frac{2N}{n}\right)\right]} \tag{3.39}$$

which are always real valued [108, p. 79] and where

$$\begin{aligned}R^2 =& \gamma_a^2\left(1 + \frac{n_e}{n}\right)^2 + 2\gamma_e\gamma_a\left(1 + \frac{n_e}{n}\right)\left(1 + \frac{n_a}{n}\right) + \gamma_e^2\left(1 + \frac{n_a}{n}\right)^2 \\ & - 4\gamma_e\gamma_a\left[1 + \frac{n_a}{n} + \frac{n_e}{n} - \frac{M_{ae}}{L_a L_e}\left(M_{ae} + \frac{2N}{n}\right)\right].\end{aligned}$$

One can observe that, in absence of plasma, $n_a = n_e = N = 0$ and Eq. (3.37) is exactly the transfer function from coil voltage to current in presence of the vessel. In particular, the matrix

$$\mathbf{E}\begin{bmatrix} L_e & \\ & L_a \end{bmatrix} = \begin{bmatrix} L_e(1 + n_e/n) & (M_{ea} + N/n) \\ (M_{ae} + N/n) & L_a(1 + n_a/n) \end{bmatrix} \tag{3.40}$$

is the matrix of self and mutual inductance of the coupled circuits in absence of plasma, or, when plasma is considered, an equivalent matrix of mutual inductance modified by the plasma coupling.

3.1.2 Interpretation of the single filament model

Despite its simple structure, several results on the plasma vessel coil dynamics can be obtained from a study of the single filament model. This will be illustrated and discussed in the remainder of this section to provide a further insight in this simple but useful control oriented model. The present treatment is supported by the fact that in system identification experiments a second-order system was observed to correctly describe the plasma vertical dynamics in response to external perturbations [109].

Validity of the singular perturbation

The conductive structures surrounding the plasma slow the vertical instability down to time scales comparable to the vessel resistive time scale, $\tau_e = L_e/R_e$ in the single filament model. This effect is important since it allows the integration of feedback control, whose main limit is the response time of the power supplies. As the elongation grows, the impedance of the conductive structures is too large for the current induced in them by the plasma motion to generate a radial field fast enough to slow down the vertical instability. The plasma vertical position consequently evolves on Alfvèn time scales [38], [110], which are too fast for power supplies to react.

This effect is included in the single filament model of Eq. (3.27) as well. As a further simplification, only the first up-down asymmetric vessel eigenvalue is considered while the coil dynamics is neglected and using again the singular perturbation approximation, the
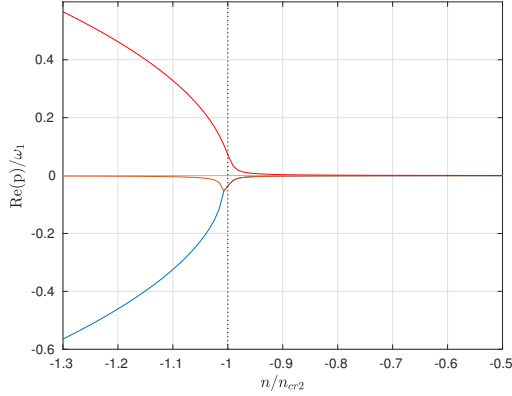
Figure 3.1 – The poles of the complete (fourth order) linearized model for shot #51437 where $\omega_1 = 47$ kHz. One of the poles (red) is always unstable for $n < 0$, one is marginally stable (yellow) due to the second order derivative and two (blue, orange) are stable for any n.
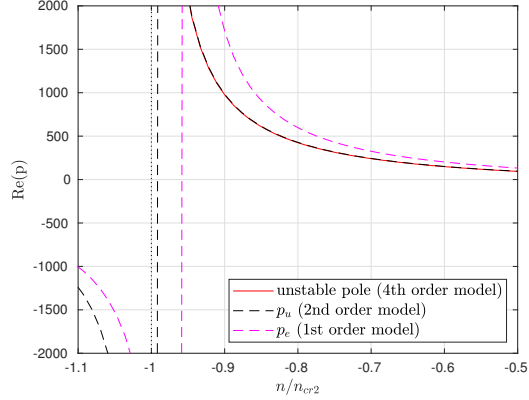
Figure 3.2 – The unstable poles for the different models. The singular perturbation reducing the fourth order model (red) to a second order model (black) is valid for $n > n_{cr2}$ while the pole of first order model (magenta) from Eq. 3.41 gets a correct order of magnitude but overestimates the actual unstable pole and is valid only for $n > -n_e$.

only pole of the resulting first order transfer function is

$$p_e = -\gamma_e/(1 + n_e/n). \tag{3.41}$$

The pole is unstable for $n < 0$ but becomes apparently stable as well when

$$n < -n_e \tag{3.42}$$

which corresponds to high elongation. The second condition is not physical and is a consequence of the loss of validity of the singular perturbation approximation.

Including the coil in the single filament model and considering an elongated plasma ($n < 0$), the Routh-Hurwitz criterion is used to determine the following stability condition for n from Eq. (3.27) which is a second order system resulting in

$$n < n_{cr2} = \left(2N\frac{M_{ae}}{L_aL_e} - (n_a + n_e)\right)\left(1 - \frac{M_{ae}^2}{L_aL_e}\right)^{-1} < 0 \tag{3.43}$$

which can be considered an extension of Eq. (3.42), considering also the passive stabilizing effect of the coil. The details of the derivation are provided in Appendix B.1.1

The single filament model without the approximation of singular perturbation Eq. (3.23) remains a fourth order system whose poles are plotted as a function of n in Fig. (3.1). A numerical study of the stability provides a clear insight in the thresholds for apparent stability $-n_e$ and n_{cr2}. As n is decreased overcoming these thresholds, a discontinuity in the stability appears for the models featuring singular perturbation, while one pole remains

unstable for the fourth order system as seen in Fig. 3.2. This means that for the lower order models singular perturbation is not valid anymore at large elongations (condition Eq. (3.43) for the second order model and Eq. (3.42) for the first order model).

The most general treatment considers the whole passive structure as a set of discrete conductive elements, resulting in a necessary condition for passive stabilization in terms of the inductive stability margin [111]

$$m = \frac{\mathbf{g}^T \mathbf{L}^{-1} \mathbf{g}}{F_z} - 1 > 0 \tag{3.44}$$

where $\mathbf{g}^T$ is the vertical force on the plasma per unit of current in the passive structure (analogous to $I_{p0} M'_{ep}$) and F_z is the linearized vertical force on the plasma per unit of vertical displacement (analogous to $m_p \omega_1^2 n$). In particular the condition for the validity of the singular perturbation $-n_e < n$ is exactly equivalent to Eq. (3.44) if a single mode approximation for the vessel is used [110]. If the coupling between plasma and vessel is too low or if the elongation is too large, one gets $m < 0$ and the growth rate of the instability becomes comparable to $p_z \approx \omega_1 \sim 10^5/s$ such that no feedback control can be applied. Tokamaks with elongated plasmas including TCV operate regularly at $m > 0$ [112] which allows considering the singular perturbation approximation valid in the following.

Single unstable mode

An elongated plasma is always vertically unstable when $n_{cr2} < n < 0$ (see B.1.1) despite the passive stabilizing effect of coils and vessel. Evaluating the limit for $n \to 0^-$ of the poles defined in Eq. (3.39) leads to

$$\lim_{n \to 0^-} p_{1,2} = \begin{cases} -\frac{n_a \gamma_e + n_e \gamma_a}{na + ne - NM_{ae} L_a^{-1} L_e^{-1}} \xrightarrow[\substack{M_{ae} \to 0 \\ n_e \gg n_a > 0}]{} -\gamma_a \\ 0 \end{cases} \tag{3.45}$$

where the last limit is valid for a plasma highly coupled to the vessel ($n_e \gg n_a$) and a small coupling between the vessel and the coil $M_{ae} \to 0$, underlining the major role of the coil in the stable (dissipative) pole, well approximated with γ_a. This means that in model Eq. (3.27) there will always be a stable pole $p_s < 0$ relative to the dissipative structures (coils and vessel) and one unstable mode $p_u > 0$ when $n_{cr2} < n < 0$ due to the vertical instability. One can therefore write

$$P(s) = a_2 (s - p_u)(s - p_s) \tag{3.46}$$

with a_2 the coefficient of the second order term in $P(s)$.

Resistive compensation and stabilizability using positive feedback

As discussed in Sec. 2.4, resistive compensation is added to include an approximate integration effect. In the simplified model, this corresponds to $V_a = R_a I_a + L_a u$ as an input or, equivalently, to setting $\gamma_a = 0$ and $V_a = L_a u$ in the previously derived expressions,

obtaining two new poles $\tilde{p}_u$ and $\tilde{p}_s$. This leads to two important consequences. The first one is that the stable pole p_s which is largely determined by the coil's resistive effect moves to $\tilde{p}_s \sim 0$ (the coil behaves as an integrator). The second one is that, when using resistive compensation, there is a new stability threshold for n such that the stability of the system even for elongated plasmas is obtained when

$$- n_a < n < 0 \tag{3.47}$$

yielding in this case $\tilde{p}_u < 0$. This can be easily derived substituting $\gamma_a = 0$ in the expression for the poles of Eq. (3.39) and checking for the sign of the real part of the pole. The origin of this stabilization is the positive feedback loop closed on the plasma current to compensate the coil resistivity which is sufficient for stabilizing the vertical instability as long as Eq. (3.47) is satisfied, due to the sign of the transfer function $V_a \to I_a$ which is opposite to the one of $V_a \to z$. Note that however an integrator pole remains in $\tilde{p}_s \sim 0$ so formal stability (e.g. BIBO stability) is not provided. Note that the same effect is also obtained with a superconductive coil behaving as an integrator coupled to the plasma motion. It is observed that in general $n_a \ll |n_{cr2}|$ thus only plasmas with extremely low elongation can be stabilized using only resistive compensation.

Zero of G_I

The transfer function $G_I : V_a \to I_a$ (Eq. (3.37)) determines the dynamic evolution of the coil current. Even in the simplified model, an important feature is observed: the presence of a zero in the transfer function $G_I(s)$

$$z_I = - \left(1 + \frac{n_e}{n} \right)^{-1} \gamma_e \tag{3.48}$$

which is RHP[I] as long as $n > -n_e$ where in general $n_e \approx n_{cr2}$ as seen in Fig. 3.2, so for most plasmas but the ones with highest elongation. The presence of a single RHP zero in the coil dynamics determines an inverse response of the coil current in the unstable system.

In the simple model one can prove that, when making use of resistive compensation

$$z_I > \tilde{p}_u \tag{3.49}$$

is true for any $n > -n_e$ (see Appendix B.1.2). This justifies the stabilization at low elongation using resistive compensation only (when $n > n_a$), since, if the opposite was true ($z_I < \tilde{p}_u$ for some $n > -n_e$), this stabilization would have been made impossible by the parity-interlacing-property [113]. This RHP zero affects the model dynamics at time scales comparable to the vertical instability since $z_I = p_e$ from Eq. (3.41) and in general p_e is comparable to p_u in magnitude for moderate elongations as observed in Fig. 3.2.

[I]lies on the plane for which $\mathrm{Re}(s) > 0$

Federico Pesamosca

Zero of G_z

An improved coupling between plasma and vessel (M'_{ep} in the simple model) leads to an increase in m (Eq. (3.44)), but the resulting better passive stabilization will serve little purpose if it corresponds to a strong screening of the control field provided by active control coils [110] which is necessary to stabilize the plasma vertical instability.

This trade-off is retained in the simple model in the zero of $G_z : V_a \to z$ (Eq. (3.36))

$$z_z = -\left(1 - \frac{M'_{ep}M_{ae}}{M'_{ap}L_e}\right)^{-1}\gamma_e. \tag{3.50}$$

This zero physically originates due to the inverse response of the vessel eddy currents since the same zero is found in the (stable) transfer function from a coil voltage input to the radial magnetic field at the position of the plasma.

$$V_a \to B_{R,x} : G_B(s) = \frac{1}{P_s(s)}\left[s\left(1 - \frac{M'_{ex}M_{ae}}{M'_{ax}L_e}\right) + \gamma_e\right]\frac{M'_{ax}}{2\pi R_0 L_a}. \tag{3.51}$$

which is determined by a competing effect between the field generated by the coil and the field generated by the eddy current generated in the vessel (see Appendix B.1.3 for the derivation of the transfer function of the plasmaless model). Here $M_{a,ex}$ is the mutual inductance between the coil or the vessel and the location where the magnetic field is measured $x = [R_0, z_0]$ and $P_s(s)$ is the characteristic polynomial of the (stable) model.

In [38] the single filament model of Eq. (3.27) is derived for the DIII-D tokamak and it is noted that using coils satisfying $M'_{ap}/M_{ae} < M'_{ep}/L_e$, the model for plasmas at high elongation cannot be stabilized with feedback control on the plasma position, but no relation to the zero z_z is explicitly derived. In fact, we can see from (3.50) that this condition corresponds to $z_z > 0$. This leads to a limitation in the possibility of stabilizing the RHP pole, which requires high feedback gain, as the RHP zero leads to high gain instability [101, p. 184]. As long as $z_z > p_u$, it is still possible stabilizing the plant using only this SISO loop, but with worse performance degradation the more p_u increases towards z_z. Specifically, regardless of the controller used, the combination of a single RHP pole and a single RHP zero has the following lower limit for the closed loop sensitivity magnitude ($M_{S,min}$) and lower limit for the closed loop transfer sensitivity ($M_{T,min}$) [101, p. 197]

$$M_{S,min} = M_{S,min} = |z_z + p_u|/|z_z - p_u| \tag{3.52}$$

which tends to infinity as $p_u \to z_z$ while they should be kept below 6 dB for $M_{S,min}$ and 2 dB $M_{T,min}$ for ideal performance [101, p. 36].

Physically, when z_z is a RHP zero, the plasma vertical position in G_z (unstable) or the magnetic field in the plasmaless model G_B (stable) have an initial inverse response following a voltage step. This means that the highly conductive continuous vessel is able to perfectly exclude the prompt magnetic field of an external coil on short time scales and creates a transient opposite field to the desired one.

When using an eigenmode representation for the vessel, however, the discrete nature of

the vessel mode incorrectly estimates the shielding capability of the vessel. Several coils are not shielded when including only the first up-down asymmetric eigenvalue in the single filament model, resulting in an instantaneous effect (e.g. without the inverse response) on the plasma. This fact is noted also in [38] for the DIII-D case, where only a subset of the external coils is actively shielded by the vessel. The proposed solution, studied in detail in Sec. 3.2.1 also for the TCV model, consists of including a larger number of eigenvalues in the model. When a sufficiently high number of eigenvalues is included, a RHP zero is present in $V_a \to z$ using any E or F coils for V_a (and not for the G coil, which is within the vessel) and it is observed that $z_z \gg p_u > 0$.

The fact that it is not possible to correctly model the vessel shielding using a single eigenmode representation is a main limitation to this approach and motivates the use of a model with a more detailed representation of the vessel and the full coil system. This, however, does not allow for such a simple analytical treatment as the one discussed in the present section and other methods, among which frequency response, are exploited for controller design. The shielding effect of the vessel is in fact, along with the power supply delays, the main limitation for stabilizing the vertical instability of most elongated plasmas using only the external coils.

3.2 The RZIp model

The so-called 'RZIp' model is a linear time-invariant dynamical model for the plasma-vessel-coil coupled dynamics [105]. Its main assumption is that the plasma current distribution remains constant during any control action, while its centroid $[r_C \ z_C]$ can move vertically and radially and its integral, the total plasma current, can change. The vector of electrical currents in all PF coils and a set of discrete vessel filaments I_c and the total scalar plasma current I_p can vary in magnitude and their coupling with the plasma is explicitly considered.

The derivation of this model is based on circuit equations for the conducting elements, combined with plasma vertical and radial force balance and flux conservation

$$
\begin{cases}
M_c \dot{I}_c + R_c I_c + \dot{\psi}_{cp} = V_a, \\
m_p \ddot{z}_c = -2\pi r_C I_p \bar{B}_r(r_C, z_C, I_c, I_p) \\
m_p \ddot{r}_c = +2\pi r_C I_p \bar{B}_z(r_C, z_C, I_c, I_p) + F_r(r_C, I_p, \beta_p, \ell_i), \\
(d/dt)[L_p(r_C)I_p] + R_p I_p + \dot{\psi}_{pc} = 0.
\end{cases}
\tag{3.53}
$$

Here M_c is the matrix of self and mutual inductances of conducting elements (coils and vessel) and R_c the diagonal matrix of their resistances. The vector ψ_{cp} is the flux due to the plasma current distribution enclosed by each circuit k, with components

$$
\psi_{cp,k} = M_{kp} I_p = \int_{plasma} \tilde{M}_{kJ}(R, z) J(R, z) dR \, dz,
$$

where $J(R, z)$ is the plasma toroidal current distribution obtained from a reference Grad-Shafranov equilibrium and $\tilde{M}_{kJ}(R, z)$ is the mutual inductance between the points on the poloidal plane and each discrete conductor k, including coils and vessel filaments. The scalar ψ_{pc} is instead the flux due to each circuit enclosed by the plasma, computed as

$$
\psi_{pc} = \sum_k M_{pk} I_{c,k},
$$

where $M_{pk} = M_{kp}^T$. The term V_a includes the externally applied voltages on the active circuits only (E, F, G and OH coils) through the corresponding power supplies, since there is no active voltage on the plasma current and the vessel circuits. The magnetic field due to the external conductors acting on the plasma has vertical and radial components $\bar{B}_z$ and $\bar{B}_r$. These components are estimated through the computation a weighted average of the Lorentz force due to the poloidal magnetic field $[B_r \ B_z]$ generated by external conductors and acting on the toroidal plasma current distribution. Furthermore the term F_r is the net radial outward force deriving from plasma pressure and tokamak toroidal geometry, a function of the plasma poloidal beta β_p and internal inductance ℓ_i. Finally L_p and R_p are respectively the plasma (radially dependent) self inductance and the plasma resistance.

Due to the time scales involved, the force balance equations are assumed to be at equilibrium at all instants. This results in a static relation between coil and plasma currents

and plasma position. The validity of the so-called massless approximation, typical for this kind of electromagnetic plasma model, is discussed in detail in [97]. The plasma radial and vertical force balance equations are linearized around a plasma equilibrium at a given time for a desired discharge and differentiated with respect to time, resulting in a linear model that depends on the plasma equilibrium current distribution and geometric and electromagnetic properties of the surrounding coils and vessel. The model can be written in state space form as

$$\dot{x} = \mathbf{A}x + \mathbf{B}V_a \tag{3.54}$$

$$y = \mathbf{C}x + \mathbf{D}V_a. \tag{3.55}$$

The static relation between coil and plasma currents and plasma position is substituted in the dynamic equations for the circuits, such that the state is the vector including only the coil current perturbation from their reference value and the plasma current perturbation as

$$x = \begin{bmatrix} \delta I_c^T & \delta I_p \end{bmatrix}^T. \tag{3.56}$$

which is the results of a formal application of the singular perturbation method described in detail in Appendix B.2.1.

The resulting model inputs are the voltages $V_a = [V_G \ V_{EF} \ V_{OH}] \in \mathbb{R}^{19}$ applied to the single poloidal field coils and the outputs $y \in \mathbb{R}^{n_y}$ are the TCV magnetic measurements, which result from a set of electromagnetic Green's fuction mapping of the state currents into the output of flux loops, magnetic probes, time derivatives thereof, along with the coil current estimates [83]. The details of matrices of the state space representation are described in Appendix B.2.2

The corresponding MIMO (multi-input-multi-output) transfer function from V_a to y resulting from the Laplace transform of the system is

$$G(s) = C(sI - A)^{-1}B + D \tag{3.57}$$

with s the Laplace variable.

A key feature of the RZIp model is the presence of a single unstable mode that defines the vertical instability of elongated plasmas [108, p. 84]. As discussed in Sec. 3.1, its origin lies in the unstable characteristics of the vertical force balance, where the Lorentz force due to the curvature of the vacuum field required for elongating a plasma makes the equilibrium of the system linearly unstable [12]. The passive stabilizing effect of the surrounding conducting structures [110] slows down the instability growth rate from MHD time scales (10^6 s^{-1}) to wall resistive time scales (10^2 s^{-1}) but is not sufficient to stabilize it alone [114]. This motivates the design of feedback control of plasma position to ensure stationary, safe tokamak operation which can be performed using linearized models [38]. The agreement of rigid plasma models for vertical controller design with experimental data and deformable plasma models was studied in detail for the TCV case in [115] and was found to be valid for most cases except extremely high elongation.
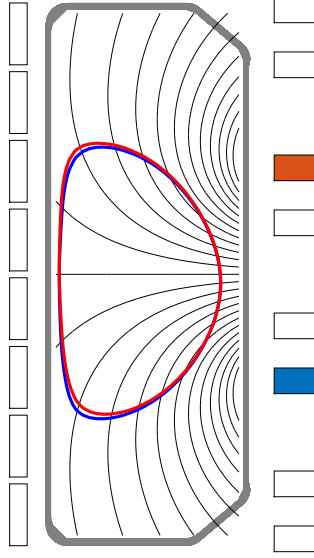
Figure 3.3 – Effect of a static current flowing in antiseries in F_6 and F_3 on the plasma's preprogrammed last closed flux surface (blue) resulting in a new Grad-Shafranov equilibrium (red).
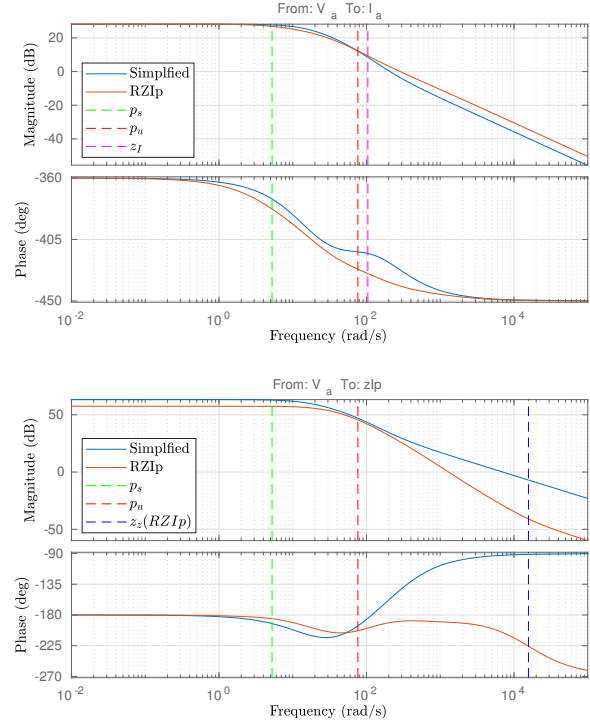
Figure 3.4 – Bode plots of the transfer functions for the channels $V_a \to I_a$ (above) and $V_a \to z_C I_{p0}$ (below) comparing the RZIp and the single filament (Simplified) model.

3.2.1 Dynamic comparison with the single filament model

A first study of the dynamics predicted by the RZIp model is performed comparing it with the single filament model. A coil combination is selected such that it generates a radial field on the plasma axis by actuating in antiseries coils F3 and F6, approximately symmetric above and below the plasma midplane for shot #51437 illustrated in Fig. 3.3. The complete RZIp model is derived for TCV. A vector $T_z \in \mathbb{R}^{19}$ multiplies its input such that the only input voltage V_a is applied to coils F_3 and F_6 in antiseries. The retained outputs are the plasma centroid vertical position as $z_C I_{p0}$ and the coil current $I_a = I_{F6} - I_{F3}$ in response to a voltage input V_a. The simplified single filament model is augmented considering two coils ($F3$ and $F6$), one vessel eigenmodes and one plasma filament, and all coefficients are computed as discussed in Sec. 3.1 for the TCV case. As for the RZIp case, a single voltage input V_a is considered such that $[V_{F6} \ V_{F3}]^T = [\ 1 \quad -1\ ]^T V_a$. The dynamics of interest is given by the evolution of the plasma vertical position as $z I_{p0}$ and the coil current $I_a = I_{F6} - I_{F3}$ in response to a voltage input V_a.

The dynamics of the systems are studied using a Bode plot, which provides a useful tool to illustrate the frequency response of a linear system in terms of magnitude and phase
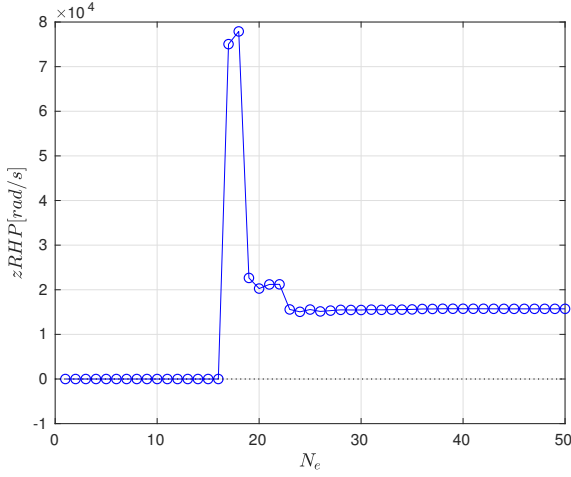
Figure 3.5 − The location of the RHP zero in the transfer function $V_a \rightarrow z_C I_{p0}$ of RZIp as a function of the number of the vessel eigenvalues N_e.
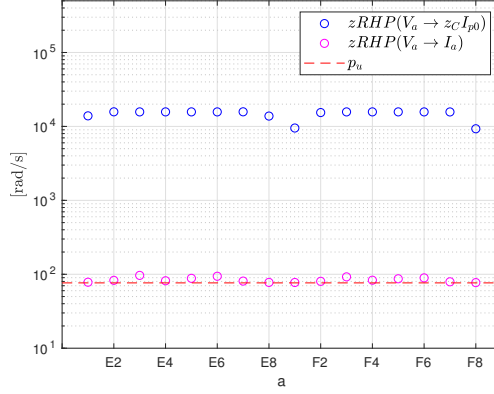
Figure 3.6 − The RHP zeros in the RZIp model transfer functions considered for comparison with the simplified model.

of the response to a sinusoidal perturbation in its input. This tool will be used extensively in the following chapters in order to synthesize controllers and make predictions on the closed loop dynamics. Despite the plasma response is unstable, the Bode plot summarizes several information for the open loop response.

Fig. 3.4 provides the Bode plots for the transfer functions $V_a \rightarrow I_a$ and $V_a \rightarrow z_C I_{p0}$, comparing the two models. One can see that the main dynamics is mainly dictated by a low number of parameters despite the large dimensionality of the RZIp model which can be easily evaluated numerically. A stable pole $p_s = R_a/L_a$ approximates well the frequency at which the initial drop of magnitude and loss of phase is observed. The two models also share a unique unstable pole p_u, which represents the vertical instability, which can be matched for the simplified model by varying n until it is approximately the same for the RZIp one. The unstable pole corresponds to a further loss of magnitude in the frequency response but increases the phase.

While the poles are shared in the denominator of a transfer function for the same system, the numerator including the zeros depends on the considered channel, and in this case only on the output. For the channel $V_a \rightarrow I_a$ the transfer functions qualitatively match. Both in the RZIp model and in the simplified model, a unique RHP zero (z_I for the simplified model) provides a further loss of phase at higher frequencies and counterbalances the change in magnitude resulting from p_u, since it appears at frequencies only slightly larger than the unstable pole. This makes the magnitude response of the channel $V_a \rightarrow I_a$ to appear as the one of a single pole system.

The limits in the predictive capability of the simplified model compared to RZIp are evident in the transfer $V_a \rightarrow z_C I_{p0}$ where the two transfer functions have a different behavior at high frequencies above 10^3 rad/s. The simplified model does not consider correctly the vessel ability to shield external fields, since it features only the first up-down

asymmetric current distribution (the second eigenmode of an eigenmode decomposition of the discrete vessel filaments). This is evident in the transfer function $G_I(s)$, where $z_z < 0$ results in a phase gain at frequencies above the unstable pole. In the corresponding transfer function for the RZIp model, instead, a RHP zero results in a loss of phase. Vertical control and stabilization of the vertical instability is typically done closing a loop on the vertical observer and the presence of RHP zeros is detrimental for performance [101, p. 235].

In the RZIp model generated for the TCV tokamak it is observed that a single RHP zero is present in the transfer functions $V_a \to I_a$ and $V_a \to z_C I_{p0}$ for each E and F coil. The only exception is the G coil which does not feature a RHP zero in the transfer function $V_a \to z_C I_{p0}$ as the magnetic field it generates when a current is imposed in it is not dynamically shielded since the G coil is located within the vessel. The RHP zeros in the mentioned transfer functions are represented in Fig. 3.6 for shot #51437s and a voltage input in the single E and F coils. One can see that the characteristic frequencies at which the zero appears are well separated, with the RHP zero of $V_a \to I_a$ influencing the dynamics approximately at the unstable pole frequency p_u in analogy with z_I (see Sec. 3.1.2) and the RHP zero of $V_a \to z_C I_{p0}$ appearing at much larger frequencies. A RHP zero is evaluated also in experimental system identification of the low order transfer functions for vertical control [109], where the order of magnitude of the fitted RHP zeros is comparable to the one observed in the RZIp model.

3.2.2 Effect of varying number of vessel eigenmodes

The role of the RHP zero is fundamental in limiting the ability to stabilize highly elongated plasmas using the external coils. The full dynamics of the system is more complex than the single filament model and the different properties of the E, F and G coils will be exploited in the following chapters for the purpose of magnetic control of TCV plasmas. The main difference originates from the coupled dynamics of the coils and a more detailed model of the vessel which in the RZIp model is represented by a set of filaments or their truncated eigenmode representation. In particular in Eq. (3.53) the currents in the conductive elements are $I_c = [I_a^T \ I_e^T]^T$ with $I_a \in \mathbb{R}^{N_a}$ representing the current in the N_a active coils and $I_e \in \mathbb{R}^{N_e}$ the current in the vessel circuits. The current distribution in the vessel is represented either using 256 toroidal filaments or a variable number of vessel eigenmodes up to $N_e = 256$. The vessel eigenmodes are orthogonal in the sense that M_{ee} is diagonal (see Appendix A of [38] for the details on the eigenmode representation of the vessel). The order of the truncation is important in dynamic modeling since a low order model allows faster simulations but can lead to wrong predictions when an important part of the dynamics is neglected.

It is observed that the RHP zeros in $V_a \to z_C I_{p0}$ for the E and F coils are included in the model only when a sufficiently high number of eigenmodes of the vessel is considered. In the eigenmode representation, each of the successive vessel eigenmode has a higher degree of spatial structure and decays at a faster rate [38]. A possible motivation for the disappearance of the RHP zero before a specific N_e is therefore that the spatial structure allowed in the vessel current is at that point insufficient for shielding the magnetic field
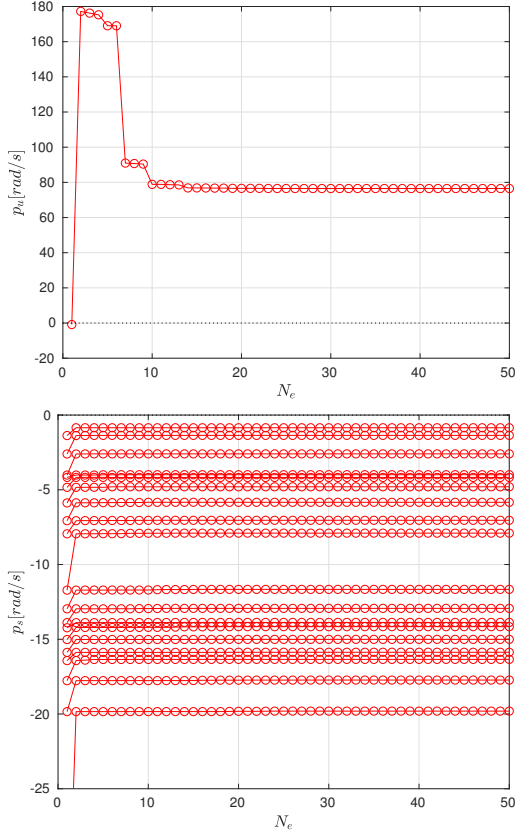
Figure 3.7 – The location of the unstable pole (above) and the first 20 stable poles of RZIp as a function of the number of the vessel eigenvalues N_e.
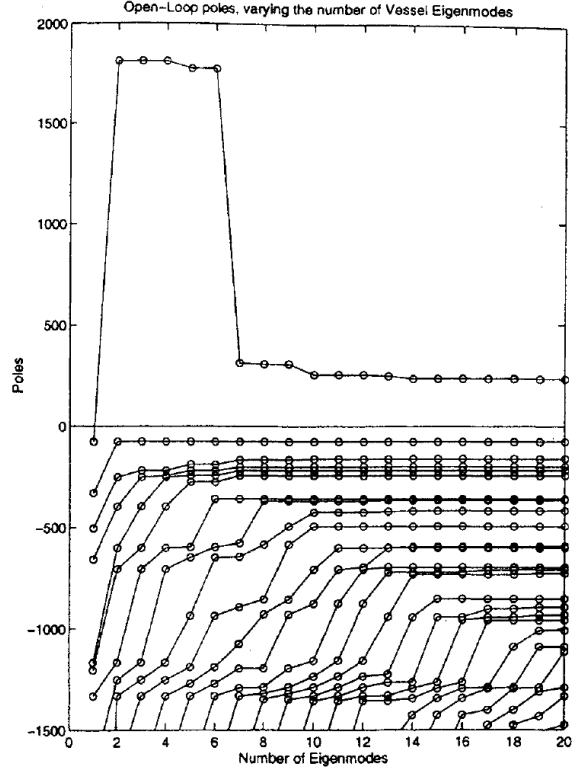
Figure 3.8 – The corresponding figure for a rigid current displacement model (Fig. 7 [98])

generated by the coil and the approximation of the full model is not valid anymore. After the 30th eigenvalue is included, no variation of the RHP zero is observed for any E and F coil and the fast inverse response determined by $z_z \approx 10^4 \mathrm{rad}/s$ is motivated by the fast decay of the eddy currents in the vessel.

The number of vessel eigenmodes has an effect as well on the location of the unstable mode p_u, since additional up-down asymmetric current distributions able to couple with the vertical instability are included for larger N_e. As observed already for other rigid plasma displacement models [98], whose result is reproduced in Fig. 3.8, the number of eigenmodes necessary for the poles to finally settle is $N_e = 20$. Note that for $N_e = 1$ there is no unstable mode due to the violation of the passive stabilization criterion Eq. (3.44). For N_e larger than 20 the location of the system poles is not further modified and the increasing order of the model corresponds to the addition of further vessel eigenvalues with their characteristic pole.
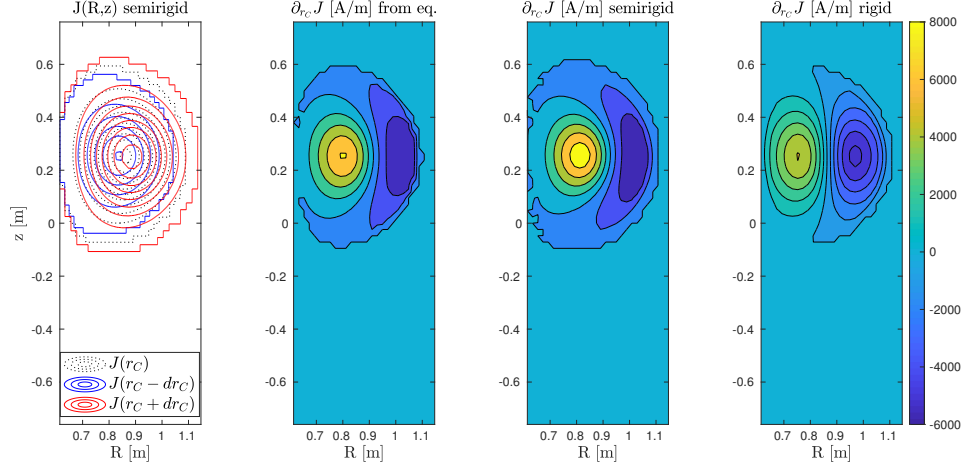
Figure 3.9 – The result of a radial displacement in an HFS limited plasma. In the first poloidal cross section of TCV, an exaggerated plot of the current distribution following a radial displacement as predicted by the semirigid model evidences the plasma scaling. In the following plots, $\partial_{r_C} J$ is evaluated with the different models: derived from Grad-Shafranov equilibria, predicted by the semirigid model and from the rigid one. It is already possible to observe that, also qualitatively, the semirigid model better reproduces the results from the Grad-Shafranov equilibria than the rigid model.

3.3 Extension to a semirigid model

One of the key assumptions of the RZIp model is that the plasma column rigidly translates following a perturbation in the coil currents. The translation happens without deformation of the plasma cross section on the poloidal plane of a toroidal reference frame described with radial and vertical coordinates. This is a fair assumption in the vertical direction where the plasma is unbounded by the vessel. However plasmas can be limited, having the last closed flux surface lying on the wall on the vessel either on the high field or on the low field side of the tokamak. In this case, a rigid plasma movement in the radial direction would lead to unrealistic equilibria such as an overlap of plasma and wall or a transition to a plasma whose last closed flux surface is suspended and not in contact with the wall. The actual behavior of the plasma from the ideal MHD equilibrium point of view, as modeled by the Grad-Shafranov equation, can be described qualitatively as an inflation (or a compression) as the plasma moves away from the HFS wall (or onto the LFS wall) as represented in Fig. 3.9.

The assumption of rigid radial displacement is included in the RZIp model through the radial derivatives

$$\frac{\partial J}{\partial r_C} = -\frac{\partial J}{\partial R} \quad \text{as in [116]} \tag{3.58}$$

$$\frac{\partial \Gamma}{\partial r_C} = \frac{1}{r_C} \quad \text{from its definition in Eq. (3.3)} \tag{3.59}$$
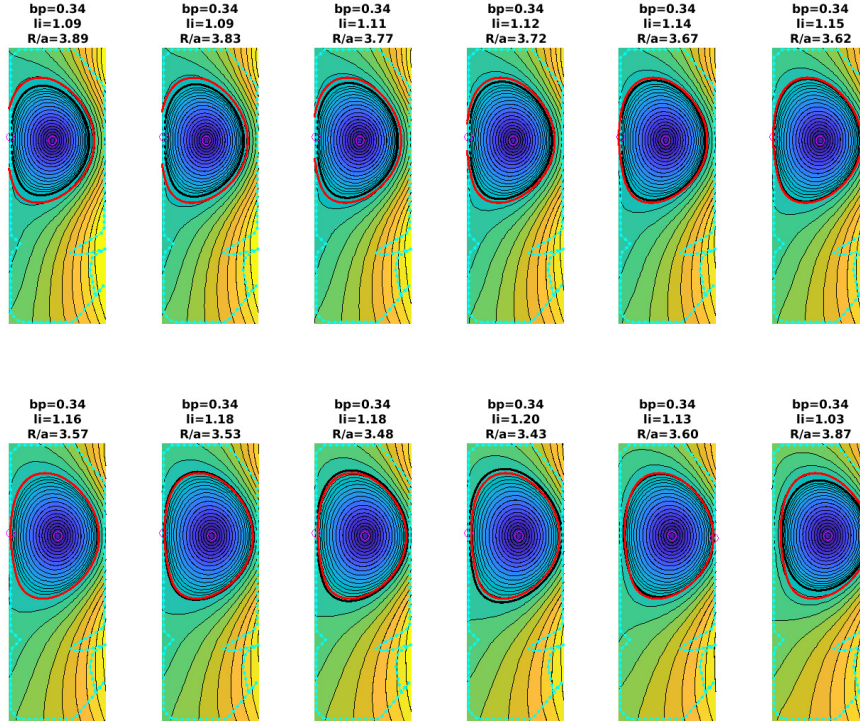
Figure 3.10 – Some of the different equilibria for different plasma currents $I_p = k\, I_{p0}$ used for validating the semirigid model. In black the GS equilibria and in red the rigid radial shift of the equilibrium with $I_p = I_{p0}$, showing the change in the shape and the overlap of the first and last equilibria with the tiles in the case of rigid shift.

The proposed solution to this issue is a new computation of two parameters already included in the RZIp model: the radial derivative of the Shafranov parameter $\partial_{r_C}\Gamma$ and the radial derivative the plasma current distribution $\partial_{r_C}J$, both functions of the plasma shape modification following a radial displacement. A new analytical computation for the derivative of Γ and a new numerical computation for the isotropic scaling of J are now included in the RZIp model to match the Grad-Shafranov (GS) equilibria for a displacement of the plasma centroid in the radial direction. This new semirigid model (rigid following a vertical displacement and deformable in the radial direction) results in a more accurate model for the coupled plasma vessel coils dynamics, allowing more reliable controller design.

The main results are summarized in the remaining of the present section and the details of the derivation are provided in Appendix B.3. The quantitative validation of the semirigid model, still discussed in in Appendix B.3, is based on its ability to reproduce the results of a set of Grad-Shafranov equlibria for scalar parameters independent on the total plasma current better than the original rigid model. A subset of the considered equlibria is presented in Fig. 3.10.

3.3.1 Radial derivative of the Shafranov parameter

The semirigid approximation of a plasma radial expansion allows evaluating a radial derivative of the Shafranov parameter which matches the numerical equilibria at different radii closer than the rigid approximation. This is obtained maintaining a set of simplifying assumptions, in particular assuming constant κ, β_p and ℓ_i which are given by the equilibrium reconstruction around which RZIp is linearized. Under these assumptions, the radial derivative of Γ reduces to

$$\partial_{r_C}\Gamma = \frac{\partial}{\partial r_C}\left(\ln\frac{8r_C}{a(r_C)\sqrt{\kappa}} + \beta_p + \frac{\ell_i}{2} - \frac{3}{2}\right) = \frac{\partial}{\partial r_C}\ln\frac{8r_C}{a(r_C)\sqrt{\kappa}} \tag{3.60}$$

and depends on the value of r_C/a. The main assumption of the semirigid approximation is that the minor radius of the plasma a is not constant during a radial displacement but is a function of the major radius, considered here as the radial position of the centroid r_C.

When the plasma is limited on the HFS and the contact point with the tile $r_b = r_{HFS} < r_C$

$$\frac{r_C}{a} = \frac{r_C}{(r_C - r_{HFS})} \quad \rightarrow \quad \partial_{r_C}\Gamma = \frac{\partial}{\partial r_C}\ln\frac{8r_C}{a(r_C)\sqrt{\kappa}} = -\frac{r_{HFS}}{r_C(r_C - r_{HFS})} < 0. \tag{3.61}$$

When the plasma is limited on the LFS and the contact point with the tile $r_b = r_{LFS} > r_C$

$$\frac{r_C}{a} = \frac{r_C}{(r_{LFS} - r_C)} \quad \rightarrow \quad \partial_{r_C}\Gamma = \frac{\partial}{\partial r_C}\ln\frac{8r_C}{a(r_C)\sqrt{\kappa}} = +\frac{r_{LFS}}{r_C(r_{LFS} - r_C)} > 0 \tag{3.62}$$

The validation is performed comparing the values of Γ and $\partial_{r_C}\Gamma$ derived from the Grad-Shafranov equilibria obtained for a variation of the plasma current around its nominal value, which results in a displacement of the plasma radial equilibrium position. The Shafranov parameter and its radial derivative are evaluated from the numerical equilibria and compared with the predictions obtained from the rigid and the semirigid model. It is found that the latter provides the best fit to the numerical equilibria. Note in particular that the semirigid model for plasmas limited on the HFS results in a change of sign of the term $\partial_{r_C}\Gamma$ compared to the rigid model.

The radial derivative of Γ appears in the plasma linearized current equation and the linearized radial force balance which are modified accordingly in RZIp.

3.3.2 Radial derivative of the current distribution

The assumption that, following a radial displacement, a limited plasma undergoes a uniform (isotropic) scaling in all directions from the contact point with the tile (r_b, z_b), as represented in Fig. 3.9, is consistent with the previous assumption that $a = a(r_C)$, with the dependencies that can be extracted from Eq. (3.61) and Eq. (3.62). This assumption has a consequence in particular on the evaluation of the derivative of the plasma current

distribution $J(R, z)$ following a displacement of its centroid and evaluated as

$$\partial_{r_C} J = \lim_{\substack{r_C^+ \to r_C \\ r_C^- \to r_C}} \frac{J_{r_C^+} - J_{r_C^-}}{r_C^+ - r_C^-} = \lim_{\Delta r_C \to 0} \frac{J_{r_C^+} - J_{r_C^-}}{\Delta r_C} \tag{3.63}$$

where r_C^+ and r_C^- are the new centroid positions following a radial displacement of the current distribution computed as

$$r_C^+ = r_b + (r_C - r_b)(1 + s)$$
$$r_C^- = r_b + (r_C - r_b)(1 - s)$$

and the perturbed current distribution is not a GS equilibrium but a uniform (isotropic) scaling with $s > 0$ from the limiting point (r_b, z_b) on the tiles such that

$$J_{r_C^+} = J\left(\frac{R + r_b}{h} - r_b, \frac{z + z_b}{h} - z_b, I_{p0}\right) k_I \tag{3.64}$$

where $h = s + 1$ for $J_{r_C^+}$ while $h = s - 1$ for $J_{r_C^-}$ and the term k_I maintains constant the total plasma current I_{p0} following the scaling [II]. For comparison, in the rigid model the displaced current distribution is evaluated with a simple translation by $\Delta r_C \to 0^+$

$$J_{r_C^+} = J(R - \Delta r_C, z, I_{p0}) \tag{3.65}$$

and with $\Delta r_C \to 0^-$ for $J_{r_C^-}$.

The scalar amplitude of the radial Lorentz force acting on the plasma due to known currents in the conductive elements F_L is a function of the plasma current distribution. The radial derivative of this force $\partial_{r_C} F_L$ is in turn a function of $\partial_{r_C} J$ and can be computed numerically from the expression of $\partial_{r_C} J$ for the rigid or semirigid model or with a numerical derivative from the different Grad-Shafranov equilibria used to validate this approach. As the Grad-Shafranov equilibria at different radial positions are derived with a scan of plasma current, the derivative of the Lorentz force is scaled using the total plasma current to obtain $\partial_{r_C} F_L / I_p$ which is independent of I_p.

The validation of $\partial_{r_C} J$ is performed comparing the values of $\partial_{r_C} F_L / I_p$ obtained from the Grad-Shafranov equilibria and using the different definition of $\partial_{r_C} J$ either from the semirigid Eq. (3.64) or rigid model Eq. (3.65). It is found that the semirigid model better fits the result obtained from the Grad-Shafranov equilibria, validating this approach.

The evaluation of the derivative of the current distribution allows correcting the term $\partial \mathcal{J} / \partial r_C$ in the RZIp model which considers now a non rigid plasma displacement in the radial direction.

[II]The semirigid model requires an interpolation on a thinner grid than the one provided by equilibrium reconstruction for a correct evaluation of the numerical derivative for $s \to 1$. See in particular Eq. (B.92) for details on the thinner grid.

3.3.3 Limitations and possible extension

While the presented semirigid model is a better approximation for the linearized dynamics of RZIp when considering limited plasmas, the extension to diverted plasmas, whose core plasma is not in contact with the tiles, requires further analysis. The current distribution of limited plasmas is clearly observed to scale (inflating or compressing) as they move away or towards the wall as observed in Fig. 3.10. Instead, there is not such a simple interpretation for the evolution of the plasma current distribution of diverted plasmas following a radial displacement of their centroid. The approach presented here is therefore restricted to limited plasmas. It is suggested that the behavior of a diverted plasma following a radial displacement could be different from a rigid translation and closer to a self-similar expansion of a current ring [117] which maintains $r_C/a = const.$ leading to $\partial_{r_C}\Gamma = 0$ which would lay between the two extremes of $\partial_{r_C}\Gamma < 0$ and $\partial_{r_C}\Gamma > 0$ with a continuous transition. This however requires also a coherent expression of the radial derivative of the plasma current distribution for diverted plasmas as it was done for the limited case, which is not performed here. The development of a generalized semi-rigid model could be the step between rigid and deformable linearized models and could provide further insights for this control-oriented approach with its simple interpretation of the physics of interest.

3.4 Modeling of the power supplies

A critical nonlinearity in the magnetic control loop not modeled by RZIp is the coil power supply characteristics. These include voltage and current saturation and a maximum operational frequency of the 12-phase rectifiers (for the PF coils) and the H bridge of the FPS (for the G coil) [80]. The control synthesis techniques used in this thesis require operating on a linear dynamical system, while the power electronics systems feature nonlinear components. This is an important feature which requires to be modeled for correct controller synthesis, since it determines the most stringent constraints in terms of instability deriving from excessive controller gain (high-gain instability). These highly nonlinear elements are included using linear models for controller design, therefore saturation effects, the details of the power electronics and the dead zone of the FPS, are not included in the evaluation of the controllers. The working principles of the power supplies are briefly discussed here to motivate the approximations used in this thesis. Finally, a nonlinear model of the FPS is derived, and implemented in SIMULINK , which will be included in particular in the simulations performed in Chapter 5.

3.4.1 Delay model for the E, F, OH coil power supplies

As discussed in Chapter 2, the E F and OH coils are each connected to an independent power supply, which generates the voltage (in voltage mode) required by the control system, typically as the matrix M output.

Each power supply consists of 12-pulse thyristor rectifiers: two six pulses bridges connected in series with a phase shifting between the two secondaries. The principle of the six pulses bridge working system is illustrated in Fig. 3.11 and 3.12. The power supply imposes a voltage on the coil depending on the firing angle $\alpha \in [0 \ \pi]$, which is the regulation parameter evaluated in voltage mode as a function of the reference voltage requested by the control system. The mean value of the ideal rectified voltage U_{load} for a single six pulses bridge as a function of the firing angle is

$$U_{di}(\alpha) = \frac{sq\sqrt{2}}{2\pi} U_{AC} \cos \alpha \qquad (3.66)$$

where $s = 2$ is the number of commutation groups, $q = 3$ the number of phases for the transformer and U_{AC} the phase-to-phase voltage. For the E, F and OH coils this results in a maximum appliable voltage (for $\alpha = 0$) using two bridges in series of

$$U_{E,max} = 2U_{di}(0) = 650\text{V} \qquad (U_{AC} = 241\text{V})$$
$$U_{F,max} = 2U_{di}(0) = 1250\text{V} \qquad (U_{AC} = 463\text{V})$$
$$U_{OH,max} = 2U_{di}(0) = 1400\text{V} \qquad (U_{AC} = 519\text{V})$$

In the remaining of this study a linear approximation is used, assuming that saturation of the power supplies is not reached in standard operations, which is reasonable when
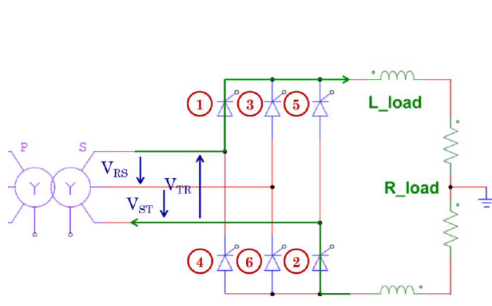
Figure 3.11 – Working principle of a 6-pulse thyristor rectifier: on the left, the transformer provides the AC voltages, on the right the controlled SCR block alternates the conduction phases. ([118]).
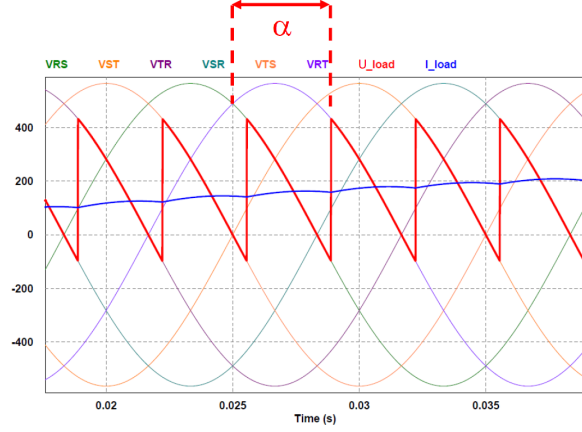
Figure 3.12 – Simulation of the 6-pulse thyristor rectifier with a fixed firing angle α imposing U_{load}, closing the circuits as 1-3,3-2,3-4,5-4,5-6,1-6 and repeating ([118]).

considering small variations around the reference. During a shot, the effect of saturation is indeed critical since it starts a vertical displacement event as the feedback system is not able to control the plasma vertical position anymore. This will be avoided attempting to minimize the input voltage reference in a linear system, as discussed in Sec 5.2 .

Apart from saturation, the nonlinear behavior of the power supply, which can be seen for a plasma discharge in TCV in Fig. 3.13, introduces another critical effect: the delay in the applied voltage on the coil U_{load} with respect to the required one U_{ref}. Although the effect can be asymmetric for large variations, it is reasonable to assume that for small variations the change in the reference can happen statistically with the same probability between two pulses, therefore in the following delay is assumed

$$\tau = \frac{1}{2}\frac{T_p}{12} = 0.35\,\mathrm{ms} \tag{3.67}$$

where $T_p = 1/120$ s is the period of each AC voltage source of the transformer. In the Laplace space that will be used in the following, the power supplies modeled as $U_{load}(t) = U_{ref}(t - \tau)$ is either treated as a pure delay or included as Padè approximations [101, p. 127] of its transform

$$PS_{E,F,OH}(s) = \frac{U_{load}(s)}{U_{ref}(s)} = e^{-\tau s} \approx \frac{(1 - \frac{s\tau}{2n})^n}{(1 + \frac{s\tau}{2n})^n} \tag{3.68}$$

where $n \in \mathbb{R}$ is the order of the approximation, which corresponds to a transfer function with unitary gain and progressively larger phase losses at increasing frequencies.
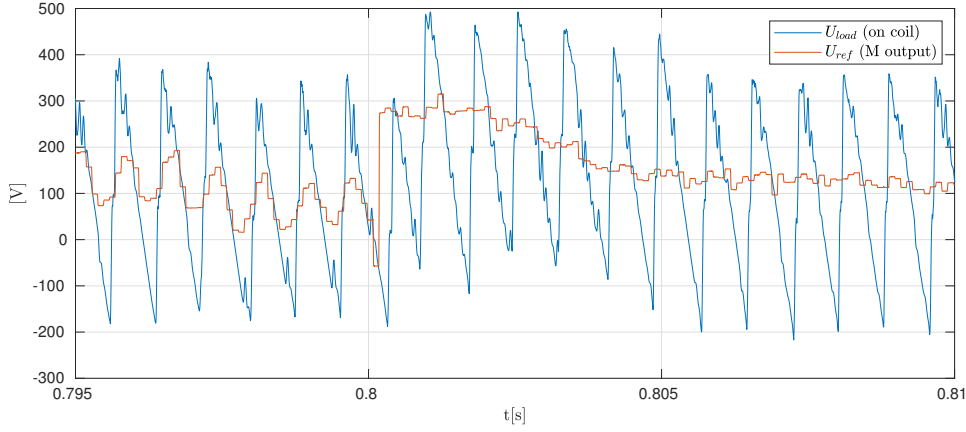
Figure 3.13 – Actual U_{ref} requested by the control system and the corresponding U_{load} applied to the F5 coil by its power supply in shot #68072, evidencing the reaction to a step-like reference change of the output.

3.4.2   Delay model for the G coil power supplies

The FPS (fast power supply) is designed to rapidly impose a current flowing on the G coil for vertical control. The DC power source includes a thyristor rectifier whose role is providing a constant voltage of $U_{DC} = 280V$ (with a nominal maximum of 566 V) on a fast output stage (FOS) including an H-bridge.

The working principle of the H-bridge is illustrated in Fig. 3.14 and 3.15. The fast output stage applies on the G coil the voltage U_{FOS}, ideally either U_{DC}, $-U_{DC}$ or 0. The four IGBT switches operate at a switching frequency of 10 kHz providing the fastest actuation for magnetic control in the TCV tokamak. The direction of the imposed voltage and the direction of the pulse are based on the input voltage $U_{ref,G}$ and is discussed in more detail in the next Sec. 3.4.3. The behavior of the FPS is therefore strongly nonlinear, but for the purpose of controller synthesis is approximated with a delay.

The delay approximation is motivated by the fact that, for a constant voltage $U_{ref,G}$ and an ideal H-bridge, the average of the U_{FOS} voltage applied on the coil by the H-bridge is equivalent to the same voltage imposed directly on the coil $U_{ref,G}$ for times multiple of half the switching period of 0.1 ms. Since the fastest characteristic time of the dynamics of interest is the growth rate of the vertical instability, which in this work are typically $\tau_z \approx 1$ ms, the approximation is justified.

The power supply is modeled with a delay on the input applied on the G coil, where in the Laplace domain

$$PS_G(s) = \frac{U_{FOS}(s)}{U_{ref,G}(s)} = e^{-\tau_G s} \approx \frac{(1 - \frac{s\tau_G}{2n})^n}{(1 + \frac{s\tau_G}{2n})^n}. \tag{3.69}$$

In this case the delay

$$\tau_G = \frac{1}{2}\frac{1}{f_{switch}} = 0.05\text{ms} \tag{3.70}$$
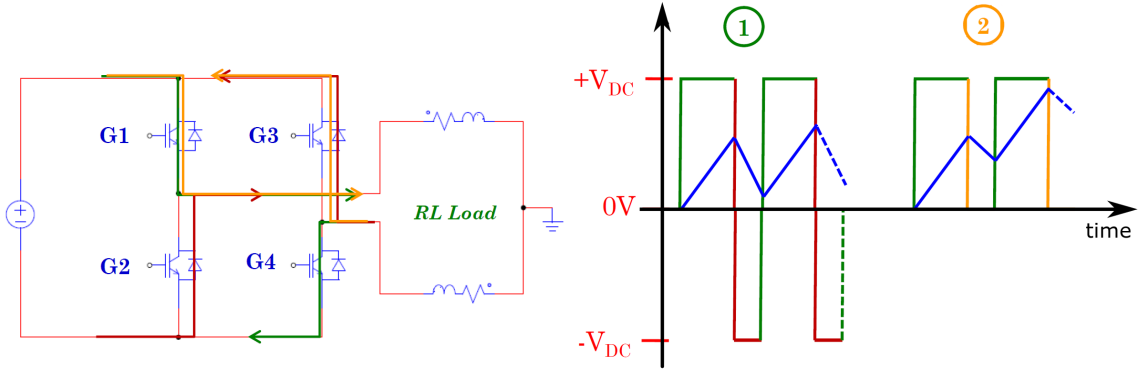
Figure 3.14 − Working principle of the H-bridge connected to a DC voltage (left): the circuits can be closed in couples, with several combinations allowing the voltage to be applied in different directions on the load (right) with the same color coding of Fig. 3.15 ([118]).

Figure 3.15 − Simplified behavior of the voltage (square wave) and the current on the load (blue). In phase 1, G1-G4 is followed by G2-G3. In phase 2 G1-G4 is followed by G1-G3 where no voltage is applied ([118]).

is determined by the fact that the change in the reference for the FPS happens statistically with the same probability during a period of the triangular wave and the maximum time that the FPS could take to react to a variation in $U_{ref,G}$ is 0.1 ms.

3.4.3 A nonlinear simplified model for the FPS

Modeling the FPS as a delay is useful for linear controller synthesis but a more complete FPS model was derived for including part of its nonlinear effects in plasma discharge simulations when the RZIp model is set in feedback with the magnetic controller.

The FPS model is designed in Simulink which includes libraries for the nonlinear elements required for simulating the FPS dynamics. The block scheme illustrated in Fig. 3.16 emulates the FPS characteristics better than a simple delay and its working principle is illustrated as follows.

When used in voltage mode, the switching frequency of the the H-bridge is fixed and the FPS can impose a voltage on the G coil ($\pm U_{DC}, 0$) for a fraction of the switching time. This fraction is determined by a comparison of the reference signal provided by the magnetic controller $U_{ref,G}$ with a triangular waveform of 10 kHz period. As the reference signal in absolute value is larger than the waveform a circuit is closed and the U_{DC} voltage is applied on the coil with the sign corresponding to the one of the reference signal. In order to retain the effects of the dead zone, no output is provided for a reference voltage of $|U_{ref,G}| < 10$ V.

Although this model provides a useful tool for simulations of the FPS, it does not include further nonlinear effects. In particular:

- The shape of the output U_{FOS} is never an actual square wave (see also [87]) but has a temporal evolution defined by the FPS power electronics.
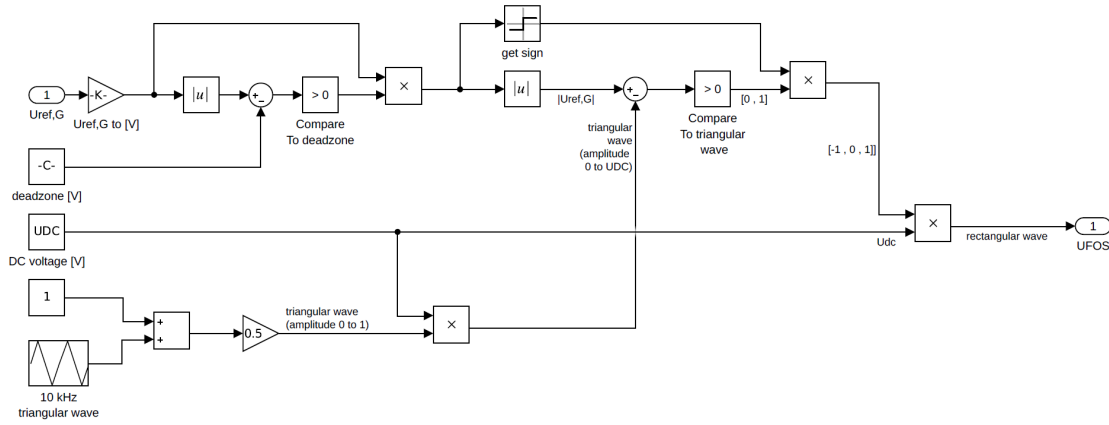
Figure 3.16 – The FPS nonlinear model block scheme as implemented in Simulink The input is the reference voltage $U_{ref,G}$ and the output is U_{FOS} .

- During a shot the U_{DC} signal is not fixed but decreases when a continuous current flows on the G coil, and is recovered when the circuit is open.

- Over voltage and over current protection trigger an alarm triggering the termination of the shot.

- An offset in the H-bridge voltage is observed to be proportional to the G coil current.

Despite the simplifying assumptions, the FPS model remains valid for introducing a first approximation of the nonlinearities of the FPS, in particular its switching behavior and the dead zone. The inclusion of the remaining nonlinearities was studied in [119]
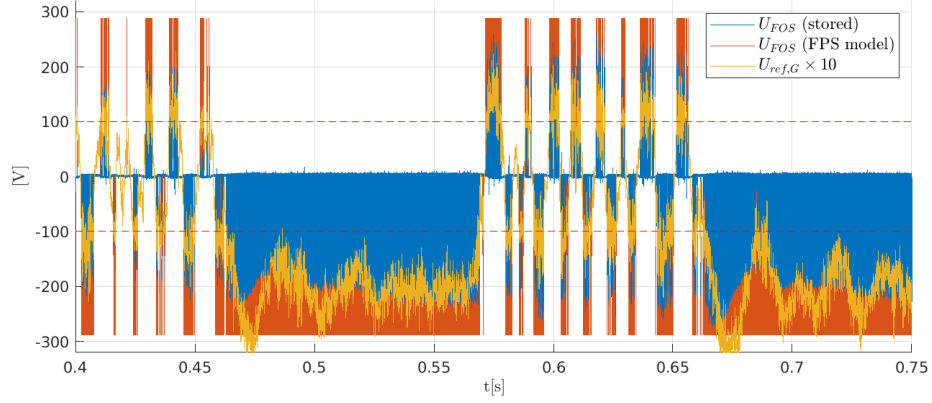
Figure 3.17 − Simulation of the FPS nonlinear model block and comparison with the actual voltage U_{FOS} provided by the FPS in shot #65530. The input of the model is the signal $U_{ref,G}$ which is scaled for comparison. The horizontal dashed line is the (scaled) dead zone threshold and the FPS is active only when the reference is above it. The dense colored zones derive from the fast oscillating dynamics of the FPS (stored in blue and simulated in orange) and clearly show the time separation in the variation of $U_{ref,G}$ from the digital control system and the reaction of the FPS. A zoom in this fast dynamics is provided in Fig. 3.18.
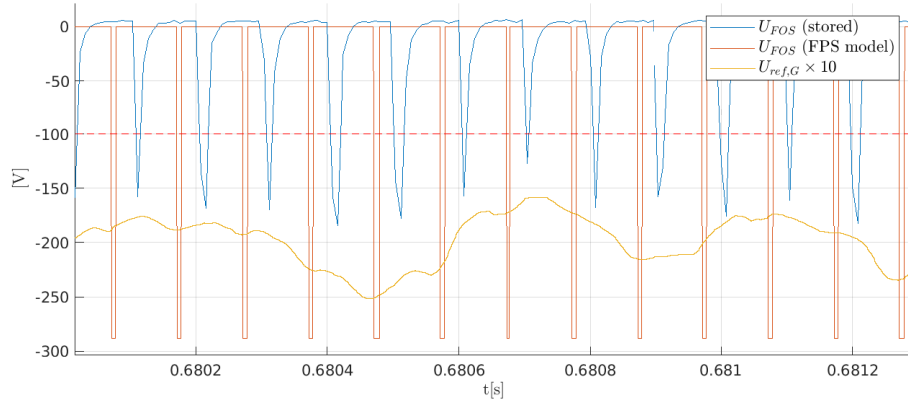
Figure 3.18 − Zoom in the previous Fig. 3.17 where $U_{ref,G}$ appears approximately constant and the fast dynamics of the FPS is highlighted. The FPS model correctly models the switching behavior and the dead zone dynamics, but is too simple to model the shape of the real output U_{FOS}. Note that, as the reference amplitude $U_{ref,G}$ is larger in amplitude, the length of the pulse is longer. The phase shift of the impulses depends on the initial condition of the simulation and it is observed to be approximately constant with the predicted 10 kHz of the FPS.
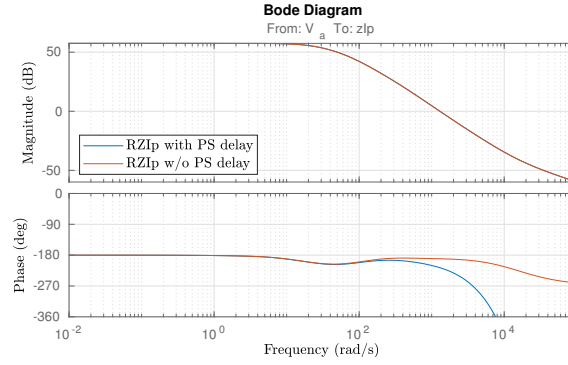
Figure 3.19 – Bode plot of the transfer functions for the RZIp channel $V_a \to z_C I_{p0}$ using $F3$ and $F6$ in antiseries for shot #51437 including the effect of the power supply delay model.
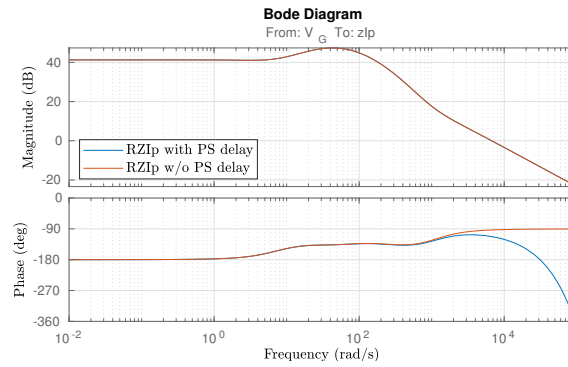
Figure 3.20 – Bode plot of the transfer functions for RZIp channel $V_G \to z_C I_{p0}$ for shot #51437 including the effect of the power supply delay model.

3.4.4 Effect on controllability of the vertical instability in TCV

The main limiting factor for vertical stabilization of highly elongated plasmas is the delay included to model the high frequency dynamics of the power supplies, which for the PF coils is combined with the shielding effect of the vessel. This is observed in Fig. 3.19 where the transfer function of the RZIp model $V_a \to z_C I_{p0}$ without delay at high frequencies has a phase lower by π compared to $V_G \to z_C I_{p0}$ reproduced in Fig. 3.20.

Bode plots can be used to determine the closed loop stability of a SISO (single-input-single-output) transfer function. The addition of a controller K in series with the plant, which in this case would provide V_a or V_G as a function of the vertical position error, allows defining the SISO open loop for stabilization such that $L = G_z K$. Classical SISO loop shaping techniques [101, p. 26] require for closed loop stability that at the crossover frequency, where the magnitude of the open loop transfer function (L_z in this case) falls below unity, the phase should be larger than $-\pi$. One can clearly see that there is a wide range of frequencies for which the phase is larger than $-\pi$ in $V_G \to z_C I_{p0}$, which suggests that a simple proportional feedback controller $K_g = P_g$ with $P_g \in \mathbb{R}$ allows stabilizing the vertical instability. However, the FPS cannot be operated in this way as it cannot sustain DC currents and it typically includes only derivative control $K_z = sD_g$, insufficient to stabilize the plasma alone [97]. On the other hand, for guaranteeing stability

when closing a control loop on $V_a \to z_C I_{p0}$ only, a controller is required to provide the necessary phase margin by modifying the loop around the crossover frequency (e.g. using a proportional-derivative controller $K_z = P_z + sD_z$). This is in general sufficient only when the unstable pole is slow compared to the inverse of the delay of the power supplies and for most elongated plasmas a synergy with the FPS is required.

The delay limits the range of frequency at which stability can be provided as it corresponds to a rapid loss of phase at frequencies larger than the inverse of its characteristic time scale [101, p. 182]. Over this critical frequency, no practical controller can be included to stabilize the vertical instability as the delay between actuation and growth of the instability is too large.

Stabilization of the vertical instability in TCV is typically performed with a combination of feedback on the internal and external coils. This makes the use of SISO loop shaping inadequate for the purpose of finding an optimized solution for the vertical control problem and closed loop multivariable techniques will be applied in Chapter 5 to optimize vertical control in TCV.

4 Decoupled shape and position control design

In the present chapter, a new design procedure for the TCV shape controller is proposed and simulations in closed loop with the RZIp model are provided to discuss the considered solutions. The previous shape controller design neglected the vertical instability dynamics and allowed a simple implementation which was tested in TCV shots but required extensive tuning for stable operation. An extension is proposed in this chapter, where the tuning of the controller for the plasma position, in charge of vertical stabilization, can be designed separately from the shape controller, which acts on the plasma on a different time scale. To this aim, frequency decoupling of position and shape control is achieved and the shape controller can be designed on a stable system. This will require a correction of the plasma position observers to be consistent with the ones used for shape control based on the last closed flux surface location. Furthermore, tuning of the vertical controller can rely on the former experience of TCV operators, since the same scheme used in standard TCV shots is maintained which could improve the range for stable and regular operation of the shape controller.

In Section 1 the standard position and current control in TCV is introduced using the RZIp model and showing the effects of current coupling in steady state. An upgrade to the standard approach to mutual decoupling and resistive compensation is also presented.

In Section 2, the problem of separating plasma shape and position control is discussed and the combined fast and slow observers for the plasma position are introduced.

In Section 3, the new design procedure for the shape controller is presented. This is based on the static gain of a stable plant where position control is closed to stabilize the vertical instability using the standard TCV control loop. Different cases are illustrated, discussing the flexibility of the new method.

In Section 4, simulations of the RZIp model in closed loop with the decoupled shape and position controller are presented for a TCV shot, which allows discussing the best scheme for shape control. Position, coil current and shape controllers are tuned in order. A main issue derives from the uncertainty in the model used for shape control design.

In Section 5, the model used for shape control design is discussed, showing that a model derived from a linearization of the Grad-Shafranov equation provides a better solution compared to a simpler one based on Green's electromagnetic functions in vacuum.
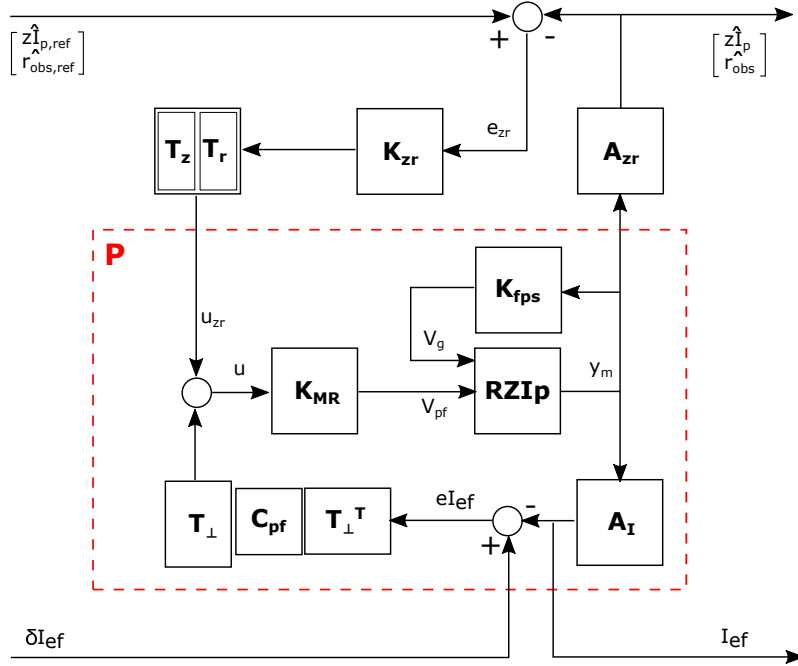
Figure 4.1 – Block scheme for standard position and coil current control, including the definition of block P used in the remaining of this chapter.

4.1 Standard position and current control

The block scheme for standard position and current control is reproduced in Fig. 4.1. The plant P, used also in the following, contains the dynamical RZIp model. The controller K_{fps} provides the voltage command to the FPS, using derivative control on the vertical plasma position, which however is not sufficient to stabilize the plasma alone. The block K_{MR} represents the mutual decoupling and resistive compensation described in the following Sec. 4.1.1, including an integral term in position and coil current control. In general, the objective of the position controller K_{zr} is tracking a reference for the plasma position observers $z\hat{I}_{p,ref}$ and $\hat{r}_{obs,ref}$ and stabilizing the vertical instability by providing the signal u_{zr} to the K_{MR} block as a function of the plasma position. In Fig. 4.1 and in the following the matrix A_{rz} is a subset of the A matrix which maps the magnetic measurements y_m in position observers $z\hat{I}_p$ and $\hat{r}_{obs}$. These observers will be referred to as *analog* position observers since the A matrix is exactly the one used in the analog control system of TCV. Position control requires assigning a combination of E and F coils, represented as T_z and T_r, for providing the necessary feedback for correcting the position errors. Only the remaining columns of $T_\perp = \text{Im}(\text{ker}([T_z \; T_r]))$ define a set of vectors in $\mathbb{R}^{16}$ which correspond to coil current combinations orthogonal to T_z and T_r that can track exactly a current reference using a controller C_{pf}. These coil current references are pre-programmed to obtain a desired plasma shape.

A variation in a coil current reference is not tracked only by the corresponding coil direction but has an effect on the coil currents $I_z = T_z^T I_{ef}$ and $I_r = T_r^T I_{ef}$ due to the
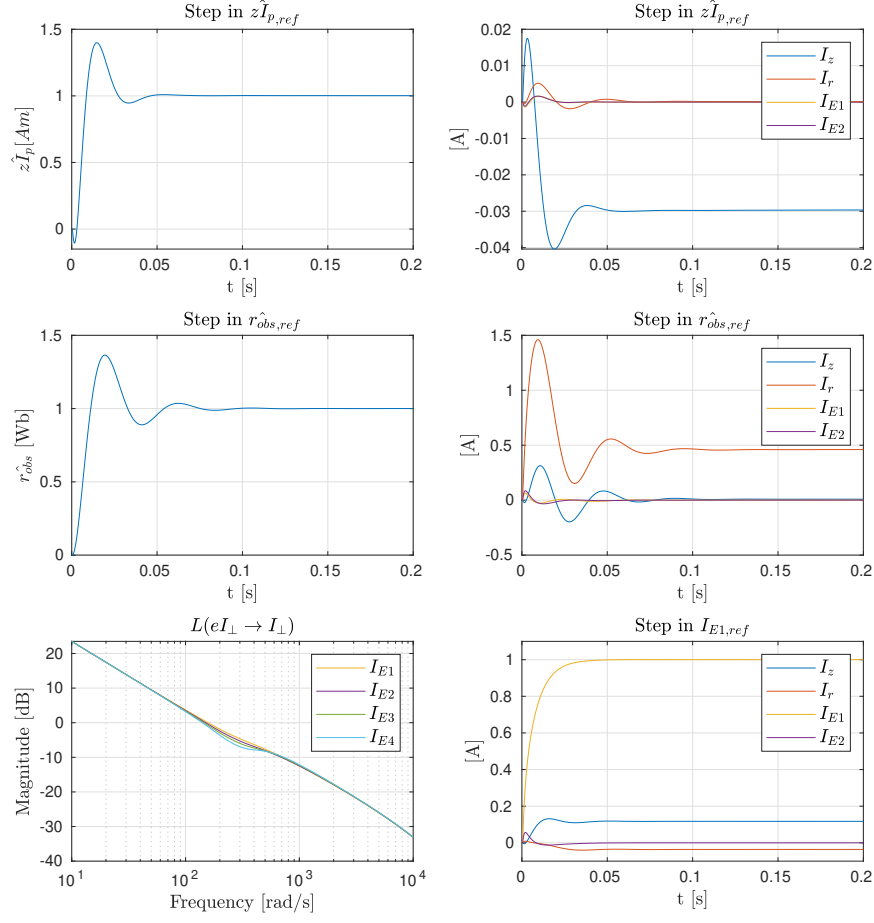
Figure 4.2 – Step of the plant P in closed loop with $[T_z \, T_r] \, K_{rz}$ for position control considering only the analog observers.

coupled dynamic with the plasma equilibrium and positioning. This will be fundamental in the new design of the shape controller and a simplified case is studied in this section to illustrate this effect.

In Fig. 4.2, the dynamical response to a set of stepwise variations in the inputs of block scheme of Fig. 4.1 is reproduced. The RZIp model is generated for shot #63693 and the same matrices used for standard analog control in that shot are included. One can observe that steps in the plasma vertical and radial position references are tracked exactly on a time scale of approximately 50ms. The new position is maintained by variation of the currents I_z and I_r, modifying the static magnetic fields on the plasma current distribution for achieving a new force balance. As the static plasma equilibrium position does not influence the coil currents in the remaining coil combinations $T_\perp I_{ef}$, no perturbation is observed in steady state in the remaining directions. For this shot, standard coil combinations including only the coils $F3 - F4$ and $F7 - F8$ are used for plasma position control, defined
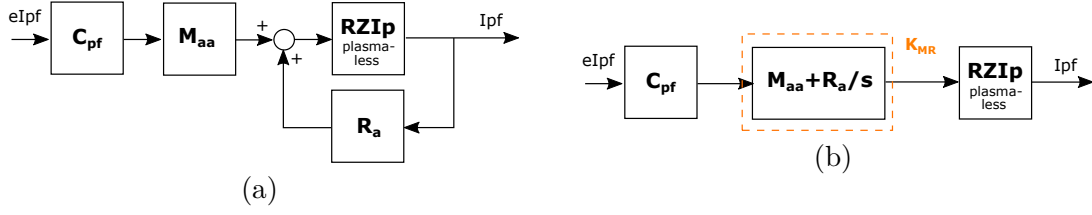
Figure 4.3 – Block schemes for mutual decoupling and resistive compensation.
(a) Standard approach, (b) new PI approach.

as $T_{z,std}$ and $T_{r,std}$. The generated magnetic field in steady state and the effect on the plasma equilibrium can be seen in Fig. 4.11 (a) and (b). In Fig. 4.2, the effect of a step in the reference current of coil E_1, orthogonal to $T_{z,std}$ and $T_{r,std}$, is reproduced. One can see that the coil current reference is exactly tracked but a finite steady state current is required in I_z and I_r for correcting the induced plasma equilibrium position perturbation due to the static current in $E1$.

4.1.1 Alternative scheme for mutual decoupling and resistive compensation

The legacy TCV control system includes a so-called 'Mutual decoupling and resistive compensation' term. When controlling only the PF coil currents (e.g. during the breakdown phase), this has the effect of providing an approximate integral effect for tracking the coil current references and decouples the current dynamics. This term is retained, without modification, also when plasma quantities (position, current) are being controlled. In the hybrid controller (Sec. 2.4), this is implemented via the control law:

$$V_{pf} = V_{ff} + R_a \hat{I}_{pf} + M_{aa} C_{pf} e_{I_{pf}} \tag{4.1}$$

where V_{ff} is a pre-computed feedforward voltage, R_a are the active coil resistances, $\hat{I}_{pf}$ the measured coil currents, M_{aa} the matrix of mutual inductances between the coils (excluding the G coil), C_{pf} the gains for coil current control and $e_{I_{pf}} = I_{pf,ref} - \hat{I}_{pf}$ the error between the measured coil current and its reference. From now on this approach to mutual decoupling and resistive compensation will be referred to as 'standard'.

Considering a simplified plasmaless model for the current dynamics and neglecting the vessel, the Laplace transform of the coil dynamics from a voltage input to the current output reads

$$I_{pf}(s) = (sM_{aa} + R_a)^{-1} V_{pf}(s). \tag{4.2}$$

In the assumption that the coil resistances are constant and correctly estimated and that the currents are measured exactly ($\hat{I}_{pf} = I_{pf}$), using Eq. (4.1) for the input voltage one can reformulate the current dynamics as

$$sM_{aa}I_{pf} + R_a I_{pf} = V_{pf} = R_a I_{pf} + M_{aa} C_{pf} e_{I_{pf}}. \tag{4.3}$$
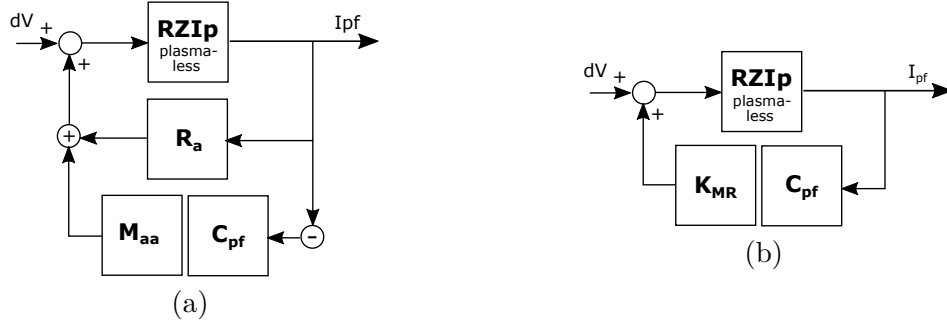
Figure 4.4 − Block schemes for the evaluation of the current response to a voltage disturbance in input.
(a) Standard approach, (b) new PI approach.

where the Laplace variable s was omitted in the dependent terms V and I for simplicity. Simplifying this expression, the resulting transfer function from current errors to the coil currents remains

$$I_{pf} = (1/s)C_{pf}e_{I_{pf}}. \tag{4.4}$$

This allows introducing an integrator effect where the open loop bandwidth is determined by the gain C_{pf} and removing completely the coils coupling in an ideal case. It should be noted that this is achieved by positive feedback of the coil currents, attempting to move the slow poles of the coils to the imaginary axis, rather than by explicit inclusion of an integrating element in the control loop. This was an advantage when the implementation was done using analog hardware of the original TCV hybrid controller, as it avoids the need of dealing with integrator windup. The corresponding block scheme is represented in Fig. 4.3.a.

An improvement (from now on referred to as PI) to this approach can be obtained with a mutual decoupling and resistive compensation block $K_{MR}(s)$ operating on the coil current errors only as

$$V_{pf} = K_{MR}(s)e_{I_{pf}} = (M_{aa} + R_a/s)C_{pf}e_{I_{pf}} \tag{4.5}$$

. This control law includes an explicit integrator term R_a/s and is implemented in the digital control system only. With this modification, the transfer function from an input voltage to coil currents becomes

$$I_{pf} = (sM_{aa} + R_a)^{-1}(sM_{aa} + R_a)(C_{pf}/s)e_{I_{pf}} = (1/s)C_{pf}e_{I_{pf}}. \tag{4.6}$$

which is equivalent to the previous result. The corresponding block scheme is represented in Fig.4.3.b.

It is observed that, when the vessel dynamics is included, off-diagonal coupling is present in the open loop transfer function. This dynamics is included computing a plasmaless RZIp model, where only the dissipative dynamics of PF coils and vessel is considered. Since the full expression is complicated, a comparison between the two methods is illustrated using
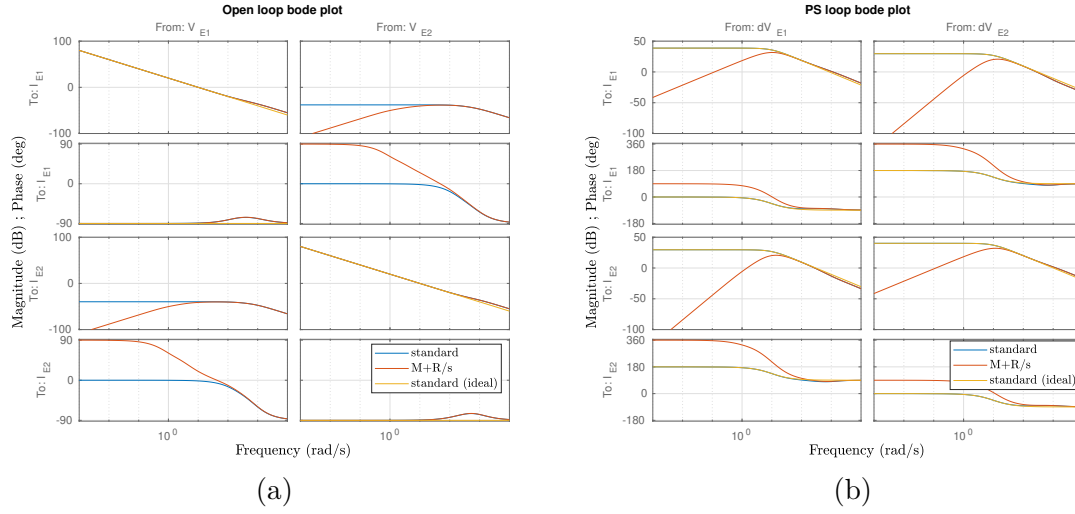
Figure 4.5 – Bode plot for comparing the different approaches for mutual decoupling and resistive compensation. (a) The open loop illustrated in Fig.4.3. (b) The disturbance response corresponding to the block schemes of Fig. 4.4. In blue, the standard approach used on the plasmaless RZIp model, in red the PI approach on the plasmaless RZIp and in yellow the ideal response neglecting the vessel.

bode plots for two coils (E_1 and E_2) as reproduced in Fig.4.5.a. The standard approach shows a finite steady state value for the off-diagonal transfer functions, indicating that decoupling is not exact due to the vessel presence. This effect is reduced on long time scales using the PI approach.

The actual advantage of the PI approach compared to the standard one is evident when considering the process sensitivity for current control, whose block schemes are reproduced for the two approaches in Fig. 4.4.

The process sensitivity considered is the transfer function from d_V to I_{pf}. This transfer function has an unavoidable static value when using the standard approach to mutual decoupling and resistive compensation for the off-diagonal terms both for the ideal case (neglecting the vessel) and the plasmaless RZIp. This effect can be avoided when an explicit integrator is included in the coil current controller using the PI approach. The bode plots of the corresponding transfer functions are plotted in Fig. 4.5.b.

Summarizing, the standard approach

- Neglects the variation in the coil resistances to include the integrator dynamics, resulting in approximate integrators only.

- incorrectly neglects the vessel (and the plasma) dynamics when decoupling the off-diagonal terms, which also results in a steady-state error.

- Does not reject low frequency disturbances in the voltage.

while the modified approach
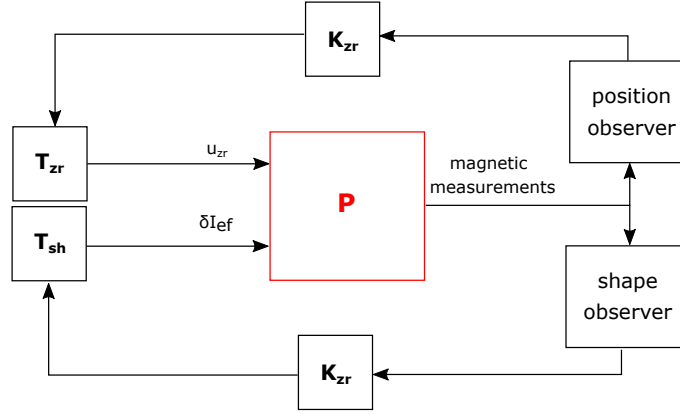
Figure 4.6 – The simplified scheme for decoupled shape and position control design including P from Sec. 4.1. The position controller provides the input signal u_{zr} to the mutual decoupling and resistive compensation block while the correction to the E and F coil reference currents δI_{ef} is provided by the shape controller.

- Explicitly includes an integral term insensitive to the variation of the coil current resistances.

- Allows the correction of disturbances in the input voltage.

In the following treatment, only the PI approach for mutual decoupling and resistive compensation is considered.

4.2 Separation of position and shape control

When including the previous version of the digital shape and position controller described in Sec. 2.5 in TCV discharges, this controller plays an essential role in vertical stabilization of the plasma.

The approach of this shape and position controller [79] to vertical stabilization consists of maintaining differential control in the loop for vertical control as set in the standard hybrid controller in order to slow down the instability until the shape controller is able to provide the necessary proportional control for stabilization [97]. This allows controlling the first singular value, mainly aligned to the vertical position observer, to zero. The shape and position controller is constrained to act on the plasma on relatively long time scales, where the real-time equilibrium reconstruction [41] adds significant extra delay to the control loop, further limiting the operational space in term of valid gains and hampering the stabilization of high-elongation plasmas.

The pre- and post-compensation controller used for shape control design allows exact decoupling of a stable, static model but does not focus on the stabilization of the vertical instability. Consequently, the main drawback for regular use of the existing shape control is the requirement for extensive tuning over many shots for most vertically unstable plasmas. Furthermore, it is likely that the range of high-elongation plasmas that can be stabilized is reduced, though this was not investigated in detail. This is mainly due to the new
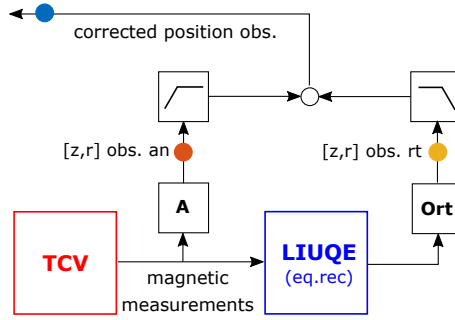
Figure 4.7 – The corrected position observer as a block diagram, with the same color coding of the signal presented in Fig. 4.8. The block A is the A matrix containing $O_{z,an}$ and $O_{r,an}$ while the block O_{rt} contains the linear combinations to obtain real time position observers from equilibrium reconstruction

control loops closed on new actuation directions (changing the coil current combination references) and observers (linear combination of flux at control points determined by real time equilibrium reconstruction) which cannot rely on former gains and actuation directions for standard magnetic control.

The approach proposed in this chapter and illustrated in its essence in Fig. 4.6 consists of separating position and shape control from the point of view of actuators and observers. This is done to stabilize the plasma vertical instability and track a desired reference position using a position controller acting on the input of the mutual decoupling and resistive compensation block u, while the shape controller remains in charge of correcting the shape deformations only by modifying the coil current references δI_{ef} on slower time scales. This separation maintains the reliable structure of standard position control for stabilizing the vertical position, on which the new position controller tuning is based, and could avoid the extensive tuning characterizing the former shape and position controller. The first step is the redefinition of the position observers such that they are consistent with the ones used for shape control, which is discussed in the next section.

4.2.1 Combined fast and slow observers for plasma position

An improved observer for the plasma position is obtained combining the fast but imprecise plasma displacement estimate from analog measurements and the slow but reliable position estimate defined from equilibrium reconstruction. When performing a shot controlled using SCD, the analog magnetic measurements are acquired at the SCD sampling rate and are linearly combined to provide an estimate of the plasma displacement, which is considered the fastest observer available for position estimation but subject to low frequency systematic errors due to the simplifying assumptions in its definition (see Appendix A.2). This analog observer provides a high frequency correction to the combined position observer. The position observers from equilibrium reconstruction instead require a run of real time LIUQE to be available for feedback, from which its latency is derived, since it is based on the knowledge of the equilibrium LCFS. The plasma displacement from equilibrium reconstruction provides the low frequency contribution to the combined position observer.

The low and high frequency contributions are combined to obtain a unique observer (one for the vertical and one for the radial position) used for position control by using a system of first order lowpass (F_{LP}) and highpass (F_{HP}) filter with transfer functions

	continuous time	discrete time
F_{LP}	$p/(s+p)$	$(1 - e^{-p_f T_s})/(z - e^{-p_f T_s})$
F_{HP}	$s/(s+p)$	$(z - 1)/(z - e^{-p_f T_s})$

whose discrete version (in the discrete version of the Laplace variable z) was implemented in SCD with sampling time T_s for the experimental runs. The characteristic pole p_f is set at 50 rad/s which is faster than the shot duration and also:

- lower than the characteristic growth rate estimated from RZIp for typical TCV plasmas (10^2 rad/s [79])

- lower than the vessel characteristic time for the first (slowest) up-down asymmetric eigenmode coupled to vertical dynamics $L_e/R_e = 120$ rad/s

- lower than the typical bandwith for position control observed in the linear RZIp model in closed loop with the hybrid controller $\omega_{bw} = 200$ rad/s

this choice guarantees that, on fast time scales, the hybrid controller is in charge of vertical stabilization without relying on equilibrium reconstruction.

The block scheme signal routing to obtain the corrected position observer is presented in Fig. 4.7. For each position estimator, the measurement unit should be equalized in order to have a coherent estimator. It is chosen to have the same measurement unit of the analog observer since the controller gains are selected basing on the former position controller which uses only analog estimators. The definition of the vertical and radial position observers is provided in the following.

The analog vertical and radial position observers are derived from a linear combination of magnetic measurements using the A matrix. The vertical position observer is an estimate of the plasma vertical position times the plasma current obtained as

$$z_{an} = z\hat{I}_p = A_{z,an}y_m \tag{4.7}$$

where *an* stands for *analog*. The analog radial position observer is based on the difference of reconstructed flux perturbation in two points on the HFS (o) and LFS (i) of the LCFS mutiplied by a constant as

$$r_{an} = \hat{r_{obs}} = K_\psi(\tilde{\psi}_o - \tilde{\psi}_i) = A_{r,an}y_m \tag{4.8}$$

In the previous Eq. (4.7) and (4.8), the vectors $A_{z,an}$ and $A_{r,an}$, described in detail in Appendix A.2.3, linearly combine the magnetic measurements y_m including magnetic probes, flux loops and coil current measurements available in real time. The corresponding references $z\hat{I}_{p,ref}$ and $\hat{r}_{obs,ref}$ contain corrections for the systematic estimation errors and are designed by the MGAMS suite during shot preparation.
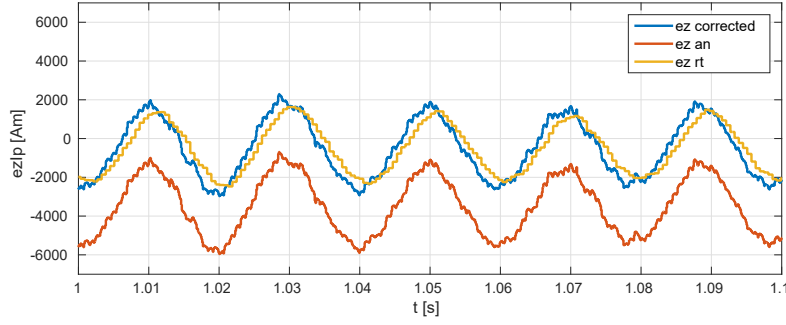
Figure 4.8 – The corrected error for the vertical position computed for shot #57796 which was characterized by periodic vertical oscillations. The latency of the real time error is compensated and the static error due to the incoherent observers is corrected.

The position observers derived from real-time equilibrium reconstruction rely on flux estimates w interpolated at the control points to recover an estimate for the plasma rigid displacement ΔZ and ΔR from the pre-programmed LCFS. In order to be combined with analog observers, these are rescaled to obtain signals with the same physical units of measurements. This requires a careful definition of the observers O_z and O_r which will be discussed in the following Sec. 4.3.3. For the moment it is sufficient to consider that the observers derive an estimate of the plasma position from the reconstructed fluxes at the LCFS with linear operations as

$$z_{rt} = O_z w \tag{4.9}$$

$$r_{rt} = O_r w \tag{4.10}$$

where *rt* stands for *real time* (equilibrium reconstruction). As the two signals are essentially a scaled measure of the plasma displacement, their reference is always 0.

Corrected vertical and radial estimators combining analog and digital measurements are obtained as (in the Laplace domain)

$$z_{corr}(s) = F_{LP}(s)z_{an}(s) + F_{HP}(s)z_{rt}(s) = F_{LP}(s)O_{rt,z}w(s) + F_{HP}(s)A_{z,an}y_m(s) \tag{4.11}$$

$$r_{corr}(s) = F_{LP}(s)r_{rt}(s) + F_{HP}(s)r_{an}(s) = F_{LP}(s)O_{rt,r}w(s) + F_{HP}(s)A_{r,an}y_m(s) \tag{4.12}$$

Indeed the correct implementation should be one defining the error as a corrected combination of errors, due to the possibly non static reference for the analog observer.

$$e_{z,corr}(s) = F_{LP}(s)e_{z,rt}(s) + F_{LP}(s)e_{z,an}(s) \tag{4.13}$$

$$e_{r,corr}(s) = F_{LP}(s)e_{r,rt}(s) + F_{HP}(s)e_{r,an}(s) \tag{4.14}$$

where the errors are defined as the reference minus the corresponding signal. This is however not considered in the present for simplifying the block schemes and without loss
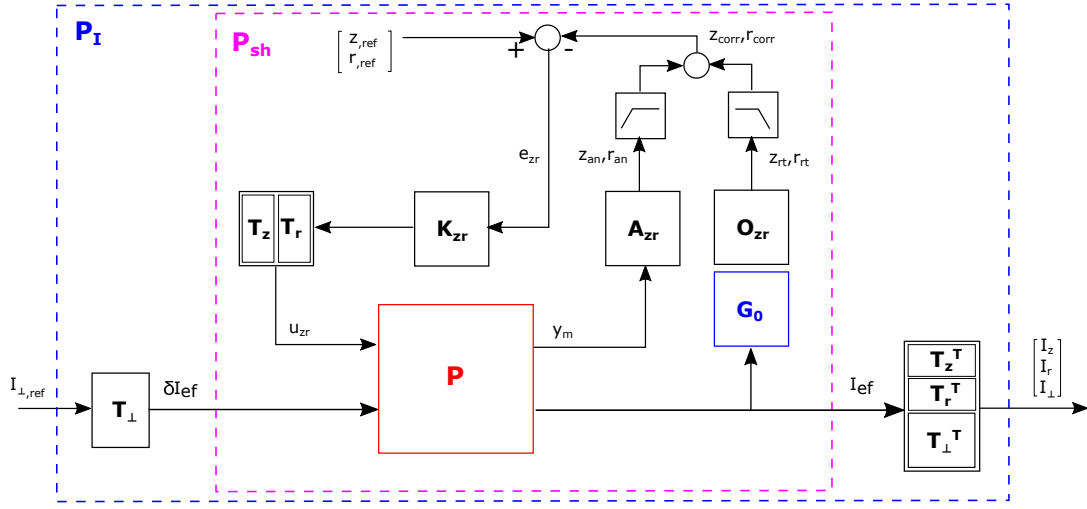
Figure 4.9 – Block schemes for definition of different plants for shape control design including the plant P featuring RZIp (Sec. 4.1). The shape controller is closed on P_{sh} and the coil current decoupling will be defined based on P_I.

of generality of the results.

4.3 Shape controller design

The goal of this section is to introduce an algorithm to formally derive a shape controller which is decoupled from the position control loop and based on the static gain of a plant P_{dec}. The definition of decoupling is specified in Sec. 4.3.2.

Consider the block scheme of Fig.4.9. For shape control design, it is assumed that a position controller (K_{zr}), PF coil controller (C_{pf}), OH and plasma current controllers can be tuned to have a stable system P (see Sec. 4.1) in negative feedback from $[z_{an}, r_{an}]$ to e_{zr} for given T_z and T_r. These are coil directions for position control analogous to the ones discussed in Sec.2.4.3 for the standard hybrid controller, which are vector in $\mathbb{R}^{16}$ selecting combinations of E and F coils. In this treatment, T_z and T_r are intentionally left generic as they will be computed. In P, the block $T_\perp$ defines the set of coil combinations orthogonal to T_z and T_r such that $T = [T_z \, T_r \, T_\perp]$ is an orthonormal basis for $\mathbb{R}^{16}$ which spans all possible E and F coil combinations. The stabilization of the vertical instability is a critical point and one should consider that

- the position controller K_{zr} design can be performed on the plant P for stabilizing it and does not require a model for equilibrium reconstruction or a shape controller, but is based only on the choice of directions T_z and T_r and a linearized model for vertical instability and coil current dynamics (RZIp in this study).

- the low frequency correction of the position observer with the system of lowpass and highpass filters is included in a way not to modify the stability characteristics of the system (not influencing the position control loop around the bandwidth
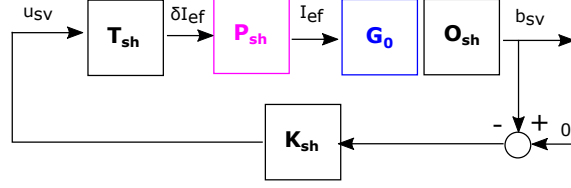
Figure 4.10 – Shape control loop

frequency). G_0 represents the static relation between coil currents perturbation and flux perturbations at the control points, and will be discussed later.

An in-depth discussion on the vertical controller synthesis can be found in Chapter 5. The main consequence of closing the position control loop is that the shape controller can be designed on a stable plant and relies on the ability of system P_I to track a set of reference currents without affecting plasma positioning in steady state.

The columns of $T_\perp$ define the coil combinations used for E and F coil current control. A static reference for the currents $I_{\perp,ref}$ provides a perturbation to the coil currents $\delta I_{ef} = T_\perp I_{\perp,ref}$, which can be tracked exactly in $I_\perp = T_\perp^T I_{ef}$ thanks to the integral effect of mutual decoupling and resistive compensation. However, in the absence of decoupling of current and position control, a current in $I_\perp$ can have an influence on vertical or radial equilibrium, therefore any effect $I_{\perp,ref}$ on the plasma position is compensated with a non zero current $I_z = T_z^T I_{ef}$ and $I_r = T_r^T I_{ef}$ for correcting the position perturbation thanks to the controller K_{zr}, influencing the plasma shape.

The previous statements are summarized using the static gain of the plant $P_I(s)$, defined in Fig. 4.9 where

$$I_{\perp,ref} \rightarrow \begin{bmatrix} I_z \\ I_r \\ \hline I_\perp \end{bmatrix} : P_I(0) = \begin{bmatrix} H \\ \hline I^{14 \times 14} \end{bmatrix} \tag{4.15}$$

The currents I_z and I_r resulting from $I_{\perp,ref}$ should be considered for shape control due to their effect on the Grad-Shafranov equilibrium and H is derived in Sec. 4.3.1

When including shape control, one should correct the analog observer for position control (fast but imprecise) on long time scales using a different position observer derived from equilibrium reconstruction (slower but reliable). This corrections avoids the inconsistency of the user specified analog vertical reference and the shape vertical reference, constrained by the pre-programmed LCFS. This is done using a position observer matrix $O_{zr} = [O_z^T \ O_r^T]^T$ to be defined, linearly combining the outputs of equilibrium reconstruction w.

Note that, when low frequency correction of the position is performed, the matrix $H \in \mathbb{R}^{2 \times 14}$ will depend only on the actuation directions T_z and T_r, on the observers $O_z \ O_r$ and on the model used for shape control.

Shape control is performed on the plant P_{sh} represented in Fig. 4.9, whose inputs are corrections to the E and F coil current references and outputs are the actual coil current perturbations determining a perturbation of the plasma equilibrium in steady state. The relation between P_{sh} and P_I is a rotation of the outputs and a reduction of the inputs such

that

$$P_I = T^T P_{sh} T_\perp. \tag{4.16}$$

No information on the coil current reference modification is lost in the projection $\delta I_{EF} = T_\perp I_{\perp,ref}$ when it is assumed that only the columns of $T_\perp$ are used for shape control. In the remainder of this chapter, the relation between coil current perturbations and the resulting flux perturbation on the shape control points is modeled with a static matrix

$$I_{ef} \to w : G_0 = \frac{\partial \psi_b}{\partial I_{ef}} \tag{4.17}$$

mapping the current in E and F coils to flux w at the boundary points, which is valid only in steady state [I]. A discussion on the model used for shape control design is provided in Sec. 4.5. The closed loop for shape control is represented in Fig. 4.10. For the purposes of determining the shape errors, an observation matrix O_{sh} is defined, combining the output of equilibrium reconstruction into shape deformations b_{sv}. For performing shape control, an actuation matrix T_{sh} provides the correction for the current references δI_{ef} based on the output of the shape controller u_{sv}. The decoupling design introduced in this chapter allows diagonal control, where a variation in each component of u_{sv} influences only the corresponding component in b_{sv}. A diagonal controller K_{sh} is then closed providing the signal u_{sv} with the goal of taking the error vector $e_{sv} = -b_{sv}$ to zero. The combination of actuation directions and observers should be done such that the shape controller does not try to modify the plasma position but acts only on shape deformations. This statement will be formalized in the following Sec. 4.3.2

Summarizing, in the assumption that stabilizing controllers can be tuned, one has to compute T_z, T_r, O_z, O_r, O_{sh} and T_{sh} with the goal of performing shape control using a diagonal $K_{sh} = (C_{sh}/s)I^{n_{sh} \times n_{sh}}$, where $C_{sh} < C_{pf}$ and n_{sh} is the number of shape parameters to be controlled. This is limited by the number of available actuators, the E and F coils, and by the fact that the position control loop is already closed. In order to apply decentralized integral control the ideal goal is having

$$u_{sv} \to b_{sv} : O_{sh} G_0 P_{sh}(0) T_{sh} \tag{4.18}$$

diagonal. This approximation of a dynamical system with its static (DC) gain is considered valid up to the current controller bandwidth C_{pf} rad/s, which determines the maximum rate of change of $I_{\perp,ref}$ that can be tracked with negligible error in $I_\perp$. This bandwidth is generally lower than the one for position control, and allows designing a shape controller whose characteristic time scale is lower than the one for position control, thus achieving frequency decoupling for minimizing the interaction. It is at this point necessary considering the decoupling of the shape control loop from the position control loop in steady state as is formalized in the following.

[I]This matrix can be easily extended to output magnetic fields at locations of interest (such as the the X-point(s) or strike points for diverted plasmas.

4.3.1 Coil current reference tracking

Shape control relies on the ability to track on long times scales a set of coil currents used to modify the plasma equilibrium. This motivates the study of the plant $P_I(s)$ and its static gain $P_I(0)$ of Eq. (4.15).

Considering the static equilibrium G_0 only (i.e. neglecting the vertical instability) the following results are valid for a generic choice of T_z, T_r and the corresponding $T_\perp$ without including position feedback

- the effect of a current in $\delta I_{EF} = T_\perp I_\perp$ tracking exactly $I_{\perp,ref}$ can modify the plasma equilibrium position seen by the vertical and radial observer

- the effect of a current $I_z = T_z^T I_{EF}$ may not only be an effect on the plasma vertical equilibrium position but also on the plasma radial position and vice-versa for $I_r = T_r^T I_{EF}$

The combined results lead to

$$\begin{bmatrix} z_{rt} \\ r_{rt} \end{bmatrix} = \begin{bmatrix} H_{z\perp} \\ H_{r\perp} \end{bmatrix} I_{\perp,ref} + H_{rzI} \begin{bmatrix} I_z \\ I_r \end{bmatrix} \tag{4.19}$$

$$= \begin{bmatrix} O_z G_0 T_\perp \\ O_r G_0 T_\perp \end{bmatrix} I_{\perp,ref} + \begin{bmatrix} O_z G_0 T_z & O_z G_0 T_r \\ O_r G_0 T_z & O_r G_0 T_r \end{bmatrix} \begin{bmatrix} I_z \\ I_r \end{bmatrix} \tag{4.20}$$

Once feedback on the plasma position and coil currents is considered, for an input $I_{\perp,ref}$ in $P_I(s)$ the controller acts to control $I_\perp$ to $I_{\perp,ref}$ and track the position reference. The closed loop system P_I will then generate steady state currents I_r and I_z in response to $I_{\perp,ref}$ as

$$\begin{bmatrix} I_z \\ I_r \end{bmatrix} = -H_{rzI}^{-1} \begin{bmatrix} H_{z\perp} \\ H_{r\perp} \end{bmatrix} I_{\perp,ref} = H I_{\perp,ref}. \tag{4.21}$$

This result is confirmed numerically for any consistent choice of T_z, T_r and $T_\perp$, typical position observation matrices O_r O_z based on equilibrium reconstruction and a stable $P_I(s)$. The consequences for defining a correct steady state decoupling of shape and position controller are illustrated in the following.

4.3.2 Definition of partial and full static decoupling

A plant P_{dec} is derived for defining shape and position control decoupling in open loop. Start considering a steady state plant derived from Fig. 4.9 mapping the steady state effect of a change in the reference to the vertical and radial position and the currents $I_\perp$ to the currents I_{EF} projected by T^T in $[I_z \ I_r \ I_\perp]$ as

$$\begin{bmatrix} z_{ref} \\ r_{ref} \\ \hline I_{\perp,ref} \end{bmatrix} \rightarrow \begin{bmatrix} I_z \\ I_r \\ \hline I_\perp \end{bmatrix} : P_{zrI}(0) = \left[\begin{array}{c|c} H_{rzI}^{-1} & H \\ \hline 0^{14\times 2} & I^{14\times 14} \end{array} \right] \tag{4.22}$$

Note that it is simply the matrix $P_I(0)$ augmented with $[(H_{zrI}^{-1})^T \, 0]^T$ where H_{rzI} was discussed in the previous subsection. The 0 block instead derives from the fact that only I_z and I_r are used for plasma positioning thanks to the choice of $T_\perp$ orthogonal to T_r and T_z and a change of z_{ref} or r_{ref} does not result in an output in $I_\perp$.

The plant for defining decoupling $P_{dec} : [z_{ref} \, r_{ref} \, u_{sv}] \to [z_{rt} \, r_{rt} \, b_{sv}]$ is derived from the previous one. The input reference currents are provided to P_{zrI} by the actuation direction T_{sh} which will always be selected to modify only the references of $I_{\perp,ref}$, thus having structure like $T_{sh} = T_\perp Q$, with $Q \in \mathbb{R}^{14 \times n_y}$ a generic real matrix to be determined and n_y is equal to the number of flux differences used for shape and position control. In this way the reference current corrections are

$$I_{\perp,ref} = T_\perp^T T_{sh} u_{sv} = Q u_{sv}. \tag{4.23}$$

The output currents $[I_z \, I_r \, I_\perp]$ for any input result in a plasma equilibrium perturbation given by the output of G_0 and are mapped into position and shape observers using the observation matrices as

$$\begin{bmatrix} z_{rt} \\ r_{rt} \\ b_{sv} \end{bmatrix} = \begin{bmatrix} O_z \\ O_r \\ O_{sh} \end{bmatrix} G_0 T \begin{bmatrix} I_z \\ I_r \\ I_\perp \end{bmatrix} \tag{4.24}$$

The resulting plant to be decoupled is, omitting part of the algebraic simplifications,

$$\begin{bmatrix} z_{ref} \\ r_{ref} \\ \hline u_{sv} \end{bmatrix} \to \begin{bmatrix} z_{rt} \\ r_{rt} \\ \hline b_{sv} \end{bmatrix} : P_{dec} = \begin{bmatrix} O_z \\ O_r \\ O_{sh} \end{bmatrix} G_0 T P_{zrI}(0) \begin{bmatrix} I^{2 \times 2} & \\ & T_\perp^T T_{sh} \end{bmatrix} \tag{4.25}$$

$$= \left[\begin{array}{c|c} I^{2 \times 2} & 0^{2 \times n_y} \\ \hline O_{sh} G_0 [T_z \, T_r] H_{rzI}^{-1} & -O_{sh} G_0 [T_z \, T_r] H_{rzI}^{-1} \begin{bmatrix} O_z G_0 T_{sh} \\ O_r G_0 T_{sh} \end{bmatrix} + O_{sh} G_0 T_{sh} \end{array} \right] \tag{4.26}$$

$$= \left[\begin{array}{c|c} I^{2 \times 2} & 0^{2 \times n_y} \\ \hline O_{sh} G_0 [T_z \, T_r] H_{rzI}^{-1} & O_{sh} G_0 P_{sh}(0) T_{sh} \end{array} \right] = \left[\begin{array}{c|c} P_{dec,11} & P_{dec,12} \\ \hline P_{dec,21} & P_{dec,22} \end{array} \right] \tag{4.27}$$

where the equality of line Eq. (4.27) for the element $P_{dec,22}$ is derived from the block scheme of Fig. 4.10 considering the transfer $u_{sv} \to b_{sv}$. Note that up to this point no assumption is made on the choice of O_z, O_r and O_{sh} and it was only required that the columns of $T_\perp$ are orthogonal to T_z and T_r.

An optimal selection of actuation directions and observers for position and shape control will allow decoupling the plant to the point where

$$P_{dec} = \left[\begin{array}{c|c} I^{2 \times 2} & \\ \hline & \begin{array}{cc} I^{N_1 \times N_1} & \\ & 0^{N_2 \times N_2} \end{array} \end{array} \right] \in \mathbb{R}^{(n_y+2) \times (n_y+2)} \tag{4.28}$$

with N_1 and N_2 to be determined. Note that $N_2 \geq 2$ for $n_y \geq 2$ since two combinations of

flux differences are always used for position control. This is optimal for closing integral diagonal control with K_{sh} on $u_{sv} \rightarrow b_{sv}$ in the sense that off-diagonal coupling in steady state is zero by design and does not require correction from the controller.

Partial decoupling

For applying diagonal control of the plasma shape, it is sufficient to have $P_{dec,22}$ diagonal and ignore $P_{dec,21}$ since the diagonal integrator in K_{sh} will cancel the coupling due to the off-diagonal term. This, however, comes at the cost of an increased control sensitivity compared to full decoupling described later. Partial decoupling will be in general obtained by selecting actuation directions for shape control T_{sh} that do not have an influence on vertical and radial displacement observers such that

$$\begin{bmatrix} O_z G_0 T_{sh} \\ O_r G_0 T_{sh} \end{bmatrix} = 0 \tag{4.29}$$

and furthermore deriving O_{sh} and T_{sh} such that $O_{sh} G_0 T_{sh}$ is diagonal, resulting in diagonal $P_{dec,22}$.

Full decoupling

Improved decoupling can be achieved with further constraints on the directions used for position control T_z and T_r such that they have no influence on the shape observers or equivalently $P_{dec,21} = 0$. This will require enforcing

$$O_{sh} G_0 [T_z \ T_r] = 0. \tag{4.30}$$

Note that this condition is sufficient also for partial decoupling as long as $O_{sh} G_0 T_{sh}$ is diagonal. Since in this way it is not required that the shape controller corrects the effects of the currents used for plasma positioning, the control effort in terms of the amplitude of the current correction (control sensitivity) will be lower by design than the previous case for off diagonal elements.

4.3.3 Derivation of shape and position controller matrices

The matrices T_z, T_r, O_z, O_r, O_{sh} and T_{sh} are evaluated providing a solution for the decoupled shape and position control problem.

The shape controller matrices will be derived inverting a plant

$$G_\Delta = M_\Delta S_0 G_0 \tag{4.31}$$

which maps E and F coil perturbation δI_{ef} into y, representing scaled differences of fluxes evaluated at the target boundary points. These differences are evaluated using M_Δ from Eq. (2.8) on the output of G_0 scaled with S_0. The definition of the shape controller matrices will be based on the following steps

- Defining actuation direction and observers for position control T_r T_z and O_r O_z.

- Constraining the remaining directions for shape control to act on the shape only (and not on the position).

- Diagonalizing a system mapping the available currents for shape control to shape variables $I_{\perp,ref} \rightarrow y$.

- Verifying that the open loop for shape control $u_{sv} \rightarrow b_{sv} : P_{dec,22} = O_{sh}G_0 P_{sh}(0)T_{sh}$ is diagonal and evaluating O_{sh} and T_{sh} explicitly.

In several steps of the derivations we will use $P_{sh}(s)T_\perp = TP_I(s)$, obtained by post-multiplying by T the relation between P_{sh} and P_I defined in Eq. (4.16).

Three cases are presented for a decoupled shape controller, whose main advantages and drawbacks are summarized here for an overview.

Decoupling cases
- Case A: uses the same actuation directions of standard control which leaves at most 12 coil combinations for decoupled shape control. Partial decoupling is provided. Potentially, this solution can be used in combination with standard position control.

- Case B: uses new optimized directions for position control which allow using at most 14 coil combinations for decoupled shape control but requires tuning of the position control. Partial decoupling is obtained, but a new position controller has to be tuned.

- Case C: uses new optimized directions for position control and at most 14 coil combinations for decoupled shape control while also granting full decoupling. A new position controller has to be tuned.

The effect of the shape control directions on the plasma equilibrium for shot #63693 at flattop are reproduced in Fig. 4.11, highlighting the fact that only coil combinations used for position control generate a static field on the plasma axis and a consequent equilibrium displacement in the vetrtical or radial direction.

(a) $T_{z,A}$ (b) $T_{r,A}$ (c) $T_{sh1,A}$ (d) $T_{sh2,A}$

(e) T_{zB} (f) T_{rB} (g) $T_{sh1,B}$ (h) $T_{sh2,B}$

(i) $T_{z,C}$ (j) $T_{r,C}$ (k) $T_{sh1,C}$ (l) $T_{sh1,C}$
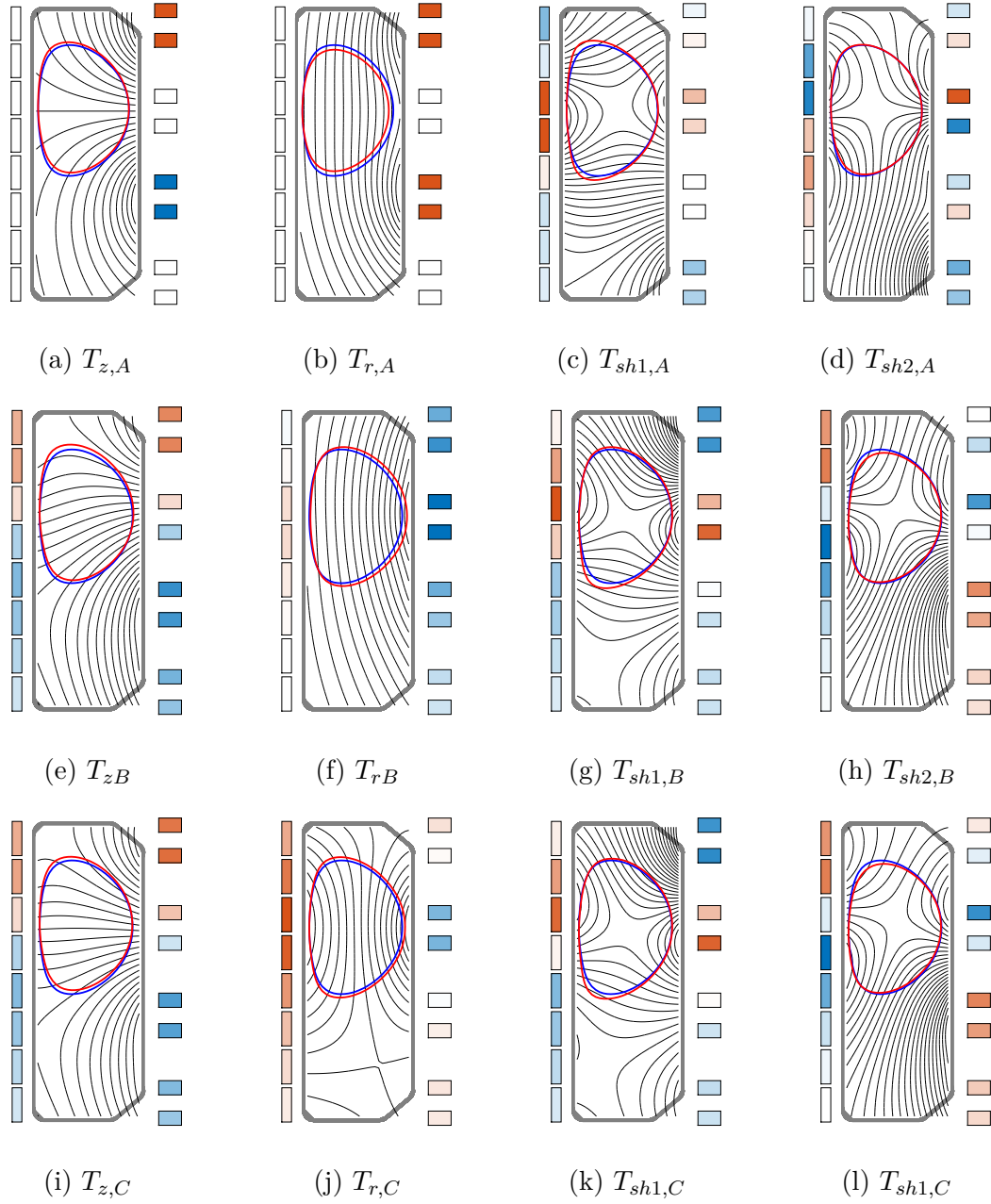
Figure 4.11 – Current directions and effects on the plasma for the different cases. A current u in each current direction generates a flux in vacuum (black) and the effect on the unperturbed LCFS (blue) is obtained solving the Grad-Shafranov equation with modified boundary conditions adding Tu to the unperturbed coil currents resulting in a new equilibrium (red). The coils are color-coded with darker red for positive and darker blue for negative currents in a (R, ϕ, z) reference frame.
Case A: (a) to (d). Case B: (e) to (h). Case C: (i) to (l).

Case A: Partial decoupling with standard control directions

In this case, coil combinations for position control are selected a priori and independently of the shape controller, and gains are sought to achieve closed loop stability for the system P in negative feedback from $[z_{an}, r_{an}]$ to e_{zr}. Consider in this example maintaining the standard position controller, which means setting

- $T_z = T_{z,std}$

- $T_r = T_{r,std}$

Consequently $T_\perp = N_{pf} = \mathrm{Im}(\ker([T_z\,T_r]))$ provides the normalized basis for the null space of T_z and T_r and is the standard approach for coil current control. The position observers are defined from rigid plasma displacement from equilibrium as

- $O_z = I_{p0}O_{\Delta z}[M_b\,0\,0] = -I_{p0}\left(\left.\dfrac{\partial \psi_{eq}}{\partial z}\right|_b M_b\right)^\dagger [M_b\,0\,0]$

- $O_r = F_\psi O_{\Delta r}[M_b\,0\,0] = -F_\psi\left(\left.\dfrac{\partial \psi_{eq}}{\partial z}\right|_b M_b\right)^\dagger [M_b\,0\,0]$

such that $I_{p0}\Delta z = O_z w$ and $F_\psi \Delta R = O_r w$ have the same units of analog observers. The matrix $[M_b\,0\,0]$ is used to obtain the flux differences on the LCFS used to determine the plasma displacement from output of equilibrium reconstruction w (see Eq. (2.8)). The vectors $O_{\Delta z}$ and $O_{\Delta r}$ define plasma displacement from the flux differences at the target boundary points (see Eq. (2.10) and (2.11)). Finally, I_{p0} is the equilibrium plasma current and F_ψ from Eq.A.29 scales a radial rigid plasma displacement to have the same units of a radial position observer.

At this point, since in general $[O_z^T O_r^T]^T G_0 N_{pf} = 0$ is not guaranteed by the choice of T_z and T_r determining N_{pf}, a further constraint is added on the coil combinations that are allowed for shape control to obtain partial decoupling. This is done defining the singular value decomposition of

$$\left[O_z^T O_r^T\right]^T G_0 N_{pf} = u_{zr}\sigma_{zr}v_{zr}^T \tag{4.32}$$

and noting that only a static current in the directions defined by the first two columns of

$$N_{pf}v_{zr} = N_{pf}\left[v_z\,v_r\,v_{sh}\right], \tag{4.33}$$

namely $N_{pf}v_z \in \mathbb{R}^{16}$ and $N_{pf}v_r \in \mathbb{R}^{16}$, can generate a plasma equilibrium displacement measured by the vertical and radial observers. In this way, the coil combinations for shape control are restricted to $\tilde{I}_{perp} \in \mathbb{R}^{12}$, a subset of the of $I_{perp} \in \mathbb{R}^{14}$ defined by N_{pf}.

The plant for designing the shape controller is in this case

$$\tilde{I}_{\perp,ref} \to y : P_A = G_\Delta \left[\begin{array}{cc|c} T_z & T_r & N_{pf} \end{array}\right] P_I(0)v_{sh} = G_\Delta N_{pf}v_{sh} \tag{4.34}$$

where the second equality is granted by the fact that one gets

$$Hv_{sh} = -H_{rzI}^{-1} \begin{bmatrix} O_z G_0 N_{pf} \\ O_r G_0 N_{pf} \end{bmatrix} v_{sh} = 0 \tag{4.35}$$

thanks to the properties of v_{sh} obtained from the SVD of Eq. (4.32). This means that a static current in the coil combinations used for shape control $N_{pf} v_{sh} \in \mathbb{R}^{12 \times 16}$ does not require a correction from the position controller for maintaining the plasma to its reference position in steady state. In this sense partial decoupling is achieved.

A further singular value decomposition of system

$$\tilde{I}_{\perp,ref} \to y : P_A = G_\Delta N_{pf} v_{sh} = U_A \Sigma_A V_A^T \tag{4.36}$$

allows decentralized control for the shape controller in the sense that the open loop for shape control is diagonal when it is defined as

$$u_{sv} \to b_{sv} : P_{dec,22} = U_A^T P_A (\Sigma_A V_A^T)^\dagger \tag{4.37}$$

$$= U_A^T G_\Delta P_{sh}(0) N_{pf} v_{sh} (\Sigma_A V_A^T)^\dagger \tag{4.38}$$

$$= O_{sh} G_0 T_{sh} \tag{4.39}$$

$$= \begin{bmatrix} I^{N_1 \times N_1} & \\ & 0^{N_2 \times N_2} \end{bmatrix} \tag{4.40}$$

where we used $N_{pf} = T P_I(0) = P_{sh}(0) T_\perp = P_{sh}(0) N_{pf}$. The dimensions of the final matrix are $N_1 = \min(n_y - 4, n_c - 4)$ and $N_2 = n_y - N_1$. Therefore in the case where $n_y = 16$ are used, then $N_1 = n_y - 4 = 12$ coil combinations can control 12 shape variables at most while $N_2 = 4$. This allows defining

- $O_{sh} = U_A^T M_\Delta S_0$

- $T_{sh} = N_{pf} v_{sh} (\Sigma_A V_A^T)^\dagger$

Note that, however, in this case $O_{sh} G_0 [T_z \, T_r] \neq 0$ in general, thus following a displacement in the plasma reference position requires a correction from the shape controller: full decoupling is not achieved.

Case B: Partial decoupling with optimized control directions
An improved decoupling scheme relies on different directions for position control to avoid sacrificing several coil combinations to achieve partial decoupling.

Observers for the plasma's vertical and radial displacements $O_{\Delta z}$ and $O_{\Delta r}$ illustrated above are considered for defining decoupled directions and observers for plasma position control. This is performed introducing a plant and performing the corresponding SVD

$$P_{zr} = \begin{bmatrix} W_z O_{\Delta z} [M_b \, 0 \, 0] \\ O_{\Delta r} [M_b \, 0 \, 0] \end{bmatrix} G_0 = \begin{bmatrix} U_z & U_r \end{bmatrix} \Sigma_{rz} \begin{bmatrix} V_z^T \\ V_r^T \\ V_{sh}^T \end{bmatrix} \tag{4.41}$$

and a $W_z \gg 1$ guarantees that the first output of $U_z^T P_{zr} T_z$ corresponds to a vertical displacement and the directions used for position control are

- $T_z = V_z$

- $T_r = V_r$

while the observers are now redefined to be exactly orthonormal as

- $O_z = I_{p0} \dfrac{U_z^T}{W_z} \begin{bmatrix} W_z O_{\Delta z} \\ O_{\Delta r} \end{bmatrix} [M_b \ 0 \ 0]$

- $O_r = F_\psi U_r^T \begin{bmatrix} W_z O_{\Delta z} \\ O_{\Delta r} \end{bmatrix} [M_b \ 0 \ 0]$

where $1/W_z$ is used to rescale the output of the observer to the correct dimension and I_{p0} and F_ψ are introduced to have the same dimension of analog observers .

Note that $[V_z \, V_r \, V_{sh}]$ define an orthonormal basis for $\mathbb{R}^{16}$, therefore $T_\perp = V_{sh}$ is a natural choice for defining the directions for E and F coil current control. The plant used for defining a diagonal shape controller is in this case, using

$$I_{\perp,ref} \to y : P_B = G_\Delta \begin{bmatrix} T_z & T_r & | & V_{sh} \end{bmatrix} P_I(0) = G_\Delta V_{sh} \tag{4.42}$$

where for the second equality we used $TP_I(0) = V_{sh}$ which is granted by the fact that $O_z G_0 V_{sh} = O_r G_0 V_{sh} = 0^{14 \times 1}$ from the singular value decomposition of Eq. (4.41) and consequently $H = 0^{14 \times 2}$. This means again that a perturbative current in the coil combinations used for shape control does not require a correction from the position controller for maintaining the plasma to its reference in steady state.

A second singular value decomposition of the system

$$I_{\perp,ref} \to y : P_B = G_\Delta V_{sh} = U_B \Sigma_B V_B^T \tag{4.43}$$

allows designing a diagonal controller for the shape variables when the open loop for shape control is obtained as

$$u_{sv} \to b_{sv} : P_{dec,22} = U_B^T P_B (\Sigma_2 V_B^T)^\dagger \tag{4.44}$$

$$= U_B^T G_\Delta P_{sh}(0) V_{sh} (\Sigma_B V_B^T)^\dagger \tag{4.45}$$

$$= O_{sh} G_0 T_{sh} \tag{4.46}$$

$$= \begin{bmatrix} I^{N_1 \times N_1} & \\ & 0^{N_2 \times N_2} \end{bmatrix} \tag{4.47}$$

where we used $V_{sh} = TP_I(0) = P_{sh}(0)V_{sh}$. The dimensions of the final matrix are $N_1 = \min(n_y - 2, n_c - 2)$ and $N_2 = n_o - 2 - N_1$. Therefore in the case where $n_y = 16$ are used, then $N_1 = n_y - 2 = 14$ coil combinations can control 14 shape variables at most while $N_2 = 2$. This allows defining

- $O_{sh} = U_B^T M_\Delta S_0$

- $T_{sh} = V_{sh}(\Sigma_B V_B^T)^\dagger$

This case, differently from the previous, allows using all 14 available directions not assigned to position control for shape control. Note that, however, in this case $O_{sh}G_0[T_z\,T_r] \neq 0$ in general, thus following a displacement in the plasma reference position requires a correction from the shape controller: full decoupling is not achieved in the sense that $P_{dec,21} \neq 0$. Furthermore, it is not granted that the same K_{zr} used in standard control can stabilize the system and may require new tuning.

Case C: Full decoupling

Full decoupling is obtained deriving the dimensionless position and shape observers from the previous shape controller algorithm which is summarized here as

$$I_{ef} \to y_{es} : P_0 = W_t O G_0 = U_0 \Sigma_0 V_0^T. \tag{4.48}$$

where O was defined in Eq. (2.14) and W_t contains the weighting for vertical and radial observers W_{tz} and W_{tr}. Notably, N_c, is not included[II].

The pre- and post- compensators diagonalizing P_0 are

$$T_{sv} = (\Sigma_0 V_0^T)^\dagger \qquad O_{sv} = U_0^T W_t O \tag{4.49}$$

obtaining

$$O_{sv}G_0T_{sv} = \begin{bmatrix} O_{sv,z} \\ O_{sv,r} \\ \hline O_{sv,sh} \end{bmatrix} G_0 \begin{bmatrix} T_{sv,z} & T_{sv,r} & \vline & T_{sv,sh} \end{bmatrix} = \begin{bmatrix} I^{n_{sv} \times n_{sv}} & \\ & 0^{(n_o - n_{sv}) \times (n_o - n_{sv})} \end{bmatrix} \tag{4.50}$$

where $n_{sv} = \min(n_c, n_y)$ and $n_o = n_y + 2$, therefore using $n_y > 16$, one gets $n_{sv} = 16$ which are the maximum position and shape variables that can be controlled with the 16 available PF coils.

Actuation direction for vertical and radial control are selected as

- $T_z = T_{sv,z}/||T_{sv,z}||_2$

- $T_r = T_{sv,r}/||T_{sv,r}||_2$

Vertical and radial observers O_z and O_r are selected as

- $O_z = k_z O_{sv,z}$

- $O_r = k_r O_{sv,r}$

[II]The matrix N_c was used in the existing shape controller to exclude directions which added net flux on the LCFS (see Sec. 2.5) but is not included here as it does not provide any explicit advantage to the design.

where

$$k_z = I_{p0} \frac{|\psi_{ax}|}{W_{tz}} \left\| M_b \frac{\partial \psi_{eq}}{\partial z} \right|_b \right\|_2^{-1} \tag{4.51}$$

and

$$k_r = F_\psi \frac{|\psi_{ax}|}{W_{tr}} \left\| M_b \frac{\partial \psi_{eq}}{\partial R} \right|_b \right\|_2^{-1} \tag{4.52}$$

rescale the dimensionless outputs of $z_{sv} = O_{sv,z}w$ and $y_{sv} = O_{sv,r}w$ to be comparable to the analog position observers.

The columns of $T_{sv,sh}$ are orthogonal by the properties of the singular value decomposition and can be written as

$$T_{sv,sh} = T_{sv,sh}^{(n)} D_{sv} \tag{4.53}$$

with D_{sv} is a diagonal matrix and the columns of $T_{sv,sh}^{(n)}$ are normalized. In this way using

- $O_{sh} = O_{sv,sh}$

- $T_{sh} = T_{sv,sh}$

and setting $T_\perp = T_{sv,sh}^{(n)}$ one gets for the open loop for shape control

$$u_{sv} \to b_{sv} : P_{dec,22} = O_{sh} G_0 P_{sh}(0) T_{sh} \tag{4.54}$$

$$= O_{sh} G_0 T P_I(0) \tag{4.55}$$

$$= O_{sh} G_0 \left[\begin{array}{cc|c} T_z & T_r & T_{sv,sh}^{(n)} \end{array} \right] \left[\begin{array}{c} H \\ \hline I \end{array} \right] D_{sv} \tag{4.56}$$

$$= \left[\begin{array}{cc|c} O_{sh} G_0 T_z & O_{sh} G_0 T_r & O_{sh} G_0 T_{sv,sh}^{(n)} \end{array} \right] \left[\begin{array}{c} H \\ \hline I \end{array} \right] D_{sv} \tag{4.57}$$

$$= O_{sh} G_0 T_{sv,sh}^{(n)} D_{sv} \tag{4.58}$$

$$= O_{sv,sh} G_0 T_{sv,sh} \tag{4.59}$$

$$= \left[\begin{array}{cc} I^{N_1 \times N_1} & \\ & 0^{N_2 \times N_2} \end{array} \right] \tag{4.60}$$

since from the singular value decomposition of the full plant $O_z G_0 T_{sh} = O_r G_0 T_{sh} = 0$ and one gets $H = 0$ from Eq. (4.21): tracking a variation in the shape of the singular values does not require a current I_z or I_r compensating for the position.

The dimensions of the final matrix are $N_1 = \min(n_y - 2, n_c - 2)$ and $N_2 = n_y - N_1$. Therefore in the case where $n_y = 16$ are used, then $N_1 = n_y - 2 = 14$ coil combinations can control 14 shape variables at most, while $N_2 = 2$.

Furthermore this set of directions and observers satisfies $O_{sh} G_0 T_z = O_{sh} G_0 T_r = 0$ from the singular value decomposition of Eq. (4.50), which guarantees full decoupling since $P_{dec,21} = 0$.

The only drawback of this scheme is that it requires a tuning of the controller using the new directions, which can be performed with structured $\mathcal{H}_\infty$ as discussed in Chapter 5. A comparison with open loop for decoupling the former shape and position controller once the position control is closed on the coil current reference is provided in Appendix C, showing that analogous results are achieved with the case C proposed here.

4.4 Controller tuning and simulations

Simulations of the dynamical RZIp system in closed loop with the position, current and shape controller are performed and the results are discussed in order to confirm that that shape controller design can be performed based on static decoupling. The RZIp model is generated for shot #63693 at $t = 0.6$ s, in the flattop: this is a limited plasma with a vertical growth rate of 180 rad/s thus rather simple to stabilize. The corresponding A, M and R matrices are also recovered. The specific analog position observer for the shot are recovered from the A matrix and the matrices of mutual inductance M and coil resistances R for TCV are used. First, position (K_{rz}) and coil current (C_{pf}) controllers will be tuned to stabilize the P plant in negative feedback, as will be demonstrated in this section. The coil current reference tracking capability is then demonstrated and only then is the shape controller (requiring O_{sh}, T_{sh} and K_{sh} with a gain C_{sh} to be determined) will be included. These matrices are evaluated starting from the model G_0 based on the pre-programmed plasma equilibrium for the shot, discussed in detail in Sec. 4.5.

4.4.1 Position controller tuning

The plasma position controller K_{zr} involves proportional-derivative (PD) feedback on the vertical position and proportional control on the radial position observers as described in Sec. 2.4.3. The main advantage of the decoupled position controller is that it maintains the same structure of the standard magnetic control, allowing a simple first guess for the tuning of the position controller using the new directions based on the former gains. Considering the new directions T_z and T_r (several choices are possible as discussed above), the new gains P_z, D_z and P_r are derived from the standard gains as

$$\min_{P_z} \|2\pi I_{px} B_{r,xa} T_z P_z - 2\pi I_{px} B_{r,xa} T_{z,std} P_{z,std}\|_2^2 \tag{4.61}$$

$$\min_{D_z} \|2\pi I_{px} B_{r,xa} T_z D_z - 2\pi I_{px} B_{r,xa} T_{z,std} D_{z,std}\|_2^2 \tag{4.62}$$

$$\min_{P_r} \|2\pi I_{px} B_{z,xa} T_r P_r - 2\pi I_{px} B_{z,xa} T_{z,std} P_{r,std}\|_2^2 \tag{4.63}$$

This means that, given a unitary current flowing in the new coil directions, the gains are computed to generate the same magnetic field modification weighted on the plasma current distribution (in the vertical direction for vertical control and in the radial direction for radial control) as would be generated by the standard gains using the standard directions.

This approach can be considered valid in steady state when plasma positioning is involved but does not consider the full dynamics in particular for the vertical instability for
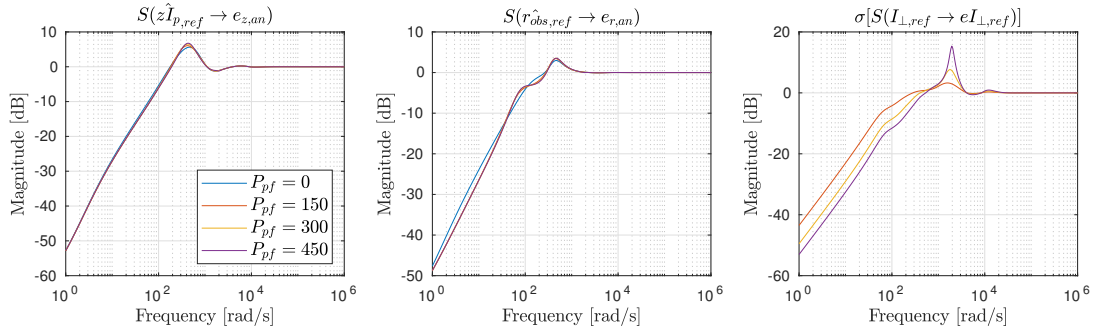
Figure 4.12 – The sensitivities considered for tuning the current controller with different P_{pf}
.

which these gains may not be optimal. The new gains rely on the validity of the gains $P_{z,std}$, $D_{z,std}$ and $P_{r,std}$ provided by the standard controller, which can require extensive tuning for elongated plasmas due to the limits imposed by the vertical instability. Furthermore, the vertical loop including the G coil is not modified in this scheme, maintaining the standard gain $G_{z,std}$. An optimization of the vertical controller tuning, including the choice of directions and the tuning of P_z, D_z and G_z is can be carried out starting from these values as first guess. This is presented in Chapter 5.

The first guess for the position gains presented in this section was used in the experimental tests of the decoupled shape and position controller, which were performed on shots that did not require extensive tuning of the vertical controller.

4.4.2 Coil current controller tuning

Following the derivation of the new position and shape control matrices, the coil combinations orthogonal to T_r and T_z defined by the columns of $T_\perp$ are controlled with a new set of directions. The currents to be controlled for plasma shaping are defined as a vector $I_\perp \in \mathbb{R}^{14}$.

The current controller, which has to be tuned, is a proportional controller $C_{pf} = P_{pf}$ which ensures using the same gain for all coil combinations to be controlled. The mutual decoupling and resistive compensation block $M + R/s$ guarantees the same frequency response and decoupling of all coils in the plasmaless model and the open loop bandwidth is determined by the gain P_{pf} even in the model with plasma. In Fig. 4.12, once the position and the plasma current controllers are closed, the coil current controller gain is progressively increased starting from $P_{pf} = 0$ (i.e. no coil current control) to gradually higher gains. As the bandwidth is increased, little effect is observed in the sensitivities $S(z\hat{I}_{p,ref} \to e_{z,an})$ and $S(r\hat{obs}_{,ref} \to e_{er,an})$ but a progressively larger peak is observed in $S(I_{\perp,ref} \to eI_\perp)$. This peak, which is unavoidable due to the presence of delay and RHP zeros due to the Bode sensitivity integral, indicates poor stability margins when larger than 6 dB. It is found that a gain of $P_{pf} = 150$ provides satisfactory margins and a bandwidth (which corresponds to a tracking speed for a given reference) which is sufficient for the purposes of shape control. It is further noticed that this gain is similar to the one used for
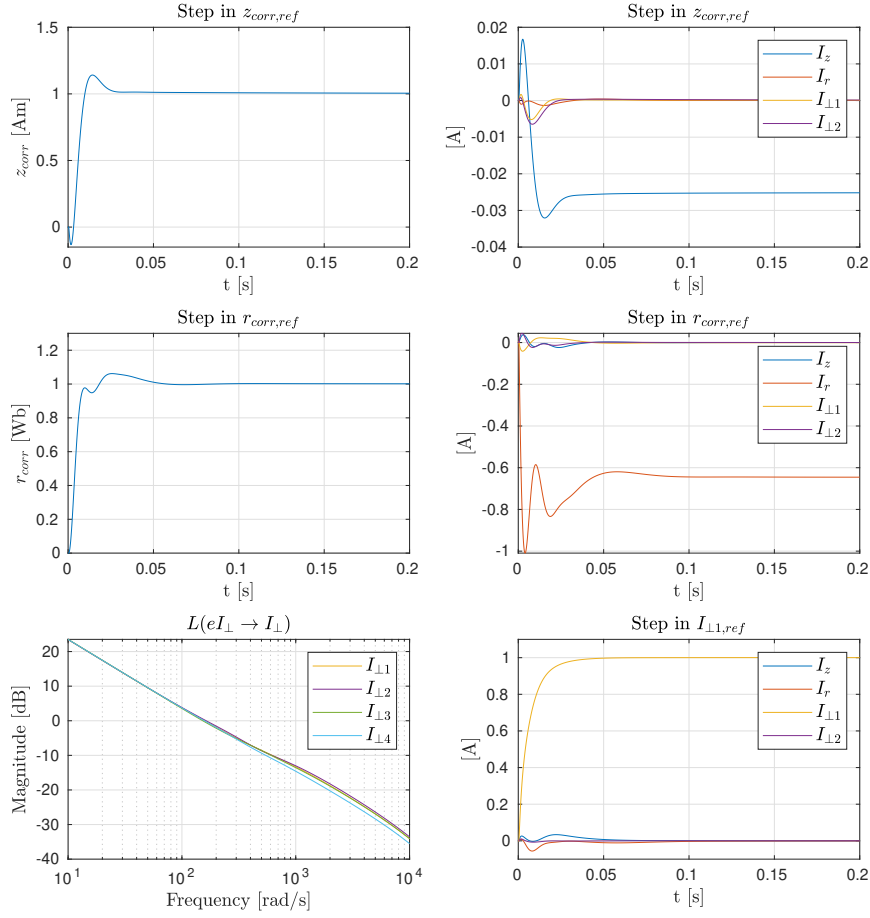
Figure 4.13 – Step of the plant P in closed loop with $[T_z\,T_r]\,K_{rz}$ for position control considering only the analog observers.

the single E coils in standard control.

4.4.3   Simulations of current tracking

The plant P in closed loop with the controller is simulated to test its ability to track the corrected plasma position and study the effects on current reference tracking. Furthermore, the position observers are corrected as represented in Fig. 4.9. In the system step response presented in Fig. 4.13, coil actuation directions T_z and T_r are derived from case C and position and current controllers are tuned as described in the previous subsections.

In Fig. 4.13 one can observe the following

- Reference unitary steps in plasma vertical and radial position reference are correctly tracked.

- In the vertical position reference step, the effects of the RHP zeros in $z_{corr,ref} \to z_{corr}$
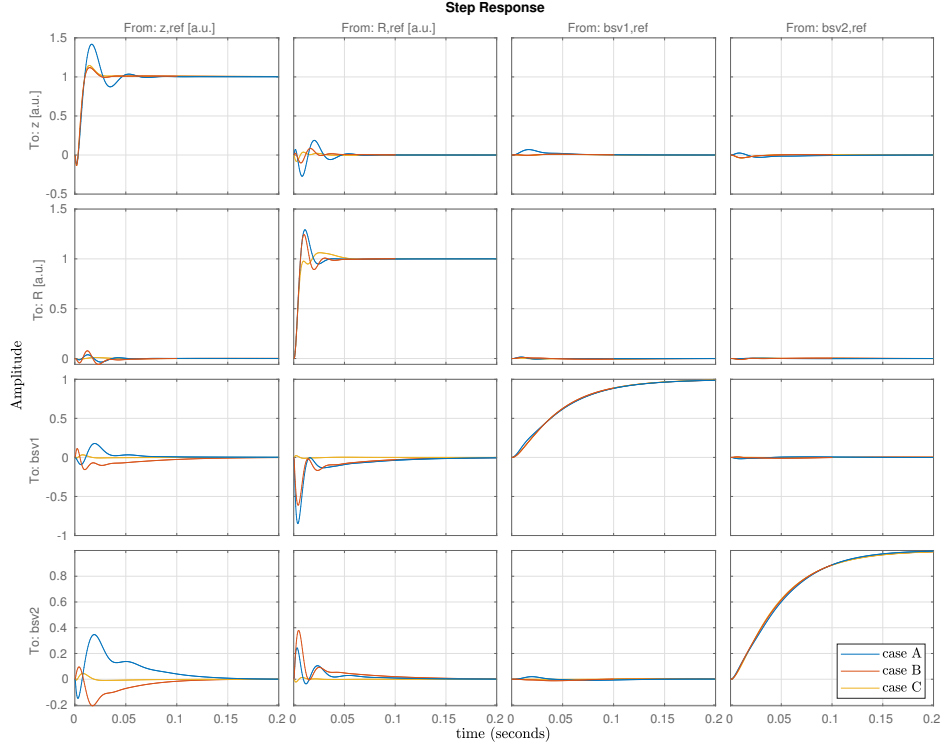
Figure 4.14 – Step comparison of the different cases A B and C. The largest transient amplitude in the off-diagonal terms is for case A, the lowest for case C.

and in $z_{corr,ref} \rightarrow I_z$ are maintained from the open loop with an initial transient opposite response.

- Radial and vertical control loop are exactly decoupled: no corrective current in I_r is required for a step in $z_{corr,ref}$ and vice versa for current I_z due to a step in $r_{corr,ref}$ (this was not true for the standard case of Fig. 4.2 although this effect is low due to the good choice of $T_{z,std}$ and $T_{r,std}$).

- Open loops for coil currents $L(e_{I_\perp \rightarrow I_\perp})$ clearly show the effect of mutual decoupling and resistive compensation and confirm that C_{pf} determines the bandwidth for the coil currents at 150 rad/s.

- A step in $I_{\perp 1,ref}$ is correctly tracked by $I_{\perp 1}$ and does not require corrective currents in I_z and I_r in steady state (compare the standard control case of Fig. 4.2 where this correction was indeed consistent) as the system is correctly decoupled.
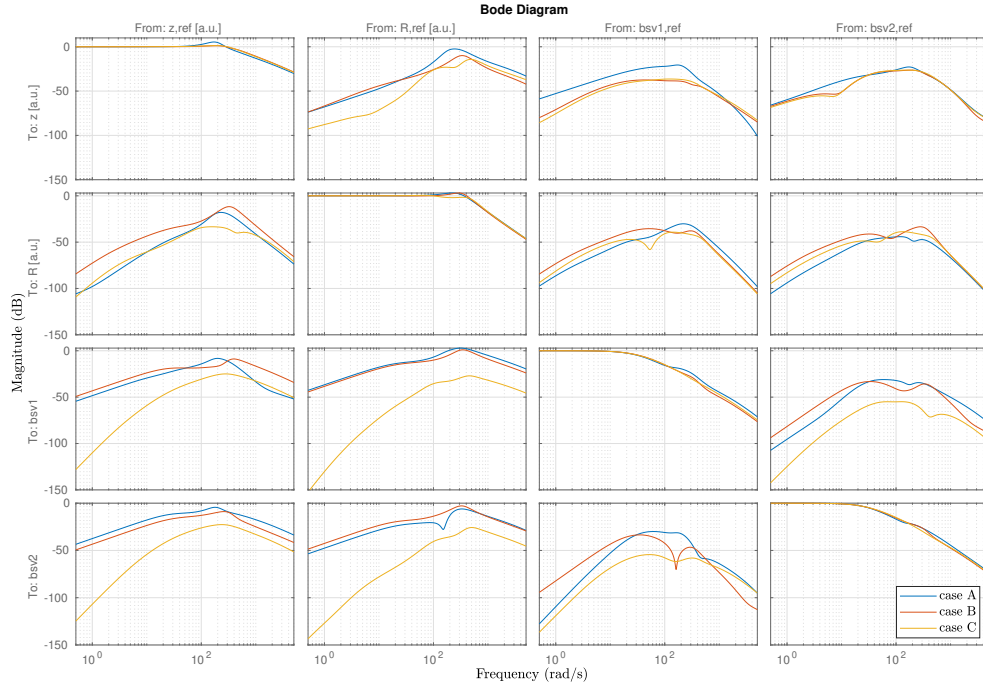
Figure 4.15 – Bode plots for the closed loop of $P_{dec}(s)$ with $K_{sh}(s)$. The transfer functions on the diagonal show exact tracking of the reference up to the bandwidth, the off-diagonal terms show no residual coupling in steady state. The peaks of off-diagonal terms are highest by the bandwidth but never larger than 0 dB.

4.4.4   Simulations of shape control

Comparison of cases

The shape control designed for different cases (A, B and C) is tested in closed loop simulations with the RZIp model.

For all cases, the directions for position control T_r and T_z are derived, the position controller K_{zr} is tuned as described above and the same $C_{pf} = 150$ is used.

The shape controller matrices O_{sh} and T_{sh} are then obtained for the shot and the case as a function of the equilibrium, the control directions used for position control and the observation matrices for position. The controller $K_{sh} = (C_{sh}/s)I^{n_{sh} \times n_{sh}}$ uses $C_{sh} = 20$ and $n_{sh} = 6$ in every case.

The plant P_{dec} is set in closed loop with the shape controller for the channel $u_{sv} \to b_{sv}$. The step responses and the magnitude of the closed loop transfer functions are studied in Fig. 4.14 and 4.15 respectively. In these figures, only a limited number of singular values are shown. Inputs and outputs are scaled to be comparable in magnitude. As the shape parameters are already scaled (see Eq. 2.14), also position references and observers are
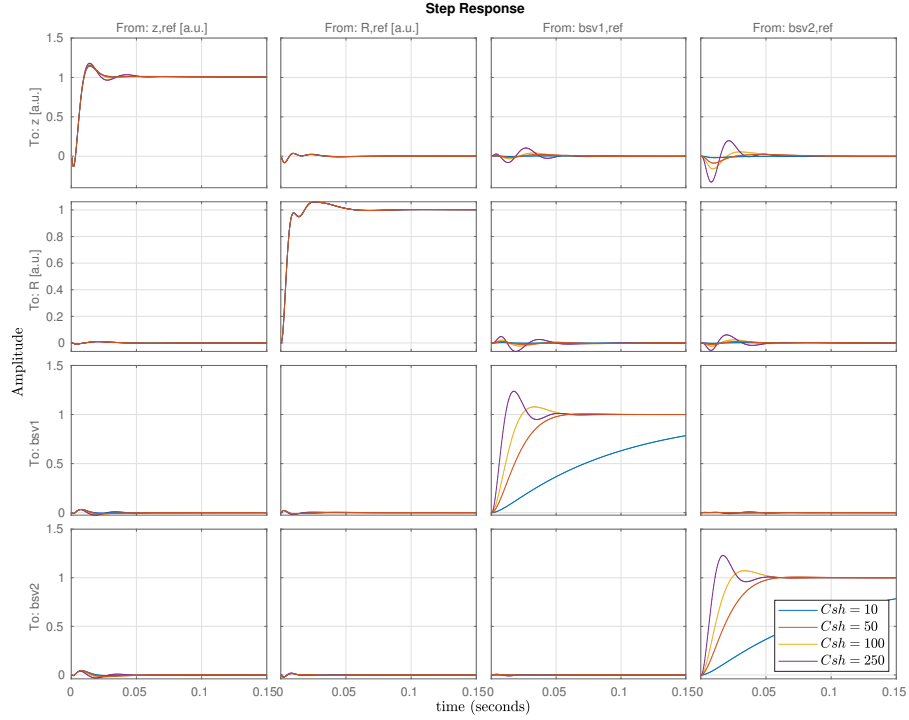
Figure 4.16 – Step comparison for the closed loop with varying gain for the shape controller.

scaled back to dimensionless quantities. This is performed using a matrix

$$
S_{rz} = \begin{bmatrix} \frac{\|M_b(\partial\psi_{eq}/\partial z)\|_2}{|\psi_{ax}|I_{p0}} & \\ & \frac{\|M_b(\partial\psi_{eq}/\partial R)\|_2}{|\psi_{ax}|F_\psi} \end{bmatrix}
\tag{4.64}
$$

multiplying the corrected position observers, and using its inverse to scale the references. One can note that

- The system is correctly decoupled in steady state as each variable tracks the corresponding references and the steady state of off-diagonal transfers is zero.

- The bandwidth, intended here as the frequency at which the complementary sensitivity starts decreasing from 0 dB in the transfer functions along the diagonal, is one order of magnitude different for the position (200 rad/s) and the shape (20 rad/s).

- The peak gain of off-diagonal terms (providing a measure of the largest expected effect on other outputs for a given perturbation) is the largest in most cases for case A and the lowest in all cases for case C.

- The effect (and the advantage) of full decoupling is clearly visible in $[z_{ref}\, r_{ref}] \to b_{sv}$ where the slope at low frequency is 60 dB/dec for case C while for the remaining
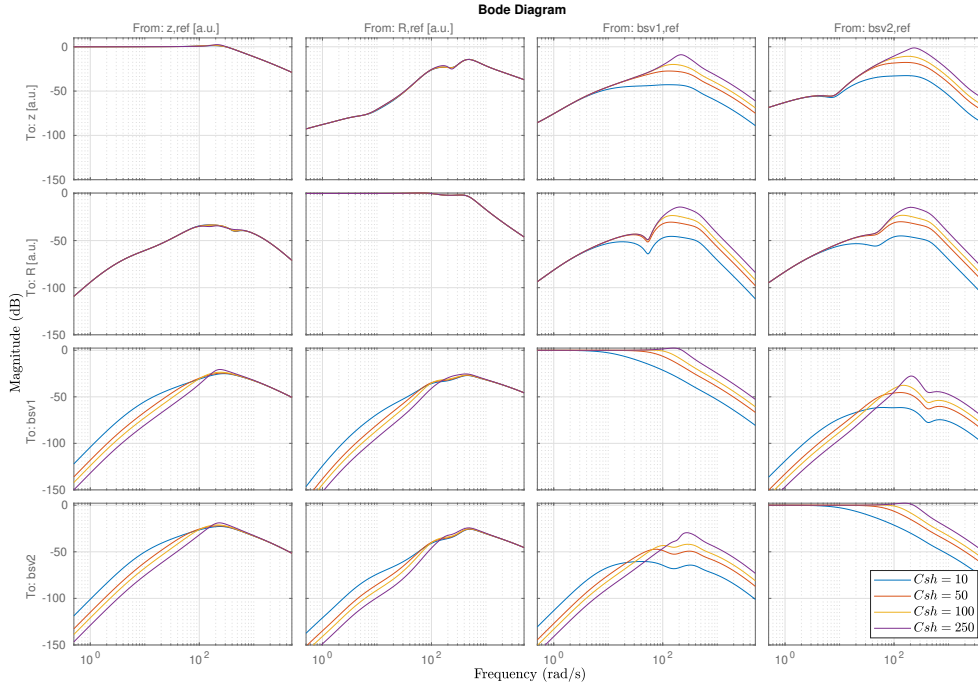
Figure 4.17 – Bode plot magnitude for comparing the effects of different gains used for the shape controller. The benefits of the larger bandwidth for shape control are compensated by the increase in the peak value of off-diagonal terms indicating larger coupling at the bandwidth frequency.

cases A and B is 20 dB/dec and steady state decoupling is only provided by the integrator.

Gain dependence

Considering only case C, which was shown to be the most effective, a simple gain scan for C_{sh} is performed. A higher C_{sh} has several advantages, providing a larger bandwidth and thus a faster response and better rejection disturbance. This however, due to the Bode sensitivity integral, comes with a larger cost in terms of control action and possibly lower stability margin and an increased sensitivity to perturbations. In particular, the controller is designed to be effective in steady state and the coupling which peaks at frequencies around the position bandwidth is enhanced with a larger gain, as it is observed in Fig. 4.16 and 4.17. The transient response, that is expected as soon as the shape control is switched during a shot, can have a large effect on the plasma position to the point where the linearization is not valid anymore or a VDE can be initiated. This effect can be reduced using a proper bumpless transfer. At the same time, an excessively low gain should be avoided since the shape correction ought to be performed on time scales much faster than the shot duration and comparable to the physics of interest (0.1 s). A gain of $C_{sh} = 50$ corresponding to a bandwidth of $w_{sh} = 50$ rad/s leads to an ideal response time
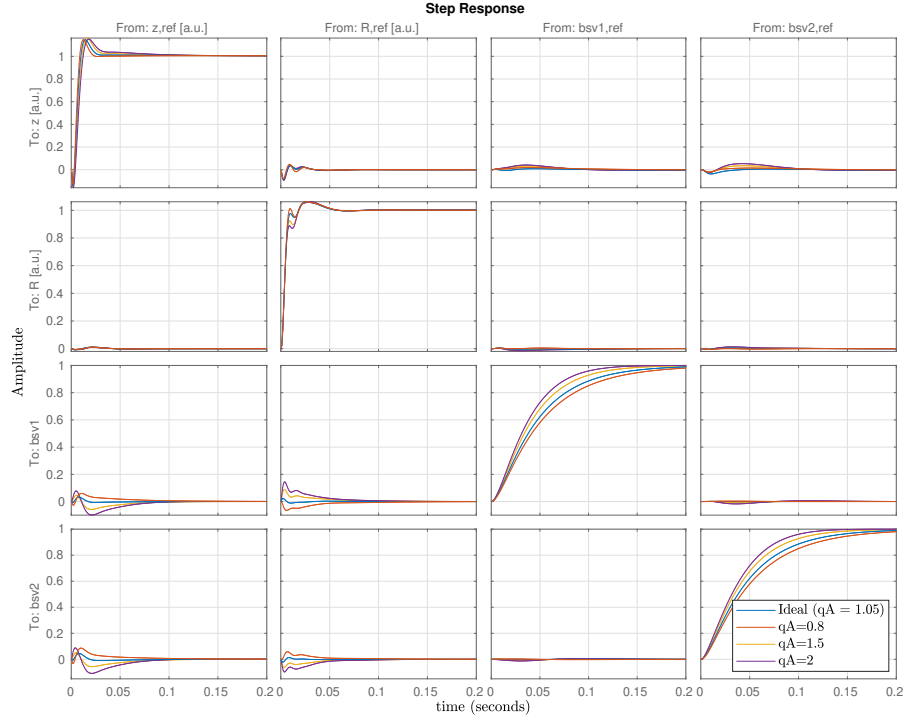
Figure 4.18 – Step response comparison for case C with perturbed q_A resulting in a perturbed plant.

$\tau = 2\pi/w_{sh} = 0.12$ s.

Typically the different problems of plasma stabilization and shape control present themselves on different time scales and a clear frequency separation occurs. In this case, plasma stabilization and positioning should still be performed with a larger bandwidth than the one for shape control in particular for minimizing the transient behavior.

Plant perturbation

In order to validate the approach of case C, a perturbation of both the plant used to model plasma deformation G_0 and the RZIp plant are considered. This is performed perturbing the internal plasma profiles used to define the plasma equilibrium around which the models are linearized. As it will be discussed in the following Sec. 4.5, the plant for plasma deformation is derived from a plasma current distribution which satisfies the Grad-Shafranov equation. The same perturbed current distribution is used to compute the state evolution in the coupled plasma-vessel-coil model RZIp.

Specifically, perturbations in β_p (plasma poloidal beta) and q_A (safety factor at the axis) are considered. In experimental runs, a difference in the actual plasma profiles compared to the expected one is motivated by their internal evolution, which is not treated in the dynamical RZIp model and is a consequence of particle and energy transport and flux
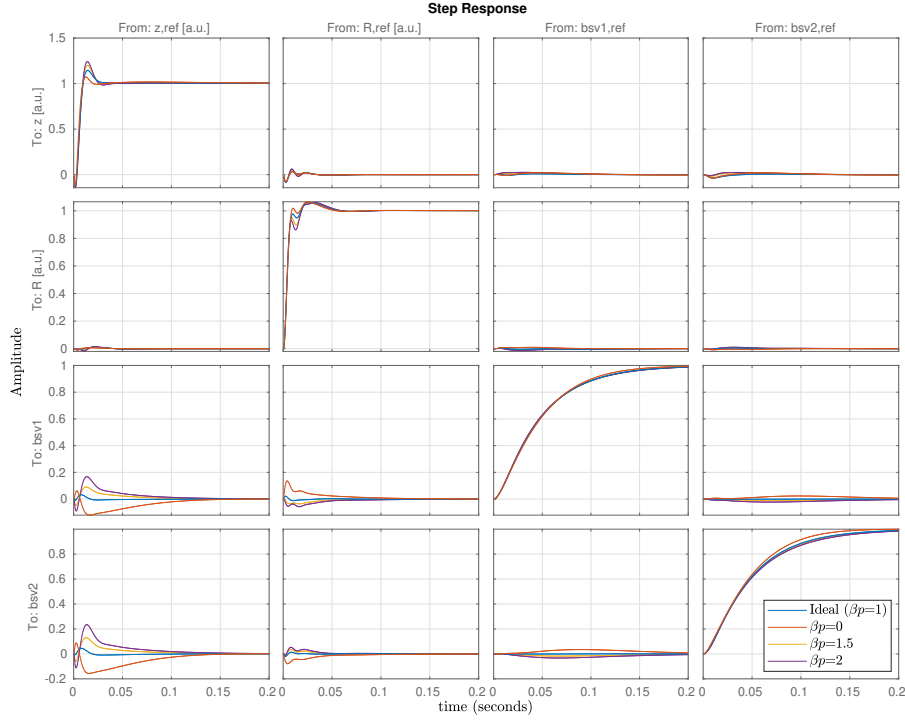
Figure 4.19 – Step response comparison for case C with perturbed β_p resulting in a perturbed plant.

diffusion. Variations in β_p are expected, for example, by variations of confinement (e.g. due to tearing modes) or by variations in external heating. Variations in q_A are instead connected to a variation in the plasma internal inductance ℓ_i which increases with the peaking of the current distribution, moving the current distribution further away from the walls and increasing the vertical instability growth rate. Variations in the plasma q profile arise due to changes in density and temperature profile (affecting the resistivity profile and bootstrap current), due to MHD activity or due to non-inductive current drive (NBI, EC).

The resulting perturbed plant does not correspond exactly to the one used to design the shape controller. It is therefore important to determine what is the consequence on the closed loop dynamics, since observation matrices and actuation directions are computed relying on an inverse-based design. A set of ad-hoc but reasonable values for q_A and β_p are assumed for evaluating the perturbed equilibrium,

$$\beta_p \in [0 \ 1.5 \ 2] \qquad\qquad q_A \in [0.8 \ 1.5 \ 2] \qquad\qquad (4.65)$$

while the original plasma features $\beta_{p0} = 1$ and $q_A = 1.05$. On the lower end, $\beta_p = 0$ is considered as a limiting case with very low plasma pressure. Furthermore, $q_A = 0.8$ is considered as an average value obtained during periodic relaxations expected by sawtooth
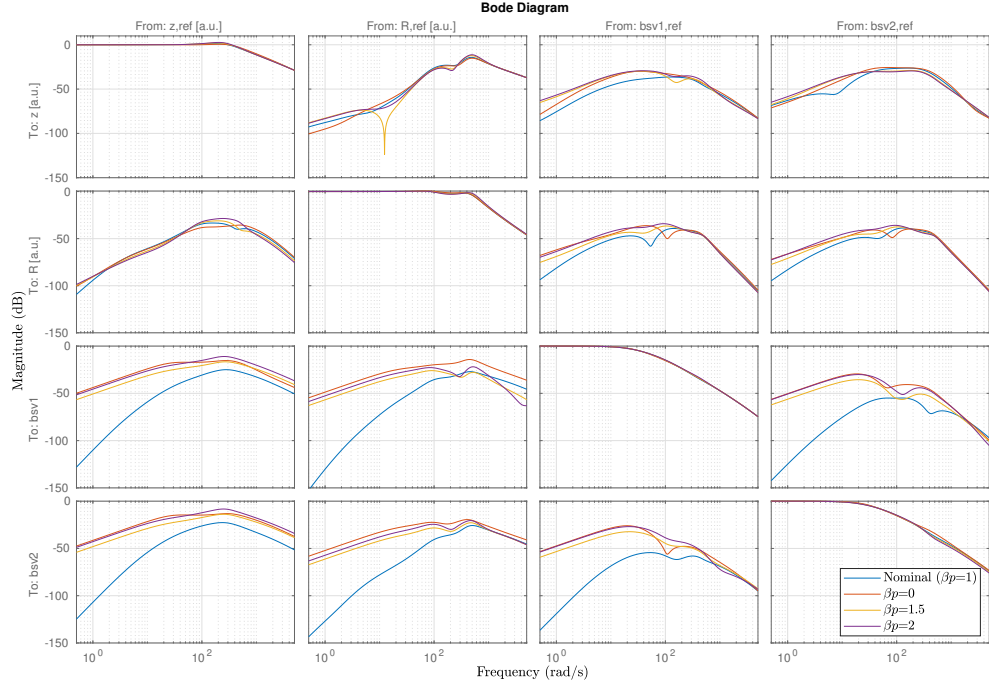
Figure 4.20 − Bode plot magnitude comparison for case C with perturbed β_p resulting in a perturbed plant: worse decoupling is achieved as can be seen by the larger magnitude of the transfer functions compared to the ideal case. .

instabilities.

The decoupled shape and position controller derived for case C is tuned for the nominal case and the RZIp and G_0 plant are perturbed. The perturbation can in principle influence the stability margin of position control. Indeed the unstable pole of RZIp varies with the different q_A and β_p but no instability is triggered. The results are presented in Fig.4.18 and 4.19 for the step responses of the models obtained perturbing q_A and β_p respectively and in Fig.4.21 and 4.20 the closed loop Bode plots are reproduced.

The most noticeable result is that a small variation in the plant due to the perturbation leads to the loss of ideal full decoupling. This is a typical issue of inverse-based controllers [101, p. 93] which are very sensitive to modeling errors. One can see in particular in Fig.4.21 and 4.20 that in almost all off-diagonal transfer functions the slope at low frequency and the peaks increase with respect to the original case. This can be explained by the fact that the decoupling is not exact following the perturbation. Consequently, for example, a variation in the plasma position of the perturbed plant generates an output in the shape observers designed for the ideal plant.

Despite this issue, the controller is still able to stabilize the plasma vertical instability and control the required errors to zero, proving indirectly (but not quantifying) the robustness to plant variations. In particular, the integrator included in the shape controller
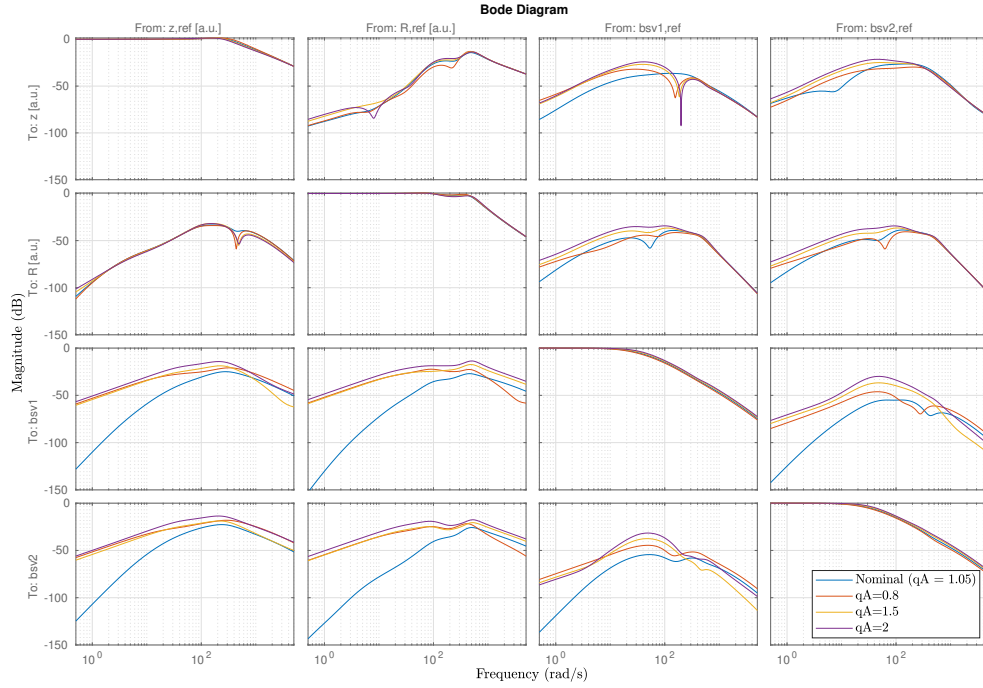
Figure 4.21 – Bode plot magnitude comparison for case C with perturbed q_A resulting in a perturbed plant: worse decoupling is achieved as can be seen by the larger magnitude of the transfer functions compared to the ideal case.

provides the low frequency decoupling such that the slope of off-diagonal transfer functions from $[z_{ref} \; r_{ref}] \rightarrow b_{sv}$ remains at 20 dB/dec.

One can conclude that the presented approach provides a valid way to perform shape control correcting the current reference δI_{ef} as a function of the shape deformation while maintaining plasma position control with the original structure based on providing the input u_{zr} to the mutual decoupling and resistive compensation block.

4.5 Considerations on the model used for shape control design

In this section, the static model used for designing and testing the shape controller is presented and compared with the one that was used for standard shape control design, which considered only the magnetic flux generated by the coils and considered the plasma perturbation at the LCFS negligible.

Although a full nonlinear free-boundary solver could provide a better tool for testing the design of the controller, the RZIp model coupled with a static model for the linearized flux perturbation at the boundary remains a valid approximation for studying the closed loop dynamics. The reason is that this static matrix represent the DC part of a free boundary solver determining the equilibrium modification due to a change in the coil currents.

The design of the shape controller relies on a model for the effect of a perturbative current in the E and F coils resulting in the flux (or magnetic field) variation from the unperturbed equilibrium given by ψ_0. In its linearized form, this is a static matrix

$$G = \frac{\partial \psi(R, z)}{\partial I_{ef}} \tag{4.66}$$

where ψ is the flux at a given point of the numerical grid used for equilibrium reconstruction and I_{ef} is the vector of currents in the E and F coils.

The model used in [79] (from now on referred to as Green's function model) is the static relation based on the assumption that the vacuum field generated by a coil current perturbation $\Delta I_{ef} \in \mathbb{R}^{16}$ dominates the perturbed field, thus the plasma response is ignored when evaluating

$$\tilde{\psi}_{Green}(\Delta I_{ef}) = \psi_0 + \frac{\partial \psi_{Green}}{\partial I_{ef}} \Delta I_{ef}. \tag{4.67}$$

In this case G can be simply computed with a linear combination of geometrical Green's functions providing the magnetic flux in a point (R, z) of the computational domain from a current flowing toroidally in the location of a specific coil.

The latter (from now on referred to as GS model) includes instead the plasma modified equilibrium in the perturbed flux

$$\tilde{\psi}_{GS}(\Delta I_{ef}) = \psi_0 + \frac{\partial \psi_{GS}}{\partial I_{ef}} \Delta I_{ef}. \tag{4.68}$$

In this case G will be computed from a Grad-Shafranov equilibrium where the boundary condition for obtaining the equilibrium flux solving the Grad-Shafranov equation includes both the unperturbed coil PF coil currents $I_{a,0}$ and the perturbation ΔI_{ef}.

Both models can be derived as follows.

The forward (nonlinear) Grad-Shafranov equation can be solved with known p', TT'
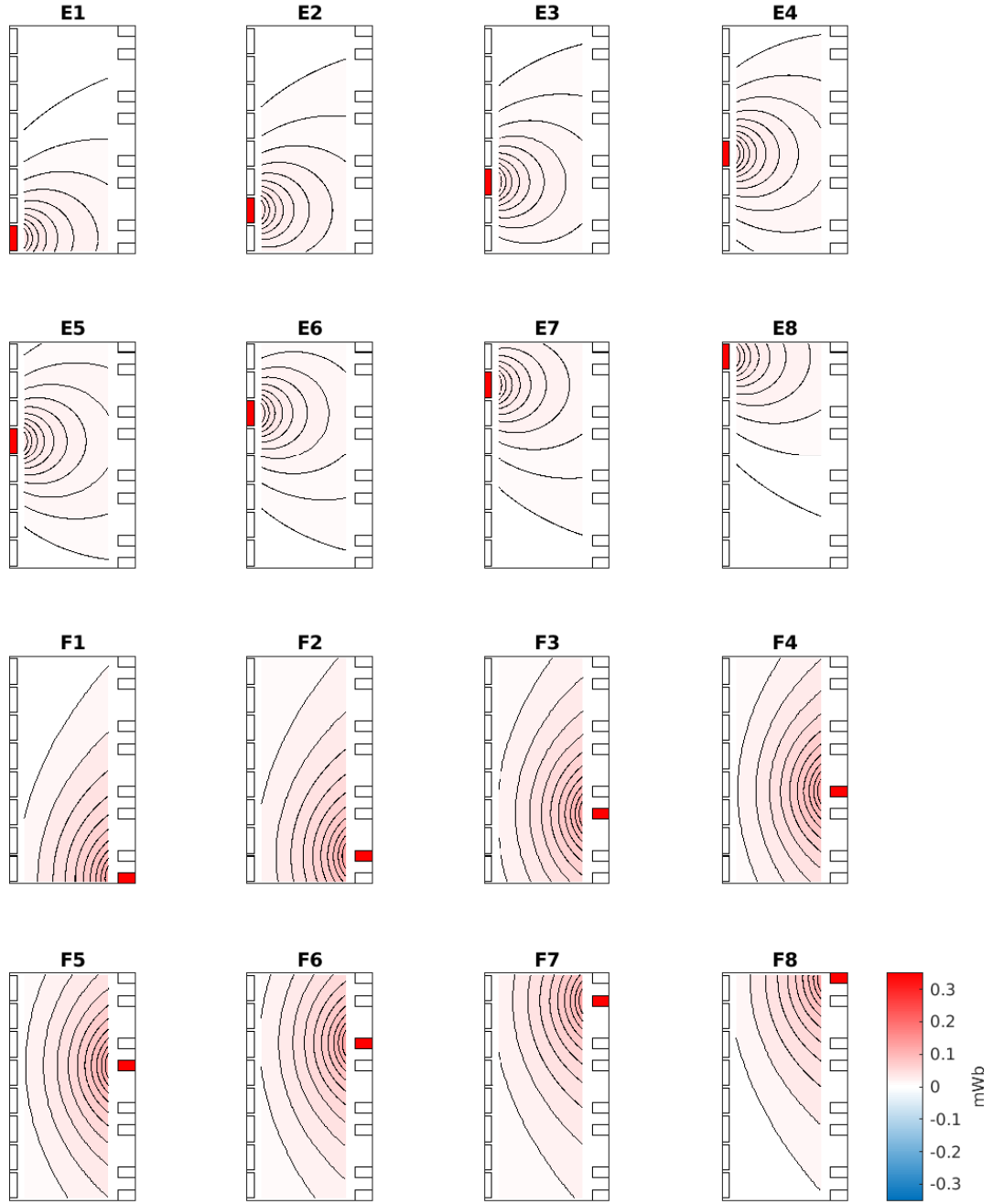
Figure 4.22 − Flux perturbation $(\partial\psi/\partial I_{ef})\Delta I_{ef}$ in the computational domain (R, z) used for equilibrium reconstruction deriving from 1 A current flowing in each E and F coil as predicted by the Green model.
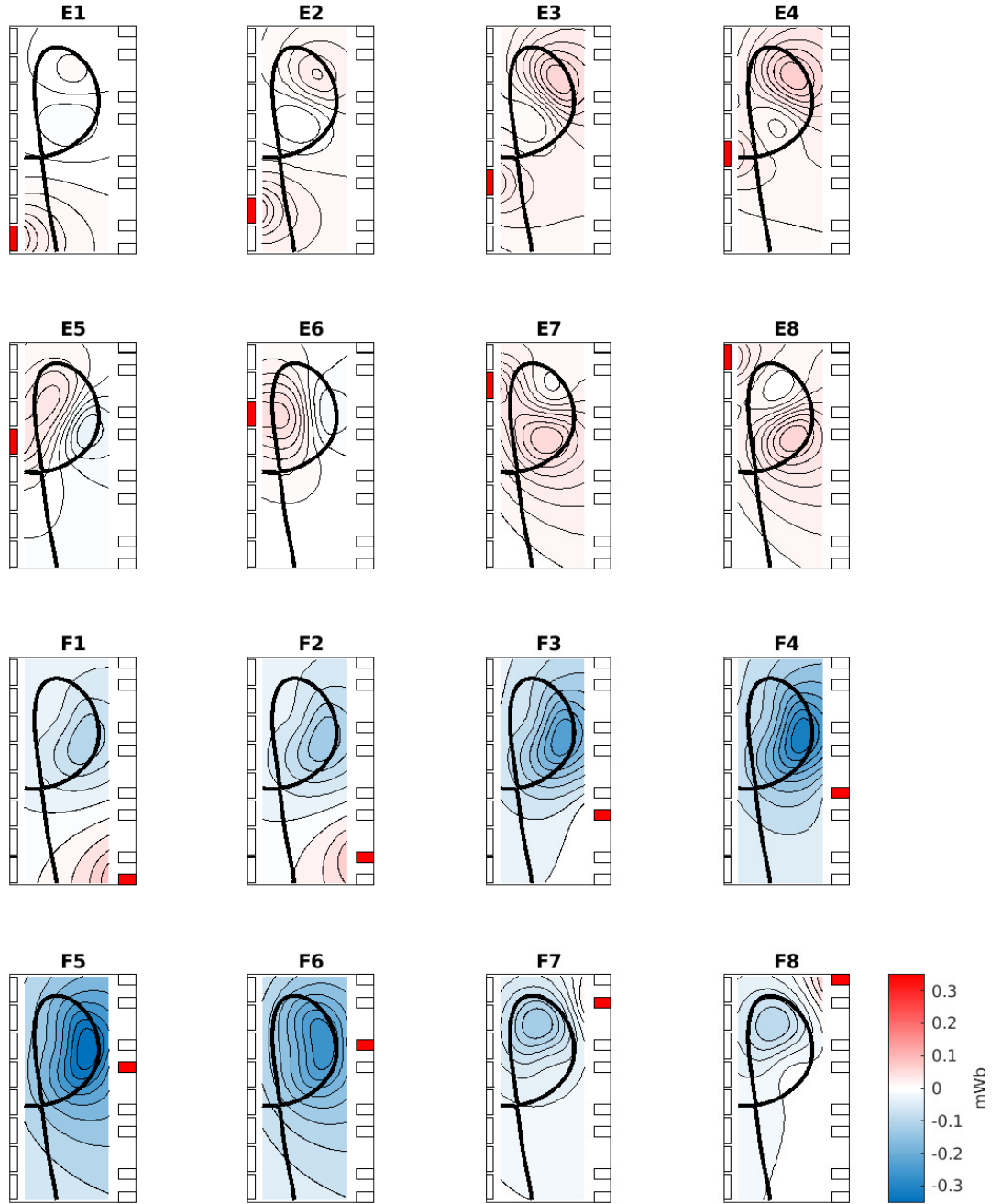
Figure 4.23 – Flux perturbation $(\partial\psi/\partial I_{ef})\Delta I_{ef}$ in the computational domain (R, z) used for equilibrium reconstruction deriving from 1 A current flowing in each E and F coil as predicted by the linearized Grad-Shafranov (GS) model for shot #65299. The LCFS of the pre-programmed equilibrium is included (in black) highlighting the difference compared to the Green's function model by the core plasma region.

and external currents I_a so that we get the nominal equilibrium

$$\psi_0(R, Z) = \psi(p', TT', I_{a0}).$$ (4.69)

where p' and TT' are the functions determining internal plasma profiles (see Appendix A).

The Green's function model considers a perturbation in the coil current ignoring the effects on the plasma

$$\psi_{Green} = \psi(p', TT', I_{a0}) + M_{ef}\Delta I_{ef}$$ (4.70)

with $M_{ef}(R, Z)$ the vacuum Green's functions relating currents in the E/F coils to the poloidal flux.

The Green's function model is therefore obtained as

$$G^{Green} = \frac{\partial\psi_{Green}}{\partial I_{ef}} = M_{ef}$$ (4.71)

which corresponds exactly to Green's electromagnetic functions in vacuum.

The GS model instead considers the contribution to the flux due to the modified boundary conditions to the Grad-Shafranov equation following a perturbation in the E and F currents as

$$\psi_{GS} = \psi(p', TT', I_{a0} + \Delta I_{ef})$$ (4.72)

and is linearized around the unperturbed equilibrium with a central derivative

$$G^{GS} = \frac{\partial\psi_{GS}}{\partial I_{ef}} = \lim_{\Delta I_{ef} \to 0} \frac{\psi(p', TT', I_{a0} + \Delta I_{ef}) - \psi(p', TT', I_{a0} - \Delta I_{ef})}{2\Delta I_{ef}}$$ (4.73)

which can be easily approximated numerically.

The difference in the two models is evident in the comparison between the flux perturbations $(\partial\psi/\partial I_{ef})\Delta I_{ef}$ obtained for a current in each coil represented in Fig. 4.22 and Fig. 4.23. Note that this clearly shows that the contribution of the plasma is not negligible as it is assumed in the Green model.

A simplified validation of the GS model is presented in Fig. 4.24 for shot #63693. In this figure, the coil current perturbation is selected to obtain a plasma equilibrium displacement using $\Delta I_{ef} = Tu$ with $T \in \mathbb{R}^{16}$ a coil direction and $u \in \mathbb{R}$ the perturbation amplitude. Vertical and radial displacements are obtained selecting respectively as $T_z = T_{sv,z}/||T_{sv,z}||_2$ and $T_r = T_{sv,r}/||T_{sv,r}||_2$ from Eq. (4.50), corresponding to the optimal vertical and radial actuation directions derived using the GS model for case C. The perturbation u is increased progressively. As expected, the GS model is valid only in the proximity of the linearization point: the more u is increased, the more nonlinear effects prevail and the linearized solution is no longer a valid approximation of the full Grad-Shafranov equation. The amplitude of the perturbation for which the linearized solution remains locally valid is fit for linear control design, as the limit of 5 cm for initiating a VDE in TCV [112] should be never reached.
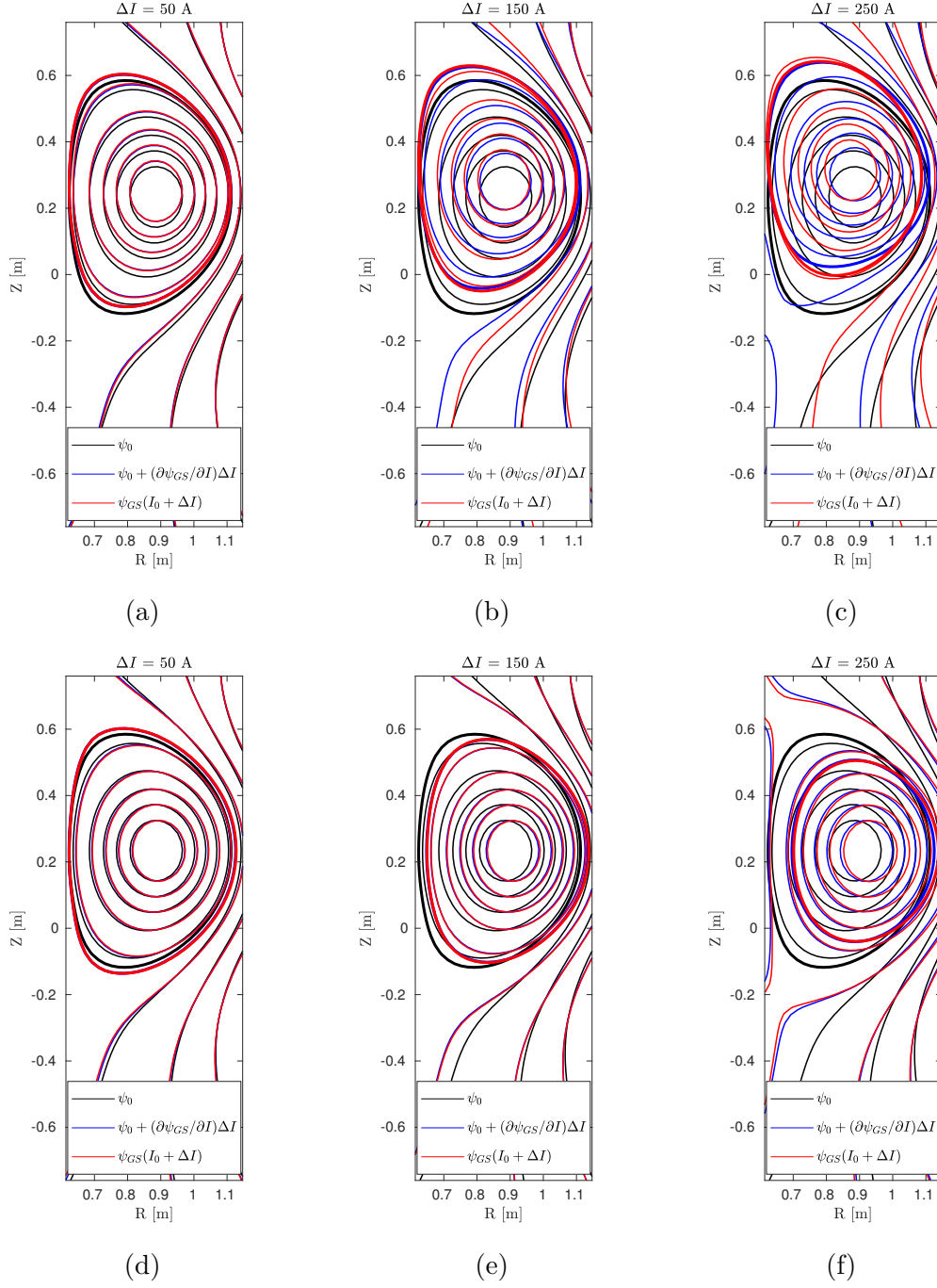
Figure 4.24 − Validation of the GS model using T_z and increasing u in (a), (b) and (c), showing progressively larger vertical displacements of the equilibrium, or T_r with increasing u in (d), (e) and (f), showing progressively larger radial displacements until the plasma moves from limited on the HFS to limited on the LFS. It is observed that the amplitude of the current perturbation (hundreds of Amperes) and the corresponding plasma displacement (several cm) at which the linearized GS model is not able to predict the results of the nonlinear Grad-Shafranov equation are larger than the values expected to be observed during a shape controlled shot.

4.5.1   Model comparison through vertical and radial displacements

The Green and GS models are compared considering the effect on a static equilibrium ψ_0 for the shot #63693 with $I_p = -120$ kA of a current ΔI_{ef} in the directions T_z and T_r. A constant current in these directions results in a displacement of the plasma equilibrium position. The results are reproduced in Fig 4.25.a and 4.25.d illustrating the effects on the LCFS in particular, which is the flux surface considered for shape control.

One can observe that a perturbation in the same coil current direction generates opposite results using T_z and similar results using T_r with the two models. This can be interpreted through the fact that the two models make different assumptions on the plasma behavior following a perturbation in the coil currents and it was observed also in [102]. Furthermore, it will be computed that, in order to obtain comparable displacements, the current used for the Green's function model is much larger than the one used for the GS model. Finally, only the GS model is coherent with equilibrium displacements predicted by the RZIp model as they are both derived from the plasma force balance. Consequently, when the flux perturbation model is combined with RZIp to design the shape and position controller, only a design performed using the GS model allows a consistent correction at low frequency of the position observers.

Green's function model predicted displacements
The Green's function model considers the perturbed flux

$$\tilde{\psi}_{Green} = \psi_0 + \frac{\partial \psi_{Green}}{\partial I_{ef}} \Delta I_{ef} = \psi_0 + M_{ef}\, Tu \tag{4.74}$$

where $T \in \mathbb{R}^{16}$ is a generic coil current combination. When $T = T_z$, the corresponding static coil current perturbation generates a vacuum magnetic field perturbation with a dominating radial component $B_R(T_z u)$, while for $T = T_r$ it generates vacuum magnetic field perturbation with a dominating vertical component $B_z(T_r u)$. Consequently one approximately has for the coil directions represented in Fig 4.25.a and 4.25.d and $u > 0$ at the magnetic axis (R_0, z_0) the following

$$B_R(T_z u)|_{(R_0,z_0)} < 0 \rightarrow \left.\frac{\partial \psi_v(T_z u)}{\partial z}\right|_{(R_0,z_0)} < 0 \tag{4.75}$$

$$B_z(T_r u)|_{(R_0,z_0)} < 0 \rightarrow \left.\frac{\partial \psi_v(T_z u)}{\partial R}\right|_{(R_0,z_0)} < 0 \tag{4.76}$$

from the relation between magnetic flux and field. The effects on the perturbed equilibrium are clear on the sketches presented in Fig 4.25.b and 4.25.e. In these figures, following the Green's function model, the displacement of the unperturbed plasma described by ψ_0 combined with the addition of the externally generated magnetic field due to Tu can be visualized when the flux distributions ψ_0, $\psi_v(Tu)$ and $\tilde{\psi}$ are projected along the vertical and radial axes. The direction of the displacements considered by the Green's function model is consistent with the direction of the Lorentz force that is exerted on a current

flowing in the same direction of the plasma current I_p by a magnetic field generated by Tu but the resulting flux distribution is not a Grad-Shafranov equilibrium. In particular, for the used directions and $u > 0$ one gets

$$\Delta z(T_z u) < 0$$
$$\Delta R(T_r u) > 0$$

GS model predicted displacements

The GS model is derived from the Grad-Shafranov equation which includes the plasma response via the MHD force balance. The perturbed flux in this case

$$\tilde{\psi}_{GS} = \psi_0 + \frac{\partial \psi_{GS}}{\partial I_{ef}} \Delta I_{ef} \approx \psi_{GS}(p', TT', I_{a0} + \Delta I_{ef}) \tag{4.77}$$

where the last term is the actual solution of the Grad-Shafranov equation for modified boundary conditions.

The direction of the displacements of the perturbed equilibrium can be interpreted using the same force balance used in the simplified single filament model of Eq. (3.1). In this model, the vertical force balance for a toroidal current filament in an external magnetic field described in a toroidal reference frame

$$F_z = -2\pi R B_R I_p = 0. \tag{4.78}$$

Its linearization around z_0 and B_{R0} to find a new equilibrium position reads

$$0 = \frac{\partial F_z}{\partial z}\Delta z + \frac{\partial F_z}{\partial B_R}B_R(T_z u) = -2\pi R_0 \frac{\partial B_R}{\partial z}I_{p0}\Delta z - 2\pi R_0 I_{p0}B_R(T_z u) \tag{4.79}$$

in the assumption that an approximately constant $B_R(T_z u)$ is added uniformly along z and that I_{p0} is constant for a vertical displacement. The partial derivatives are evaluated at the unperturbed equilibrium position of the filament for $u = 0$. Recalling the results obtained from the single filament model, an elongated plasma requires the decay index of the vertical field along R to be $n < 0$ where from Eq. (3.11) one gets

$$n = -\frac{R_0}{B_{z,0}}\frac{\partial B_R}{\partial Z}. \tag{4.80}$$

Following the radial force balance of Eq. (3.2), for the plasma current of #63693 the external equilibrium vertical field for compensating the radially expanding forces is $B_{z,0} > 0$ while the field variation at the axis for elongating the plasma ensures that $\partial B_R/\partial z > 0$. The unperturbed vertical equilibrium position is defined at z_0 where $B_{R,0}(z_0) = 0$. It is then straightforward to consider that the new (unstable) equilibrium position lies at $z(T_z u)$
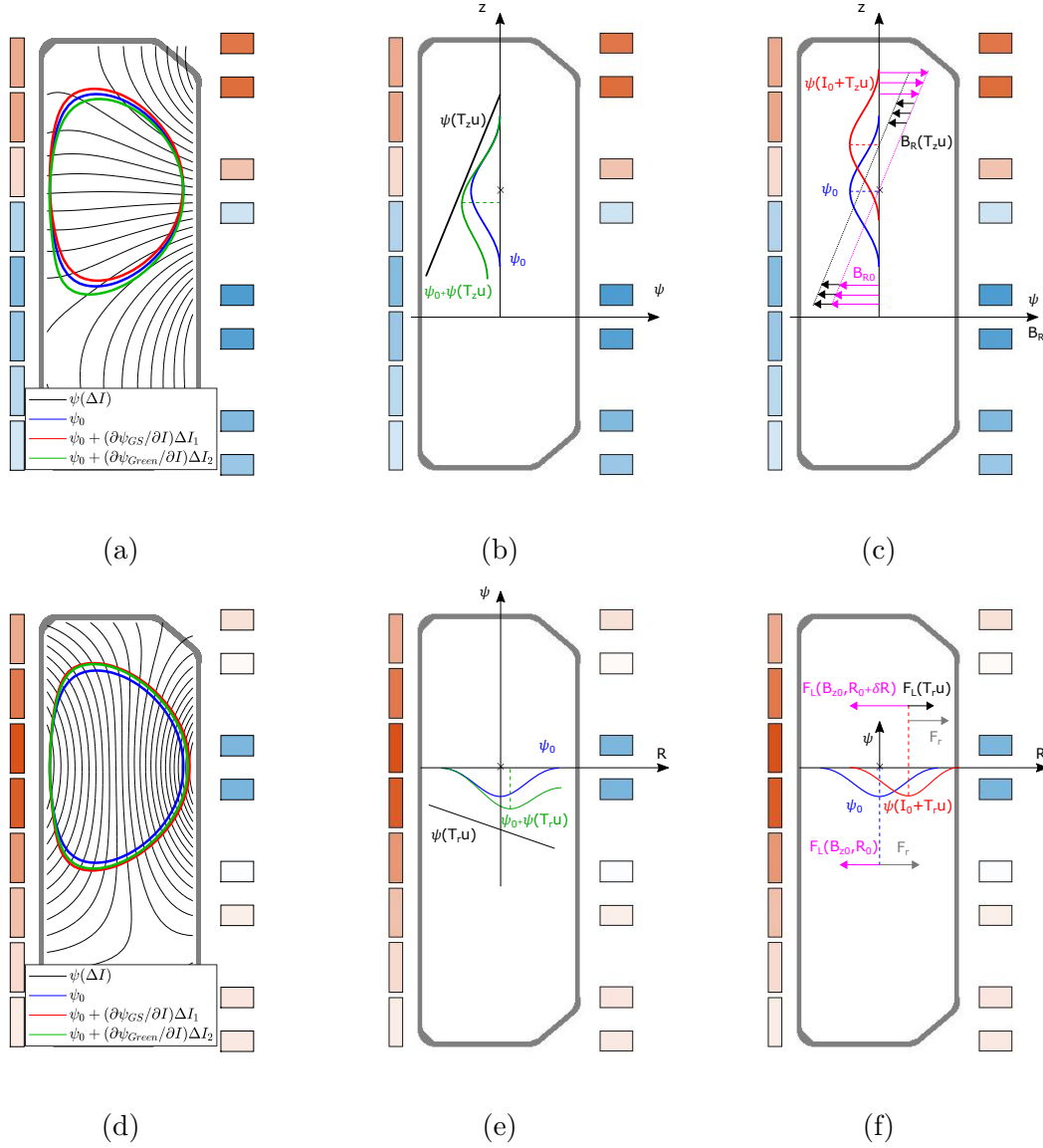
Figure 4.25 – Displacements generated by a constant current in the T_z and T_r directions using the GS and Green model and sketches for their motivation. The equilibrium is for #63693 at flattop with $I_p = -120$ kA. The coils are color-coded with darker red for positive and darker blue for negative currents in a (R, ϕ, z) reference frame. (a) Vertical displacement for a current $|\Delta I_1| = |T_z u_1| = 50$ A using the GS model and $|\Delta I_2| = |T_z u_2| = 150$ A using the Green model. (b) Sketch of the projection along z of the magnetic fluxes used to evaluate the vertical displacement predicted by the Green model. (c) Sketch of the projection along z of the fluxes and the magnetic fields to motivate the displacements predicted by the GS model using the single filament model. (d) Radial displacement for a current $|\Delta I_1| = |T_r u_1| = 75$ A using the GS model and $|\Delta I_2| = |T_r u_2| = 225$ A using the Green model. (e) Sketch of the projection along R of the magnetic fluxes used to evaluate the radial displacement predicted by the Green model. (f) Sketch of the projection along R of the forces acting on the single filament model used to motivate the direction for the radial displacement predicted by the GS model using $u > 0$.

where the radial magnetic field due to external conductors is zero, such that, for $u > 0$

$$\Delta z = z(T_z u) - z_0 = -\frac{\partial F_z/\partial B_R}{\partial F_z/\partial z} B_R(T_z u) = -\frac{1}{\partial B_R/\partial z} B_R(T_z u) > 0. \tag{4.81}$$

since $B_R(T_z u) < 0$ (see Fig. 4.25.a). In the sketch of Fig. 4.25.c it is clear how the addition of a uniform $B_R(T_z u)$ generates a displacement of the vertical equilibrium position where the vertical force balance is satisfied.

The radial displacement instead can be derived from the radial force balance of Eq. (3.2)

$$F_R = F_L + F_r = +2\pi R B_z I_p + \frac{1}{2}\mu_0 I_p^2 \Gamma = 0 \tag{4.82}$$

where F_L is the Lorentz force and F_r is the combination of Hoop and tire tube force sketched in Fig 4.25.f always expanding the plasma in the positive radial direction. The linearization around R_0 and B_{z0} is provided for estimating the new radial equilibrium position and reads

$$F_R = \frac{\partial F_R}{\partial R}\Delta R + \frac{\partial F_R}{\partial B_z} B_z(T_r u) \tag{4.83}$$

$$= \left[2\pi B_{z0} I_{p0} + 2\pi R_0 \frac{\partial B_z}{\partial R} I_{p0} + 2\pi R_0 B_{z0} \frac{\partial I_p}{\partial R} \right. \tag{4.84}$$

$$\left. + \frac{1}{2}\mu_0 \frac{\partial(I_p^2 \Gamma)}{\partial R} \right] \Delta R + 2\pi R_0 I_{p0} B_z(T_r u) \tag{4.85}$$

$$\approx 2\pi I_{p0} B_{z0} \left(\frac{3}{2} - n \right) \Delta R + 2\pi R_0 I_{p0} B_z(T_r u) \tag{4.86}$$

where the approximation is valid for a radial displacement conserving the flux enclosed by the filament and $\Gamma \gg 1$ as discussed in [12], [120]. Here it was also assumed that an approximately constant $B_z(T_r u)$ is added uniformly along R. Consequently the new radial equilibrium position (stable for $n < 0$) lies at $R(T_r u)$ where the force balance is satisfied, such that for $u > 0$

$$\Delta R = R(T_r u) - R_0 = -\frac{\partial F_R/\partial B_z}{\partial F_R/\partial R} B_z(T_r u) = -\frac{R_0/B_{z0}}{(3/2 - n)} B_z(T_r u) > 0 \tag{4.87}$$

since $B_z(T_r u) < 0$ (see Fig. 4.25.c). In Fig. 4.25.f, a sketch is provided showing the new force equilibrium leading to a displacement in R following the perturbation with a magnetic field $B_z(T_r u)$.

4.5.2 Static and dynamic comparison with RZIp

An estimate for the vertical and radial displacements can be provided in comparison with the results from RZIp. Indeed, the model contains the radial and vertical force balance corresponding to the linearized projections along the vertical and radial axes of the force balance equation $\mathbf{J} \times \mathbf{B} = \nabla p$ used for deriving the Grad-Shafranov equation (see also Eq. (A.3)).

The estimated displacement of the LCFS following a variation in the coil currents is given as

$$\Delta z = O_{\Delta z} \left[M_b \; 0 \; 0 \right] G_0 T_z u \tag{4.88}$$

$$\Delta R = O_{\Delta R} \left[M_b \; 0 \; 0 \right] G_0 T_r u \tag{4.89}$$

where G_0 considers the interpolation of the outputs of G at the target boundary points and $O_{\Delta z}$ and $O_{\Delta z}$ combine the flux differences for an estimate of the displacement as described by Eq. (2.10) and 2.11.

The vertical and radial displacements of the plasma centroid in the RZIp model due to the same variation of the coil current are instead computed from the linearized force balance as

$$\Delta z_C = -\frac{\partial F_z / \partial I_{ef}}{\partial F_z / \partial z} T_z u = -\frac{1}{I_{p0}} M_{22}^{-1} M_{21}^{ef} T_z u \tag{4.90}$$

$$\Delta r_C = -\frac{\partial F_R / \partial I_{ef}}{\partial F_R / \partial R} T_r u = -\frac{1}{I_{p0}} M_{33}^{-1} M_{31}^{ef} T_r u \tag{4.91}$$

where the details of RZIp matrices M_{21}^{ef}, M_{22}, M_{31}^{ef} and M_{33} are provided in Appendix B.2.1. In particular M_{21}^{ef}, and M_{31}^{ef} consider only the part of the vector M_{21} and M_{31} multiplying the E and F coil currents.

The results of the comparison are summarized in the following Fig. 4.26 for varying u. One can observe that the GS equilibrium displacement and the RZIp force balance give comparable results both in terms of direction and amplitude of the displacement, although with an increasing difference for larger perturbations as they are linear relationships. The Green's function model instead, consistently with the simplified analysis on the single filament model discussed in Sec. 4.5.1 , predicts the wrong direction for the vertical displacement and does not provide a comparable amplitude even for the radial displacement.

A dynamical comparison is finally provided by coupling the models in series as reproduced in Fig. 4.27 with the resulting Bode plots of the open loop transfer function reproduced in Fig. 4.28. In this case, matrices O_z and O_r are the ones derived from case C providing the decoupled observation directions. It is important to note that, although the approximation of the static model G is valid only in steady state, the phase loss at frequency comparable to the expected bandwidth (10^2 rad/s), present also in standard equilibrium reconstruction due to the computational delay, can be avoided when correcting the rt observer with their analog counterpart. Recall that the SISO open loop for vertical
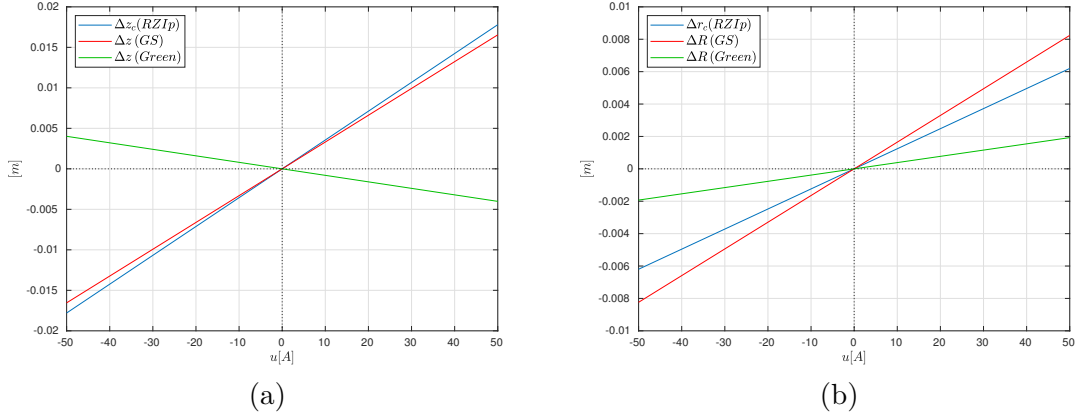
Figure 4.26 – Comparison of equilibrium displacement between RZIp force balance and using the Green and GS model for (a) vertical and (b) radial actuation directions and observers with varying amplitude of the current.
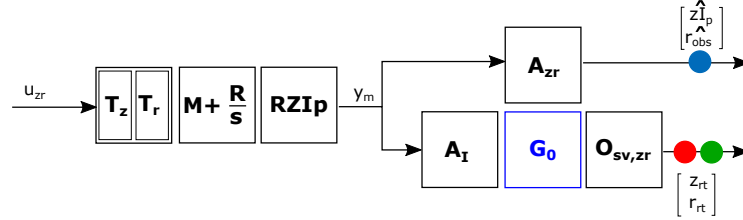
Figure 4.27 – Block scheme, color coded for the plots of Fig. 4.28 . In this open loop, the signal $u_{zr} \in \mathbb{R}^2$ acts along T_z and T_r for vertical and radial control respectively. The unstable RZIp model outputs the magnetic signal y_m, mapped in analog observers with A_{zI} or currents with A_I which determine the equilibrium displacement as $O_{sv}G_0 I_{ef}$.

control cannot be used to determine the closed loop stability since it does not consider the paramount role of the G coil, discussed in the following chapter. In the Bode plot one can notice the difference in phase of the vertical loop for the Green model (due to the opposite sign) and the valid scaling of the real time observer to match the analog only in the case of the GS model. The largely different behavior at high frequency of the real time radial loops compared to the analog is due to the presence of two complex zeros at $z = 1.6 \pm 24i$ rad/s showing their effect at $|z| \approx 24$ rad/s.

It is concluded that the GS model provides a better approximation for the effects of a perturbative current in the E and F coils on the plasma equilibrium than the Green model, in particular for the vertical and radial dynamics. The quantitative agreement with RZIp justifies its use to define the corrections to vertical and radial observer at low frequency.

When using the Green's function model, this difference can result in an incorrect estimate both of the sign and the gain to apply for equalizing real time and analog observers for the position control. This can be seen in Fig. 4.28 where both magnitude and phase at low frequency are consistent only using the GS model

(a) (b)
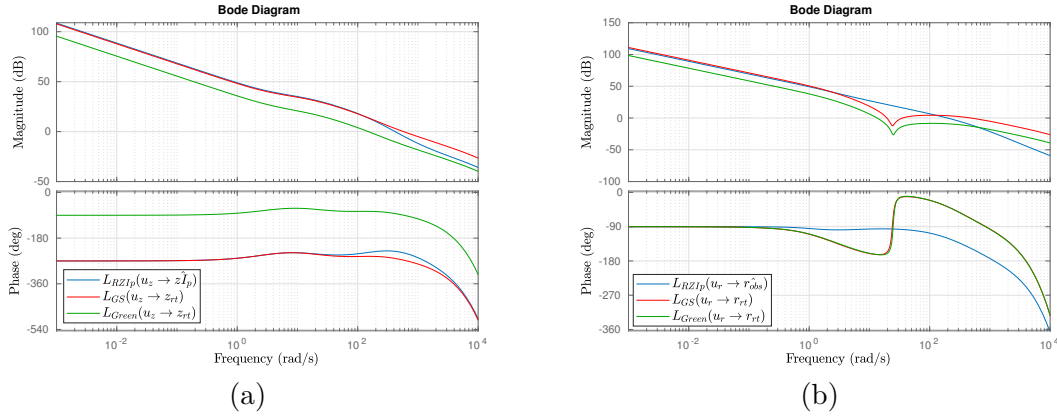
Figure 4.28 – Open loop Bode plot comparison using directions for vertical (a) and radial actuation (b) and the corresponding analog observers from matrix A or equilibrium reconstruction from matrices O_z and O_r. The results are considered for shot #63693 in flattop.

4.6 Conclusions

In this chapter, a new design for the shape controller in TCV is proposed. This is based on the separate tuning of the position controller and leaves the shape controller responsible for modifying the plasma shape only, without attempting to position the plasma column. In order to be consistent with the shape controller, the position observer is modified at low frequency with a signal derived from equilibrium reconstruction, while at high frequency the fast analog observers are used for stabilizing the plasma in closed loop with the position controller. Furthermore, the position controller uses actuation directions which are orthogonal to those used by shape control. This allows a separate tuning of the position controller that will be discussed in the next chapter.

Several cases are presented for deriving the shape and position controller matrices and it is observed that the matrices derived from the standard shape and position controller provide the best steady state decoupling (full decoupling).

A discussion on the model used for shape control is provided, showing that a model derived from a linearization of the perturbed solution of the Grad-Shafranov equation (GS model) is better than the previously used model based on electromagnetic Green's functions in vacuum. The GS model is quantitatively consistent with vertical and radial displacements predicted by the RZIp force balances and its use to correct the plasma position observer at low frequency is justified.

Although a more complete verification requires relying on free-boundary GS models or linearized GS models, one can see that a simpler model (RZIP + static GS) is sufficient for designing a coupled position and shape controller, as it retains the physics of interest.

Possible further improvements to this approach are the following

- The robustness to uncertainty in the model used for shape control design should be quantified to gain better insight on modeling errors that could lead to degraded performance or instability.

- The radial observer could be adapted to consider the inflation/compression predicted by the semirigid model, consistent with the Grad-Shafranov perturbed equilibria, rather than limiting it to a rigid radial displacement.

- The effects of using different models should be quantified in terms of the amplitude of the correction required to the E and F coils currents δI_{EF} to the preprogrammed ones.

- Feedforwards and references should be added to the simulations, in particular to quantify the effects of the fast ramps in the OH coil currents

- A better model could be used in the simulations for equilibrium reconstruction considering the vessel currents as well, thus testing the control loop in closed-loop with an equilibrium vessel current reconstruction code that is valid also during transients.

- A model based on the linearized Grad-Shafranov equation coupled to circuit equations, such as CREATE-L [121] could be used instead of the RZIp model combined with the GS model, providing a finer tool for simulations.

- Free boundary evolution codes such as [122]–[125] could be performed to validate the controller design in more detailed simulations in closed-loop.

The following step, presented in the next chapter, is an optimized tuning of the vertical controller using the new directions for vertical and radial actuation.

5 Optimized vertical control in TCV

In this chapter a new method for designing the vertical position controller is introduced, including the dynamics of the vertical instability as an integral part of the procedure for selecting the coils used for vertical stabilization. In particular, we propose a new design algorithm based on control theory in combination with a linearized model of the plasma vertical instability dynamics and a model for the plasma equilibrium modification following a static perturbation in the coil currents.

This method allows more complete exploitation of the flexibility of the TCV tokamak, allowing all PF coils to be used for vertical stabilization. The method's generality and the automated synthesis algorithm allow in principle the possibility to extend this approach to any shape that can be realized in TCV as long as the model used for controller design remains valid. At the same time, the new controller maintains the structure of the existing vertical control system, allowing a quantitative performance comparison and facilitating its use in standard operation. The objective of the optimization is to preserve the plasma control system performance in terms of operation margins and response time to plasma position disturbances, while reducing the risk of power supply saturation, which from a linear control theory perspective corresponds to minimizing the control sensitivity of the closed loop. This is a critical issue since the saturation of the voltage that a power supply can provide results in the initiation of a vertical displacement event that cannot be corrected in feedback since the coil system then behaves as if in open loop. The new controller was successfully tested experimentally and was proven to stabilize effectively TCV plasma discharges while improving the control performance. This chapter is structured as follows.

In Section 1, a summary of the state of the art for vertical control is provided.

in Section 2, optimized actuation directions for vertical control in TCV are derived.

In Section 3, the vertical controller structure is discussed and the choice of structured $\mathcal{H}_\infty$ is motivated.

In Section 4, the generalized plant used for $\mathcal{H}_\infty$ synthesis is discussed.

In Section 5, the results of controller synthesis are presented.

In Section 6, the controller is validated in dedicated shots on TCV and the performance improvement is quantified.

In Section 7, the conclusions on the optimized vertical stabilization are provided.

The material in this chapter has been submitted for publication in Fusion Sci. Technol.

5.1   State of the art for vertical control

All tokamaks use external and, when available, internal poloidal field coils as actuators for stabilizing and controlling the unstable vertical position of elongated plasmas [40]. In the envisaged vertical control system of ITER the plasma is stabilized with in-vessel coils only [126], although the possibility of employing a set of coils external to the vacuum vessel is also considered, to reduce the RMS value of the current in the internal coils [127]. In a similar fashion, in the ASDEX-Upgrade tokamak [72], the internal coils respond to deviations of the vertical position from equilibrium and a set of external coils react to minimize the time averaged current in the internal coil and control the equilibrium position of the plasma [73]. The EAST tokamak features an ITER-like control system where the in-vessel coil is used to stabilize the vertical instability, by controlling only the plasma vertical velocity to zero together with the internal coil current. In this way, the vertical stabilization and the shape and position control problems are decoupled, with the latter system left in charge of plasma positioning using the external coils as actuators [128]. Different schemes are possible for decoupling, such as the version tested in KSTAR. In its control system, a frequency separation is achieved with lowpass and highpass filters, such that the plasma vertical position and velocity can be directly fed back to the controller for the internal coil voltage, while leaving the vertical control on longer time scales to the external superconducting coils [129]. The JET tokamak, the largest operating device of this kind, features instead no coils internal to the vacuum vessel but stabilizes the vertical instability with a combination of external coils and feedback on the plasma velocity [130], still leaving the exact plasma positioning to the shape controller [74]. The control system of the DIII-D tokamak [131] is designed such that a dedicated set of coils, external to the vessel in this case also, is able to effectively and robustly control the plasma vertical position for the programmed discharges [132] and includes a model based multivariable controller for the shape parameters [133]. Finally in the case of NSTX-U, the plasma discharge is designed such that, during the flattop phase, there is a time scale separation of fast and slow vertical control systems. The vertical position is indirectly controlled on long time scales by the shape controller regulating the position of the upper/lower outer boundary points (and the X-point locations), so that the fast vertical control algorithm only provides stabilizing velocity control using a limited subset of the external coils [77]. Other methods for example for automated PID tuning based only on online plasma measurements [134], have also been explored.

The method we propose in this work studies the possibility to synthesize high-performance vertical controllers directly from models, which allows finding a solution on a simulator tool which is then validated in experiments. In particular, we make use of all 16 available external field coils in combination with the internal coil for vertical stabilization instead of assigning a single direction of a single coil to this task thanks to the unique flexibility of the TCV control system.
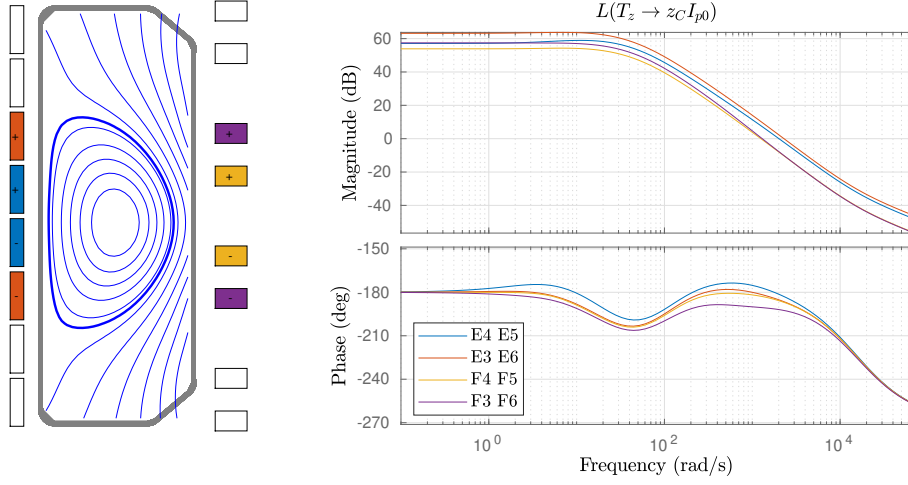
Figure 5.1 − (a) Pair of coils used for the vertical control open loop comparison $L(T_z \rightarrow z_C)$ in $[Am/V]$ with the LCFS of shot #51437 at flattop and (b) the corresponding Bode plots.

5.2 Derivation of the optimal coil combinations for magnetic control

The first step in the presented approach for designing an optimal controller is the redefinition of the coil combinations for magnetic control. This will be based model-based derivation of optimal directions for vertical control, constraining the remaining actuation directions for the RZIp MIMO system $G(s) = C(sI - A)^{-1}B + D$ from Eq. (3.57).

Focusing on position control, the selection of PF coil combinations for vertical control presents several trade-offs due to their different coupling with the unstable plasma dynamics and the different characteristics of their power supplies. The magnetic field used for generating a Lorentz force contributing to the plasma force balance is generated by a current flowing in the PF coils. The field generated by coils external to the vacuum vessel is dynamically shielded by the vessel eddy currents while the one generated by the G coil, internal to the vacuum vessel, is not (see also Sec. 3.2.1) Focusing on vertical control only, the different actuators which can be used make this a MISO (multi-input-single-output) problem, where the controlled output is a vertical position observer, typically $\hat{zI_p}$.

In TCV, the complexity is reduced achieving a lower dimensional MISO problem by using E and F coil combinations for vertical control. These are described with a normalized vector $T_z \in \mathbb{R}^{16}$ in the space of coil directions which multiplies a scalar controller output resulting in a command to each coil. The E and F coils provide both a contribution to plasma stabilization around the bandwidth frequency and positioning on long time scales. The G coil instead is controlled separately in order to guarantee a further degree of flexibility and avoid using it for plasma positioning within the vessel. Its fast switching power supply (FPS) is in fact not designed to sustain continuous current on time scales comparable to the shot duration.

Maintaining this separation makes standard SISO (single-input-single-output) loop shaping techniques not suited for finding an optimal solution, as they are limited to a single channel only. This calls for more advanced techniques for optimizing the controller for this MISO problem. The synthesis of an optimized corresponding SIMO (single-input-multi-output) controller K_z for the vertical instability is the goal of this Chapter.

5.2.1 Comparison of PF coils for vertical control

One of the main steps in the present approach is the selection of coils for vertical control. An introduction to this problem is provided with a simplified analysis which will supports the selection of the vertical actuation direction performed in the following.

The different properties of E and F coils of TCV for vertical control are illustrated in the present section comparing pairs of coils located symmetrically with respect to the vertical plasma axis for shot #51437. Each pair of coils defines a direction $T_z \in \mathbb{R}^{16}$ which actuates the two coils with opposite voltage generating a radial magnetic field in a toroidal reference frame in DC.

The transfer function from a voltage applied along T_z to the plasma vertical position times the plasma current $z_C I_{p0}$ is illustrated in Fig. 5.1.b. One can notice that the transfer functions for the coils located on the HFS (couples $E4$ $E5$ and $E3$ $E6$) are characterized by a larger magnitude and phase than the ones located on the LFS (couples $F4$ $F5$ and $F3$ $F6$). The larger phase in particular is explained by the fact that the magnetic field generated by coils on the LFS is more efficiently shielded by the eddy currents in the vessel [135]. Larger magnitude and phase are advantageous for vertical stabilization as one can consider that lower controller gains are required in a stabilizing controller modifying the open loop, thus reducing the control sensitivity from the reference position to the voltage request to the power supplies.

This advantage is compensated by the fact that the coils on the LFS exert a larger force per Ampere on the plasma, resulting in a larger displacement of the vertical equilibrium position for the same current in steady state. This is computed as in Eq. 4.91, reproduced here

$$\frac{\partial \Delta z_C}{\partial I_{ef}} = -\left(\frac{\partial F_z}{\partial z_C}\right)^{-1} \frac{\partial F_z}{\partial I_{ef}} T_z = -\frac{1}{I_{p0}} M_{22}^{-1} M_{21}^{ef} T_z \tag{5.1}$$

where for the studied cases the results are reported in Table 5.1.

T_z	$\left(\dfrac{\partial \Delta z_C}{\partial I_{ef}}\right) T_z$
E4 E5	35 mm/kA
E3 E6	71 mm/kA
F4 F5	81 mm/kA
F3 F6	122 mm/kA

Table 5.1 – Comparison of equilibrium displacement from RZIp for #51437 at flattop using the different coil combinations illustrated in Fig. 5.1.

(a) $T_{z,std}$ (b) T_{zI} (c) T_{zV}
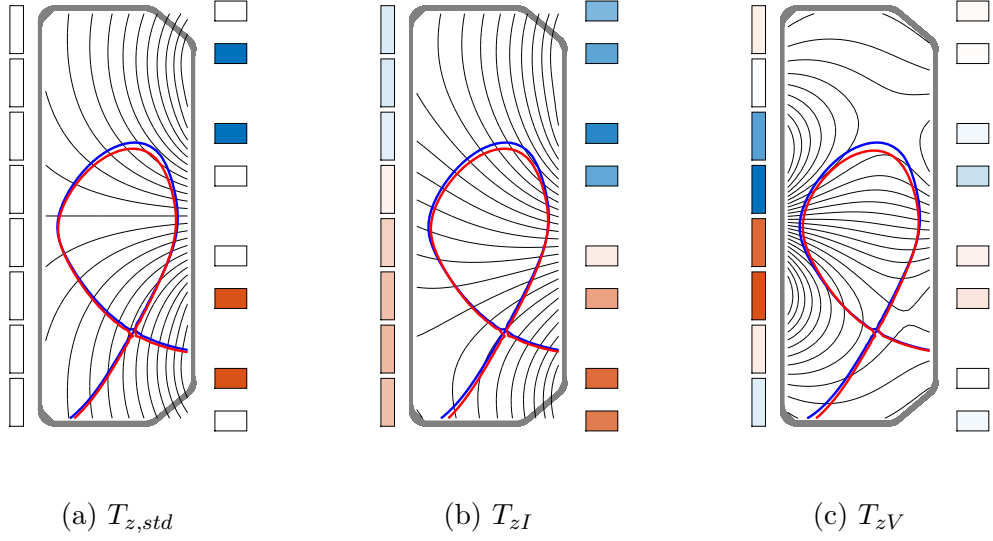
Figure 5.2 – Representation of $\psi(TI_o)$, flux surfaces (black) for the poloidal magnetic field generated in vacuum by a static current I_o flowing in different (normalized) E and F coil combinations $T \in \mathbb{R}^{16}$ used for vertical control. The coils are color coded for each component of the combination indicating positive (dark red) or negative (dark blue) values. The effect on the plasma's preprogrammed last closed flux surface (blue) of shot #68912 at 1 s is computed solving the Grad-Shafranov equation including the perturbative currents TI_o in the boundary conditions and resulting in a new plasma equilibrium (red) whose axis is moved by $\Delta z = -1.5$ cm. The flux is plotted for (a) the standard vertical control direction $T_{z,std}$, (b) the direction used on long time scales derived from the shape controller T_{zI} and (c) the direction used on short time scales derived from the input pole vector T_{zV}.

5.2.2   Directions for control at low frequency

On time scales longer than the vertical instability growth time but shorter than the plasma discharge, directions for position control are derived to satisfy the following requirements

- control the plasma vertical and radial position to a desired reference

- remain orthogonal to the coil current control directions used to control shape deformation by the shape controller

- avoid using the G coil for plasma positioning to avoid DC currents in the FPS.

Following the first two requirements, the directions T_{zI} and T_{rI} for vertical and radial control respectively, are determined with the same algorithm used for shape control [79] discussed in Sec. 4.3.3. In particular, T_{zI} and T_{rI} are the first two columns of T_{sv}, which allow full decoupling in the shape controller.

In this way the coil directions orthogonal to T_{zI} and T_{rI} are defined as

$$N_{pfI} = \text{Im}\left(\text{ker}\left[T_{zI}, \quad T_{rI}\right]\right) \in \mathbb{R}^{16 \times 14}. \tag{5.2}$$

These directions are used for current control in the E and F coils and remain available for the shape controller excluding position control. The steady state flux generated by T_{zI} is represented in Fig. 5.2. In order to avoid current flowing in the G coil in steady state, this is not used for plasma positioning over long timescales.

5.2.3 Direction for control at high frequency

On time scales faster than or comparable to the characteristic vertical instability growth time, vertical control is performed with the goal of input minimization in terms of voltage request to the power supplies. Two separate directions are used, one including the shaping coils external to the vessel $T_{zV} \in \mathbb{R}^{16}$ and one including only the G coil. This distinction is necessary for optimizing the vertical control from the two sets of actuators due to the different nature of the power supplies of internal and external coils. This will result in simply adding a degree of freedom in the optimization without fixing the ratio in the coil usage at high frequency. The choice of direction T_{zV} is based on the following definition of input pole vector.

For an unstable plant, a lower bound exists for the closed loop control sensitivity. This can be explained by the fact that, provided a stabilizing controller, it is always possible to destabilize the system by simply decreasing the controller gain. From a physical point of view, there is a minimum threshold for the voltage to be applied to the coils following a plasma vertical displacement to avoid the initiation of a vertical displacement event. In this study, the control sensitivity estimates the frequency response of the power supplies to a disturbance in the plasma vertical position.

The following theorem quantifies, for a generic MIMO unstable plant $G(s) = B(sI - A)^{-1}C + D$ with a single unstable mode, a useful lower bound for the control sensitivity based on the plant only.

Theorem 1 (Input usage for stabilization [136]). *For a rational plant $G(s)$ with a single unstable mode p, the minimal $\mathcal{H}_\infty$ norm of the transfer function KS is given as*

$$\min_K ||KS||_\infty = \frac{2p\,|q^T t|}{||u_p||_2 ||y_p||_2} \tag{5.3}$$

Here t and q are the right and left eigenvectors of the matrix A satisfying $At = pt$ and $q^T A = q^T p$ respectively while u_p and y_p are defined as the input and output pole vectors of the plant defined as $u_p = B^T q$ and $y_p = Ct$.

It is further specified that the input pole vector, or pole direction, can be obtained from a singular value decomposition of the matrix $G(p) = U \Sigma V^T$, with U and V real matrices for the RZIp model, where the input pole vector is the first column of V corresponding to the only infinite singular value of the unstable RZIp system. Note finally that the choice of inputs and outputs can be performed independently, which allows applying this theory for input selection only. In the present study, the $\mathcal{H}_\infty$ norm of the control sensitivity determines the largest voltage request to the power supplies in any coil combination in response to a plasma position disturbance at any frequency thus should be kept small to

avoid voltage saturation of the power supplies.

For this purpose, the actuation direction for vertical control on fast time scales is defined in the following way. The matrix $B_{EF} \in \mathbb{R}^{n_x \times 16}$ is extracted from the full B matrix of (3.55) with n_x states in order to select the inputs for the E and F coils only, excluding the OH and G coils. The direction for vertical actuation at high frequencies is defined as

$$T_{zV} = M_{EF}^{-1} B_{EF}^T q_u \tag{5.4}$$

where $M_{EF} \in \mathbb{R}^{16 \times 16}$ is the matrix of mutual inductances between the E and F coils and q_u is the only unstable pole vector of (3.55) corresponding to the vertical unstable mode. In this way, at time scales comparable to the vertical instability, the voltage requested from the E and F power supplies following a vertical error e_{zIp} is

$$V_{EF} = (M_{EF} + R_{EF}/s)T_{zV}C_{zV}(s)e_{zIp} \tag{5.5}$$
$$\approx B_{EF}^T q_u C_{zV}(s)e_{zIp} \tag{5.6}$$

where $C_{zV}(s)$ is a SISO controller discussed in Sec. 5.3.1 which is designed to be dominating at high frequencies. This allows minimizing the voltage request to the power supplies required for stabilization, effectively aligning at fast time scales the actuation direction for vertical control with the input pole vector of the RZIp model corresponding to the E and F coils.

5.2.4 Comparison of the different vertical control directions

By acting along the input pole vector, it is expected that using T_{zV} for high frequency vertical control will lead to a reduction of the voltage request to the power supplies in operation. In agreement with previous quantitative evaluations [38] [137] [135], the input pole vector corresponds to a prevailing use of the E coils situated on the high field side as seen in Fig. 5.2, since the generated magnetic field is only weakly shielded by the vessel eddy currents and can thus generate a radial magnetic field on the plasma axis for vertical control faster than the F coils. This observation justifies the use of coils on the high field side for high frequency vertical stabilization as is done in DIII-D discharges [109]. On long time scales, instead, the direction T_{zI} with prevailing use of the F coils should be preferred for plasma positioning due to the larger radial field per Ampère that can be generated on the plasma by the coils on the low field side [135] [109].

The frequency separation of the two actuators, together with the evaluation of closed loop performance, requires the tuning of the vertical controller which is performed in the following sections.

5.3 Synthesis procedure for an optimized vertical controller

Once the actuation directions are constrained, the controller structure selected for magnetic control is defined as a PID controller. In order to apply $\mathcal{H}_\infty$ techniques, a set of performance

requests are specified for constraining the controller synthesis.

5.3.1   Structured $\mathcal{H}_\infty$ and controller structure

Different strategies were considered for model-based synthesis of the SIMO (single-input-mult-output) vertical controller K_z, taking as input the error for the plasma vertical position e_{zIp}. Standard PID manual tuning is the typical approach used on TCV where the gains are defined by the operator, starting from preprogrammed values. The drawback of manually tuning the controller using the new actuation direction is that there is no guarantee of optimality. A possible solution is the derivation of an optimal LQG controller combining a Kalman filter and LQR control, which however provides no guarantee on the stability margins [138] leading to possible poor robustness properties.

Standard $\mathcal{H}_\infty$ control synthesis [139], providing a robust stabilizing controller for a given model, is studied for tokamak control system design, both for position [140]–[144] or shape control [145], [146]. This technique, however, provides controllers whose degree (number of poles) is the same as the one of the model used for the synthesis. In some cases, this leads to high-order controllers, with a difficult realization or complicated interpretation of its dynamical transfer function, compared for example to standard PID controllers. In other cases, the controller synthesis requires a consistent approximation of the dynamics through model reduction. The consequent loss of precision and possible decrease of closed loop robustness ought to be tested with more advanced techniques or directly in an experiment.

The new approach proposed in this work is based on structured $\mathcal{H}_\infty$ [147], extending classical $\mathcal{H}_\infty$ to fixed-structure control systems. The main advantage of this approach is that, regardless of the number of states in the model, the output controller has a structure that can be specified in advance. In the present study in particular, in order to respect the constraints of having no DC currents in the G coil and actuating along a different coil combination only at high frequencies, the following structure for the controller is fixed

$$
\begin{aligned}
C_g(s) &= sG_{z,opt}R_o(s), \\
C_{zI}(s) &= P_{z,opt}/(1 + s\tau_p), \\
C_{zV}(s) &= sD_{z,opt}R_o(s).
\end{aligned}
\tag{5.7}
$$

These define the SIMO controller for the vertical position, $K_z = [C_g(s), C_{zI}(s), C_{zV}(s)]^T$, taking as input the error in the plasma vertical position estimator e_{zIp}.

Only three real tunable parameters are allowed to vary: $P_{z,opt}$, $D_{z,opt}$ and $G_{z,opt}$, respectively the proportional and derivative terms for the external E and F coils in the different directions T_{zI} and T_{zV} along with the derivative gain for the internal G coil. This allows defining a controller which keeps the structure of standard vertical control at TCV and can be easily integrated both in the former analog and in the new digital control system.

5.3.2 Performance requirements

Structured $\mathcal{H}_\infty$ provides the framework for fixed structure controller synthesis which is designed to satisfy different performance specifications. The main objectives of the vertical position controller are defined as:

- stabilizing the vertical instability with adequate stability margins

- guaranteeing an adequate response (maximum overshoot, settling time) following plasma perturbations to bring back the plasma to its reference position

- minimizing the plant input requirements in terms of voltage request to the power supplies

- minimizing the current flowing in the coils in response to a perturbation in the plasma position

- having no DC current flowing in the internal coil.

There are a set of inherent trade-offs in these requirements, for example due to the fact that a reference tracking control at high frequency would result in an undesired amplification of measurement noise. Controller synthesis with $\mathcal{H}_\infty$ requires the formalization of these performance requests in terms of frequency dependent dynamical filters $W(s)$ to bound a set of closed loop transfer functions. The considered transfer functions are the sensitivities determining the response, to an input noise on the plasma vertical position n_z, of the vertical observer $z\hat{I}_p$ ($S(n_z \to z)$), of the current in the E and F coils ($S(n_z \to I_{EF})$) and of the current in the G coil ($S(n_z \to I_G)$); also, the control sensitivities from noise on the plasma vertical position to the voltage request to the power supplies for the EF coils ($KS(n_z \to V_{EF})$) and the G coil ($KS(n_z \to V_G)$). In order to satisfy the listed objectives for the controller, the performance filters are determined by the following characteristics:

- The transfer function $S(n_z \to z)$ should have a highpass filter behavior to reject low frequency disturbances and should not have a peak larger than 6 dB to guarantee adequate stability margins, as provided by classical control rules [101, p. 36].

- The bandwidth of the system, specified by the frequency at which the sensitivity $S(n_z \to z)$ crosses zero, should be above 250 rad/s. This value was found studying the closed loop response of a wide variety of shots performed in TCV and pushing the bandwidth for a faster response until the optimization could not satisfy all request in terms of closed loop transfer functions.

- The worst amplification of noise in the vertical position in the E and F coil currents specified by $\sigma(S(n_z \to I_{EF}))$ should be limited to -10 dB, with a maximum allowed current used to reject a static disturbance set at -25 dB and decay at -20 dB/dec for frequencies above 10^4 rad/s.

- A static disturbance in the vertical position should not be corrected using a static current in the G coil, while at larger frequencies the worst amplification of noise in the vertical position in the G coil current specified by $S(n_z \to I_G)$ should be limited to 0 dB around 10^3 rad/s, and decay at -20 dB/dec for frequencies above 10^4 rad/s.

- The amplification from noise in the vertical position to the voltage request to the E and F coils power supplies specified by $\sigma(KS(n_z \to V_G))$ should be limited to $5dB$ and decay at -20 dB/dec for frequencies above 10^5 rad/s

- The amplification from noise in the vertical position to the voltage request to the G coil power supplies specified by $KS(n_z \to V_G)$ should be limited to $-8dB$ and decay at -20 dB/dec for frequencies above 10^5 rad/s, while requiring no voltage for a static disturbance.

With the exception of the required peak of the sensitivity function $S(n_z \to z)$ at 6 dB and its bandwidth, the remaining sensitivities and control sensitivities filters are the result of manual tuning. A first estimate of the suggested values (peak values, crossover frequencies and rolloffs) is obtained examining the transfer functions resulting from the RZIp model in closed loop with the standard magnetic controller (in the presented case, the yellow lines in Fig. 5.4 for shot #68912) and tightened for improved performance. While the values could and should be adapted based on the operators' experience (tuning cannot be avoided in controller synthesis), the ones presented here are general enough to allow controller synthesis for a wide variety of plasma shapes realized in TCV. It is possible for example to require a further reduction in the G coil voltage request. In this case the operator could reduce the maximum allowed $KS(n_z \to V_G)$ and generate a controller satisfying the new constraints until they become too restrictive. The presented constraints are observed to provide a satisfactory solution not only for the closed loop model, but most importantly in the performance obtained in the experimental runs.

The set of rational proper filters W representing the aforementioned performance requests are designed in MATLAB [148] and can be seen in Fig. 5.4. It can be stated that all performance conditions are satisfied when the magnitude of the corresponding sensitivity lies below the filter or equivalently, using the $\mathcal{H}_\infty$ norm

$$
\begin{aligned}
&\left\| W_{S(n_z \to z)}^{-1} \, S(n_z \to z) \right\|_\infty < 1 \\
&\left\| W_{S(n_z \to I_{EF})}^{-1} \, S(n_z \to I_{EF}) \right\|_\infty < 1 \\
&\left\| W_{S(n_z \to I_G)}^{-1} \, S(n_z \to I_G) \right\|_\infty < 1 \\
&\left\| W_{KS(n_z \to V_{EF})}^{-1} \, KS(n_z \to V_{EF}) \right\|_\infty < 1 \\
&\left\| W_{KS(n_z \to V_G)}^{-1} \, KS(n_z \to V_G) \right\|_\infty < 1.
\end{aligned}
\tag{5.8}
$$

In the case of SIMO transfer functions, such as $KS(n_z \to V_{EF})$ with 16 outputs, the filter is set as $W_{KS(n_z \to V_{EF})}^{-1} \times I^{16 \times 16}$.

5.4 Controller synthesis with $\mathcal{H}_\infty$

Figure 5.3 – Block diagram of the generalized plant $\tilde{P}$ (contained in the orange dashed line) used to synthesize the controller K_z by minimizing the $\mathcal{H}_\infty$ norm of $N = \tilde{P}\star K$. The block Z determines the actuation directions for vertical control. The block K_z is the vertical position controller where the structure can be imposed as described in Eq. (5.7). The block $\tilde{G}$ includes RZIp, the delay for the power supplies and the A matrix for estimating the controlled variables. Once the vertical control loop is closed, the only input of N is n_z and the only output is w.

5.4.1 Generalized plant

In order to optimize the vertical controller with $\mathcal{H}_\infty$ techniques, it is necessary to consider the general method of formulating control problems introduced by Doyle [139]. A generalized plant for this problem is defined as represented in Fig. 5.3. The inputs are the noise n_z, affecting the vertical observer, and the vertical control signals u_z. The outputs are instead the performance variables w, outputs of the inverse weights, and the vertical observer error e_{zIp}.

The $\tilde{G}(s)$ block contains the RZIp model, including input delays modeling the power supplies, followed by the A matrix providing the estimators for magnetic control as outputs. The inverse filters W^{-1} are included in the generalized plant, having for inputs the variable of the corresponding sensitivity: $\hat{zI}_p$ for $W^{-1}_{S(n_z \to z)}$, I_{EF} for $W^{-1}_{S(n_z \to I_{EF})}$, I_G for $W^{-1}_{S(n_z \to I_G)}$ and so on (refer to Fig. 5.3 for the detailed interconnection).

The vertical controller outputs u_z are mapped using the block Z. The signal V_G represents the voltage request to the FPS. For generating the signal u, input to the mutual decoupling and resistive compensation block, the remaining outputs of Z are added to the

outputs of the radial, plasma current and PF current controllers, closed as follows:

- The plasma current control loop is closed using the loop on the OH coils as in the standard hybrid controller.

- The radial control loop is closed using the new radial control direction T_{rI}, which in turn requires a new tuning of the radial controller. The gain of the controller $C_r(s) = P_{r,opt}/(s\tau_P + 1)$ is selected minimizing the difference between the radially directed Lorentz force on the equilibrium plasma current distribution from a static current flowing in the old and the new coil combination for radial control.

- The coil current control is closed only for coil current directions orthogonal to those used for vertical and radial control at low frequencies, T_{zI} and T_{rI}. The bandwidth, which corresponds to $C_{pf,opt}$, is selected to be lower than the one used for vertical control specified by the frequency at which the filter $W_{S(n_z \to z)}$ crosses 0 dB. This is done to decouple the control of the PF coil currents at low frequency and the control of the vertical position at higher frequency as the directions T_{zV} is not orthogonal to N_{pfI}.

Contrary to the sequential design [101, p. 430] where the fast inner loop is closed before the slow ones, in this controller design the vertical stabilization loop is the last being closed to consider the effect of a slower control loop on the performance at low frequencies.

Note that the open loop system $\tilde{P}$ is still unstable since the vertical controller is not included. The objective of $\mathcal{H}_\infty$ is precisely to synthesize this controller.

5.4.2 Optimized controller synthesis

The generalized plant $\tilde{P}$ represented in FIg. 5.3 allows expressing the overall control objective of Fig. 5.8 as a minimization of the $\mathcal{H}_\infty$ norm of $\tilde{N} = \tilde{P} \star K_z$, the transfer function from n_z to w, where $\star$ represents the lower linear fractional transformation. Formally, given $\tilde{P}$ and an initial guess for the controller $K_{z0}(P_{z0}, D_{z0}, G_{z0})$, structured $\mathcal{H}_\infty$ algorithm [147] tunes K_z and computes γ which determine a local solution to the following problem

$$\gamma = \min_{K_z} \left\| \tilde{P} \star K_z \right\|_\infty$$
$$\text{subject to} \quad \begin{cases} K_z \text{ stabilizes } \tilde{P} \\ K_z \in \mathcal{K} \end{cases} \tag{5.9}$$

where $K_z \in \mathcal{K}$ represents the structural constraint of Eq. (5.7) for structured $\mathcal{H}_\infty$. The scalar parameter $\gamma \in \mathbb{R}$ can be considered as a scalar measure of the optimization result. A result of $\gamma < 1$ is a sufficient condition for Eq. (5.8) to hold.

In this study, the solution of Eq. (5.9) is computed iteratively in MATLAB [148] using `hinfstruct`. The minimization is initialized for several randomly distributed initial guesses of the controller close to $K_{z,0}$ to avoid local minima due to the nonsmooth nature of the optimization as suggested by [147] and it is verified that the optimization converges to

the same final result from different perturbations of $K_{z,0}$. When using structured $\mathcal{H}_\infty$ for controller synthesis, the fastest convergence is observed when specifying the frequency dependence of the desired transfer only for $S(n_z \to z)$ while requiring only the $\mathcal{H}_\infty$ norm (the peak value) of the remaining transfer functions, since the controller structure $\mathcal{K}$ already constraints the frequency dependence of the closed loop sensitivities (e.g. $R_o(s)$ specifies the rolloff frequency in KS). The initial controller gains P_{z0}, D_{z0} are computed by equalizing the radial field generated on the plasma current distribution by the standard directions $T_{z,std}P_{z,std}$, $T_{z,std}D_{z,std}$ computed in MGAMS and the optimized ones $T_{zI}P_{z0}$, $T_{zV}D_{z0}$, while $G_{z0} = G_{z,std}$. The running time of the optimization is less than one minute which makes the algorithm suited to be integrated in the shot preparation cycle.

5.5 Controller synthesis and simulations

An optimized vertical controller for a given plasma equilibrium is synthesized using $\mathcal{H}_\infty$ techniques. In order to validate the method, it is verified that the performance requirements are respected examining the frequency response of closed loop transfer functions and a plasma discharge is simulated to illustrate the advantages of the optimized controller.

5.5.1 Optimization results for shot #68912

A test case is presented to support the validity of the presented approach for vertical control optimization for the shot #68912, which features the negative triangularity diverted plasma ($\kappa = 1.52, \delta = -0.23$) depicted in Fig. 5.2. The corresponding RZIp model is generated for the preprogrammed equilibrium at $t = 1$ s when the plasma is in the flattop phase. The characteristic time for the vertical instability of this plasma is $\tau \approx 1$ ms, which is particularly challenging to stabilize, compared for example to the standard shot of TCV where $\tau > 2$ ms. The controller K_z is synthesized with $\mathcal{H}_\infty$ as described in detail in Sec. 5.4 to respect the control objective of Eq. (5.8). Closing the loop with the resulting magnetic controller allows stabilizing the system and evaluating the closed loop transfer functions of a stable plant. In Fig. 5.4, the transfer functions of four different sets of closed loop transfer functions are compared with the specified performance set W. The following cases are shown:

1. The optimized controller K_z with structure Eq. (5.7) using T_{zI} on long time scales and T_{zV} on fast time scales for vertical control is synthesized to respect the required performance set W. Vertical stability margins within the requirements are obtained with a control cost reduced from the marginally stable standard case. This results shows the efficacy of this method in synthesizing an optimized controller.

2. In order to test the efficacy of the direction T_{zV} in reducing the voltage request to power supplies for vertical stabilization, another structured controller is tuned using T_{zI} both at long and short time scales (i.e. substituting T_{zV} with T_{zI} in the generalized plant described in Sec. 5.4.1). The resulting transfer functions show comparable performance in terms of stability margins and G coil usage, a reduced
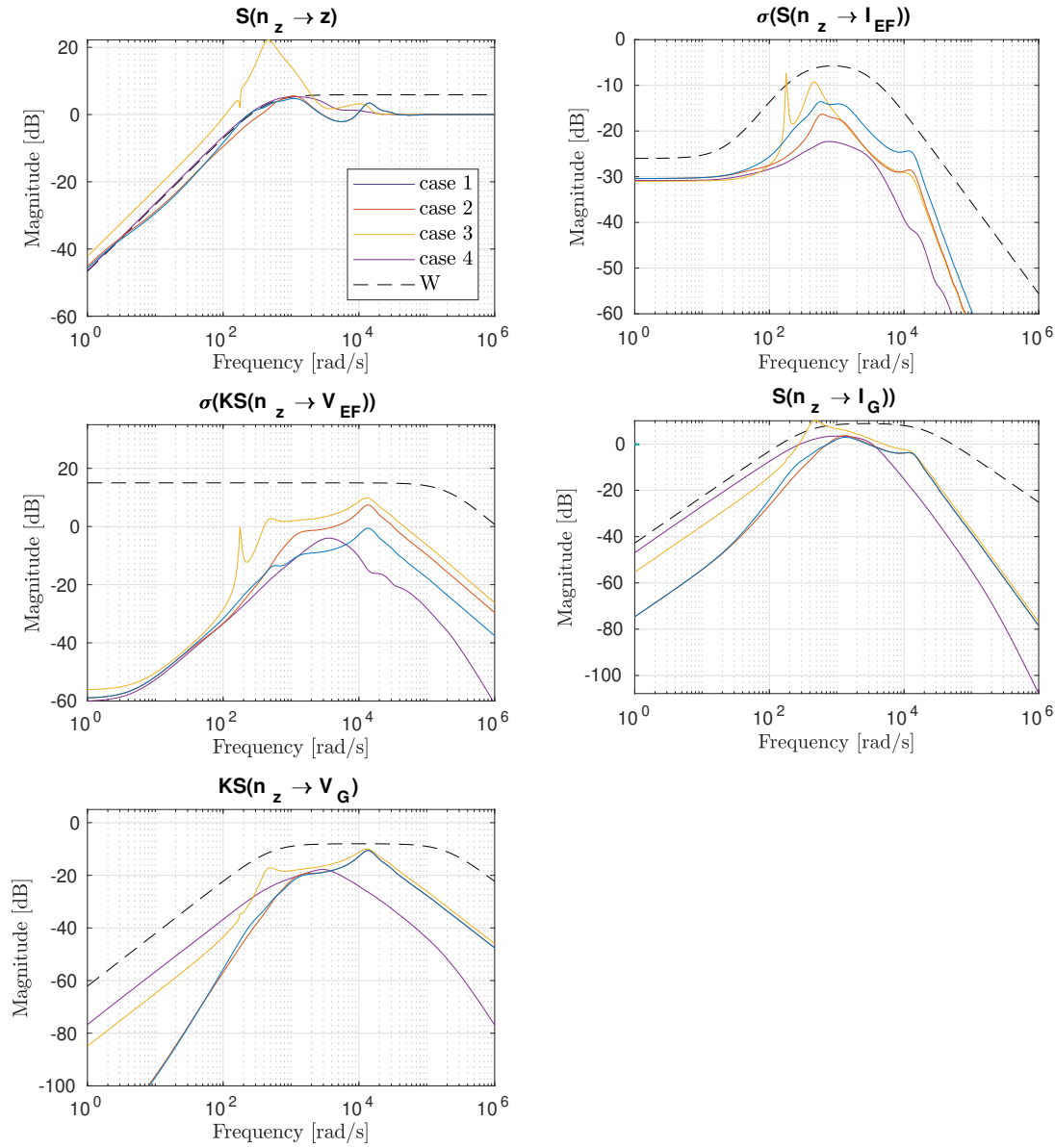
Figure 5.4 − Magnitude of selected closed loop frequency response for the TCV model from shot #68912 at $t = 1$ s featuring different vertical control directions and controllers. The black dashed lines represent the performance requirements W. The full lines represent the closed loop featuring the structured $\mathcal{H}_\infty$ controller with separate directions T_{zV} and T_{zI} (case 1, blue), the structured $\mathcal{H}_\infty$ controller using only T_{zI} (case 2, orange), the standard controller (case 3, yellow) and the unstructured $\mathcal{H}_\infty$ controller (case 4, purple). The main difference between case 1 and case 2 performance is in the voltage request of E and F coils at high frequency in $\sigma(KS(n_z \to V_{EF}))$, which is reduced for case 1 in agreement with the observations of Sec. 5.2.4.

current request at higher frequencies and worse performance compared to the previous case in terms of voltage request to the power supply at high frequency

3. Using standard control leads to low performance with a high sensitivity peak, much larger than the requested 6 dB around 55 Hz, which corresponds to low stability margins. This controller is the one obtained with standard shot preparation in TCV. The performance requirements are violated also at different frequencies for other control sensitivities. The different slope in the standard and optimized case for the transfer $KS(n_z \rightarrow V_G)$ is motivated by the use of a dedicated observer for velocity control in the standard case and a unique vertical position observer for the optimized case.

4. Standard $\mathcal{H}_\infty$ is used in order to synthesize the theoretical optimal controller for the specified performance set W, not requiring a structure for the vertical controller and not constraining the vertical actuation directions (this is done by setting the block $Z = I^{17 \times 17}$ in the generalized plant described in Sec. 5.4.1). This controller outperforms every other case, since the structure of the controller is not constrained and the controller results in a transfer function $K_z(s)$ with 1 input, 17 outputs and the same number of states of the plant, making it not suited for running in real time and not compatible with the analog control system of TCV. This comparison, although purely theoretical, is useful since the transfer functions obtained with the structured controller overlap with the unstructured controller at different frequencies, showing that a simplified controller allows good performance.

5.5.2   Closed loop simulations for shot #68912

The plant is simulated using SIMULINK with the RZIp model in closed loop with the controllers for plasma current, poloidal field coil currents, radial and vertical control. The same controller switching of the TCV tokamak is included in order to move from one controller to the next at selected times. In this way, it is possible to design an experiment to test the results of the optimization.

A nonlinear model for the FPS is included, featuring a simulation of the pulse width modulation behaviour and a dead zone which does not respond when the voltage reference of the analog signal for the controller $|V_G| < 11$ V. This model takes as an input the voltage request V_G, sums it to the voltage reference $V_{G,ref}$ for the FPS and outputs the voltage applied to the G coil $V_{G,a}$. Note that this model is not included in the optimization where the linear model considers $V_{G,a}(t) = V_G(t - \tau_{FPS})$. White noise is added as an input to the power supplies for the external coils, in order to seed a perturbation to the linearized state and include the unmodeled dynamics of the poloidal field coils thyristor based power supplies which are simply modeled with a delay.

In Fig. 5.6, the results of simulations are plotted along with the experimental results analyzed in the next Sec. 5.6. In the initial phase, standard control is kept until 0.7 s when plasma current flattop is reached. In the first phase (case 1: $t \in t_1 = [0.7, 1.2]$ s) the optimized controller featuring the optimized directions T_{zI} and T_{zV} for vertical control

is switched in. In the second phase (case 2: $t \in t_2 = [1.2, 1.6]$ s) the optimized controller featuring only the optimized direction T_{zI} is switched in. In the third and last phase (case 3: $t \in t_3 = [1.6, 2]$ s) the control is switched again to the standard one.

A square wave disturbance alternating between $V_{G,ref} = 16$ V and $V_{G,ref} = 0$ V is applied to the internal G coil reference voltage during the three described phases. This reference is set at 0 V during standard shots. In this way, the generated average radial magnetic field results in a perturbation on the vertical position. This approach has the advantage of forcing a continuous electric current to flow in the G coil for timescales tolerable to the FPS safety system. This leads it to work in a linear regime out of the nonlinear FPS dead zone and achieving a behavior closer to the linear one for which vertical control was optimized.

It can be observed that during the phases with standard control ($t < 0.7$ s and $t \in t_3 > 1.6$ s) large oscillations are present in the vertical plasma position estimator error at approximately 70 Hz. This is due to the low stability margin, which corresponds to the peak at 450 rad/s evident in the sensitivity function $S(n_z \to z)$ and present also in the others for standard control. As soon as the controller is switched to the optimized control scheme ($t \in t_1$), the large oscillations disappear and the plasma is stabilized around its reference with e_{zIp} around 0. Also when the same vertical control direction is used both at low and high frequencies ($t \in t_2$) the controller remains able to stabilize the plasma vertical position with improved performance compared to the standard case. When the standard controller is switched in again ($t \in t_3$), large oscillations reappear and remain throughout the shot, indicating proximity to instability. An analogous behaviour is observed in the G coil current I_G where the large oscillations are correlated to the vertical motion since it is driven by a voltage corresponding to the derivative of the vertical plasma position error.

5.6   Experimental results

The optimized vertical controller and the resulting magnetic controller are validated in experimental shots on TCV. The addition of an integrator allows removing steady state error without negatively influencing the improved closed loop performance, which are quantified with a unified metrics.

5.6.1   Integrator inclusion

The same vertical controller derived from the previous approach was included in TCV shots in early tests of this controller. Despite performance improvement being observed in comparison to the standard controller, a steady state error remained in the plasma position. Its origin lies in a disturbance generated by the various coil currents ramping in time (OH coils for plasma current induction and E and F coil for feedforward compensation of the resulting stray magnetic field). The RZIp model is indeed linearized around an operating point and does not consider these effects. An alternative solution was explored in this
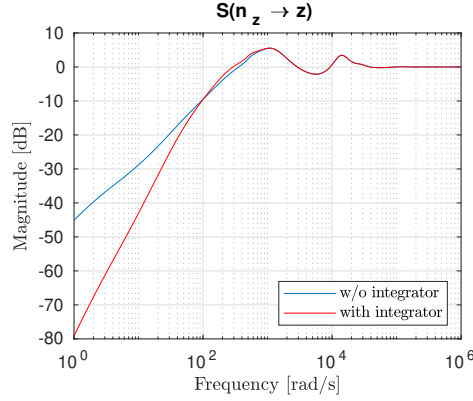
Figure 5.5 – Magnitude of the sensitivity function $S(n_z \to z)$ for vertical position control. The addition of the integrator in the controller converts the original transfer function (blue) to a new one (red) in which the slope of the magnitude at low frequency is adjusted from 20 dB/dec to 40 dB/dec without modifying the behavior around the bandwidth. This guarantees rejection of ramp disturbance without violating the required closed loop performance.

work, including an integrator at low frequency modifying C_{zI} as

$$C_{zI}(s) = P_{z,opt}/(1 + s\tau_p) \times (1 + I_z/s) \tag{5.10}$$

with $I_z = 0.02$, effectively converting this proportional controller in a PI controller. The effect of the integrator was to remove the undesired steady state error in the experimental runs, without modifying the performance observed in the closed loop transfer functions around the bandwidth frequency. This is particularly important for the sensitivity $S(n_z \to z)$ determining the stability margins, represented in Figure 5.5 and comparable for the case with and without the integrator.

5.6.2 Experimental run on shots #69393 and #68044

The optimized vertical control scheme including the integrator as in Eq. (5.10) was tested in shot #69393 including the digital controller. The experimental time series and the time series corresponding to the ones described in the previous section are reproduced in Fig. 5.6. One can notice that the simulations make a qualitatively correct prediction of the shot evolution, with the three different control schemes used in the three phases t_1, t_2 and t_3. The observed dynamics confirms the improvement predicted in the vertical control during t_1 and t_2, reducing the large oscillations in the vertical control error and in I_G characterizing the previous phase featuring standard control. At $t = 0.95$ s a large oscillation is observed in the vertical position error which is quickly damped. This is due to the OH coil current crossing zero and switching polarity, which induces a disturbance in the plasma equilibrium. Furthermore, when standard control is switched back at the beginning of t_3, the plasma disrupts with a fast VDE, following the saturation of the internal coil current and supporting the claim that better stability margins are required for stable operations. In order to compare the corresponding phase with standard control, the
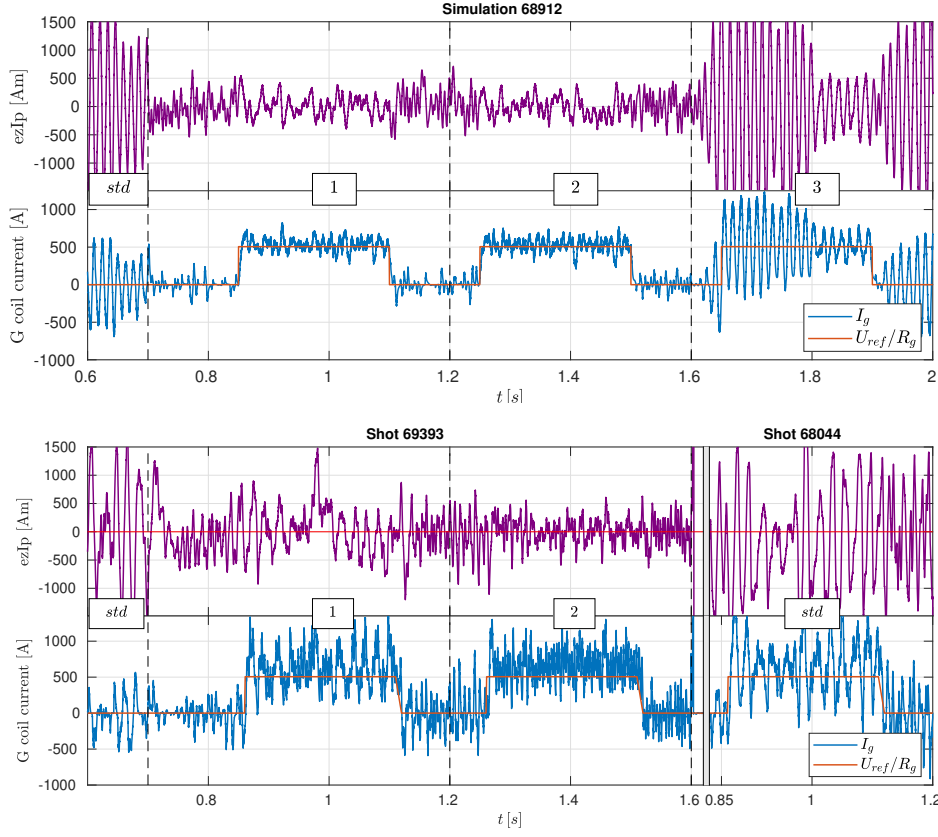
Figure 5.6 − Time evolution of different signals in simulations and the corresponding signals in the experiment to test the new vertical controller. The G coil current (blue) follows a reference voltage (orange), while the plasma response is observed in its vertical position error (purple). Different schemes for vertical control are tested. The standard controller (3, std in the figure) is used until flattop when the structured $\mathcal{H}_\infty$ controller with separate directions T_{zV} and T_{zI} (1) is switched in at $t = 0.7$ s. Subsequently at $t = 1.2$ s, the structured $\mathcal{H}_\infty$ controller is introduced using only T_{zI} (2), and the standard controller (3) is switched back in at $t = 1.6$ s. Since shot #69393 disrupted shortly after $t = 1.6$ s at the handover to the standard controller, the phase with standard control for shot #68044 is shown as well.

results from another shot (#68044) featuring the same reference for the plasma equilibrium (negative triangularity diverted plasma) are included in Fig. 5.6. In shot #68044 only standard control was used throughout the shot and the same square wave perturbation in the G coil voltage reference $V_{G,ref}$ was included. It was decided to plot the time window $t \in [0.8, 1.2]$ s and not $t \in [1.6, 2]$ s since shot #68044 disrupted at $t = 1.27$ s for loss of vertical control, which further confirms the improved stability margin of the optimized vertical controller since it was able to maintain the plasma stable for longer times than the standard controller.

We may observe that during the phases including standard control large oscillations at around 50 Hz are observed both in the vertical position error and in the coil current I_G. The frequency does not correspond to the 70 Hz observed in the simulations. We
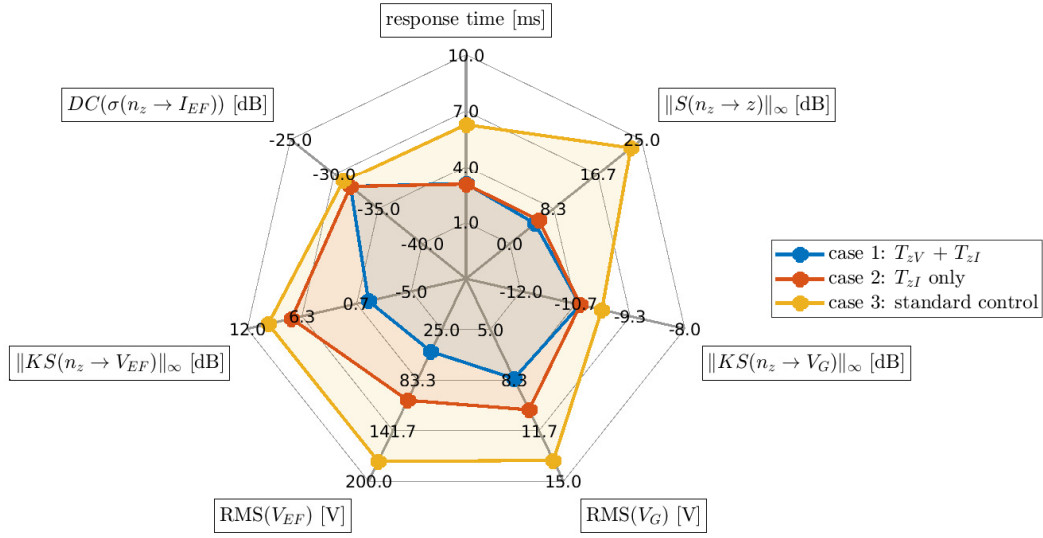
Figure 5.7 – Vertical control performance is summarized in a star plot. The different figures of merit described in Sec. 5.6 are represented for the three schemes for vertical control that were tested experimentally in shots 69393 and 68044. The best performance is defined by the smallest shaded area, which corresponds to the vertical controller combining T_{zV} and T_{zI} (case 1).

speculate that the origin of the oscillations is the response to noise combined with poor stability margins, which is quantified by the peak of the sensitivity function $S(n_z \to z)$. The difference in the frequency probably lies in unmodeled dynamics which is a consequence of the simplifications introduced in the RZIp model.

5.6.3 Unified metrics for vertical control performance

Vertical control tuning in TCV and other tokamaks results in a trade off between various parameters. Here we propose unified metrics for comparing the vertical control performance of different control schemes, consisting of a set of scalar parameters, derived both from the model and from the experiments. In Fig. 5.7-5.9 we consider the following scalar figures of merit, in clockwise direction starting from the top:

- The response time, intended as the reciprocal of the bandwidth for the transfer from a reference in the vertical position observer to its measurement. This quantifies the characteristic time for tracking a stepwise change in the position reference.

- The peak of the sensitivity function $S(n_z \to z)$, which is a measure of the reciprocal of a stability margin. Classical control design requires to keep it below 6 dB and a value larger than 0 dB is unavoidable [101, p. 169].

- The peak of control sensitivity $KS(n_z \to V_G)$ quantifying the voltage applied to the G coil to correct a sinusoidal disturbance in the plasma vertical position at any frequency.

- The RMS of the experimentally measured voltage request to the FPS, filtered above 50 Hz to avoid including low frequency changes in the reference.

- The RMS of the experimentally measured voltage request to the E and F coil power supplies, filtered above 50 Hz to avoid including low frequency changes in the reference.

- The peak of the sigma plot for the control sensitivity $KS(n_z \to V_{EF})$ quantifying the maximum voltage applied to any E and F coil combination to correct a sinusoidal disturbance in the plasma vertical position at any frequency.

- The DC gain for the sigma plot for the sensitivity $S(n_z \to I_{EF})$ quantifying the largest DC current flowing in any PF coil direction used to correct a static disturbance in the vertical position.

All these figures of merit are chosen such that the lowest value determines best performance. There are trade-offs between reducing all figures at the same time, as is done with $\mathcal{H}_\infty$ controller synthesis. For example, lowering the response time by increasing the bandwidth would increase the peak of the sensitivity function, following the waterbed effect which is a consequence of the Bode sensitivity integral [101, p. 169].

It may be noticed in Fig. 5.7 that the case using the optimized controller with two directions for vertical control T_{zV} and T_{zI} (case 1) shows the best performance with the minimal area on the star plot. In particular, the prediction that a reduced voltage request in the E and F coil power supplies would be achieved using T_{zV} at high frequencies anticipated in Sec. 5.2 is confirmed both in $\|\sigma(KS(n_z \to V_{EF})\|_\infty$ and in $\mathrm{RMS}(V_{EF})$ in comparison with the controller featuring a unique direction for vertical control T_{zI} (case 2). The standard controller (case 3) is also included. There is an inconsistency in $\|KS(n_z \to V_G)\|_\infty$ and in $\mathrm{RMS}(V_G)$ where the optimized controller with two directions (case 1) turns out to have a lower voltage request to the FPS in the experiments compared to the optimized controller with a single direction (case 2) while for the model they should be comparable. This can be motivated by unmodeled noise in the FPS which is not considered in the presented approach but does not invalidate the result.

5.6.4 Experimental runs on other shots

In order to test the generality of this algorithm, the optimized controller was already tested also on different equilibria that can be realized in TCV. The optimized controller featuring two directions at separate frequencies for vertical control was included in shot #68064 (negative triangularity limited, Fig 5.8), while the optimized controller using uniquely the T_{zV} or T_{zI} was included in separate phases of the shot in #68029 (double null diverted, Fig 5.9) and #68032 (single null with positive triangularity).
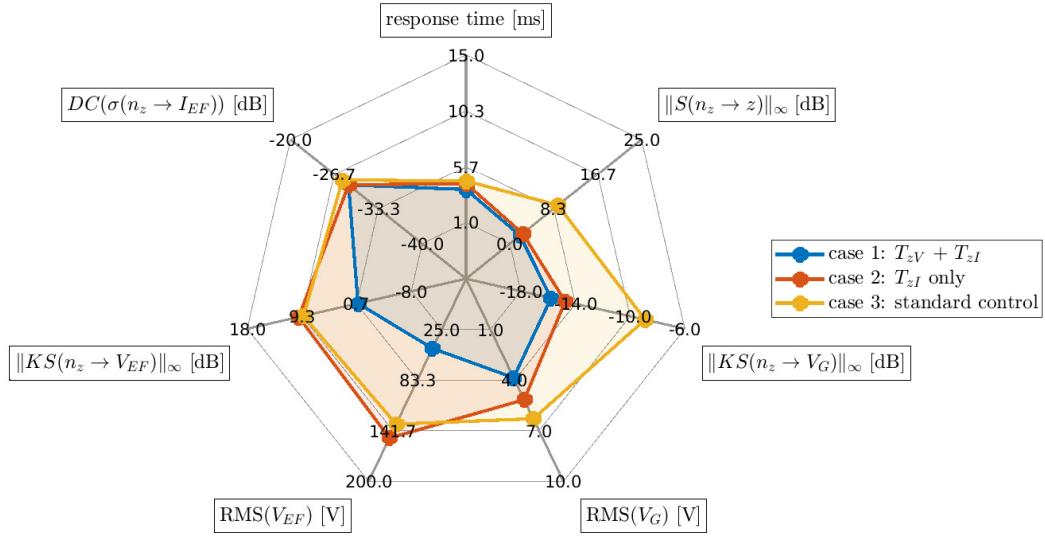
Figure 5.8 − Vertical control performance for shot #68064. Best performance are achieved also in this case combining TzV and TzI, even for a plasma with already good stability margin for standard control.
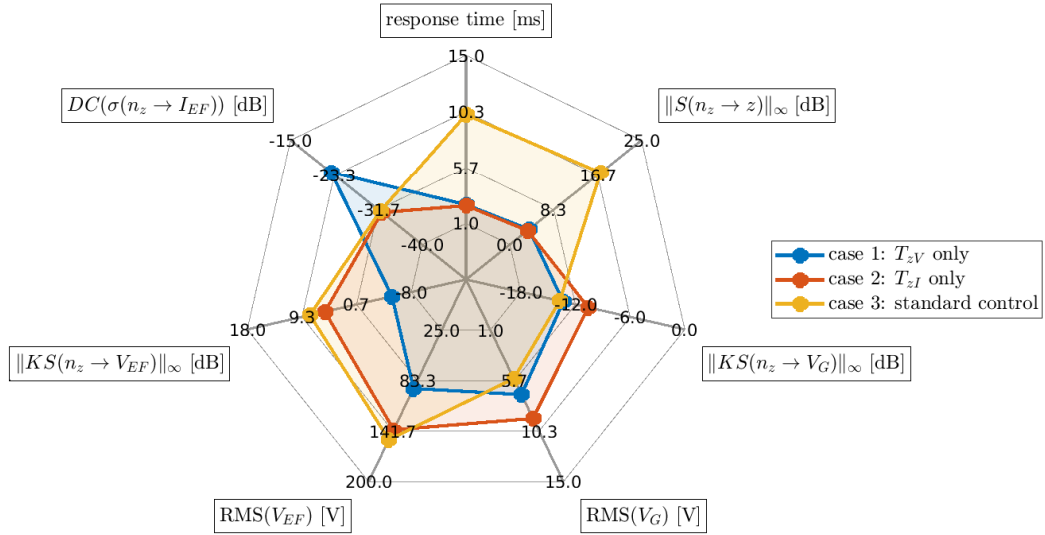
Figure 5.9 − Vertical control performance for shot #68029. Only TzV was used for vertical control in the shot phase which shows a larger current required for plasma positioning.

In all cases stability margins were improved as a result of the controller synthesis with $\mathcal{H}_\infty$ and it was experimentally confirmed that using direction T_{zV}, computed for the RZIp model corresponding to the shot flattop equilibrium, leads to a reduction of the voltage request to the power supplies compared to standard control.

5.7   Conclusions

In this chapter, the vertical control of TCV plasma was optimized based on the linearized RZIp electromagnetic model for the coupled plasma-vessel-coil dynamics.

The standard position control in TCV uses a subset of four out of sixteen coils in combination with the internal fast coil for plasma position control, which does not exploit the full potential of the TCV magnetic control system. The new approach proposed here has allowed stabilizing the plasma vertical position using all available poloidal field coils with optimized performance. A control-theory-based analysis showed that the input pole vector corresponding to the unstable eigenvalue of a dynamical model is an optimal choice for minimizing the input requirement for stabilization. This direction was used for vertical plasma control at high frequencies closing the loop with derivative control on the plasma vertical position. In agreement with previous studies, this coil combination is characterized by a prevailing use of the coils on the high field side. For proportional control we used instead a coil combination derived from the shape controller based on a static model for the deformable plasma response, which favours the use of coils on the low field side with a lower current required for positioning the plasma.

Several optimization methods were considered and structured $\mathcal{H}_\infty$ was selected to synthesize an optimal low order vertical position controller based on the RZIp model using the new combined optimal directions. Performance filters required for the controller design algorithm were derived for the closed loop model, which also allowed quantifying the performance improvement by comparing the closed loop frequency responses.

The resulting algorithm was tested experimentally for the first time on TCV. A square wave was added in the voltage reference for the internal G coil in order to induce a disturbance in the vertical plasma position. The new controller was able to stabilize the vertical instability with improved performance compared to the standard controller without requiring further tuning. For the same perturbation, the new scheme not only guarantees a lower error in the vertical position but also reduces the voltage request to the power supplies for the E and F coils in agreement with the predictions. Simulations of the switching controller correctly model the performance improvement using the optimized controller. A set of figures of merit as scalar parameters was proposed for quantifying the performance of vertical control in closed loop.

We may conclude that an approach based on plasma vessel coils linearized model combined with structured $\mathcal{H}_\infty$ can provide substantial improvements in the design of a controller for the plasma vertical instability, avoiding extensive tuning and reducing the risk of power supply saturation and the consequent plasma disruption.

6 Outlook and Conclusions

6.1 Summary

This thesis contributed to the research on thermonuclear controlled fusion by applying tools and techniques derived from control engineering to simulations and experiments for magnetic control in tokamak plasmas.

Specifically, it provides a new design procedure for the shape and position controller of the Tokamak à Configuration Variable (TCV), located at the Swiss Plasma Center - EPFL, which can contribute to improving the performance of the plasma discharges and better exploiting the extreme flexibility of this tokamak in terms of plasma shaping.

Elongated plasmas lead to improved performance in tokamaks, both in terms of magnetohydrodynamic stability and reduced transport, which will contribute to sustaining fusion conditions in reactors. The required magnetic field for shaping the plasma column however results in an unstable equilibrium that makes feedback control of the unstable vertical plasma position mandatory. Shape and position control are coupled multivariable problems in tokamaks since they share the same actuators, electromagnetic coils able to generate the required magnetic field for modifying the plasma equilibrium in real time.

In present TCV operation, the plasma shape is controlled mostly only in feedforward, providing a set of pre-programmed coil current references which generate the required equilibrium. Plasma vertical stabilization is performed by assigning a subset of the available coils to this task, chosen mainly based on physical intuition and experimental evidence about the required vacuum field necessary for inducing a vertical or radial displacement of the plasma column.

A prototype shape controller [79] has recently been developed, showing the potential for performing shape control in TCV but incorporating in its design the stabilization of the vertical instability of elongated plasmas which required extensive tuning for including it in TCV discharges.

The present work aims to overcome this limitation by proposing an optimized decoupled design for plasma shape and position controllers, where the vertical instability and the control of plasma position are performed on fast time scales and the shape controller acts on longer time scales to modify the plasma last closed flux surface without influencing the median plasma position.

The contribution of this thesis can be summarized in the following points

- The design of linear controllers is based on control-oriented linear models describing the dynamics of interest. In the present study, this is the coupled dynamics of the plasma within the tokamak and the currents in the static conducting elements surrounding it: the vessel and coil system. The axisymmetric RZIp model, where the plasma current distribution is fixed but is free to move in rigid fashion radially and vertically in the poloidal plane of a toroidal reference frame, was the main tool used for controller design and simulations.

  The model was studied in detail and extended, including in particular the singular perturbation and considering a semi-rigid approximation for limited plasmas following a radial movement of its centroid.

  The singular perturbation, typically applied in this kind of electromagnetic model but not yet included in RZIp, allowed substituting the instantaneous force balance in the remaining set of circuit equations and removed a subset of the states of the original system, leading to a reduced model in which the only state is defined by the coil currents determining the plasma equilibrium. The new semirigid model (rigid with respect to a vertical displacement and deformable in the radial direction) results in a more accurate model for the coupled plasma-vessel-coils dynamics, enabling a more reliable controller design. This is obtained in particular by providing a best fit of the linear model coefficients to match the ones derived from an actual Grad-Shafranov equilibrium following a displacement of the radial centroid position.

  Finally, the power supplies dynamics of TCV is studied in detail and included in the RZIp model either as an input delay, allowing linear optimized controller synthesis, or modeling part of its nonlinear elements for more realistic inclusion of the power supplies dynamic of the FPS coil in simulations.

- The problem of separating plasma shape and position controller synthesis is studied for the TCV case in particular. The position control loop is decoupled, stabilizing the RZIp system in closed loop and guaranteeing that the shape controller can be designed on a stable plant.

  An improvement to the standard mutual decoupling and resistive compensation is proposed, for a better correction of low frequency disturbances in the power supply inputs. The fast but imprecise observers for position control derived from linear combinations of magnetic measurements are corrected on long time scales to be consistent with the ones used for shape control based on the last closed flux surface location. Tuning of the controller for the plasma position using dedicated coil combinations, mainly coupled with a vertical or radial equilibrium displacement, can be designed separately from the shape controller, which acts on the plasma on a different time scale using only the remaining, decoupled coil directions. This approach allows maintaining the reliable standard approach for position control used in TCV.

Steady state decoupling is defined and the observers and actuators for shape control are derived for different cases and then compared using linear simulations particularly with respect to their frequency response. For controller design and simulation, a static model for plasma deformation is coupled to the RZIp model in order to validate the steady state decoupling including the vertical instability dynamics. The best scheme is proven to be robust against perturbations in the plasma equilibrium profiles which are expected during a shot and not included in the RZip model.

The model (GS) used for plasma deformation is derived from a linearization of the Grad-Shafranov equation solution around a variation of the currents in the PF coils used for shape control determining the boundary condition. This is a significant improvement with respect to the former model used for shape control which consisted of Green's functions in vacuum. The GS model is found to be consistent with the RZIp model for vertical and radial static plasma displacements following a variation in coil currents for vertical and radial control, allowing a consistent treatment of the position and shape control design.

- Relying on the possibility of tuning the vertical controller independently of the shape controller, vertical control is optimized for TCV on the basis of the RZIp model. In contrast with the shape controller design, this is done while including the dynamics of the vertical instability as an integral part of the procedure for selecting the coils used for vertical stabilization.

Two different optimal combinations of poloidal field coils for vertical control actuation are derived from linear plasma response models and used on different time scales for controlling the plasma vertical position. On fast time scales, the priority is input minimization and it is found that the coil combination corresponding to the input pole vector of the RZIp model provides the lowest voltage request for stabilizing the same plasma. On long time scales, position control is designed to be compatible with shape control and the direction for vertical control is derived from a model for the deformable plasma response. In agreement with previous studies, the optimal coil combination for control on fast time scales corresponds to a prevailing use of the coils on the high field side, less shielded by the vacuum vessel eddy currents. On long time scales instead the direction derived from the static model favours the use of coils on the low field side, which are characterized by a larger force per Ampère useful for low frequency plasma positioning.

Several algorithms for controller synthesis are considered and structured $\mathcal{H}_\infty$ is selected as it allows maintaining a simple controller structure and selectively reduce the usage of internal and external coils.

The results are successfully tested in dedicated TCV shots, showing the predictive capability of the model-based controller synthesis for stabilizing the vertical instability and improving the vertical control performance, in particular in terms of a reduction of the voltage request to the power supplies and improvement in the stability margins without requiring further tuning.

6.2 Outlook

From the work presented in this thesis the following can be considered for further extension

- The shape and position controller can be tested in more accurate simulations using a nonlinear free-boundary solver such as [122]–[125]. In the reduced model used in this thesis, RZIp approximates the high-frequency part including the vertical dynamics, while the model for plasma deformation G_0 corresponds to the DC part of a free-boundary solver.

- It is interesting to study whether position control should be performed closing a loop correcting the reference for coil currents or providing the input for mutual decoupling and resisitive compensation as is done in standard discharges. This subject can be treated with loop shaping techniques applied on a linearized model for the vertical instability like RZIp. Conversely, it is interesting to study the advantages/disadvantages of closing the shape control loop also providing directly signals to the mutual decoupling/resistive compensation, instead of modifying the current references as in this thesis.

- The new scheme for decoupled shape and position control should be tested in dedicated discharges, proving its efficacy in stabilizing the vertical instability and correcting shape disturbances. This should be done with a progressive inclusion of corrected position observers, optimized position controller and finally shape control on long time scales in order to facilitate troubleshooting.

- A complete multivariable analysis should be performed on the closed loop model for decoupled shape and position control, defining a better comparison among the several cases that were presented, in particular including the study for closed loop sensitivities and possibly further robustness analysis to model uncertainties.

- The case A illustrated in Chapter 4 maintaining standard directions for position control is particularly interesting for implementation in TCV as it does not require further controller tuning for stabilizing the vertical position and potentially is the easiest one to be integrated in standard TCV operation.

- An extension to this approach is the control of edge magnetic geometry, including flux expansion and dynamic strike point sweeping which is one of the solutions envisioned for mitigating wall heat loads in future fusion reactors like DEMO.

In conclusion, the work presented in this thesis contributed to the design of a generalized shape and position controller for the TCV tokamak presenting a decoupled design and testing the optimization of vertical control in dedicated discharges. The integration of this approach in the digital control system could further improve the performance of TCV plasma discharges to study fusion relevant scenarios as magnetic control remains an essential tool in nuclear fusion research in present and future tokamaks.

A | Plasma equilibrium reconstruction and linear observers

A.1 Equilibrium reconstruction

A.1.1 MHD equilibrium
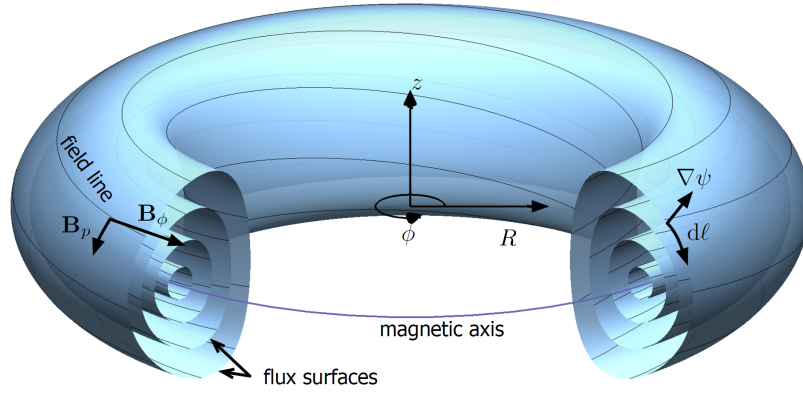
Figure A.1 – Flux surfaces in a toroidal plasma, highlighting the coordinate system (R, ϕ, z) and several plasma quantities. [57]

In a tokamak plasma, the tendency to expand due to pressure is compensated by the Lorentz force due to currents and magnetic field, leading to an axisymmetric MHD equilibrium. The Grad-Shafranov equation describes the magnetic flux surfaces, loci of constant magnetic flux on a poloidal cross section, and is derived from the equations describing MHD equilibrium in a toroidally confined plasma

$$\nabla \cdot \mathbf{B} = 0 \tag{A.1}$$

$$\nabla \times \mathbf{B} = \mu_0 \mathbf{J} \tag{A.2}$$

$$\mathbf{J} \times \mathbf{B} = \nabla p \tag{A.3}$$

as follows.

Consider a cylindrical reference frame (R, z, ϕ) where R is the radial distance from the central axis, z is the vertical coordinate and ϕ is the direction resulting from the vector product of the remaining two [86]. A generic magnetic field satisfies

$$\nabla \cdot \mathbf{B} = \frac{1}{R}\frac{\partial RB_R}{\partial R} + \frac{\partial B_Z}{\partial Z} + \frac{1}{R}\frac{\partial B_\phi}{\partial \phi} = 0. \tag{A.4}$$

Under the axisymmetry assumption, the last term is identically zero which allows defining a stream function ψ as

$$kRB_R = -\frac{\partial \psi}{\partial Z} \quad \text{and} \quad kRB_Z = \frac{\partial \psi}{\partial R} \tag{A.5}$$

with arbitrary $k = 2\pi$ satisfying Eq.A.4 written as

$$\nabla \cdot \mathbf{B} = \frac{1}{2\pi R}\left(-\frac{\partial^2 \psi}{\partial R \partial Z} + \frac{\partial^2 \psi}{\partial Z \partial R}\right) = 0$$

The magnetic field can then be decomposed in a toroidal and poloidal component as

$$\begin{aligned}
\mathbf{B} &= B_\phi \mathbf{e}_\phi + \mathbf{B_p} \\
&= T\nabla\phi + \frac{1}{2\pi}\nabla\phi \times \nabla\psi
\end{aligned} \tag{A.6}$$

where we further introduced $T = RB_\phi$ and the property $\nabla\phi = \mathbf{e}_\phi/R$ was included. It is clear that toroidal and poloidal fields are perpendicular to $\nabla\psi$, i.e. the field lines lie on surfaces of constant ψ which define magnetic flux surfaces. Due to the choice of k, the stream function ψ is furthermore equivalent to the magnetic flux crossing a disk of radius R at a given z

$$\psi(R, z) = \int \mathbf{B_p} \cdot d\mathbf{A}_z \tag{A.7}$$

which can be proven with vector identities using the magnetic field of Eq. A.6.

Including this definition of the magnetic field in Ampère's law leads to

$$\mu_0\mathbf{J} = \mu_0 j_\phi \mathbf{e}_\phi + \nabla \times (B_\phi \mathbf{e}_\phi) = \mu_0 j_\phi \mathbf{e}_\phi + \frac{1}{R}\nabla T \times \mathbf{e}_\phi \tag{A.8}$$

$$\mu_0 J_\phi = \nabla \times \left(\frac{1}{2\pi}\nabla\phi \times \nabla\psi\right) = \frac{1}{2\pi R}R^2\nabla \cdot \left(\frac{\nabla\psi}{R^2}\right) \equiv \frac{1}{2\pi R}\Delta^*\psi \tag{A.9}$$

where the Laplacian-like Grad-Shafranov operator Δ^* was introduced. This equation describes the relation between magnetic field and electrical currents regardless of their origin.

The presence of plasma is now considered, requiring that MHD equilibrium is maintained as

$$\mathbf{J} \times \mathbf{B} = \nabla p. \tag{A.10}$$

This physical relation, combined with the definitions for $\mathbf{B}$ and $\mathbf{J}$, implies that

$$0 = \mathbf{B} \cdot \nabla p = \frac{1}{2\pi} \left(\nabla \phi \times \nabla \psi \right) \cdot \nabla p = \frac{1}{2\pi R} \left[\frac{\partial \psi}{\partial Z} \frac{\partial p}{\partial R} - \frac{\partial \psi}{\partial Z} \frac{\partial p}{\partial R} \right] \tag{A.11}$$

$$0 = \mathbf{e}_\phi \cdot (\mathbf{J} \times \mathbf{B}) = J_R B_Z - J_Z B_R = \frac{1}{2\pi R^2} \left[-\frac{\partial \psi}{\partial R} \frac{\partial T}{\partial Z} + \frac{\partial \psi}{\partial Z} \frac{\partial T}{\partial R} \right]. \tag{A.12}$$

These relations state that the Jacobian determinant of ψ and p and ψ and T is null. Consequently, $p = p(\psi)$ and $T = T(\psi)$ are flux functions, meaning that they are constant on a magnetic flux surface. This property is used to simplify the radial projection of the momentum equation combined with Ampère's law in the following steps

$$(\mathbf{J} \times \mathbf{B}) \cdot \mathbf{e}_r = \nabla p \cdot \mathbf{e}_r \tag{A.13}$$

$$J_Z B_\phi - J_\phi B_Z = \frac{\partial p}{\partial R} \tag{A.14}$$

$$\left(-\frac{1}{\mu_0} \frac{1}{R} \frac{\partial T}{\partial R} \right) \left(\frac{T}{R} \right) - \left(\frac{1}{\mu_0} \frac{1}{2\pi R} \Delta^* \psi \right) \left(\frac{1}{2\pi R} \frac{\partial \psi}{\partial R} \right) = \frac{\partial p}{\partial R} \tag{A.15}$$

$$-\frac{1}{\mu_0 R^2} T \frac{\partial T}{\partial \psi} \frac{\partial \psi}{\partial R} - \frac{1}{\mu_0} \frac{1}{4\pi^2 R^2} \Delta^* \psi \frac{\partial \psi}{\partial R} = \frac{\partial p}{\partial \psi} \frac{\partial \psi}{\partial R}, \tag{A.16}$$

leading to the well-known Grad-Shafranov equation [149] [150]

$$\Delta^* \psi = -4\pi^2 \left(\mu_0 R^2 p' + TT' \right) \tag{A.17}$$

This is an elliptic nonlinear PDE for the spatial distribution of the equilibrium magnetic flux in the presence of plasma and external conductors. An MHD equilibrium is uniquely defined by the $p(\psi)$ and $T(\psi)$ profiles within the plasma and their derivatives p' and T', combined with the flux contribution of the currents in the conducting elements outside the plasma obtained from (A.9). The approximation is valid for time scales longer than the Alfvèn time $\tau_A = a\sqrt{\mu_0 \rho_m}/B_0 \approx 10^{-6} s$ (a being the tokamak size and ρ_m the mass density) determining the inertial response time of the plasma. This means that the evolution of MHD equilibrium on time scales of plasma discharges in a tokamak is dictated by the dynamics of currents flowing in external conductors (resistive time scale) and/or the profile evolution (current redistribution time) within the plasma.

Three classes of problems are solved based on the Grad-Shafranov equation.

- During a shot preparation, the PF coil current references are designed basing on the desired equilibrium. This is done imposing the desired flux distribution ψ along with realistic $p(\psi)$ and $T(\psi)$ profiles and computing the currents J_ϕ outside the plasma domain determining this equilibrium in a free boundary equilibrium problem. In TCV, this is performed with the FBTE code [88].

- Knowing the current in a set of conductors along with the profiles p' and TT' provides the boundary condition for solving the Grad-Shafranov equation, which is performed in TCV using FGS (Forward Grad-Shafranov Solver) [122].

- Processing the magnetic measurements (fields and fluxes from the probes, coil and vessel current estimates) the flux distribution within the plasma can be determined in the equilibrium reconstruction problem along with its internal profiles $p(\psi)$ and $T(\psi)$. This is performed in TCV using the LIUQE code [41] discussed in detail in the next section.

A.1.2 LIUQE and its real time implementation

The equilibrium reconstruction code LIQUE and its real time implementation are integrated in the digital control system of TCV with a sub-ms cycle time, which allowed observing and therefore controlling the plasma shape in real time.

Here only a simplified summary of the algorithm is included as an addendum to this thesis, while a complete discussion can be found in [41]

The goal of the inverse equilibrium problem is identifying the flux function $\psi(R, z)$ satisfying Eq. (A.17) and best reproducing the available measurements in the tokamak. The contributions to the toroidal current density in plasma (j_ϕ) and external conductors (j_e) are separated, considering the latter known (for the coils) or estimated (for the vessel) from measurements . Fixing an initial guess for the plasma current density $j_\phi^{(0)}$, which can be based on a linear inversion of the magnetic measurements, the toroidal projection of Ampère's law in (R, ϕ, z) [86]

$$\Delta^* \psi^{(t+1)} = -2\pi\mu_0 R \left(j_\phi^{(t)} + j_e \right) \tag{A.18}$$

is solved with Picard iteration which requires particular care for a stable numerical convergence. At each step t of the iteration, Dirichlet boundary conditions are recomputed in terms of flux at the boundary of the computational domain Ω evaluating $\psi(R, z) = \psi_p(R, z) + \psi_e(R, z)$ on $(R, z) \in \partial\Omega$ as the discrete version of

$$\psi_{\partial\Omega} = \sum_{i=p,e} \int_\Omega M(R, z, R', z') \left[j_\phi^{(t)}(R', z') + j_e(R', z') \right] dR' dz' \tag{A.19}$$

where M is the mutual inductance between coaxial circles crossing the poloidal plane at different positions on the computational grid. The following step of the algorithm requires the identification of the functions p' and TT' which best fit the available measurements. This is done parametrizing

$$p' = g_p(\psi; a_p)$$
$$TT' = g_t(\psi; a_t)$$

with parameters a_p and a_t adjusted to match the measurements basing on a fitting criterion.

The choice of the parametrized functions is limited to linear combinations of functions $g_g(\psi)$ used to express the toroidal plasma current starting from the Grad-Shafranov equation expressed as

$$j_\phi = 2\pi(rp' + TT'/(\mu_0 r)) = \sum_g a_g r^{\nu_g} g_g(\psi) \tag{A.20}$$

where $\nu_g = 1$ for the terms contributing to p' and $\nu_g = -1$ for those contributing to TT'. This scheme allows a linear regression problem where a_g is the free parameter, determining a new current distribution at each iteration. In post processing convergence is reached when the update in the poloidal flux on the inner grid points normalised by $|\psi_A - \psi_0|$ (ψ_A is the flux on axis, ψ_0 the flux on the LCFS) is below 5×10^{-5}. This usually requires less than 10 iterations. In LIUQE for TCV the computational domain, which covers the inside of the vacuum vessel only, is described as a rectangular mesh with $n_{rx} = 28$ and $n_{zx} = 65$ points in the r direction and z direction respectively. In its real time implementation, the Picard iteration scheme for one sample time is seeded with the plasma current distribution from the previous sample time instead of the approximate initial distribution from finite element fitting. A sufficiently short sampling time is fixed (< 1 ms) so that the change in the equilibrium between two successive samples is small, justifying this approach but remaining demanding in terms of computational speed. The number of iterations then required to reach a satisfactory convergence of the inverse equilibrium problem is considerably reduced: in practice, only one iteration is performed and a new measurement set is employed by the source term fitting at each cycle.

A.2 Linear observers

The linear observers for radial and vertical position and for the total plasma current used for magnetic control in the hybrid controller are derived, maintaining the same formalism used in the shot preparation code `mga.m`.

A.2.1 Radial observer

The linear observer for estimating the plasma radial displacement is obtained combining paired flux loops and magnetic probe measurements. The flux difference on a near equatorial plane between outer (o) and inner (i) plasma boundary points is in fact linearly proportional to a rigid plasma radial displacement ΔR. Referring to Fig. A.2, and assuming that in the unperturbed condition $\psi_o = \psi_i$ this is shown as following

$$\Delta\psi(\Delta R) = \tilde\psi_o - \tilde\psi_i \tag{A.21}$$

$$= (\psi_o - \left.\frac{\partial\psi}{\partial R}\right|_{o,eq} \Delta R) - (\psi_i - \left.\frac{\partial\psi}{\partial R}\right|_{i,eq} \Delta R) \tag{A.22}$$

$$= \left(\left.\frac{\partial\psi}{\partial R}\right|_{i,eq} - \left.\frac{\partial\psi}{\partial R}\right|_{o,eq}\right) \Delta R. \tag{A.23}$$
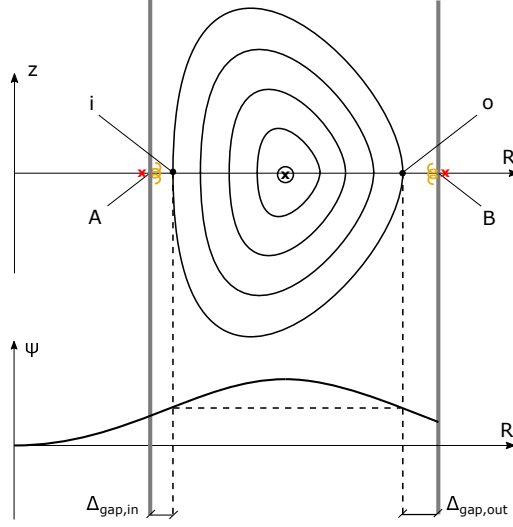
Figure A.2 – Sketch of the points used to define the radial observer, highlighting the probes (yellow) and flux loops (red) on the vessel (grey), located on the plasma equatorial plane. The plasma is limited on the tiles, not represented here. The plasma flux $\psi(R)$ on the equatorial plane is represented to visualize the properties used in the derivation of the radial observer.

Note that this definition is exactly the one used for the shape controller radial observer (Eq. 2.12), with the difference that here only two points on the LCFS are used. An estimate of the perturbed flux $\tilde{\psi}_i$ and $\tilde{\psi}_o$ is obtained from available magnetic measurements at points A and B and making use of the relationship $B_z = (1/2\pi R)(\partial\psi/\partial R)$ as

$$\tilde{\psi}_i = \psi_A + \left.\frac{\partial\psi}{\partial R}\right|_A \Delta_{gap,in} = \psi_A + 2\pi R_A \Delta_{gap,in} B_{z,A} = \mathsf{Fl}_A + 2\pi R_A \Delta_{gap,in}\mathsf{Bm}_A \quad (A.24)$$

$$\tilde{\psi}_o = \psi_B - \left.\frac{\partial\psi}{\partial R}\right|_B \Delta_{gap,out} = \psi_B - 2\pi R_B \Delta_{gap,out} B_{z,B} = \mathsf{Fl}_B + 2\pi R_B \Delta_{gap,out}\mathsf{Bm}_B \tag{A.25}$$

where the variables in serif font are the magnetic measures for the flux loops Fl and magnetic probes Bm. Note that, due to the orientation of the probes, the sign of the same vertical field measured by the inner and outer probes is reversed, thus the minus sign in Eq. A.25. Furthermore $\Delta_{gap,in} = R_i - R_A$ and $\Delta_{gap,out} = R_B - R_o$.

Finally, the radial observer in MGAMS is built as follows

$$\hat{r}_{obs}\ [\text{Wb}] = K_\psi\left(\tilde{\psi}_o - \tilde{\psi}_i\right) \tag{A.26}$$

$$= K_\psi(-\mathsf{Fl}_A + \mathsf{Fl}_B - 2\pi R_A \Delta_{gap,in}\mathsf{Bm}_A + 2\pi R_B \Delta_{gap,out}\mathsf{Bm}_B) \tag{A.27}$$

$$= A_{r,an}y_m \tag{A.28}$$

where an stays for analog. Here the full set of magnetic measurements $y_m = \begin{bmatrix} \mathsf{Fl} & \mathsf{Bm} & \mathsf{Ia} & \mathsf{Iv} \end{bmatrix}$ are the magnetic measurements of flux loops, magnetic probes and coil currents with the exception of the vessel currents which are not available in real time. The part of the

vector $A_{r,an}$ not including the vessel currents is contained in the A matrix. The coefficient K_ψ (typically 7000) is a numerical value which can be varied in MGAMS (named psifac). The remaining values $(R_A, \Delta_{gap,in}, R_B, \Delta_{gap,B})$ are obtained from the pre-programmed shape. The coefficients of Fl and Bm are saved in the A matrix to determine the linear radial observer. A useful equality to convert a radial rigid plasma displacement ΔR in the corresponding signal in the radial position observer is

$$\hat{r}_{obs} \ [\text{Wb}] = F_\psi \Delta R = K_\psi \left(\left.\frac{\partial \psi}{\partial R}\right|_{i,eq} - \left.\frac{\partial \psi}{\partial R}\right|_{o,eq} \right) \Delta R. \tag{A.29}$$

used in particular in Chapter 4.

A.2.2 Plasma current observer

TCV does not have a Rogowski coil, which in other tokamak provides a measurement of the total plasma current. It does instead feature a set of evenly spaced magnetic probes, which allow reconstructing the magnetic field along the same boundary.

Starting from Ampère's law $\nabla \times \mathbf{B} = \mu_0 \mathbf{J}$ one can evaluate the total plasma current flowing through a surface Ω defined by the TCV poloidal cross section from measurements of the magnetic field around its boundary $\partial\Omega$. This is done exploiting Stokes' theorem as

$$\oint_{\partial\Omega} \mathbf{B} \cdot d\mathbf{l} = \int_\Omega \mu_0 \mathbf{J} \cdot dA. \tag{A.30}$$

The discrete version of the integral is computed, replacing the infinitesimal $d\mathbf{l}$ by the finite distance between probes. The estimator for the plasma current is obtained from

$$\sum_{i=1}^{37} \left[\frac{1}{2}(B_{m,i} + B_{m,i+1})dL_{i,i+1} \right] + \left[\frac{1}{2}(B_{m,38} + B_{m,i+1})dL_{38,1} \right] = \mu_o I_p \tag{A.31}$$

where

$$dL_{i,j} = \sqrt{(R_i - R_j)^2 + (z_i - z_j)^2} \tag{A.32}$$

is the distance between two magnetic probes in the poloidal plane.

The observer is stored in the A matrix as the vector of coefficients $I_{pm} \in \mathbb{R}^{1 \times 38}$ derived from Eq. A.31 multiplying the magnetic measurements as

$$\hat{I}_p \ [\text{A}] = I_{pm}(\text{Bm} - B_{ma}\mathsf{I_a} - B_{mv}\mathsf{I_v}) \tag{A.33}$$

introducing the set of 38 measurements from the magnetic probes, B_m, along with their corrections for the magnetic field from measured active coil currents $\mathsf{I_a}$ and vessel currents $\mathsf{I_v}$; these are applied through the matrices of Green's functions B_{ma} and B_{mv} mapping the current in the conducting elements to the magnetic field generated on the probe. Notes:

- the correction for I_v is not available in the absence of vessel current estimators.

- the correction for I_a can optionally be included

A.2.3 Vertical observer

The vertical observer is defined as the first spatial moment of a toroidal current density distribution I_y with respect to its equilibrium position. The distribution I_y is obtained as a least squares fit of the available magnetic measurements. Due to the limited number of measurements, parametrization is required to reduce the number of free parameters and $I_y \in \mathbb{R}^{n_y}$ is typically evaluated on a coarse $n_y = 2 \times 3$ set of pyramidal finite elements. The current distribution is mapped on a finer map of n_x elements as $I_x = T_{xy}I_y \in \mathbb{R}^{n_x}$ such that the total plasma current I_p from the estimated distribution I_y is not the sum of its individual elements but

$$I_p = I_{py}I_y = \left(\sum_{i=1}^{n_x} [T_{xy}(i,1) \; T_{xy}(i,2) \; \cdots \; T_{xy}(i,ny)] \right) I_y \qquad \text{(A.34)}$$

The weighted magnetic measurements from toroidal current variations are obtained as

$$W_f\mathsf{Fl} = W_f(M_{fy}I_y + M_{fa}\mathsf{Ia} + M_{fa}\mathsf{Iv}) \qquad \text{(A.35)}$$

$$W_b\mathsf{Bm} = W_b(B_{my}I_y + B_{ma}\mathsf{Ia} + B_{ma}\mathsf{Iv}) \qquad \text{(A.36)}$$

$$W_pI_p = W_p(I_{py}I_y) \qquad \text{(A.37)}$$

The various terms in the system are discussed in the following. Flux loops Fl, magnetic probes Bm and coil currents measurements can be considered known, while Iv vessel currents are not generally available but are kept in this treatment for completeness. The weights W_k (with $k = f, b, p$) are diagonal matrices of 1 and 0 (masks) such that $W_k^T W_k = W_k$ and are used for (de)selecting a subset of available measurements. The terms M_{fj} and B_{mj} (with $j = y, a, v$) are matrices of electromagnetic Green's function mapping toroidal currents in magnetic fluxes and fields respectively at the flux loop and magnetic probe locations. Substituting I_p with the plasma current observer $\hat{I}_p$ of Eq.A.33 and isolating the unknown I_y one can write a linear system

$$\begin{bmatrix} W_f M_{fy} \\ W_m M_{my} \\ W_p I_{py} \end{bmatrix} I_y = \begin{bmatrix} W_f & 0 & -W_f M_{fa} & -W_f M_{fv} \\ 0 & W_m & -W_m B_{ma} & -W_m B_{mv} \\ 0 & W_p I_{pm} & -W_p I_{pm} B_{ma} & -W_p I_{pm} B_{mv} \end{bmatrix} \begin{bmatrix} \mathsf{Fl} \\ \mathsf{Bm} \\ \mathsf{Ia} \\ \mathsf{Iv} \end{bmatrix}. \qquad \text{(A.38)}$$

This is an overdetermined linear system, since $n_y < n_m$ with n_m the number of available magnetic measurements, in the standard form $AI_y = b$. Its solution is obtained using the Moore-Penrose (pseudo)inverse such that the solution to

$$\min_{I_y} ||AI_y - b|| \qquad \text{(A.39)}$$

is given by

$$I_y = A^\dagger b = (A^T A)^{-1} A^T b \qquad \text{(A.40)}$$

when A is real and $A^T A$ invertible. In this way, using the same convention used in the TCV shot preparation (mga.m) and introducing $A_{yy} = A^T A$ one gets

$$I_y = A_{yy}^{-1} \begin{bmatrix} A_{yf} & A_{ym} & -A_{ya} & -A_{yv} \end{bmatrix} \begin{bmatrix} \mathsf{Fl} \\ \mathsf{Bm} \\ \mathsf{Ia} \\ \mathsf{Iv} \end{bmatrix} \tag{A.41}$$

where

$$A_{yf} = M_{fy}^T W_f$$
$$A_{ym} = B_{my}^T W_m + I_{py}^T W_p I_{pm}$$
$$A_{ya} = M_{fy}^T W_f M_{fa} + B_{my}^T W_m B_{ma} + I_{py}^T W_p I_{pm} B_{ma}$$
$$A_{yv} = M_{fy}^T W_f M_{fv} + B_{my}^T W_m B_{mv} + I_{py}^T W_p I_{pm} B_{mv}.$$

At this point the plasma vertical observer is obtained from the first moment of the distribution, knowing the preprogrammed equilibrium position of the centroid $zp0$ and the vertical coordinates of the finer grid elements $z_x \in \mathbb{R}^{n_x}$. The analog vertical position observer is computed from the magnetic measurements as

$$z\hat{I}p\,[\mathrm{Am}] = (z_x - zp0)^T T_{xy} I_y = A_{z,an} y_m \tag{A.42}$$

where $y_m = \begin{bmatrix} \mathsf{Fl} & \mathsf{Bm} & \mathsf{Ia} & \mathsf{Iv} \end{bmatrix}$ with the notable exception of the vessel currents (not available in real time) are the magnetic measurements. The part of the vector $A_{z,an}$ not multiplying the vessel currents is contained in the A matrix.

Notes:

- flux loops and magnetic probes close to the G coil are usually excluded from the vertical observer

- vessel current estimates are generally not included

- various vertical observers are available in particular (general observations)

  - zIp_P for proportional control, including $\mathsf{I_a}$ (output 20 of A matrix)
  - zIp_D for derivative control, NOT including $\mathsf{I_a}$ and having a better phase but maintaining a steady state bias (output 23 of A matrix)
  - zIp_{fast} including only the non-integrated B (output 24 of A matrix)

- in practice numerous manual corrections are added to the reference for $z\hat{I}_p$ to manually compensate for several effects (stray field, nonlinear effects etc.).

- the next moment of the current distribution provides an estimator for the elongation (not used in this thesis) which can be included in the A matrix starting from $\hat{\kappa}_{obs} = [(z_x - z_{p0})^2]^T T_{xy} I_y$

B Derivations for magnetic modeling

These derivations are used in Chapter 3, for justifying analytical results on the single filament model (Sec. B.1), providing details on the RZIp matrices (Sec. B.2) and validating numerically the semi-rigid extension for RZIp limited plasmas (Sec. B.3).

B.1 Single filament model derivations

B.1.1 Stability conditions for the single filament model

Proposition 1 The characteristic polynomial $P(s)$ from Eq. (3.38) has negative real roots only for $n < n_{cr2} < 0$ defined as Eq. (3.43) or for $n > 0$.

Proof. The reduced model has only real poles [108, p. 79], thus $P(s)$ of Eq. (3.38) has only real roots. The second order chracteristic polynomial of the single filament model is

$$P(s) = s^2 \left[1 + \frac{n_a}{n} + \frac{n_e}{n} - \frac{M_{ae}}{L_a L_e} \left(M_{ae} + \frac{2N}{n} \right) \right] + s \left[\left(1 + \frac{n_e}{n} \right) \gamma_a + \left(1 + \frac{n_a}{n} \right) \gamma_e \right] + \gamma_e \gamma_a.$$
(B.1)

Applying the Routh-Hurwitz criterion to the polynomial written as

$$P(s) = s^2 a_2(n) + s a_1(n) + a_0$$

and considering $a_0 = \gamma_a \gamma_e > 0$ the condition for having negative real roots becomes

$$\begin{cases} a_1(n) > 0 \\ a_2(n) > 0 \end{cases}$$
(B.2)

which, once expressed as a function of the decay index

$$\begin{cases} n < 0 \\ n < n_{cr1} \quad \text{or} \quad \begin{cases} n > 0 \\ n > n_{cr1} \\ n > n_{cr2} \end{cases} \\ n < n_{cr2} \end{cases}$$
(B.3)

161

where

$$n_{cr1} = -\frac{n_e \gamma_a + n_a \gamma_e}{\gamma_a + \gamma_e}, \tag{B.4}$$

and

$$n_{cr2} = \left(2N\frac{M_{ae}}{L_a L_e} - (n_a + n_e)\right)\left(1 - \frac{M_{ae}^2}{L_a L_e}\right)^{-1}. \tag{B.5}$$

The critical value $n_{cr1} < 0$ since the terms $n_a, n_e, \gamma_a, \gamma_e > 0$.

Since the model has only real poles, from the definition of the roots of the characteristic equation Eq. (3.39) the following condition is always satisfied

$$a_1(n)^2 - 4a_2(n)a_0 > 0 \tag{B.6}$$

For elongated plasmas $n < 0$ and considering that at $n = n_{cr1}$ one gets $a_1(n_{cr1}) = 0$ the following holds

$$-4a_2(n_{cr1})\gamma_a\gamma_e > 0. \tag{B.7}$$

Considering $a_2(n) < 0$ when $n < 0$ corresponds to $n > n_{cr2}$ and consequently

$$n_{cr2} < n_{cr1} < 0. \tag{B.8}$$

In this way, the condition for having negative real poles of Eq. (B.3) is written as

$$\begin{cases} n < 0 \\ n < n_{cr2} \end{cases} \quad \text{or} \quad n > 0 \tag{B.9}$$

which physically means that the plasma is vertically stable for $n > 0$ (non elongated) or for $n < n_{cr2}$ (singular perturbation loses its validity). $\qquad\square$

B.1.2 RHP zero of G_I larger than the unstable pole

Proposition 2 The RHP zero z_I of Eq. (3.48) satisfies $z_I > \tilde{p}_u$ for $0 > n > -n_e$, where $\tilde{p}_u$ is the largest pole of the system when resistive compensation is included.

Proof. Consider the definition of the zero of G_I which is RHP as long as $n > -n_e$ (singular perturbation is valid for the single filament model considering only the vessel) and the definition of the unstable pole of the single filament model from its characteristic equation. The inequality $z_I > p_u$ is written as

$$-\frac{\gamma_e}{(1 + n_e/n)} > -\frac{a_1(n) - (a_1(n)^2 - 4a_2(n)a_0)^{1/2}}{2a_2(n)}. \tag{B.10}$$

When applying resistive compensation (or when having superconducting coils), ($\gamma_a = 0$), this becomes

$$-\frac{\gamma_e}{(1 + n_e/n)} > -\frac{(1 + n_a/n)\gamma_e}{a_2(n)}. \tag{B.11}$$

Since in general $n_e \gg n_a$, if $n > -n_a$ the inequality is automatically satisfied. Note that in this case, there is one negative root and one root at 0 in $P(s)$. In the case $-n_e < n < -n_a$ instead, assuming that the singular perturbation is valid ($n > n_{cr2}$ thus $a_2(n) < 0$) the inequality becomes

$$a_2(n) < (1 + n_a/n)(1 + n_e/n). \tag{B.12}$$

Expanding $a_2(n)$ in its full dependence on n and simplifying the inequality one gets

$$-\frac{M_{ae}}{L_a L_e}\left(M_{ae} + \frac{2N}{n}\right) < \frac{n_a n_e}{n^2} \tag{B.13}$$

From the definition of N (Eq. (3.30)), n_a and n_e,(Eq. (3.28)) the right term can be written as

$$\frac{n_a n_e}{n^2} = \frac{1}{n^2}\frac{1}{L_a L_e}\left(\frac{2R_0}{\mu_0 \Gamma}\right)^2 M_{ap}'^2 M_{ep}'^2 = \frac{1}{n^2}\frac{1}{L_a L_e}N^2 \tag{B.14}$$

and the inequality becomes

$$\frac{1}{L_a L_e}\left(M_{ae}^2 + 2M_{ae}\frac{N}{n} + \frac{N^2}{n^2}\right) > 0 \tag{B.15}$$

which is always satisfied as $(M_{ae} + N/n)^2 > 0$ □

B.1.3 Dissipative coil and vessel model

This toy model is used to motivate the structure of the zero appearing in the numerator of $G_z(s)$ of Eq. (3.36) with a simpler interpretation. Consider a plasmaless electromagnetic model for the current evolution in a coil I_a and in a passive conductor I_e for a given voltage V_a

$$\begin{cases} L_e \dot{I}_e + M_{ae}\dot{I}_a + R_e I_e = 0 \\ L_a \dot{I}_a + M_{ea}\dot{I}_e + R_a I_a = V_a \end{cases} \tag{B.16}$$

whose Laplace transform reads

$$\begin{cases} sL_e I_e + sM_{ae}I_a + R_e I_e = 0 \\ sL_a I_a + sM_{ea}I_e + R_a I_a = V_a. \end{cases} \tag{B.17}$$

The resulting transfer functions between $V_a(s)$ and the outputs $I_e(s)$ and $I_a(s)$ are

$$V_e \to I_e : G_e(s) = \frac{-sM_{ae}}{m(s - p_1)(s - p_2)}\frac{V_a}{L_a L_e} \tag{B.18}$$

$$V_a \to I_a : G_a(s) = \frac{s + \gamma_e}{m(s - p_1)(s - p_2)}\frac{V_a}{L_a} \tag{B.19}$$

$$\tag{B.20}$$

where $m = 1 - M_{ae}^2/(L_a L_e)$, $\gamma_{a,e} = R_{a,e}/L_{a,e}$ and the stable poles are

$$p_{1,2} = -\frac{1}{2}\frac{\gamma_a + \gamma_e}{m} \pm \frac{1}{2}\frac{\sqrt{(\gamma_a + \gamma_e)^2 - 4m\gamma_a\gamma_e}}{m} < 0. \tag{B.21}$$

The magnetic field in a given point is given by the linear superposition of the fields generated by the coil and the vessel currents. Considering axisymmetric toroidal conductors and focusing on the radial magnetic field on a poloidal reference frame (involved in the single filament model), it can be computed as

$$B_R(R, z) = -\frac{1}{2\pi R}\left(\frac{\partial \psi_a}{\partial z} + \frac{\partial \psi_e}{\partial z}\right) = -\frac{1}{2\pi R}\left(\frac{\partial M_{ax}}{\partial z}I_a + \frac{\partial M_{ex}}{\partial z}I_e\right) \tag{B.22}$$

where ψ_a and ψ_e are the fluxes generated by the currents I_a and I_e at the point (R, z) and M_{ax} and M_{ex} are the mutual inductances between a toroidal filament at the point (R, z) and coil and vessel respectively.

The transfer function between a voltage input V_a and the radial magnetic field is then obtained as

$$G_B(s) = -\frac{1}{2\pi R}\left(M'_{ax}G_a(s) + M'_{ex}G_e\right) \tag{B.23}$$

$$= -\frac{1}{2\pi R}\left(M'_{ax}\frac{s + \gamma_e}{m(s - p_1)(s - p_2)}\frac{1}{L_a} + M'_{ex}\frac{-sM_{ae}/L_e}{m(s - p_1)(s - p_2)}\frac{1}{L_a}\right) \tag{B.24}$$

$$= -\frac{1}{m(s - p_1)(s - p_2)}\left[s\left(1 - \frac{M'_{ex}M_{ae}}{M'_{ax}L_e}\right) + \gamma_e\right]\frac{1}{2\pi R}\frac{M'_{ax}}{L_a} \tag{B.25}$$

where the zero of the transfer function

$$z = -\left(1 - \frac{M'_{ex}M_{ae}}{M'_{ax}L_e}\right)^{-1}\gamma_e \tag{B.26}$$

emerges from the competing dynamic of the field generated by the coil and the opposite field generated by the vessel current vanishing over time and is RHP when $M'_{ex}/M'_{ax} > M_{ae}/L_e$.

B.2 RZIp equations

More details on the RZIp model discussed in Sec. 3.2 are provided, in particular expliciting the matrices integrated in its code (Sec. B.2.1) and including the singular perturbation (Sec. B.2.2).

B.2.1   Matrix details

State evolution equation

Following the structure of [105] maintained in the implemented code, the RZIp model equations for state evolution read

$$
\mathbf{M}\dot{x} - \mathbf{R}x = \left[\begin{array}{cccc} M_{11} & M_{12} & M_{13} & M_{14} \\ M_{21} & M_{22} & M_{23} & M_{24} \\ M_{31} & M_{32} & M_{33} & M_{34} \\ M_{41} & M_{42} & M_{43} & M_{44} \end{array}\right] x - \left[\begin{array}{cccc} R_c & 0 & 0 & 0 \\ 0 & 0 & 0 & 0 \\ 0 & 0 & 0 & 0 \\ 0 & 0 & 0 & R_p \end{array}\right] x = \mathbf{S}V_a \qquad \text{(B.27)}
$$

where, omitting the pertubation symbol δ one gets

$$
x = \left[\begin{array}{c} I_c \\ z_C I_{p0} \\ r_C I_{p0} \\ I_p \end{array}\right] \quad \text{and} \quad \mathbf{S} = \left[\begin{array}{c} S_{coils} \\ 0 \\ 0 \\ 0 \end{array}\right]. \qquad \text{(B.28)}
$$

In particular, z_C and r_C are the centroids of a plasma current vector $\mathcal{J} \in \mathbb{R}^{n_x}$ where each element corresponds to a current filament on a discrete 2D grid with n_x total elements which is considered known and can be derived either from a preprogrammed shot (FBTE) or from equilibrium reconstruction (LIUQE) once the current distribution J_p is obtained. Furthermore $S_{coils} = [I^{N_a \times N_a} \ 0^{N_a \times N_e}]^T$ applies $V_a \in \mathbb{R}^{N_a}$ on the $N_a = 19$ active coils only and not on the remaining N_e vessel circuits.

The model is linearized around an equilibrium given by $(\mathcal{J}, I_{c0}, I_{p0})$ and evolves the Kirchhoff law for conductive elements

$$
\left[\begin{array}{cccc} M_{11} & M_{12} & M_{13} & M_{14} \end{array}\right] \dot{x} - R_{11}I_c = v_c, \qquad \text{(B.29)}
$$

the plasma instantaneous ($m_p = 0$) vertical force balance derived in time

$$
I_{p0} \left[\begin{array}{cccc} M_{21} & M_{22} & M_{23} & M_{24} \end{array}\right] \dot{x} = 0, \qquad \text{(B.30)}
$$

the plasma instantaneous ($m_p = 0$) radial force balance derived in time

$$
I_{p0} \left[\begin{array}{cccc} M_{31} & M_{32} & M_{33} & M_{34} \end{array}\right] \dot{x} = 0, \qquad \text{(B.31)}
$$

and finally the Kirchhoff law for the inductively driven total plasma current

$$
\left[\begin{array}{cccc} M_{41} & M_{42} & M_{43} & M_{44} \end{array}\right] \dot{x} - R_p I_p = 0. \qquad \text{(B.32)}
$$

In the model, the resistances and self and mutual inductances of the static conductive

elements (coils and vessel eigenmodes/filaments) are included as

$$R_c = \begin{bmatrix} R_{aa} & 0 \\ 0 & R_{ee} \end{bmatrix} \qquad M_{11} = M_c = \begin{bmatrix} M_{aa} & M_{ae} \\ M_{ea} & M_{ee} \end{bmatrix}. \tag{B.33}$$

Following the formalism of [116], and considering the derivatives evaluated for the plasma equilibrium the vertical force balance elements are

$$M_{21} = \frac{1}{I_{p0}} \frac{\partial \mathcal{J}}{\partial z_C}^T M_{Jc} \tag{B.34}$$

$$M_{22} = -\frac{1}{I_{p0}^2} \frac{\partial}{\partial z_C} \sum_{i \in \text{grid}} 2\pi r_i \mathcal{J}_i B_{R,i}(I_{c0}) \tag{B.35}$$

$$M_{23} = -\frac{1}{I_{p0}^2} \frac{\partial}{\partial r_C} \sum_{i \in \text{grid}} 2\pi r_i \mathcal{J}_i B_{R,i}(I_{c0}) \approx 0 \tag{B.36}$$

$$M_{24} = 0. \tag{B.37}$$

the radial force balance elements are

$$M_{31} = \frac{1}{I_{p0}} \frac{\partial \mathcal{J}}{\partial r_C}^T M_{Jc} \tag{B.38}$$

$$M_{32} = +\frac{1}{I_{p0}^2} \frac{\partial}{\partial z_C} \sum_{i \in \text{grid}} 2\pi r_i \mathcal{J}_i B_{z,i}(I_{c0}) \approx 0 \tag{B.39}$$

$$M_{33} = +\frac{1}{I_{p0}^2} \frac{\partial}{\partial r_C} \sum_{i \in \text{grid}} 2\pi r_i \mathcal{J}_i B_{z,i}(I_{c0}) + \frac{1}{2} \mu_0 \frac{\partial \Gamma}{\partial r_C} \tag{B.40}$$

$$M_{34} = \frac{1}{I_{p0}^2} \sum_{i \in \text{grid}} 2\pi r_i \mathcal{J}_i B_{z,i}(I_{c0}) + \mu_0 \Gamma_0. \tag{B.41}$$

and the Kirchhoff law for the total plasma current elements are

$$M_{41} = \frac{1}{I_{p0}} \mathcal{J}^T M_{Jc} \tag{B.42}$$

$$M_{42} = 0 \tag{B.43}$$

$$M_{43} = \frac{1}{I_{p0}^2} \sum_{i \in \text{grid}} 2\pi r_i \mathcal{J}_i B_{z,i}(I_{c0}) + \frac{\partial L_p(r_C)}{\partial r_C} \tag{B.44}$$

$$M_{44} = L_p. \tag{B.45}$$

where from [105] the plasma self inductance is computed as (see also Appendix B.3.3)

$$L_p(r_C) = \mu_0 r_c (\Gamma - \beta_p - 1/2) = \mu_0 r_c f \tag{B.46}$$

while the plasma resistance R_p is set approximately to zero. The term M_{cJ} is the discrete version of $\tilde{M}_{kJ}(R, z)$ on the grid for all conductors while $[B_{R,i}(I_c), B_{z,i}(I_c)]$ is the radial and vertical magnetic field generated by the conductive elements on the grid points $[r_i, z_i]$.

Values M_{23} and M_{32} are set to zero in [105] and are indeed found to be smaller by about two orders of magnitude when compared to the other terms.

For symmetry arguments the system if finally completed with

$$M_{12} = M_{21}^T \tag{B.47}$$

$$M_{13} = M_{31}^T \tag{B.48}$$

$$M_{14} = M_{41}^T \tag{B.49}$$

The assumption of rigid displacement allows evaluating the following terms

$$\frac{\partial \mathcal{J}}{\partial r_C} = -\frac{\partial \mathcal{J}}{\partial R} \quad \text{and} \quad \frac{\partial \mathcal{J}}{\partial z_C} = -\frac{\partial \mathcal{J}}{\partial z} \quad \text{as in [116],} \tag{B.50}$$

$$\frac{\partial \Gamma}{\partial r_C} = \frac{1}{r_C} \quad \text{from its definition in Eq. (3.3),} \tag{B.51}$$

$$\frac{\partial L_p(r_C)}{\partial r_C} = \mu_0(f_0 + 1) \text{ derived as Eq. (B.85).} \tag{B.52}$$

The validity of the rigid approximation is discussed in Sec 3.3.

Output equation

The outputs of the RZIp model are the 19 coil currents and the magnetic measurements: magnetic field at the 38 magnetic probe location (B_m) and its derivative ($\dot{B}_m$) and 38 flux loops (ψ_m) and their derivative, corresponding to the voltage measured by the flux loop (V_m)

$$y = \begin{bmatrix} I_a \\ B_m \\ \dot{B}_m \\ \psi_m \\ V_m \end{bmatrix} = \mathbf{C}x + \mathbf{D}V_a = \begin{bmatrix} I_{coils} \\ C_{btm} \\ C_{btm}\mathbf{A} \\ C_f \\ C_f\mathbf{A} \end{bmatrix} x + \begin{bmatrix} 0 \\ 0 \\ C_{btm}\mathbf{B} \\ 0 \\ C_f\mathbf{B} \end{bmatrix} V_a. \tag{B.53}$$

The single elements are

$$I_{coils} = \begin{bmatrix} S_{coils}^T & 0 & 0 & 0 \end{bmatrix} \tag{B.54}$$

$$C_{btm} = \begin{bmatrix} B_{mc} & \frac{1}{I_{p0}}B_{mx}\frac{\partial \mathcal{J}}{\partial z_C} & \frac{1}{I_{p0}}B_{mx}\frac{\partial \mathcal{J}}{\partial r_C} & \frac{1}{I_{p0}}B_{mx}\mathcal{J} \end{bmatrix} \tag{B.55}$$

$$C_f = \begin{bmatrix} M_{fc} & \frac{1}{I_{p0}}M_{mx}\frac{\partial \mathcal{J}}{\partial z_C} & \frac{1}{I_{p0}}M_{mx}\frac{\partial \mathcal{J}}{\partial r_C} & \frac{1}{I_{p0}}M_{mx}\mathcal{J} \end{bmatrix} \tag{B.56}$$

where B_{mk} and M_{fk} with $k \in \{c, x\}$ are Green's functions mapping currents from element k to magnetic field at the probes or flux at the loops respectively. Finally, it is made use of

$$\dot{B}_m = C_{btm}\dot{x} = C_{btm}\mathbf{A}x + C_{btm}\mathbf{B}V_a \tag{B.57}$$

$$V_m = C_f\dot{x} = C_f\mathbf{A}x + C_f\mathbf{B}V_a \tag{B.58}$$

where $\mathbf{A} = \mathbf{M}^{-1}\mathbf{R}$ and $\mathbf{B} = \mathbf{M}^{-1}\mathbf{S}$.

State space model

The complete RZIp state space model finally reads

$$
\begin{cases}
\dot{x} = \mathbf{A}x + \mathbf{B}V_a \\
y = \mathbf{C}x + \mathbf{D}V_a
\end{cases}
\tag{B.59}
$$

$$
x = \begin{bmatrix} I_c \\ z_C I_{p0} \\ r_C I_{p0} \\ I_p \end{bmatrix}
\qquad
y = \begin{bmatrix} I_a \\ B_m \\ \dot{B}_m \\ \psi_m \\ V_m \end{bmatrix}
\qquad
V_a \in \mathbb{R}^{N_a}
\tag{B.60}
$$

B.2.2 Singular perturbation

Due to the time scales involved, the force balance equations are assumed to be at equilibrium at all instants. Instead of deriving the resulting linear relation in time as done in [105], the same approach used in [97] with the formalism of [151] and included in the code is performed, including the full singular perturbation method in the RZIp model.

Define

$$
\mathbf{N} = \left[\begin{array}{c|c} N_{11} & N_{12} \\ \hline N_{21} & N_{22} \end{array} \right] = \left[\begin{array}{cc|cc} M_{11} & M_{14} & M_{12} & M_{13} \\ M_{41} & M_{44} & M_{42} & M_{43} \\ \hline M_{21} & M_{24} & M_{22} & M_{23} \\ M_{31} & M_{34} & M_{32} & M_{33} \end{array} \right]
\tag{B.61}
$$

such that one can include the full force balance as system of first order differential equations in a system evolving the same Kirchhoff laws for conductive elements and total plasma current of RZIp

$$
\begin{bmatrix} N_{11} & I_{p0}N_{12} & 0 \\ 0 & I^{2\times2} & 0 \\ 0 & 0 & m_p \end{bmatrix} \begin{bmatrix} \dot{x}_1 \\ x_2 \\ x_3 \end{bmatrix} = \begin{bmatrix} R_{11} & 0 & 0 \\ 0 & 0 & I^{2\times2} \\ I_{p0}N_{21} & I_{p0}^2 N_{22} & 0 \end{bmatrix} \begin{bmatrix} x_1 \\ x_2 \\ x_3 \end{bmatrix} + \begin{bmatrix} S_{11} \\ 0 \\ 0 \end{bmatrix} V_a
\tag{B.62}
$$

where

$$
x_1 = \begin{bmatrix} I_c \\ I_p \end{bmatrix}, \quad x_2 = \begin{bmatrix} z_C \\ r_C \end{bmatrix}, \quad x_3 = \dot{x}_2, \quad S_{11} = \begin{bmatrix} S_{coils} \\ 0 \end{bmatrix}, \quad R_{11} = \begin{bmatrix} R_c & 0 \\ 0 & R_p \end{bmatrix} V_a
\tag{B.63}
$$

The model has again the structure

$$
\begin{cases}
\dot{I} = g(x, I) \\
\epsilon \dot{x} = f(x, I, \epsilon).
\end{cases}
\tag{B.64}
$$

By analogy with Eq. (B.62) here $I = x_1$ and $x = [x_2^T x_3^T]^T$. By making use of $x_3 = \dot{x}_2$ and

$m_p \to 0$, system Eq. (B.62) can be written as

$$N_{11}\dot{x}_1 = -R_{11}x_1 - I_{p0}N_{12}x_3 + S_{11}V_a \tag{B.65}$$

$$0 = I_{p0}N_{21}x_1 + I_{p0}^2 N_{22}x_2 \tag{B.66}$$

thus deriving Eq. (B.66) in time and substituting it in Eq. (B.65) one gets

$$(N_{11} - N_{12}N_{22}^{-1}N_{21})\dot{x}_1 = -R_{11}x_1 + S_{11}V_a. \tag{B.67}$$

leading to the reduced state evolution equation

$$\dot{x}_1 = \mathbf{A}_r x_1 + \mathbf{B}_r V_a. \tag{B.68}$$

where

$$\mathbf{A}_r = -(N_{11} - N_{12}N_{22}^{-1}N_{21})^{-1}R_{11} \tag{B.69}$$

$$\mathbf{B}_r = (N_{11} - N_{12}N_{22}^{-1}N_{21})^{-1}S_{11} \tag{B.70}$$

The magnetic measurements are obtained as

$$\begin{bmatrix} B_m \\ \psi_m \end{bmatrix} = \left[\begin{array}{c|c} C_{11} & C_{12} \\ \hline C_{21} & C_{22} \end{array} \right] \begin{bmatrix} x_1 \\ I_{p0}x_2 \end{bmatrix} \tag{B.71}$$

$$= \left[\begin{array}{cc|cc} B_{mc} & \frac{1}{I_{p0}}B_{mx}\mathcal{J} & \frac{1}{I_{p0}}B_{mx}\frac{\partial \mathcal{J}}{\partial z_C} & \frac{1}{I_{p0}}B_{mx}\frac{\partial \mathcal{J}}{\partial r_C} \\ M_{fc} & \frac{1}{I_{p0}}M_{fx}\mathcal{J} & \frac{1}{I_{p0}}M_{fx}\frac{\partial \mathcal{J}}{\partial z_C} & \frac{1}{I_{p0}}M_{fx}\frac{\partial \mathcal{J}}{\partial r_C} \end{array} \right] \begin{bmatrix} x_1 \\ I_{p0}x_2 \end{bmatrix} \tag{B.72}$$

In this way, making explicit the link between x_1 and x_2 of Eq. (B.66) the output equation for the reduced model reads

$$y = \begin{bmatrix} I_a \\ B_m \\ \dot{B}_m \\ \psi_m \\ V_m \end{bmatrix} = \mathbf{C}_r x_1 + \mathbf{D}_r V_a = \begin{bmatrix} I_{coils,r} \\ C_{btm,r} \\ C_{btm,r}\mathbf{A}_r \\ C_{f,r} \\ C_{f,r}\mathbf{A}_r \end{bmatrix} x_1 + \begin{bmatrix} 0 \\ 0 \\ C_{btm,r}\mathbf{B}_r \\ 0 \\ C_{f,r}\mathbf{B}_r \end{bmatrix} V_a. \tag{B.73}$$

where the single elements are

$$I_{coils,r} = \begin{bmatrix} S_{coils}^T & 0 \end{bmatrix} \tag{B.74}$$

$$C_{btm,r} = C_{11} + C_{12}N_{22}^{-1}N_{21} \tag{B.75}$$

$$C_{f,r} = C_{21} + C_{22}N_{22}^{-1}N_{21} \tag{B.76}$$

leading to a reduced model

$$\begin{cases} \dot{x}_1 = \mathbf{A}_r x_1 + \mathbf{B}_r V_a \\ y = \mathbf{C}_r x_1 + \mathbf{D}_r V_a \end{cases} \tag{B.77}$$

$$x = \begin{bmatrix} I_c \\ I_p \end{bmatrix} \qquad y = \begin{bmatrix} I_a \\ B_m \\ \dot{B}_m \\ \psi_m \\ V_m \end{bmatrix} \qquad V_a \in \mathbb{R}^{N_a}. \tag{B.78}$$

One can note that, despite the state vector is modified, the inputs and outputs are identical to the original RZIp model. The radial and vertical centroids multiplied by the plasma current can still be obtained from the state as

$$\begin{bmatrix} z_C I_{p0} \\ r_C I_{p0} \end{bmatrix} = N_{22}^{-1} N_{21} x_1 \tag{B.79}$$

which noticeably consists of solving the instantaneous force balance with known currents.

B.3 Semirigid model verification

The extension of the RZIp model for limited plasmas to a semi-rigid model discussed in Sec. 3.3 is validated numerically against a set of Grad-Shafranov equilibria for plasmas at different radial positions.

B.3.1 Objectives

The RZIp model requires computing explicitly the radial derivatives of the Shafranov parameter Γ and the radial current on the numerical grid J with respect to a displacement of the current centroid

$$\partial_{r_C}\Gamma = \partial\Gamma/\partial r_C \qquad \partial_{r_C}J = \partial J/\partial r_C. \tag{B.80}$$

Their evaluation however depends on a priori assumptions on the behavior of the plasma current distribution following a radial displacement. The focus of this study is on evaluating a realistic approximation of the plasma behavior following a displacement of its centroid to evaluate these terms.

B.3.2 Numerical equilibria

The objective of this study is determining a current distribution and an estimate of behavior of Γ following a plasma radial displacement of the plasma centroid which are more realistic than a simple rigid radial translation of the current distribution as is done in the standard RZIp model.

The Grad-Shafranov (GS) equation is solved numerically to determine the plasma equilibria starting from shot #65668 at t = 0.3 s and varying the plasma current around I_{p0} while the vacuum field generated by the external currents $\mathbf{B}(\mathbf{I_c})$ is held constant. This yields a variation of the radial equilibrium position for the plasma centroid following the (simplified) force balance

$$0 = F_{Lorentz} + F_{hoop} \;\to\; 0 = 2\pi r_C I_{p0} B_{z0}(\mathbf{I_{c0}}) + (\mu_0/2) I_{p0}^2 \Gamma_0(r_C) \tag{B.81}$$

The new equilibria allow determining the evolution of r_C/a, which is the quantity of interest for obtaining $\partial_{r_C}\Gamma$ as it will be derived, and the new current distribution J used to compute $\partial_{r_C}J$.

Note that the ideal goal would be determining how the current distribution evolves following a radial displacement while keeping all currents ($[\mathbf{I_c}\; I_p]$) fixed. However, the equilibrium of the plasma is uniquely determined by the equilibrium currents (together with assumptions on the internal profiles of the plasma, assumed known and fixed) by the GS equation. In this study, the criterion to determine which model is considered more realistic will be based on the ability to reproduce the results of the equilibria scan presented in Fig. 3.10 for scalar parameters independent of the total plasma current.

r_C/a

As the equilibrium of a plasma limited on the high field side of the tokamak (HFS) is varied by changing the plasma current while β_p is held constant, the plasma cross section expands since it is determined by both the limited point and the plasma axis, until the plasma hits the outer wall, when it becomes limited on the low field side (LFS) and starts compressing the cross section the more the current is varied. A rigid displacement model would instead predict that the major radius corresponding to the current centroid r_C increases linearly while the cross section maintains its shape or equivalently $a = $ const. Furthermore, a rigid model predicts an unrealistic overlap of the plasma with the tokamak tile when the plasma is HFS limited and the radial shift is done to smaller radii or the plasma is LFS limited and the radial shift is done to larger radii. Note that only the seventh LCFS in red in Fig. 3.10 (approximately $r_C = 0.87$ m) is an actual GS equilibrium and the rigid shifts of the LCFS are represented in the figure to emphasize the change in the plasma shape following the current scan.

The variation of the ratio r_C/a is different in different models as represented in Fig. B.1. Considering the GS numerical equilibria obtained with a discrete current scan (blue), one can observe that the ratio r_C/a decreases until the plasma hits the LFS, where it starts increasing. The rigid model instead predicts a linear growth of the ratio r_C/a with r_C, since $a = $ const. (red). The proposed model to fit the evolution of r_C/a is a semirigid model, where a variable $a(r_C)$ is considered following a radial displacement of the plasma centroid
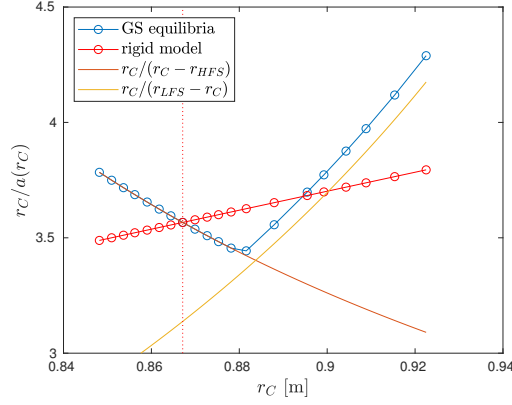
Figure B.1 – The parameters r_C/a for a radial scan of GS equilibria. Here and in the following figures, the vertical dotted line is the equilibrium for $I_p = I_{p0}$.

- when the plasma is limited on the HFS (orange line)

$$a = (r_C - r_{HFS}) \quad \rightarrow \quad \frac{r_C}{a} = \frac{r_C}{(r_C - r_{HFS})}$$

- when the plasma is limited on the LFS (yellow line)

$$a = (r_{LFS} - r_C) \quad \rightarrow \quad \frac{r_C}{a} = \frac{r_C}{(r_{LFS} - r_C)}$$

This correction from a rigid displacement model to a deformable model which better fits the actual GS equilibria leads to a correction of the expression for $\partial_{r_C} \Gamma$ and $\partial_{r_C} J$, as shown in Figure B.1.

B.3.3 $\partial_{r_C} \Gamma$

Shafranov parameter and plasma self inductance

The Shafranov parameter for a circular cross section plasma results from the evaluation of a toroidal force equilibrium in a tokamak and reads [12]

$$\Gamma = \ln \frac{8 r_C}{a} + \beta_p + \frac{\ell_i}{2} - \frac{3}{2}.$$

where r_C is the plasma major radius taken as the current centroid, a is the minor radius, β_p is the poloidal plasma beta and ℓ_i is the internal inductance per unit length described in Eq. B.83. Its extension for elongated plasma with elongation κ can be found as [116]

$$\Gamma = \ln \frac{8 r_C}{a \sqrt{\kappa}} + \frac{2\kappa}{\kappa^2 + 1} \beta_p + \frac{\ell_i}{2} - \frac{3}{2}$$

or [105]

$$\Gamma = \ln \frac{8r_C}{a\sqrt{\kappa}} + \beta_p + \frac{\ell_i}{2} - \frac{3}{2}$$

In this study the latter will be considered since it is used in the RZIp model.

The plasma self inductance determines the total magnetic energy generated by a given plasma current, related to the magnetic field generated by the plasma $\mathbf{B}_p$. One can determine the plasma internal inductance (where the integral is limited to the plasma volume) and the plasma external inductance as

$$\frac{1}{2}L_i I_p^2 = \int_{plasma} \frac{B_p^2}{2\mu_0} dV \quad \text{and} \quad \frac{1}{2}L_e I_p^2 = \int_{vacuum} \frac{B_p^2}{2\mu_0} dV$$

since the magnetic field generated by the plasma current extends outside the plasma domain as in a standard conductor. Obviously due to the linearity of integrals

$$L_p = L_i + L_e. \tag{B.82}$$

The dimensionless plasma inductance per unit length is introduced separating the internal and external dimensionless inductances. The internal inductance per unit length

$$\ell_i = \frac{4\pi}{\mu_0} \frac{L_i}{2\pi r_C} \tag{B.83}$$

is a quantity recovered by magnetic equilibrium reconstruction and it depends on the details of the internal plasma profiles. In typical rigid displacement models [105] [116] ℓ_i is considered constant with the plasma radius r_C. This approximation is motivated by the fact that both the torus volume over which it is evaluated and the circumference given by its axis vary as r_C. The external inductance is instead

$$\ell_e = \frac{4\pi}{\mu_0} \frac{L_e}{2\pi r_C} \approx 2\left(\ln \frac{8r_C}{a} - 2\right).$$

Here the approximation can be derived from standard formulas in a toroidal conductor [152, p. 311]. For an elongated plasma one may use the approximation of [105]

$$\ell_e = 2\left(\ln \frac{8r_C}{a\sqrt{\kappa}} - 2\right) \tag{B.84}$$

In conclusion the relation of the plasma self inductance with the Shafranov parameter Γ is

$$L_p = \frac{\mu_0 r_C}{2}(\ell_i + \ell_e) = \frac{\mu_0 r_C}{2}\left(\ell_i + 2\ln \frac{8r_C}{a\sqrt{\kappa}} - 4\right) = \mu_0 r_C\left(\Gamma - \beta_p - \frac{1}{2}\right) = \mu_0 r_C f \tag{B.85}$$

where we introduced

$$f = \Gamma - \beta_p - \frac{1}{2} = \frac{\ell_e + \ell_i}{2}. \tag{B.86}$$

The terms $\partial_{r_C}\Gamma$ and $\partial_{r_C}L_p$ can be eventually evaluated as in the RZIp model. In this

model, where it is assumed that κ, ℓ_i, a and β_p are constant during a plasma rigid radial displacement, one uses the following

$$\partial_{r_C} \Gamma = \frac{\partial}{\partial r_C} \ln \frac{8 r_C}{a \sqrt{\kappa}} \tag{B.87}$$

where it is clear that for the rigid model with $a = const.$ one gets $\partial_{r_C} \Gamma = 1/r_C$. The derivative with respect to the plasma radial centroid of B.85 leads to

$$\partial_{r_C} L_p = \mu_0 (f_0 + r_C f') = \mu_0 \left(f_0 + r_C \partial_{r_C} \Gamma \right) \tag{B.88}$$

and specifically for the rigid plasma model $\partial_{r_C} L_p = \mu_0 (f_0 + 1)$ which is included in the RZIp model in the Kirchhoff law for the plasma current as Eq. (B.52).

Evaluation of the Shafranov parameter
The parameter Γ is evaluated as follows for every radial equilibrium and is represented in Fig. B.2

- (blue line) from the GS equilibria, inverting the discrete radial force balance

$$\Gamma = -4\pi \sum_i r_{x,i} I_{x,i} B_{zx0,i}(\mathbf{I_{c0}}) / (\mu_0 I_{p0}^2)$$

  where r_x, I_x and B_{zx0} are column vectors that represents respectively the radial position, the plasma current and the vertical field due to external conductors in a finite number of current elements at fixed R and z locations, e.g., on a uniform grid

- (orange line) the Shafranov formula for semirigid displacement of a plasma limited on the HFS

$$\Gamma = \ln \frac{8 r_C}{(r_C - r_{HFS}) \sqrt{\kappa_0}} + \beta_p + \frac{\ell_i}{2} - \frac{3}{2}$$

  where r_C is taken from the numerical equilibria β_p and ℓ_i are taken from the GS initialization and κ_0 is the elongation for the equilibrium at $I_p = I_{p0}$.

- (yellow line) the Shafranov formula for semirigid displacement of a plasma limited on the LFS

$$\Gamma = \ln \frac{8 r_C}{(r_{LFS} - r_C) \sqrt{\kappa_0}} + \beta_p + \frac{\ell_i}{2} - \frac{3}{2}$$

  where β_p and ℓ_i and κ_0 taken as above

- (purple line) the Shafrnov formula with $a = a_{eq}$ from numerical equilibria

$$\Gamma = \ln \frac{8 r_C}{a_{eq} \sqrt{\kappa_{eq}}} + \beta_p + \frac{\ell_i}{2} - \frac{3}{2}$$

  where β_p and ℓ_i are taken as above and κ is the elongation for each equilibrium
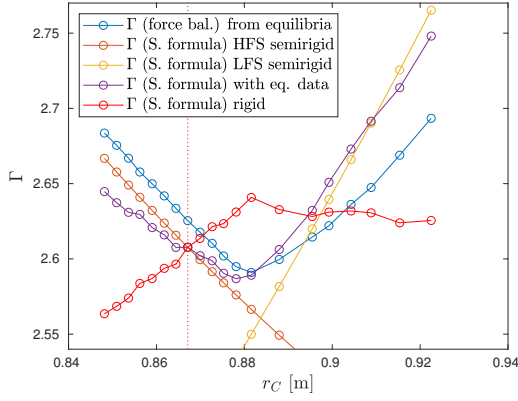
Figure B.2 – The parameter Γ for a radial scan of GS equilibria. S. is for Shafranov.
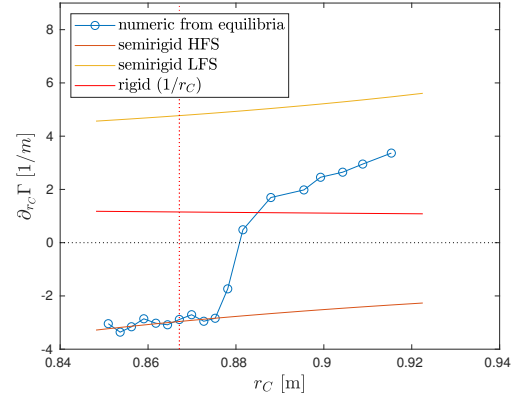
Figure B.3 – The parameter $\partial_{r_C}\Gamma$ for a radial scan of GS equilibria.

- (red line) the Shafrnov formula with a constant (rigid displacement)

$$\Gamma = \ln\frac{8r_C}{a_0\sqrt{\kappa_0}} + \beta_p + \frac{\ell_i}{2} - \frac{3}{2}$$

where β_p and ℓ_i and κ_0 taken as above and r_C from numerical equilibria.

One can observe that the Shafranov formula considering the data from the GS equilibria (purple) provides a good approximation of Γ calculated from force balance (blue). Note the inversion of the slope when the plasma moves from HFS limited to LFS limited. Including explicitly the proposed dependence of a on the radius for semirigid displacement (Sec. B.3.2) in the Shafranov formula (orange and yellow) correctly follows this fit while the rigid approximation (red) correctly estimates Γ at the equilibrium for $I_p = I_{p0}$ but fails to predict its evolution following a radial displacement.

Evaluation of the derivative of the Shafranov parameter
The derivative of Γ with respect to a radial displacement of the plasma centroid represented in Fig. B.3 is evaluated

- numerically with a forward derivative for the GS equilibria (blue) since Γ is not a function of I_p which is varied for the radial displacements

- analytically for the Shafranov formula where in particular

    – for the deformable model and plasmas limited on the HFS (orange)

$$\partial_{r_C}\Gamma = -\frac{r_{HFS}}{r_C(r_C - r_{HFS})}$$

    – for the deformable model and plasmas limited on the LFS (yellow)

$$\partial_{r_C}\Gamma = \frac{r_{HFS}}{r_C(r_{LFS} - r_C)}$$

175

  – for the rigid model (red), as described in Eq. B.87

$$\partial_{r_C} \Gamma = \frac{1}{r_C}$$

since ℓ_i, β_p and κ are assumed fixed following a radial displacement as in the RZIp model.

It is clearly possible to observe in Fig. B.3 that the semirigid model better fits the evaluation of $\partial_{r_C} \Gamma$ obtained from the numerical derivative of Γ evaluated from the force balance of different GS equilibria especially for HFS limited plasmas.

B.3.4 $\partial_{r_C} J$

At this point the only remaining term to be determined consistently is the derivative of the current distribution following a non-rigid radial displacement of the plasma radial centroid.

Derivative evaluation

The derivative of the current distribution $\partial_{r_C} J$ is not evaluated as $\partial_{r_C} \Gamma$ from an analytical formula, rather from the numerical distribution provided by equilibrium reconstruction. Consider now a plasma current distribution as solution of the GS equation for given plasma profiles and external currents, whose centroid is at r_C and integral is I_p as $J_{r_C} = J(R, z, I_p)$.

The derivative $\partial_{r_C} J$ is evaluated with a numerical derivative as

$$\partial_{r_C} J = \lim_{\substack{r_C^+ \to r_C \\ r_C^- \to r_C}} \frac{J_{r_C^+} - J_{r_C^-}}{r_C^+ - r_C^-} \tag{B.89}$$

where r_C^+ and r_C^- are the new centroid position following a radial displacement of the current distribution at larger and smaller radii respectively.

The shifted equilibria an can be evaluated in different ways basing on the model for the plasma radial displacement:

- When considering two different GS equilibria, the total plasma current is varied to obtain a radial shift while maintaining fixed the integral of the current as

$$J_{r_C^+} = J(R, z, I_p + \Delta I_p) \times I_p / (I_p + \Delta I_p)$$

and correspondingly

$$J_{r_C^-} = J(R, z, I_p - \Delta I_p) \times I_p / (I_p - \Delta I_p)$$

- for a semirigid model with varying $a(r_C)$, the perturbed current distribution is not a GS equilibrium but an isotropic scaling with h from the limiting point (r_b, z_b) on the tiles such that

$$J_{r_C^+} = J\left(\frac{R + r_b}{h} - r_b, \frac{z + z_b}{h} - z_b, I_{p0} \right) k_I \tag{B.90}$$

where the operation on the variable includes a translation of the coordinates to have the origin in (r_b, z_b) a scaling of factor $h = 1 + s > 1$ and a translation back to the origin. For the second term $J_{r_C^-}$ is the same with $h = 1 - s < 1$ The definition of $J_{r_C^\pm}$ includes a coefficient k_I such that the integral of the current for the shifted equilibrium is fixed as

$$\int_{\mathbb{R}^2} J_{r_C^+} dRdz = \int_{\mathbb{R}^2} J_{r_C^-} dRdz = \int_{\mathbb{R}^2} J_{r_C} dRdz = I_p$$

The perturbed centroids r_C^+ and r_C^- following a radial displacement of the current distribution are computed as

$$r_C^+ = r_b + (r_C - r_b)(1 + s)$$
$$r_C^- = r_b + (r_C - r_b)(1 - s)$$

- for a rigid radial displacement model the perturbed current distribution is a rigid translation of the current distribution by $\Delta r_C > 0$ to a larger radial coordinate

$$J_{r_C^+} = J(R - \Delta r_C, z, I_p)$$

and to a lower radial coordinate

$$J_{r_C^-} = J(R + \Delta r_C, z, I_p)$$

where due to the rigid translation the integral current remains constant at I_p. In this model

$$\partial_{r_C} J = \frac{\partial J}{\partial r_C} = \lim_{\Delta r_C \to 0} \frac{J_{r_C^+} - J_{r_C^-}}{r_C^+ - r_C^-}$$
$$\lim_{\Delta r_C \to 0} \frac{J(R - \Delta r_C, z, I_p) - J(R + \Delta r_C, z, I_p)}{2\Delta r_C} = -\frac{\partial J}{\partial R}.$$

Note that a simple rigid translation maintains the total current fixed.

Radial derivative on a thinner grid

While for the rigid model the numerical derivative is computed with Δr_C corresponding to the grid size, the semirigid model requires an interpolation on a thinner grid than the one provided by equilibrium reconstruction for a correct evaluation of the numerical derivative. The grid depends on a factor N such that, if the coarser grid over which the distribution is evaluated is $\mathtt{n_r} \times \mathtt{n_z}$ with $\mathtt{n_r}$ discrete steps in the radial direction and $\mathtt{n_z}$ steps in the vertical direction, the new grid is $(\mathtt{N\,n_r}) \times (\mathtt{N\,n_z})$ with $\mathtt{N\,n_r}$ discrete steps in the radial direction and $\mathtt{N\,n_z}$ steps in the vertical direction. This is done in a way to allow a reduction of the scaling factor s to converge to a valid approximation of the analytical derivative from two perturbed numerical current distributions. The convergence is based on the reduction of
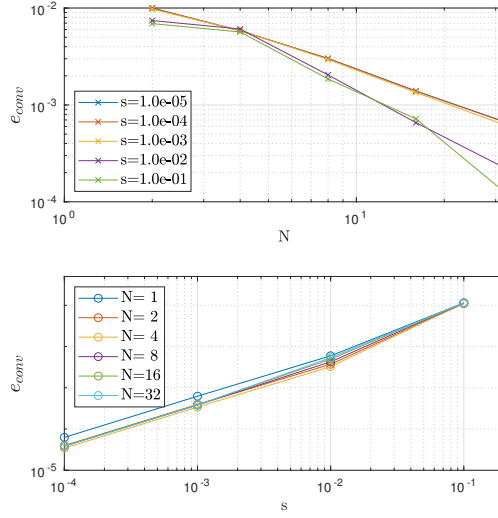
Figure B.4 – The error decreases for increasing N and decreasing s in the evaluation of the numerical derivative for the semirigid case.

an error defined as

$$e_{conv} = \frac{||\partial_{r_C} J(k) - \partial_{r_C} J(k-1)||_2}{||\partial_{r_C} J(k)||_2} \tag{B.91}$$

where k is the iteration. This error is defined for increasing N and s respectively and it is expected to converge for larger N and lower s, which is confirmed in Fig. B.4.

For an error lower than 10^{-3} the following parameters are selected to compute the numerical derivative of the current distribution on a thinner grid

$$\begin{cases} N = 20 \\ s = 1e - 4 \end{cases} \tag{B.92}$$

Once $\partial_{r_C} J$ is obtained, the result is interpolated on the coarser grid for being included in the RZIp model and for the validation provided in the following.

Validation of radial derivative of the current distribution

The total radial Lorentz force acting on the plasma is a scalar variable depending on the total current distibution. Its radial derivative is a function of $\partial_{r_C} J$.

The radial derivative of the total radial Lorentz force acting on the plasma and divided by the plasma current provides a plasma current independent scalar parameter to validate the different evaluations of $\partial_{r_C} J$.

The radial Lorentz force due to the magnetic field generated by currents outside the plasma and acting on the plasma is

$$F_L = \int_{\mathbb{R}^2} 2\pi R J(R, z) B_z(R, z) dR dZ \approx \Sigma_i 2\pi \mathtt{J}_i \mathtt{B_{z,i}} \mathtt{r}_i \mathtt{drdz} \tag{B.93}$$
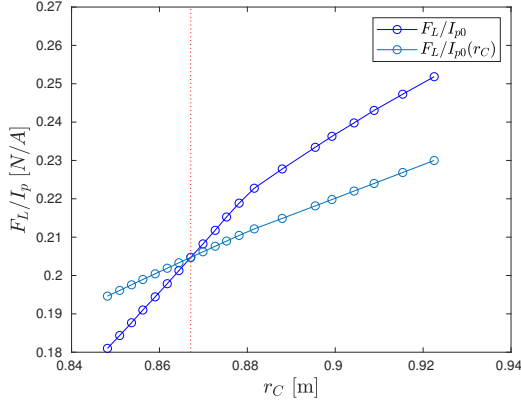
Figure B.5 − The Lorentz force computed as in Eq. B.93 from GS equilibria and divided by I_{p0} (dark blue) or for the various $I_p(r_C)$ determining the equilibrium (blue).
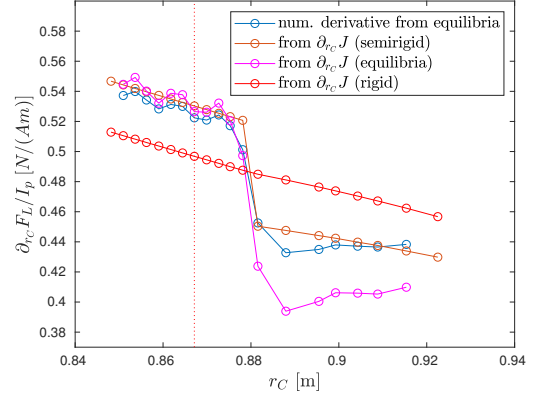
Figure B.6 − Different ways of evaluating $\partial_{r_C}F_L/I_p$.

Its derivative with respect to a radial displacement of the plasma centroid is

$$\partial_{r_C}F_L = \int_{\mathbb{R}^2} 2\pi R \partial_{r_C} J B_z(R,z) dRdZ \approx \Sigma_i 2\pi \partial_{\texttt{rc}} \texttt{J}_i \texttt{B}_{\texttt{z,i}} \texttt{r}_i \texttt{drdz} \tag{B.94}$$

where $\partial_{r_C}J$ is included. This term appears in the evaluation of the linearized model equations, in particular in the linearization of the radial force balance.

The ratio F_L/I_p does not depend on the plasma current. For the case in which F_L is evaluated from numerical GS equilibria with varying I_p from Eq. B.93, one should consider the different $I_p(r_C)$ as it is done in Fig. B.5 to compute correctly $(\partial_{r_C}F_L)/I_p$.

The term $(\partial_{r_C}F_L)/I_p$ in Fig. B.6 is evaluated

- numerically with a derivative of the Lorentz force, computed as in Eq. B.93 from GS equilibria, and divided by I_p (blue)

- with Eq. B.94 and divided by I_p using $\partial_{r_C}J$ obtained from the GS equilibria (yellow)

- with Eq. B.94 and divided by I_p using $\partial_{r_C}J$ evaluated with the semirigid model (orange)

- with Eq. B.94 and divided by I_p using $\partial_{r_C}J$ evaluated with the rigid model (red)

It is clearly possible to observe that the semirigid model provides the best approximation to the set of GS equilibria in predicting the evolution of F'_L/I_p following a displacement of the radial centroid especially for HFS limited plasmas.

B.3.5 Closed loop simulations

The RZIp model is simulated for shot #65668, which has an unstable pole of $p = 75$ Hz, very easy to stabilize. Experimentally, this shot run stably in TCV using the standard
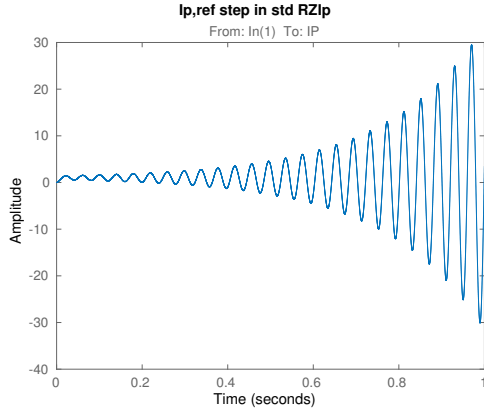
Figure B.7 – Current reference step response in closed loop with standard RZIp equations.
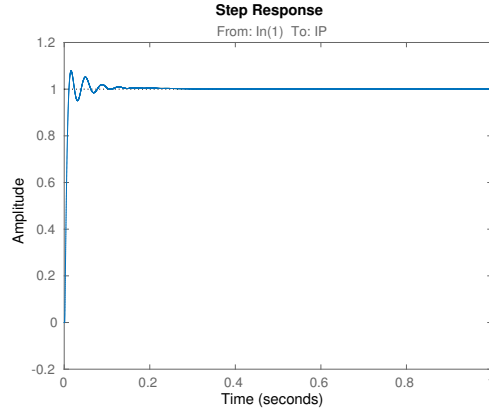
Figure B.8 – Current reference step response in closed loop with modified RZIp equations.

hybrid controller. The linearization is performed at different times during the flattop ($t \in [0.15\ 0.2\ 0.3\ 0.4]$ s) but the result of the simulation is always the same. When the RZIp model is put in closed loop with the exact controller used during the shot (TCV hybrid controller [80]) and considering a simple delay model of the power supplies

- leaving in the model the standard equation for the plasma current a slow pole at ≈ 4 Hz is left and the simulation incorrectly predicts and unstable closed loop.

- introducing the modifications for $\partial_{r_C}\Gamma\ \partial_{r_C}L_p$ for $\ell_i = const.$ and the isotropic scaling for evaluating $\partial_{r_C}J$, the simulation correctly determines a stable closed loop.

The response of the closed loop for a step in the plasma current reference are represented in the following plots.

B.3.6 Conclusions

Relaxing the approximation of a rigid radial plasma shift to a "semirigid" model which considers a plasma deformation following a displacement of the plasma centroid r_C allows recovering the evolution of r_C/a consistently with GS equilibria at different radial positions. This in turn can be included in the RZIp model with a modification of the terms $\partial_{r_C}\Gamma = \partial_{r_C}\Gamma(R/a)$ and $\partial_{r_C}L_p = \partial_{r_C}L_p(\Gamma)$. A consistent treatment requires to include an isotropic scaling of the plasma current distribution from the limiting point with the tile following a radial displacement of the plasma centroid. This leads to a new numerical evaluation of $\partial_{r_C}J$ from an equilibrium current distribution J which also better fits the evaluation of $\partial_{r_C}J$ obtained from different GS equilibria at different r_C. This extension allowed to correctly predict the stability properties when reproducing the dynamics of shots that were performed in TCV with the analog control system in feedback, where the original model incorrectly predicted instability. This provides a consistent improvement for the RZIp control-oriented model when applied to such discharges.

C Comparison of shape control open loop

In this appendix we will discuss one of the main consequences of the present treatment: that the static plant on which the shape controller acts once the position control loop is closed is equivalent for both the new proposed decoupled shape and position controller and the existing shape controller presented in Sec. 2.5. This means that, once the integral position controller only is closed on L_{dec}^{SC} of Eq. (2.18), one can obtain a plant P_{dec}^{SC} exactly equivalent to P_{dec} for a generic choice of the shape and position controller actuation direction and observation matrices T_z, T_r, O_z, O_r, O_{sh} and T_{sh}. This is derived in the remainder of the present section. In the former shape and position controller, it is assumed that the current references on each E and F coil can be exactly tracked and the vertical instability is neglected for the design. The open loop system is

$$L_{dec}^{SC} = O_{sv} G_0 T_{sv} = \left[\begin{array}{c} O_z \\ O_r \\ \hline O_{sh} \end{array} \right] G_0 \left[\begin{array}{cc|c} T_z & T_r & T_{sh} \end{array} \right] \tag{C.1}$$

$$= \left[\begin{array}{cc|c} O_z G_0 T_z & O_z G_0 T_r & O_z G_0 T_{sh} \\ O_r G_0 T_z & O_r G_0 T_r & O_r G_0 T_{sh} \\ \hline O_{sh} G_0 T_z & O_{sh} G_0 T_r & O_{sh} G_0 T_{sh} \end{array} \right] = \left[\begin{array}{c|c} O_{zr} G_0 T_{zr} & O_{zr} G_0 T_{sh} \\ \hline O_{sh} G_0 T_{zr} & O_{sh} G_0 T_{sh} \end{array} \right] \tag{C.2}$$

where the shape and position controller matrices are intentionally left generic, but it is considered that the first two variables correspond to the vertical and radial observers. Inputs and outputs relative to position control are grouped together as

$$y_1 = \left[\begin{array}{c} z_{sv} \\ r_{sv} \end{array} \right] \qquad y_2 = b_{sv} \qquad u_1 = \left[\begin{array}{c} u_{sv,1} \\ r_{sv,z} \end{array} \right] \qquad u_2 = u_{sv,sh} \tag{C.3}$$

such that

$$\left[\begin{array}{c} y_1 \\ y_2 \end{array} \right] = \left[\begin{array}{cc} O_{zr} G_0 T_{zr} & O_{zr} G_0 T_{sh} \\ O_{sh} G_0 T_{zr} & O_{sh} G_0 T_{sh} \end{array} \right] \left[\begin{array}{c} u_1 \\ u_2 \end{array} \right]. \tag{C.4}$$

At this point, integral control is added on the position only using

$$\left[\begin{array}{c} u_1 \\ u_2 \end{array} \right] = K_{rz}^{SC} \left[\begin{array}{c} e_1 \\ u_2 \end{array} \right] = \left[\begin{array}{cc} (1/s) I^{2 \times 2} & 0 \\ 0 & I^{(n_o - n_{sv} - 2) \times (n_o - n_{sv} - 2)} \end{array} \right] \left[\begin{array}{c} e_1 \\ u_2 \end{array} \right] \tag{C.5}$$

and one can write

$$L_{dec}^{SC} K_{rz}^{SC} = \begin{bmatrix} O_{zr}G_0 T_{zr}(1/s) & O_{zr}G_0 T_{sh} \\ O_{sh}G_0 T_{zr}(1/s) & O_{sh}G_0 T_{sh} \end{bmatrix} = \begin{bmatrix} a & b \\ c & d \end{bmatrix}. \tag{C.6}$$

or equivalently

$$\begin{cases} y_1 = ae_1 + bu_2 \\ y_2 = ce_1 + du_2 \end{cases}. \tag{C.7}$$

Closing negative feedback on the position means setting $e_1 = y_{ref} - y_1$ obtaining

$$\begin{cases} y_1 = -ay_1 + ay_{ref} + bu_2 \\ y_2 = -cy_1 + cy_{ref} + du_2 \end{cases} \iff \begin{cases} y_1 = (1+a)^{-1}ay_{ref} + (1+a)^{-1}bu_2 \\ y_2 = -cy_1 + cy_{ref} + du_2 \end{cases}. \tag{C.8}$$

Substituting the expression for y_1 in y_2 one gets a plant

$$\begin{bmatrix} y_{ref} \\ u_2 \end{bmatrix} \rightarrow \begin{bmatrix} y_1 \\ y_2 \end{bmatrix} : P_{dec}^{SC}(s) = \left[\begin{array}{c|c} (1+a)^{-1}a & (1+a)^{-1}b \\ \hline c(1+a)^{-1}b & -c(1+a)^{-1}b+d \end{array} \right] \tag{C.9}$$

It is assumed that the closed loop is stable (tuning of the vertical controller is not treated here). The DC gain of the plant is evaluated, considering that, due to the integral effects in a and c

$$DC[(1+a)^{-1}a] = I^{2\times2} \tag{C.10}$$

$$DC[c(1+a)^{-1}] = ca^{-1} \tag{C.11}$$

$$DC[(1+a)^{-1}b] = 0^{2\times n_y} \tag{C.12}$$

$$DC[c(1+a)^{-1}b] = ca^{-1}b \tag{C.13}$$

Finally, the steady state plant

$$\begin{bmatrix} z_{sv,ref} \\ r_{sv,ref} \\ u_{sv} \end{bmatrix} \rightarrow \begin{bmatrix} z_{sv} \\ r_{sv} \\ b_{sv} \end{bmatrix} : P_{dec}^{SC}(0) = \left[\begin{array}{c|c} I^{2\times2} & 0^{2\times n_y} \\ \hline ca^{-1} & -ca^{-1}b+d \end{array} \right] \tag{C.14}$$

$$= \left[\begin{array}{c|c} I^{2\times2} & 0^{2\times n_y} \\ \hline O_{sh}G_0 T_{zr} H_{rzI}^{-1} & -O_{sh}G_0 T_{zr}\left(H_{rzI}^{-1}\right)O_{zr}G_0 T_{sh}+O_{sh}G_0 T_{sh} \end{array} \right] \tag{C.15}$$

where we is recall from Eq. (4.20) the definition

$$H_{rzI} = O_{zr}G_0 T_{zr}. \tag{C.16}$$

The expression for $P_{dec}^{SC}(0)$ is identical to the one for $P_{dec}(0)$ from Eq. (4.26). This has the following important consequences

- From the point of view of low frequency control of plasma shape, the position controller can be closed indifferently on current references (standard shape and position controller) or on the inputs of K_{MR} and including the low frequency correction on the position observer (separation of shape and position control).

- As derived for case C (Eq. (4.50)), the same matrices used for standard position and shape control can be used for the separated shape and posiiton controller to obtain full decoupling.

Note that the dynamic properties of the position controller is not discussed here and could determine the choice between one solution or the other.

Bibliography

[1] C. Braams and P. Stott, *Nuclear Fusion, Half a Century of Magnetic Confinement Fusion Resrearch*, 1st ed. Institute of Physics Publishing, London (UK), 2002, ISBN: 0750307056.

[2] A. S. Eddington, "The Internal Constitution of the Stars", *Nature*, vol. 106, no. 2653, pp. 14–20, 1920. DOI: 10.1038/106014a0.

[3] R. Atkinson and F. G. Houtermans, "Transmutation of the Lighter Elements in Stars", *Nature*, vol. 123, no. 3102, pp. 567–568, 1929. DOI: 10.1038/123567b0.

[4] I. Langmuir, "Oscillations in Ionized Gases", *Proc. Natl. Acad. Sci.*, vol. 14, no. 8, pp. 627–637, 1928. DOI: 10.1073/PNAS.14.8.627.

[5] A. A. Vlasov, "On the Vibrational Properties of an Electron Gas", *Sov. Phys. JETP*, vol. 8, no. 3, 1946.

[6] L. Landau, "On the Vibrations of the Electronic Plasma", *Sov. Phys. JETP*, vol. 10, no. 25, 1946.

[7] H. Alfvén, *Cosmical Electrodynamics*. Oxford: Claredon Press (UK), 1950, ISBN: 1541348400.

[8] J. D. Lawson, "Some Criteria for a Power Producing Thermonuclear Reactor", *Proc. Phys. Soc. Sect. B*, vol. 70, no. 1, pp. 6–10, 1957. DOI: 10.1088/0370-1301/70/1/303.

[9] V. D. Shafranov, "The initial period in the history of nuclear fusion research at the Kurchatov Institute", *Physics-Uspekhi*, vol. 44, no. 8, pp. 835–843, 2001. DOI: 10.1070/PU2001v044n08ABEH001068.

[10] A. G. Peeters, "The bootstrap current and its consequences", *Plasma Phys. Control. Fusion*, vol. 42, no. 12B, B231–B242, 2000. DOI: 10.1088/0741-3335/42/12B/318.

[11] N. J. Peacock *et al.*, "Measurement of the Electron Temperature by Thomson Scattering in Tokamak T3", *Nature*, vol. 224, no. 5218, pp. 488–490, 1969. DOI: 10.1038/224488a0.

[12] V. Mukhovatov and V. Shafranov, "Plasma equilibrium in a Tokamak", *Nucl. Fusion*, vol. 11, no. 6, pp. 605–633, 1971. DOI: 10.1088/0029-5515/11/6/005.

[13] L. Spitzer and R. Härm, "Transport Phenomena in a Completely Ionized Gas", *Phys. Rev.*, vol. 89, no. 5, pp. 977–981, 1953. DOI: 10.1103/PhysRev.89.977.

[14] F. Wagner *et al.*, "Regime of Improved Confinement and High Beta in Neutral-Beam-Heated Divertor Discharges of the ASDEX Tokamak", *Phys. Rev. Lett.*, vol. 49, no. 19, pp. 1408–1412, 1982. DOI: 10.1103/PhysRevLett.49.1408.

[15] F. Troyon *et al.*, "MHD-Limits to Plasma Confinement", *Plasma Phys. Control. Fusion*, vol. 26, no. 1A, pp. 209–215, 1984. DOI: 10.1088/0741-3335/26/1A/319.

[16] R. Herman, *Fusion: The Search for Endless Energy*, 1st ed. Cambridge University Press (UK), 1990, p. 161, ISBN: 0521383730.

[17] JET Team, "Fusion energy production from a deuterium-tritium plasma in the JET tokamak", *Nucl. Fusion*, vol. 32, no. 2, pp. 187–203, 1992. DOI: 10.1088/0029-5515/32/2/I01.

[18] R. J. Hawryluk *et al.*, "Fusion plasma experiments on TFTR: A 20 year retrospective", *Phys. Plasmas*, vol. 5, p. 1577, 1998. DOI: 10.1063/1.872825.

[19] A. Gibson and JET Team, "Deuterium-tritium plasmas in the Joint European Torus (JET): Behavior and implications", *Phys. Plasmas*, vol. 5, p. 1839, 1998. DOI: 10.1063/1.872854.

[20] D. Meade, "50 years of fusion research", *Nucl. Fusion*, vol. 50, no. 1, p. 014 004, 2010. DOI: 10.1088/0029-5515/50/1/014004.

[21] K. Ikeda, "Progress in the ITER Physics Basis", *Nucl. Fusion*, vol. 47, no. 6, 2007. DOI: 10.1088/0029-5515/47/6/E01.

[22] F. Wagner *et al.*, "On the heating mix of ITER", *Plasma Phys. Control. Fusion*, vol. 52, no. 12, p. 124 044, 2010. DOI: 10.1088/0741-3335/52/12/124044.

[23] G. Federici *et al.*, "DEMO design activity in Europe: Progress and updates", *Fusion Eng. Des.*, vol. 136, pp. 729–741, 2018. DOI: https://doi.org/10.1016/j.fusengdes.2018.04.001.

[24] A. J. Creely *et al.*, "Overview of the SPARC tokamak", *J. Plasma Phys.*, vol. 86, no. 5, p. 865 860 502, 2020. DOI: 10.1017/S0022377820001257.

[25] International Atomic Energy Agency, *ITER Technical Basis, ITER EDA Documentation Series No. 24*. Vienna (A): IAEA, Vienna (A), 2002.

[26] M. Greenwald, "Status of the SPARC physics basis", *J. Plasma Phys.*, vol. 86, no. 5, p. 861 860 501, 2020. DOI: 10.1017/S0022377820001063.

[27] B. N. Sorbom *et al.*, "ARC: A compact, high-field, fusion nuclear science facility and demonstration power plant with demountable magnets", *Fusion Eng. Des.*, vol. 100, pp. 378–405, 2015. DOI: 10.1016/j.fusengdes.2015.07.008. arXiv: 1409.3540.

[28] C. Bissell, "A History of Automatic Control", in *Springer Handb. Autom.* S. Y. Nof, Ed., Springer Berlin Heidelberg, 2009, pp. 53–69, ISBN: 978-3-540-78831-7.

[29] J. Maxwell, "On Governors", *Proc. R. Soc. London*, vol. 16, pp. 270–283, 1868. DOI: https://doi.org/10.1098/rspl.1867.0055.

[30] E. J. Routh, *A Treatise on the Stability of a Given State of Motion: Particularly Steady Motion*, 1st ed. Macmillan, London (UK), 1877.

[31] A. M. Lyapunov, "The general problem of the stability of motion", *Int. J. Control*, vol. 55, no. 3, pp. 531–534, 1992. DOI: 10.1080/00207179208934253.

[32] H. Bode, *Network Analysis and Feedback Amplifier*, 1st ed. D. Van Nostrand company, New York (USA), 1945.

[33] J. Ziegler and N. Nichols, "Optimum Settings for Automatic Controllers", *Trans. ASME*, vol. 64, pp. 759–768, 1942.

[34] R. E. Kalman, "A New Approach to Linear Filtering and Prediction Problems", *J. Basic Eng.*, vol. 82, no. 1, pp. 35–45, 1960. DOI: 10.1115/1.3662552.

[35] A. E. Bryson, "Optimal control-1950 to 1985", *IEEE Control Syst. Mag.*, vol. 16, no. 3, pp. 26–33, 1996. DOI: 10.1109/37.506395.

[36] J. Doyle, "Analysis of feedback systems with structured uncertainties", *IEE Proc. D - Control Theory Appl.*, vol. 129, no. 6, pp. 242–250, 1982. DOI: 10.1049/ip-d.1982.0053.

[37] C. Tsironis and I. K. Giannopoulos, "Automatic control systems in tokamak plasmas: Current status and needs", *Glow Discharges Tokamaks*, pp. 1–80, 2011.

[38] E. Lazarus *et al.*, "Control of the vertical instability in tokamaks", *Nucl. Fusion*, vol. 30, no. 1, pp. 111–141, 1990. DOI: 10.1088/0029-5515/30/1/010.

[39] M. Greenwald *et al.*, "A new look at density limits in tokamaks", *Nucl. Fusion*, vol. 28, no. 12, pp. 2199–2207, 1988. DOI: 10.1088/0029-5515/28/12/009.

[40] G. Ambrosino and R. Albanese, "Magnetic control of plasma current, position, and shape in Tokamaks: a survey or modeling and control approaches", *IEEE Control Syst. Mag.*, vol. 25, no. 5, pp. 76–92, 2005. DOI: 10.1109/MCS.2005.1512797.

[41] J.-M. Moret *et al.*, "Tokamak equilibrium reconstruction code LIUQE and its real time implementation", *Fusion Eng. Des.*, vol. 91, pp. 1–15, 2015. DOI: https://doi.org/10.1016/j.fusengdes.2014.09.019.

[42] J. Ferron *et al.*, "Real time equilibrium reconstruction for tokamak discharge control", *Nucl. Fusion*, vol. 38, no. 7, pp. 1055–1066, 1998. DOI: 10.1088/0029-5515/38/7/308.

[43] G. Hommen *et al.*, "Optical boundary reconstruction of tokamak plasmas for feedback control of plasma position and shape", *Rev. Sci. Instrum.*, vol. 81, no. 11, p. 113 504, 2010. DOI: 10.1063/1.3499219.

[44] J. P. Freidberg, *Ideal MHD*. Cambridge University Press (UK), 2014, ISBN: 9781107006256. DOI: DOI:10.1017/CBO9780511795046.

[45] M. Mauel *et al.*, "Dynamics and control of resistive wall modes with magnetic feedback control coils: experiment and theory", *Nucl. Fusion*, vol. 45, no. 4, pp. 285–293, 2005. DOI: 10.1088/0029-5515/45/4/010.

[46] J. M. Hanson *et al.*, "Feedback control of the proximity to marginal RWM stability using active MHD spectroscopy", *Nucl. Fusion*, vol. 52, no. 1, p. 013 003, 2012. DOI: 10.1088/0029-5515/52/1/013003.

[47] H. Zohm, "Edge localized modes (ELMs)", *Plasma Phys. Control. Fusion*, vol. 38, no. 2, pp. 105–128, 1996. DOI: 10.1088/0741-3335/38/2/001.

[48] W. M. Solomon *et al.*, "Exploration of the Super H-mode regime on DIII-D and potential advantages for burning plasma devices", *Phys. Plasmas*, vol. 23, no. 5, p. 056 105, 2016. DOI: 10.1063/1.4944822.

[49] T. Evans *et al.*, "RMP ELM suppression in DIII-D plasmas with ITER similar shapes and collisionalities", *Nucl. Fusion*, vol. 48, no. 2, p. 024 002, 2008. DOI: 10.1088/0029-5515/48/2/024002.

[50] P. Lang *et al.*, "ELM pace making and mitigation by pellet injection in ASDEX Upgrade", *Nucl. Fusion*, vol. 44, no. 5, pp. 665–677, 2004. DOI: 10.1088/0029-5515/44/5/010.

[51] R. J. La Haye, "Neoclassical tearing modes and their control", *Phys. Plasmas*, vol. 13, no. 5, p. 055 501, 2006. DOI: 10.1063/1.2180747.

[52] T. Hender *et al.*, "Chapter 3: MHD stability, operational limits and disruptions", *Nucl. Fusion*, vol. 47, no. 6, S128–S202, 2007. DOI: 10.1088/0029-5515/47/6/S03.

[53] C. Angioni *et al.*, "Neutral beam stabilization of sawtooth oscillations in JET", *Plasma Phys. Control. Fusion*, vol. 44, no. 2, pp. 205–222, 2002. DOI: 10.1088/0741-3335/44/2/305.

[54] J. P. Graves *et al.*, "Sawtooth-Control Mechanism using Toroidally Propagating Ion-Cyclotron-Resonance Waves in Tokamaks", *Phys. Rev. Lett.*, vol. 102, no. 6, p. 65 005, 2009. DOI: 10.1103/PhysRevLett.102.065005.

[55] C. Angioni *et al.*, "Effects of localized electron heating and current drive on the sawtooth period", *Nucl. Fusion*, vol. 43, no. 6, pp. 455–468, 2003. DOI: 10.1088/0029-5515/43/6/308.

[56] J. I. Paley *et al.*, "Real time control of the sawtooth period using EC launchers", *Plasma Phys. Control. Fusion*, vol. 51, no. 5, p. 055 010, 2009. DOI: 10.1088/0741-3335/51/5/055010.

[57] F. Felici, "Real-Time Control of Tokamak Plasmas: from Control of Physics to Physics-Based Control", PhD thesis, PhD thesis no.5203, École Polytechnique Fédérale de Lausanne (EPFL), CH-1015 Lausanne, Switzerland, October 2011. DOI: dx.doi.org/10.5075/epfl-thesis-5203.

[58] A. W. Leonard, "Plasma detachment in divertor tokamaks", *Plasma Phys. Control. Fusion*, vol. 60, no. 4, p. 044 001, 2018. DOI: 10.1088/1361-6587/aaa7a9.

[59] A. Kallenbach *et al.*, "Impurity seeding for tokamak power exhaust: from present devices via ITER to DEMO", *Plasma Phys. Control. Fusion*, vol. 55, no. 12, p. 124 041, 2013. DOI: 10.1088/0741-3335/55/12/124041.

[60] T. Ravensbergen *et al.*, "Real-time feedback control of the impurity emission front in tokamak divertor plasmas", *Nat. Commun.*, vol. 12, no. 1, p. 1105, 2021. DOI: 10.1038/s41467-021-21268-3.

[61] R. Albanese *et al.*, "A MIMO architecture for integrated control of plasma shape and flux expansion for the EAST tokamak", in *2016 IEEE Conf. Control Appl.*, 2016, pp. 611–616, ISBN: VO -. DOI: 10.1109/CCA.2016.7587897.

[62] H. Anand *et al.*, "Plasma flux expansion control on the DIII-D tokamak", *Plasma Phys. Control. Fusion*, vol. 63, no. 1, p. 015 006, 2021. DOI: 10.1088/1361-6587/abc457.

[63] S. A. Silburn *et al.*, "Mitigation of divertor heat loads by strike point sweeping in high power JET discharges", *Phys. Scr.*, vol. T170, p. 014 040, 2017. DOI: 10.1088/1402-4896/aa8db1.

[64] F. Hofmann *et al.*, "Experimental and Theoretical Stability Limits of Highly Elongated Tokamak Plasmas", *Phys. Rev. Lett.*, vol. 81, no. 14, pp. 2918–2921, 1998. DOI: 10.1103/PhysRevLett.81.2918.

[65] J.-M. Moret *et al.*, "Influence of Plasma Shape on Transport in the TCV Tokamak", *Phys. Rev. Lett.*, vol. 79, no. 11, pp. 2057–2060, 1997. DOI: 10.1103/PhysRevLett.79.2057.

[66] J. B. Lister *et al.*, "Plasma control in ITER", *IEEE Control Syst. Mag.*, vol. 26, no. 2, pp. 79–91, 2006. DOI: 10.1109/MCS.2006.1615274.

[67] M. L. Walker, "Model-based decoupling control of tokamak plasmas", in *2012 Am. Control Conf.*, 2012, pp. 5029–5036, ISBN: 2378-5861 VO -. DOI: 10.1109/ACC.2012.6315244.

[68] D. Humphreys *et al.*, "Novel aspects of plasma control in ITER", *Phys. Plasmas*, vol. 22, no. 2, p. 021 806, 2015. DOI: 10.1063/1.4907901.

[69] Y. Gribov *et al.*, "Chapter 8: Plasma operation and control", *Nucl. Fusion*, vol. 47, no. 6, S385–S403, 2007. DOI: 10.1088/0029-5515/47/6/S08.

[70] B. Xiao *et al.*, "Enhancement of EAST plasma control capabilities", *Fusion Eng. Des.*, vol. 112, pp. 660–666, 2016. DOI: https://doi.org/10.1016/j.fusengdes.2016.06.004.

[71] R. Nouailletas *et al.*, "WEST Magnetic Control", in *2019 IEEE 58th Conf. Decis. Control*, 2019, pp. 3214–3219, ISBN: 2576-2370 VO -. DOI: 10.1109/CDC40024.2019.9029207.

[72] V. Mertens *et al.*, "Chapter 3: Plasma Control in ASDEX Upgrade", *Fusion Sci. Technol.*, vol. 44, no. 3, pp. 593–604, 2003. DOI: 10.13182/FST03-A401.

[73] O. Gruber *et al.*, "Position ans Shape Control on ASDEX-Upgrade", in *Proc. 17th Symp. Fusion Technol. Rome, Italy, 14&x2013;18 Sept. 1992*, C. FERRO *et al.*, Eds., Oxford: North-Holland, 1993, pp. 1042–1046, ISBN: 978-0-444-89995-8. DOI: https://doi.org/10.1016/B978-0-444-89995-8.50202-2.

[74] R. Albanese *et al.*, "Design, implementation and test of the XSC extreme shape controller in JET", *Fusion Eng. Des.*, vol. 74, no. 1-4, pp. 627–632, 2005.

[75] N. Cruz *et al.*, "Control-oriented tools for the design and validation of the JT-60SA magnetic control system", *Control Eng. Pract.*, vol. 63, pp. 81–90, 2017. DOI: https://doi.org/10.1016/j.conengprac.2017.03.009.

[76] D. A. Humphreys *et al.*, "Initial implementation of a multivariable plasma shape and position controller on the DIII-D tokamak", in *Proc. 2000. IEEE Int. Conf. Control Appl. Conf. Proc. (Cat. No.00CH37162)*, 2000, pp. 412–418, ISBN: VO -. DOI: 10.1109/CCA.2000.897459.

[77] M. Boyer *et al.*, "Plasma boundary shape control and real-time equilibrium reconstruction on NSTX-U", *Nucl. Fusion*, vol. 58, no. 3, p. 036 016, 2018. DOI: 10.1088/1741-4326/aaa4d0.

[78] S. Coda *et al.*, "Physics research on the TCV tokamak facility: from conventional to alternative scenarios and beyond", *Nucl. Fusion*, vol. 59, no. 11, p. 112 023, 2019. DOI: 10.1088/1741-4326/ab25cb.

[79] H. Anand *et al.*, "A novel plasma position and shape controller for advanced configuration development on the TCV tokamak", *Nucl. Fusion*, vol. 57, no. 12, p. 126 026, 2017. DOI: 10.1088/1741-4326/aa7f4d.

[80] J. B. Lister *et al.*, "The Control of Tokamak Configuration Variable Plasmas", *Fusion Technol.*, vol. 32, no. 3, pp. 321–373, 1997. DOI: 10.13182/FST97-A1.

[81] F. Piras *et al.*, "Snowflake divertor plasmas on TCV", *Plasma Phys. Control. Fusion*, vol. 51, no. 5, p. 055 009, 2009. DOI: 10.1088/0741-3335/51/5/055009.

[82] H. Reimerdes *et al.*, "TCV divertor upgrade for alternative magnetic configurations", *Nucl. Mater. Energy*, vol. 12, pp. 1106–1111, 2017. DOI: 10.1016/j.nme.2017.02.013.

[83] J.-M. Moret *et al.*, "Magnetic measurements on the TCV Tokamak", *Rev. Sci. Instrum.*, vol. 69, no. 6, pp. 2333–2348, 1998. DOI: 10.1063/1.1148940.

[84] F. Piras, "Extremely Shaped Plasmas to Improve the Tokamak Concept", eng, PhD thesis, PhD thesis no.5015, École Polytechnique Fédérale de Lausanne (EPFL), CH-1015 Lausanne,Switzerland, March 2011. DOI: 10.5075/epfl-thesis-5015.

[85] J.-M. Moret *et al.*, "Fast single loop diamagnetic measurements on the TCV tokamak", *Rev. Sci. Instrum.*, vol. 74, no. 11, pp. 4634–4643, 2003. DOI: 10.1063/1.1614856.

[86] O. Sauter and S. Medvedev, "Tokamak coordinate conventions: COCOS", *Comput. Phys. Commun.*, vol. 184, no. 2, pp. 293–302, 2013. DOI: https://doi.org/10.1016/j.cpc.2012.09.010.

[87] A. Favre *et al.*, "Control of highly vertically unstable plasmas in TCV with internal coils and fast power supply", in *Proc. 19th Symp. Fusion Technol. (Lisboa, Port.*, Switzerland, 1996, pp. 7–10.

[88] F. Hofmann, "FBT - a free-boundary tokamak equilibrium code for highly elongated and shaped plasmas", *Comput. Phys. Commun.*, vol. 48, no. 2, pp. 207–221, 1988. DOI: https://doi.org/10.1016/0010-4655(88)90041-0.

[89] F. Hofmann *et al.*, "Plasma shape control in TCV using MGAMS", in *22nd EPS Conf. (3-7 July 1995)*, Bournemouth (UK), pp. 17–20.

[90] J. I. Paley *et al.*, "Architecture and commissioning of the TCV distributed feedback control system", in *2010 17th IEEE-NPSS Real Time Conf. , Lisboa,*, 2010, pp. 1–6, ISBN: VO -. DOI: 10.1109/RTC.2010.5750487.

[91] H. B. Le *et al.*, "Distributed digital real-time control system for TCV tokamak", *Fusion Eng. Des.*, vol. 89, no. 3, pp. 155–164, 2014. DOI: 10.1016/j.fusengdes.2013.11.001.

[92] H. Anand *et al.*, "Distributed digital real-time control system for the TCV tokamak and its applications", *Nucl. Fusion*, vol. 57, no. 5, p. 056 005, 2017. DOI: 10.1088/1741-4326/aa6120.

[93] D-TACQ-Solutions, *D-tAcq acquisition systems*, Glasgow (Scotland,UK).

[94] M. Kong *et al.*, "Control of neoclassical tearing modes and integrated multi-actuator plasma control on TCV", *Nucl. Fusion*, vol. 59, no. 7, p. 076 035, 2019. DOI: 10.1088/1741-4326/ab1e1e.

[95] C. Galperti *et al.*, "Integration of a Real-Time Node for Magnetic Perturbations Signal Analysis in the Distributed Digital Control System of the TCV Tokamak", *IEEE Trans. Nucl. Sci.*, vol. 64, no. 6, pp. 1446–1454, 2017. DOI: 10.1109/TNS.2017.2711625.

[96] N. M. Vu *et al.*, "Tokamak-agnostic actuator management for multi-task integrated control with application to TCV and ITER", *Fusion Eng. Des.*, vol. 147, p. 111 260, 2019. DOI: 10.1016/j.fusengdes.2019.111260.

[97] M. Walker and D. Humphreys, "On feedback stabilization of the tokamak plasma vertical instability", *Automatica*, vol. 45, no. 3, pp. 665–674, 2009. DOI: 10.1016/j.automatica.2008.10.011.

[98] J. Lister *et al.*, "On locating the poloidal field coils for tokamak vertical position control", *Nucl. Fusion*, vol. 36, no. 11, pp. 1547–1560, 1996. DOI: 10.1088/0029-5515/36/11/I08.

[99] F. Hofmann *et al.*, "Feedback stabilization of axisymmetric modes in the TCV tokamak using active coils inside and outside the vacuum vessel", *Nucl. Fusion*, vol. 38, no. 3, pp. 399–408, 1998. DOI: 10.1088/0029-5515/38/3/306.

[100] J. I. Paley and S. Coda, "Real time control of the plasma current and elongation in tokamaks using ECRH actuators", *Plasma Phys. Control. Fusion*, vol. 49, no. 10, pp. 1735–1746, 2007. DOI: 10.1088/0741-3335/49/10/010.

[101] S. Skogestad and I. Postlethwaite, *Multivariable Feedback Control - Analysis and Design*, 2nd. John Wiley & Sons Ltd, Hoboken, New Jersey (USA), 2005, ISBN: 978-0-470-01167-6.

[102] I. H. Hutchinson *et al.*, "Plasma Shape Control: A General Approach and Its Application to Alcator C-Mod", *Fusion Technol.*, vol. 30, no. 2, pp. 137–150, 1996. DOI: 10.13182/FST96-A30746.

[103] R. Albanese and G. Ambrosino, "Current, position, and shape control of tokamak plasmas: a literature review", in *Proc. 2000. IEEE Int. Conf. Control Appl. Conf. Proc. (Cat. No.00CH37162)*, 2000, pp. 385–394, ISBN: VO -. DOI: 10.1109/CCA. 2000.897455.

[104] N. Cruz *et al.*, "An optimal real-time controller for vertical plasma stabilization", in *2014 19th IEEE-NPSS Real Time Conf.*, IEEE, 2014, pp. 1–5, ISBN: 978-1-4799-3659-5. DOI: 10.1109/RTC.2014.7097483.

[105] A. Coutlis *et al.*, "Measurement of the open loop plasma equilibrium response in TCV", *Nucl. Fusion*, vol. 39, no. 5, pp. 663–683, 1999. DOI: 10.1088/0029-5515/39/5/307.

[106] D. A. Humphreys and I. H. Hutchinson, "Filament-circuit analysis of Alcator C-MOD vertical stability", *MIT Plasma Sci. Fusion Cent.*, 1989.

[107] J. Wesson, "Hydromagnetic stability of tokamaks", *Nucl. Fusion*, vol. 18, no. 1, pp. 87–132, 1978. DOI: 10.1088/0029-5515/18/1/010.

[108] J.-Y. Favez, "Enhancing the control of tokamaks via a continuos nonlinear control law", PhD thesis, PhD thesis no.3034, École Polytechnique Fédérale de Lausanne (EPFL), CH-1015 Lausanne, Switzerland, 2004.

[109] J. Lister *et al.*, "Experimental study of the vertical stability of high decay index plasmas in the DIII-D tokamak", *Nucl. Fusion*, vol. 30, no. 11, pp. 2349–2366, 1990. DOI: 10.1088/0029-5515/30/11/011.

[110] A. Portone, "The stability margin of elongated plasmas", *Nucl. Fusion*, vol. 45, no. 8, pp. 926–932, 2005. DOI: 10.1088/0029-5515/45/8/021.

[111] R. Albanese *et al.*, "Analysis of vertical instabilities in air core tokamaks in the presence of three-dimensional conducting structures", *IEEE Trans. Magn.*, vol. 26, no. 2, pp. 853–856, 1990. DOI: 10.1109/20.106451.

[112] D. Humphreys *et al.*, "Experimental vertical stability studies for ITER performance and design guidance", *Nucl. Fusion*, vol. 49, no. 11, p. 115 003, 2009. DOI: 10.1088/0029-5515/49/11/115003.

[113] D. C. Youla *et al.*, "Single-loop feedback-stabilization of linear multivariable dynamical plants", *Automatica*, vol. 10, no. 2, pp. 159–173, 1974. DOI: 10.1016/0005-1098(74)90021-1.

[114] M. J. Beelen, *Stability analysis of velocity feedback for the plasma vertical instability in fusion tokamaks*, M. L. Walker *et al.*, Eds., Eindhoven, 2010.

[115] F. Hofmann *et al.*, "Vertical position control in TCV: Comparison of model predictions with experimental results", *Nucl. Fusion*, vol. 40, no. 4, pp. 767–774, 2000. DOI: 10.1088/0029-5515/40/4/302.

[116] M. L. Walker and D. A. Humphreys, "Valid Coordinate Systems for Linearized Plasma Shape Response Models in Tokamaks", *Fusion Sci. Technol.*, vol. 50, no. 4, pp. 473–489, 2006. DOI: 10.13182/FST06-A1271.

[117] B. Kliem and T. Török, "Torus Instability", *Phys. Rev. Lett.*, vol. 96, no. 25, p. 255 002, 2006. DOI: 10.1103/PhysRevLett.96.255002.

[118] D. Fasel, "High current high voltage power supplies in the context of fusion", in, EPFL Doctoral School, Course on Fusion Technology (2019).

[119] A. Langelaan, "Modelling of the FPS for the internal coils and investigating controller discretization effects in TCV", PhD thesis, Internal report INT 214/21, EPFL-SPC, Lausanne, Switzerland (2019).

[120] S. M. Osovetz *et al.*, "Plasma loop in a transverse magnetic field", *Proc. Second United Nations Int. Conf. Peac. uses At. energy (IAEA, Geneva)*, vol. 32, pp. 311–323, 1958.

[121] R. Albanese and F. Villone, "The linearized CREATE-L plasma response model for the control of current, position and shape in tokamaks", *Nucl. Fusion*, vol. 38, no. 5, pp. 723–738, 1998. DOI: 10.1088/0029-5515/38/5/307.

[122] F. Carpanese, "Development of free-boundary equilibrium and transport solvers for simulation and real-time interpretation of tokamak experiments", PhD thesis, PhD thesis (submitted), École Polytechnique Fédérale de Lausanne (EPFL), CH-1015 Lausanne, Switzerland, 2021, 2021.

[123] R. Albanese *et al.*, "CREATE-NL+: A robust control-oriented free boundary dynamic plasma equilibrium solver", *Fusion Eng. Des.*, vol. 96-97, pp. 664–667, 2015. DOI: https://doi.org/10.1016/j.fusengdes.2015.06.162.

[124] R. R. Khayrutdinov and V. E. Lukash, "Studies of Plasma Equilibrium and Transport in a Tokamak Fusion Device with the Inverse-Variable Technique", *J. Comput. Phys.*, vol. 109, no. 2, pp. 193–201, 1993. DOI: https://doi.org/10.1006/jcph.1993.1211.

[125] H. Heumann *et al.*, "Quasi-static free-boundary equilibrium of toroidal plasma with CEDRES++: Computational methods and applications", *J. Plasma Phys.*, vol. 81, no. 3, p. 905 810 301, 2015. DOI: DOI:10.1017/S0022377814001251.

[126] G. Ambrosino *et al.*, "Design of the Plasma Position and Shape Control in the ITER Tokamak Using In-Vessel Coils", *IEEE Trans. Plasma Sci.*, vol. 37, no. 7, pp. 1324–1331, 2009. DOI: 10.1109/TPS.2009.2021476.

[127] G. Ambrosino *et al.*, "Plasma Vertical Stabilization in the ITER Tokamak via Constrained Static Output Feedback", *IEEE Trans. Control Syst. Technol.*, vol. 19, no. 2, pp. 376–381, 2011. DOI: 10.1109/TCST.2010.2042601.

[128] R. Albanese *et al.*, "ITER-like vertical stabilization system for the EAST Tokamak", *Nucl. Fusion*, vol. 57, no. 8, p. 086 039, 2017. DOI: 10.1088/1741-4326/aa7a78.

[129] S. H. Hahn *et al.*, "Measuring and extending vertical stabilization controllability of KSTAR", in *26th IAEA Fusion Energy Conf. Kyoto, Japan EX/P4-12*, 2006.

[130] F. Sartori *et al.*, "The PCU JET Plasma Vertical Stabilization control system", *Fusion Eng. Des.*, vol. 85, no. 3, pp. 438–442, 2010. DOI: https://doi.org/10.1016/j. fusengdes.2010.02.007.

[131] D. A. Humphreys *et al.*, "DIII-D Integrated plasma control solutions for ITER and next-generation tokamaks", *Fusion Eng. Des.*, vol. 83, no. 2, pp. 193–197, 2008. DOI: https://doi.org/10.1016/j.fusengdes.2008.01.012.

[132] M. L. Walker *et al.*, "Control of plasma poloidal shape and position in the DIII-D tokamak", in *Proc. 36th IEEE Conf. Decis. Control*, vol. 4, IEEE, 1997, pp. 3703–3708, ISBN: 0780341872.

[133] M. L. Walker *et al.*, "Implementation of model-based multivariable control on DIII–D", *Fusion Eng. Des.*, vol. 56-57, pp. 727–731, 2001. DOI: https://doi.org/10. 1016/S0920-3796(01)00393-3.

[134] E. Kolemen *et al.*, "Plasma modelling results and shape control improvements for NSTX", *Nucl. Fusion*, vol. 51, no. 11, p. 113 024, 2011. DOI: 10.1088/0029-5515/51/11/113024.

[135] A. Portone, "Active and passive stabilization of n = 0 RWMs in future tokamak devices", *Nucl. Fusion*, vol. 57, no. 12, p. 126 060, 2017. DOI: 10.1088/1741-4326/aa8386.

[136] K. Havre and S. Skogestad, "Selection of variables for stabilizing control using pole vectors", *IEEE Trans. Automat. Contr.*, vol. 48, no. 8, pp. 1393–1398, 2003. DOI: 10.1109/TAC.2003.816062.

[137] D. Ward and F. Hofmann, "Active feedback stabilization of axisymmetric modes in highly elongated tokamak plasmas", *Nucl. Fusion*, vol. 34, no. 3, pp. 401–415, 1994. DOI: 10.1088/0029-5515/34/3/I08.

[138] J. Doyle, "Guaranteed margins for LQG regulators", *IEEE Trans. Automat. Contr.*, vol. 23, no. 4, pp. 756–757, 1978. DOI: 10.1109/TAC.1978.1101812.

[139] J. C. Doyle *et al.*, "State-space solutions to standard H-2 and H-infinity control problems", *IEEE Trans. Automat. Contr.*, vol. 34, no. 8, pp. 831–847, 1989. DOI: 10.1109/9.29425.

[140] M. M. M. Al-Husari *et al.*, "Vertical stabilisation of Tokamak plasmas", in *Proc. 30th IEEE Conf. Decis. Control*, 1991, 1165–1170 vol.2, ISBN: VO -. DOI: 10.1109/ CDC.1991.261545.

[141] P. Vyas *et al.*, "Vertical Position Control on COMPASS-D", *Fusion Technol.*, vol. 33, no. 2, pp. 97–105, 1998. DOI: 10.13182/FST98-A20.

[142]   X. Liu *et al.*, "H-infinity Loop Shaping Control for Plasma Vertical Position Insta-bility on QUEST", *Plasma Sci. Technol.*, vol. 15, no. 3, pp. 295–299, 2013. DOI: 10.1088/1009-0630/15/3/21.

[143]   Y. V. Mitrishkin *et al.*, "Stabilization of unstable vertical position of plasma in T-15 tokamak. I", *Autom. Remote Control*, vol. 75, no. 2, pp. 281–293, 2014. DOI: 10.1134/S0005117914020088.

[144]   R. Nouailletas *et al.*, "Robust Vertical Plasma Stabilization of the future tungsten divertor configuration of Tore Supra", *IFAC Proc. Vol.*, vol. 47, no. 3, pp. 1349–1354, 2014. DOI: https://doi.org/10.3182/20140824-6-ZA-1003.01521.

[145]   M. Ariola *et al.*, "Design and experimental testing of a robust multivariable controller on a tokamak", *IEEE Trans. Control Syst. Technol.*, vol. 10, no. 5, pp. 646–653, 2002. DOI: 10.1109/TCST.2002.801805.

[146]   Y. V. Mitrishkin *et al.*, "Hierarchical robust switching control method with the Improved Moving Filaments equilibrium reconstruction code in the feedback for tokamak plasma shape", *Fusion Eng. Des.*, vol. 138, pp. 138–150, 2019. DOI: https://doi.org/10.1016/j.fusengdes.2018.10.031.

[147]   P. Apkarian and D. Noll, "Nonsmooth H-infinity Synthesis", *IEEE Trans. Automat. Contr.*, vol. 51, no. 1, pp. 71–86, 2006. DOI: 10.1109/TAC.2005.860290.

[148]   MathWorks, *Matlab 2019a*, Natick, Massachusetts (USA).

[149]   H. Grad and H. Rubin, "Hydromagnetic equilibria and force-free fields", *Proc. Second United Nations Int. Conf. Peac. uses At. energy (IAEA, Geneva)*, vol. 31, p. 190, 1958.

[150]   V. Shafranov, "On Magnetohydrodynamical Equilibrium Configurations", *Sov. Phys. JETP*, vol. 6, no. 3, p. 545, 1958.

[151]   T. Verdonschot, "Enhanced magnetic control of tokamak plasma using loop-shaping techniques", PhD thesis, Graduation Project CST 2016.138, TU/e, Netherlands, October 2016.

[152]   J. C. Maxwell, *A Treatise on Electricity and Magnetism (vol. 2)*. Oxford University Press (UK), 1873.

Acknowledgements

This PhD has been a long and wonderful journey in an immense sea of knowledge that previously I could just observe from the seashore. Embarking for this trip was difficult but being part of the outstanding SPC crew allowed me facing any challenge and living some of the best adventures of my scientific and personal life. I cannot stress enough the pivotal role my supervisors had in this experience and the admiration I have for them as researchers and as persons.

I consider Stefano Coda an exceptional scientist, characterized by a passion for his work that emerges from his composed attitude in each and every of his actions and words. Among his numerous qualities, I always admired his ability to transmit his serenity every time we had a conversation. When the storm was rising, he could always point me in the right direction with a firm and reliable adjustment of the course. Thank you for teaching me how to learn from experience, for always trusting my work and for greatly improving my English. And most of all thank you for solving my issues with the TCV control system with your expertise, which from my point of view is still closer to magic than to science.

I was incredibly lucky to have had a supervisor like Federico Felici, who was always leading from the front and motivating me to do my best. Thank you for your infinite patience, for your constant availability and for your tireless attention to the details of my work. Your skillful mentoring and scientific enthusiasm slowly transformed me in a way I can see only now into a better control engineer. You taught me not only how to program properly but more importantly how to realize my ideas and to react to the unexpected, which I consider the most valuable skills in experimental science. Working together was an awe-inspiring experience. I really hope to have learnt as much as I could from you, not only on tokamak operations.

Thank you for the opportunity you gave me. I will always remember our exchanges, from the first one in the control room during my interview, to the last (remote) one in the final hours of my thesis writing.

For all the work on the SCD, I want to thank Cristian Galperti, who maintains such a complex system and was willing at any time to share his knowledge and passion with a young PhD student like me. Cristian is one of the kindest persons I met at SPC, his support was fundamental for my experiments and for my formation.

197

Acknowledgements

The Swiss Plasma Center is an extraordinary environment for a PhD, and performing experimental work on a complex machine such as TCV requires a great team that I am pleased and honored to have joined. Thanks to the people who give their best every day in and out of the control room and who were always available to help me. Out of all the amazing PhD colleagues I had (shoutout to PPH 277, hands down the best office) I am grateful to have met Lorenzo who was the best fellow in this adventure, both in the darkest and in the brightest times. And thanks also to Nico for the deep conversations, for the bad movies and for always pushing my limits a step further. See you on Thursday.

I want to thank as well the postdocs and in particular Matteo, Umar and Davide along with Mateusz for showing me how to enjoy all aspects of the researcher's life in and out of the lab, especially in the mountains. Keep taking care of the new PhD students! And thanks to Damiano and Timo, that made the beginning of my PhD journey in the Netherlands a memorable adventure, and to Peter, that helped me start it in the best way.

I am grateful to have spent a great time with Alessandro (in particular for his patience in the last months), Francesco, Matteo and Tania that were fantastic flatmates, colleagues and, of course, friends. And my thoughts go as well to my unofficial colocs Anne-Charlotte and Marco: thank you for the best soirées in Lausanne and for constantly trying to teach me some French.

I am also very happy that I could maintain some precious long-term bonds with those I knew before moving to Switzerland, that motivated me in the most different ways during this journey.

Therefore, thank you Edo and Sonia for inspiring me with your proactive life in and out of Poli and EPFL. One day I will discover your secret source of energy.

Furthermore, thanks to Stoipiz, Giangi, Raffo, Fante and Giulio, with whom I have been now sharing over half of my life. And to Alessandro, Federico and Luca whom I have known for as long as I can remember. I am also grateful to Peppo and Kiav, who travelled a lot to hike with me here, and Fabio for always finding some time for me when I was back.

I would also like to thank Hebron, Beppe, Giacomo[3] and Prisco: our trips, reunions and calls were really important to remind me of life outside of academia (and of the good ol' times). I am delighted that we always managed to keep the fire burning.

Moreover, a special acknowledgement to Miriam for making me travel and discover some very good music, whose importance is hard to overstate during such hard times.

A ship is not built to remain in the harbor, and I did have the opportunity to explore a lot. But when the fatigue was too much, I knew I could always sail back home. I am therefore grateful to my parents Renzo and Liliana that were always encouraging me to pursue my goals and always ready to support me when I needed them. And thanks to my family: they were always warmly welcoming me when I was returning for just a few days, as if I never left. Despite my long absences, my thoughts were often with you.

And finally, thanks to Marie who was for me a safe island in the hurricane.

Lausanne, 14th April 2021

Federico Pesamosca

Italian, born on 1st June 1991

federico.pesamosca@gmail.com

RESEARCH EXPERIENCE

École Polytechnique Fédérale de Lausanne (EPFL)   Oct 2016 - present
Swiss Plasma Center, Lausanne, Switzerland

PhD student in Plasma Physics

- Experimental research on real time control of TCV tokamak plasmas.
- Active work on the TCV tokamak analog and digital control systems.
- Focus on optimization of the magnetic controller for plasma shape and position.
- Advisors: Dr. Federico Felici, Dr. Stefano Coda.

Max Planck Institute for Plasma Physics   Sep 2015 - Mar 2016
Garching bei München, Germany

Internship student

- Development of a nonlinear dynamical model for the study of plasma edge equilibrium bifurcation during the L-H transition.
- Data analysis on the ASDEX-Upgrade tokamak.
- Supported by EUROFUSION: FuseNet Master Student Internship Support.
- Advisors: Prof. Matteo Passoni, Dr. Peter Manz.

EDUCATION

Eindhoven University of Technology (TU/e), Netherlands Sep 2016 – Feb 2017
Visiting graduate student, GPA: 8.55/10
Relevant coursework:
Control and operations of tokamaks, Robust control, Optimal control

Polytechnic University of Milan, Italy   Sep 2013 - Apr 2016
M.Sc in Nuclear Engineering, GPA: 110/110 cum Laude
Relevant coursework:
Plasma physics, Nuclear design and technology, Heat and Mass Transfer

ETH Zürich, Switzerland   Feb 2014 – Aug 2014
ERASMUS Exchange Semester, GPA: 5.75/6.00
Relevant Coursework:
Nonlinear dynamics and chaos, Nuclear fuels and materials, CFD

Polytechnic University of Milan, Italy   Sep 2010 – Sep 2013
B. Sc. in Energy Engineering, GPA: 110/110 cum Laude

Conference contributions

62nd Annual Meeting of the APS DPP, virtual conference   Nov 09-13, 2020
F. Pesamosca, F. Felici, S. Coda, C. Galperti (poster)
"Improved vertical control by optimal actuator selection on TCV"

24th Workshop on MHD Stability Control, New York, USA   Oct 28-30, 2019
F. Pesamosca, F. Felici, S. Coda, C. Galperti(contributed presentation)
"Optimized decoupled control of the axisymmetric n=0 plasma instability in TCV"

61st Annual Meeting of the APS DPP, Ft. Lauderdale, USA   Oct 21–25, 2019
F. Pesamosca, F. Felici, S. Coda, C. Galperti (poster)
"Decoupling shape and position control at TCV"

45th Conference on Plasma Physics (EPS), Prague, Czechia   Jul 02-06, 2018
F. Pesamosca, F. Felici, S. Coda, H. Anand (poster)
"A generalized plasma shape and position controller for the TCV tokamak"

Publications

First Author
F. Pesamosca *et al.* (2021) "Improved plasma vertical position control on TCV using model-based optimized controller synthesis" Submitted to: *Fusion Sci. Technol.*

Co-authored
M. Kong *et al.* (2019) "Control of neoclassical tearing modes and integrated multi-actuator plasma control on TCV" In: *Nucl. Fusion* **59** 076035

Public service, outreach and awards

École Polytechnique Fédérale de Lausanne (EPFL)   Sep 2018 – Jul 2020
Elected PhD student representative for the doctoral program in Physics

Consorzio RFX, Padua, Italy   Aug 2016
Prize for M.Sc. thesis in physics of plasmas and thermonuclear controlled fusion 2016

Boy Scouts of Italy AGESCI, Udine and Milan, Italy   Sep 2007 – Aug 2012
Organising member for summer camps and youth activities

Teaching experience

École Polytechnique Fédérale de Lausanne (EPFL),   Feb 2017 – Mar 2020
Selected teaching assistant for exercise sessions, designing and grading exams

- Control and Operations of Tokamaks, doctoral course (Dr. F. Felici)
- General Physics I, Mechanics (Dr. J.-P. Hogge)
- General Physics II, Thermodynamics (Prof. A. Fasoli, Prof. I. Furno)

Skills

Languages: Italian (native), English (fluent), French (working), German (basic)
Software: Matlab and Simulink, Python, Inkscape, MS Office, LaTeX